VNIVERSITAT DE VALÈNCIA

SYNTHESIS AND CHARACTERIZATION OF MULTIFUNCTIONAL NANOCOMPOSITE-BASED MATERIALS FOR NEXT-GEN ENERGY SOLUTIONS

Programa de Doctorat en Química
Tesi Doctoral

Jaume Noguera Gómez

Director: Dr. Rafael Abargues López

Co-director: Dr. Pablo P. Boix

Departament de Química Inorgànica
Facultat de Química
Universitat de València

December 2024

El Dr. **Rafael Abargues López**, professor permanent laboral de la Universitat de València en l'Institut de Ciència de Materials de la Universitat de València (ICMUV), i Dr. **Pablo P. Boix**, Científic Titular del CSIC a l'Intitut de Tecnología Química de la Universitat Politécnica de València (ITQ).

CERTIFIQUEN:

Que la memòria presentada per l'estudiant de doctorat **Jaume Noguera Gómez**, amb el títol "*Synthesis and characterization of multifunctional nanocomposite-based materials for next-gen energy solutions*", correspon a la seua Tesi Doctoral i ha estat realitzada sota la seua direcció i co-direcció, autoritzant mitjançant aquest escrit la presentació d'aquesta.

Paterna, Desembre de 2024

Rafael Abargues López
(Director i Tutor)

Pablo P. Boix
(Co-director)

Membres del tribunal

	Titulars	Suplents
President	Prof. Iván Mora Seró	Prof. Sofia Masi
Secretari	Prof. Michele Sessolo	Dra. Teresa Ripollés Sanchis
Vocal	Prof. Mónica Morales Masis	Prof. Annalisa Bruno

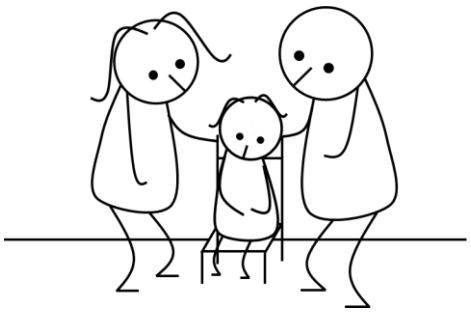

Als de casa.

Gràcies.

“Imagination will often carry us to worlds that never were, but without it we go nowhere.”

Carl Sagan

“It's the questions we can't answer that teach us the most. They teach us how to think. If you give a man an answer, all he gains is a little fact. But give him a question and he'll look for his own answers.”

The Kingkiller Chronicle

Acknowledgements - Agraïments

Aquestes línies – que ja se'm fan bola només de pensar-les –, versaran sobre la part que sens dubte és l'eix central d'aquesta tesi: la gent. M'he promès i repromès, què per tal de mantenir la naturalitat evitaré corregir-me *ad infinitum*. Ja d'entrada, l'idioma serà més bé una mescla i la prosa anirà saltejant entre presumptuosa, farragosa i desordenada: a la babalà! (Perdoneu, no ho faig a posta). Açò cavalca entre un "gràcies, au s'ha acabat!", i allò, que, si bé no he dit, voldria que sabéssiu. En realitat tendisc a pensar, més bé, que açò és en realitat una mena d'arxiu personal per a una futura versió de Jaume, explicant-li: com va començar tot (amb una èpica inexistent). Ahí va.

El primer dels agraïments és per a Rafael Abargues. Si algú és la peça clau i l'inici d'aquesta tesi, són ell i la seua contagiosa passió per fer ciència. Rafa, muchas gracias por el apoyo y la confianza todos estos años. Trabajar contigo ha sido todo un enorme placer. Sin duda, la ilusión que transmites en cada idea, resultado (*ooojo!*) o experimento han sido un combustible vital para pelear cada día por entender un poco más el mundo de los *thin films* y nanocomposites. Estas pocas líneas no hacen gala de la fortuna de tenerte como tutor. Por todo, muchas gracias.

El segon dels agraïments és per a Pablo P. Boix. Encara recorde aquells primers dies fent cafè al teu despatx i començant a veure créixer el grup. Acostumes a intentar no ser la persona més llesta de la sala, però, i encara que em coste reconèixer-ho, gran part del temps està molt renyit. Pel suport, la confiança, i per les lliçons de vida però encara més per les de ciència, moltes gràcies, Pablo.

Antes de seguir, me gustaría mencionar que tutores hay de diversa índole. Están aquellos que aparecen sobre el papel (los que firman), y aquellos que, sin serlo *per se*, brindan su ayuda y actúan como tales. En este sentido, mi más sincero agradecimiento en estos años a figuras como la de Juan Martínez, Alejandro Molina y Pedro Javier Rodríguez. Vuestro apoyo y consejos han sido también parte del éxito de esta tesis.

Una vegada agraïdes les persones que han influït a nivell científic i personal cal agrair també als qui fan possible que tot l'entramat s'hi mantinga en peu.

Al personal de secretaria, Maria Ángeles Yuste y Amparo Alarcón, por su inagotable paciencia y su inmensa ayuda durante todos estos años. El Instituto de Ciencia de Materiales es lo que es gracias a vosotras. De igual forma, gracias a Julián Heredero, Lola Garrido, José Serrano, Hamid, Setatira Gorji, Guillermo, Jamal, Pedro Amorós, Clara Gómez, Sonia Murcia, Ana Cros, Núria Garro, Juan Francisco Sánchez, Maria del Carmen Asensio, Rafa Muñoz, Silver Hamil, Mahesh, Jesús, Parmenio, Jorge Cervantes, Isaac Suárez, Sandra, Archit Dhingra, Joao Fonseca, Borja Caja, Sixto Giménez, Vladimir, Miguel García y Rafael Sánchez. Seguro me dejo a mucha gente, a todos y al curioso lector, gracias.

Mención especial merece David Vie, a quién le quiero agradecer muchos momentos de esta tesis. Ser un *crack* en tantos aspectos de la vida no debe ser un trabajo fácil. Este *pájaro* te estará en eterno agradecimiento. No quiero olvidarme de agradecer a la gente de los *Lunes de Fútbol*; las risas y postpartidos han hecho más llevadera la elaboración de esta tesis.

En aquest punt voldria moure'm allí on comença tot, i m'agradaria agrair a la gent del poble que de forma directa o indirecta m'han influït al llarg dels anys.
A tota la gent del Club Basket Ondara *CBO* per acollir-me sempre i fer-me sentir part de l'equip, així fora visitant el Pavelló cada molt més temps del que m'agradaria. Gràcies.
A tota la gent del grup de *Bestial*; sempre és un plaer retrobar-nos i gaudir de veure per on vos porta la vida. Sou un grapat de gent bonica de debò! A tots, gràcies.
Al meu grup d'amics de S*enyors*, Marc, Adrià, Josep i Christian. Veient el temps amb perspectiva pense que soc un afortunat per haver crescut al vostre costat. Ací teniu un amic per al que necessiteu. Gràcies.

Moviendo el foco de nuevo hacia Valencia me gustaría agradecer de forma personal, por muchos momentos en estos años de tesis, a Paco y Jaume. Ya desde el máster de nanociencia los años que han ido sucediendo han sido un camino más fácil al tener vuestras voces cerca. Tenéis el arte de conjugar un gran sentido del humor con una gran inteligencia, supongo que van de la mano. A los dos, mil gracias. Os deseo lo mejor del mundo.

At this point, before shifting my focus to the people in my laboratory, I want

to express my heartfelt gratitude to everyone I had the pleasure of meeting during my internship in the beautiful Lausanne. First and foremost, I extend my deepest thanks to Professor Michael Grätzel for accepting me as a visiting student in the Laboratory of Photonics and Interfaces at EPFL. This opportunity was truly transformative for me. A special and well-deserved thank you goes to Sandy Sanchez, who not only hosted me but also introduced me to the fascinating world of Flash Infrared Annealing. Sandy, I'm incredibly grateful for everything you taught me and for welcoming me into your lab.
To Algirdas, you truly made my stay more enjoyable, playing basketball and hanging out with you is something I still miss today.
To Anand, thank you for sharing your time, ideas, the nice hikes and the deep conversations we had about everything from cinema to the meaning of life.
I also want to thank all the people who made me feel at home from the very beginning. Ghewa, Massaud, George, Arman, Lukas, Felix, Brendan, Ursula, Rebecca, Socci, and Esther, thank you for your friendship, support, and for making this journey so memorable. I'm forever grateful. *Merci*.

Llegando ya a casi al final de los agradecimientos me gustaría agradecer a los actuales y antiguos participantes del grupo. Gente que tanto del *umdo* como del *ABX$_3$Lab* han ayudado de una forma u otra en hacer más fáciles los días en el instituto. Quiero agradecer especialmente a Juan Navarro Arenas y a sus todavía visibles obras del despacho; a Daniel Andrés Penares por compartir pasión por cine, tecnología, videojuegos, pero sobre todo por ayudarme con contratos, memorias, convocatorias, documentos y en resumen por iniciarme en el mundo académico siempre con la broma por delante (muchas gracias Dani!); a Raúl Iván Sánchez quien ya ha demostrado con su dedicación que no tendrá que ir a la *escuela de payasos*; a Clara Aranda y Cristina Momblona, por ser dos científicas que valen su peso en "Au"; a Marta Vallés por bajarme los pies a la tierra y acompañarme metido en la *glovebox*, consiguiendo muchas veces capear el temporal entre risas con una simple referencia a los *monigotes* amarillos; a Alejandro Saura por su predisposición a ayudar y su paciencia infinita. En este punto no puedo empezar a nombraros al resto (la pequeña familia) sin antes agradeceros todos los momentos vividos juntos. Así pues, gracias a Noemí Farinós, por organizar siempre todo con ilusión; a Omar E. Solis, solo los mejores tienen un busto en su pueblo; a Víctor Sagra por su cabezonería pero a la vez enorme disposición para todo; a Miriam Mínguez por su *justo y a veces correcto* sentido del humor y por demostrar

que no es la cantidad sinó la calidad del trabajo; a Ismael Fernández por ser el verdadero *Ser de luz* y por mostrar siempre la cara bonita de la vida, como tu bien dices *chumacho* no hay resultados malos o buenos, hay *resultados*; a Pablo Franco le podría dedicar un párrafo entero y aun así me quedaría corto, gracias por ser un pilar en muchos momentos de esta tesis y por tu sinceridad, espero haberte aportado la mitad que tú a mí; ya por último a uno de los más antiguos compañeros de batalla, a Rodolfo E. Canet hacerle saber que le admiro en muchos aspectos de la vida, como persona y como científico, gracias por todos los ratos y buenas conversaciones. En este punto, citando el **First Ideal**: *Journey before destination*, os agradezco el haber sido parte de este viaje. Os deseo lo mejor en vuestros futuros pasos.

Quasi al final d'aquestos agraïments cal tornar a casa, i ací voldria referir-me a Mar. Gràcies per tot el suport i afecte durant aquestos anys. En comparació amb la de la resta, la teua faena ha estat la més difícil: la del que no s'hi veu. Tu més bé que ningú has viscut els alts i baixos i saps ben bé de què va açò, i tot això has posat gana, il·lusió i compromís en aquestos anys. Aquesta tesi és, en gran part, teua també. Per tot, gràcies. T'estime.

En els darrers, però no menys importants agraïments, voldria donar les gràcies als de casa. Mentre jo estic ací en València intentant treure la millor versió, i pensant en un següent pas, vosaltres esteu ahí, en casa, lluitant cada dia. A ma mare, Belinda, esta tesi va per tu, per confiar en mi i per haver-me-ho donat tot en aquesta vida. A mon pare, Jose, gràcies per haver-me ensenyat a ser lluitador, curiós i conscient, actituds que sens dubte han influït en aquesta tesi. És una gran sort ser el vostre fill. Estes últimes línies son per a la menuda de casa, a Mireia, moltes gràcies.

Aquesta tesi és per a vosaltres, és el millor que tinc fins al moment.

Jaume.

Abstract

Metal halide perovskites have garnered significant attention due to their outstanding optoelectronic properties, positioning them as promising candidates for a wide range of applications, from light-emission technologies to photovoltaics. Despite their potential, practical implementation faces challenges such as stability issues, material degradation, and scalability. In this context, this Thesis investigates innovative strategies to address these challenges, emphasizing the controlled synthesis of perovskite nanocrystals within a metal-organic host matrixes and extending this methodology to explore their potential in perovskite solar cells.

Chapters 4, 5 and 6 explore the potential of the in situ synthesis of perovskite nanocrystals within host matrixes, effectively addressing the limitations associated with conventional synthetic methods. This approach leverages critical parameters, including precursor concentration and ambient conditions, to precisely control crystallization dynamics, enabling fine-tuning of nanoparticle size and emission properties. Building upon this foundation, a detailed protocol is developed for synthesizing $MAPbBr_3$ nanocrystals within a $Ni(AcO)_2$ matrix, ensuring reproducibility and scalability. The protocol outlines how particle size, and hence optical characteristics, can be finely tuned during the crystallization process. The approach demonstrates versatility by enabling the synthesis of nanocrystals with diverse halide compositions, such as chloride, bromide, iodide, and their mixtures, while significantly enhancing stability against degradation factors like oxygen, UV light, temperature, and moisture. Additionally, the water-mediated crystallization mechanism of the nanocrystals is further explored, revealing that humid conditions facilitate the transformation of 0D MA_4PbBr_6 structures into highly emissive 3D $MAPbBr_3$ NCs. The acetate plays a pivotal role as a mediator, driving hydroxide ions generation and subsequent trap passivation. Detailed spectroscopic and structural analyzes elucidate the reversible role of hydroxide ions in enhancing stability and optical performance. In Chapter 7, the incorporation of $Ni(AcO)_2$ to stabilize $CsPbI_3$, a promising inorganic perovskite with an optimal bandgap (~1.73 eV) for solar cells, is further explored. Devices fabricated using this approach demonstrated power conversion efficiencies exceeding 12%, with prolonged operational stability of over

600 hours at MPPT under controlled inert conditions. Furthermore, efficiencies of 15–17% under white illumination highlight their potential for indoor energy harvesting.

Overall, these findings present a robust, scalable, and cost-effective method for synthesizing diverse perovskite semiconductor materials, paving the way for their integration into next-gen optoelectronic devices.

Table of Contents

Chapter 1: Introduction

Abstract

This chapter provides an overview and analyzes one of the major challenges that humanity is facing: climate change. It is important to note that the intention is not to leave the reader with a sense of despair. Quite the opposite. It is crucial to articulate the narrative around this issue clearly and objectively, emphasizing that inaction will lead us to a point of no return. Thus, abandoning short-term thinking, prioritizing delocalization, and investing in the development and improvement of materials for energy solutions are essential steps.

1.1 SETTING THE SCENE

The concept of Planetary Boundaries was first introduced by Johan Rockström and a group of 28 leading scientists in 2009.[1] The framework defines limits within which humanity can safely operate to avoid catastrophic environmental changes.[2] These boundaries (described in Table 1), grounded in scientific research, identify critical thresholds in key Earth system processes. Crossing one of them risks triggering abrupt non-linear changes.

Table 1. Planetary boundaries.

Boundaries	Description
Climate change	Increased greenhouse gases trap more heat, raising global temperatures and altering climate patterns.
Novel entities	Synthetic chemicals, microplastics, and GMOs are released into the environment without sufficient testing, surpassing safe levels.
Stratospheric ozone	The ozone layer is recovering but remains below mid-20th-century levels, staying within safe limits.
Atmospheric aerosol loading	Human activities increase airborne particles that affect climate; the current level remains within safe bounds.
Ocean acidification	Rising ocean acidity due to CO_2 absorption impacts marine life and carbon storage, nearing the unsafe threshold.
Biogeochemical flows	Excessive nitrogen and phosphorus cycles are disrupted by human activity, breaching safe levels
Freshwater use	Human activities have disrupted global water cycles, exceeding safe limits for rivers and soil moisture.
Land system change	Deforestation and urbanization reduce natural carbon sinks and habitats, crossing the safe boundary
Biosphere integrity	Loss of species diversity and ecosystem health surpasses safe levels, endangering planetary regulation mechanisms

Of the nine proposed boundaries, by 2023 humanity has already exceeded six of them (Figure 1).[3] At this point, the need for sustainable governance to maintain a safe operating space for human development on a planetary scale is essential.

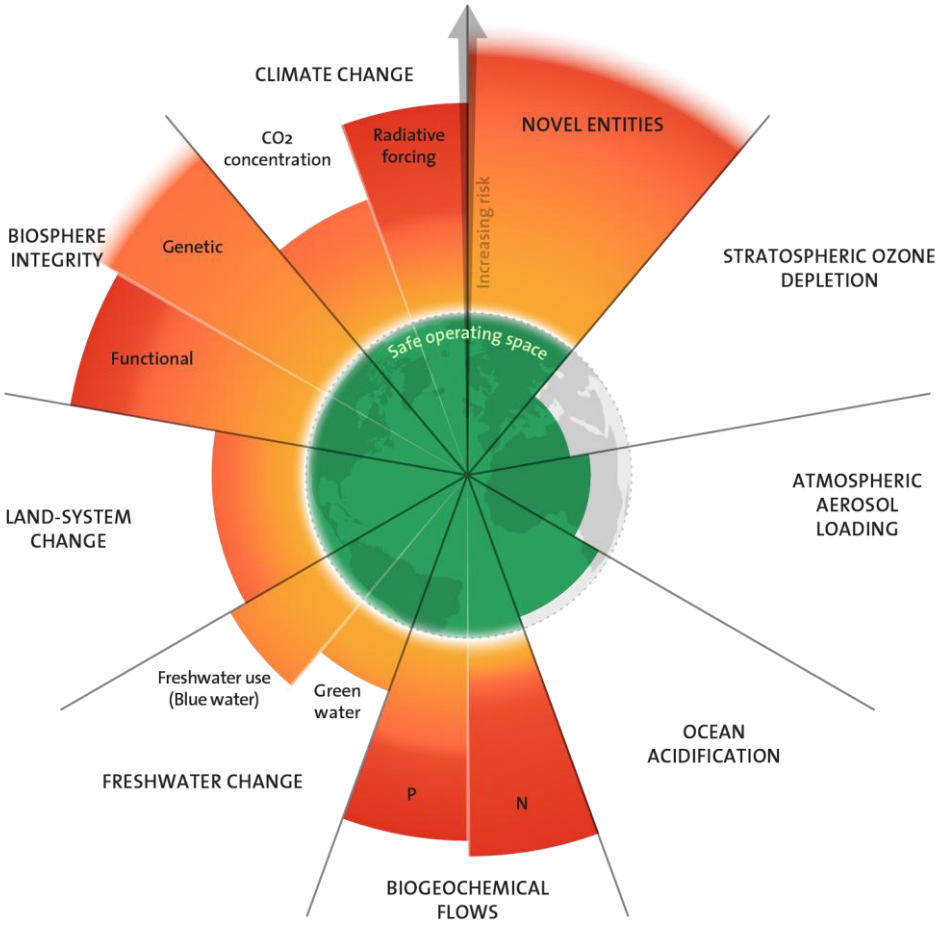

Figure 1. The planetary boundaries framework based on Richardson et al. 2023, adapted from literature.[3]

Besides, the interconnectedness of Planetary Boundary processes suggests that achieving goals such as limiting global warming to a certain threshold requires action in all of them at once. While this complex scenario may seem challenging, it offers a significant opportunity for sustainable development. Addressing the factors that drive systems toward tipping points can lead to synergistic benefits in conservation and resilience.

1.2 AN URGENT NEED

In this scenario a direct question arises: How can we effectively confront the challenge of moving away from fossil fuels, a resource that has fundamentally shaped human development and progress in our recent history?

Since the Industrial Revolution, fossil fuels have long been the backbone of global energy systems, powering industries, transportation, and homes.[4] However, as

society progresses, the drawbacks of relying on fossil fuels have become increasingly apparent. The environmental, economic, and health impacts associated with fossil fuel consumption raise significant concerns about their sustainability in our current society. In essence this can be articulated through the following issues:

- Environmental Degradation: The extraction and burning of fossil fuels contribute to severe environmental degradation.[5] Oil spills, coal mining, and natural gas extraction disrupt ecosystems and lead to habitat loss.[6] Moreover, the combustion of fossil fuels releases greenhouse gases, primarily carbon dioxide, which is a major driver of climate change. This phenomenon results in extreme weather events, rising sea levels, and biodiversity loss, threatening the very fabric of life on Earth.
- Health Risks: The health implications of fossil fuels use are profound. Air pollution from burning fossil fuels is linked to respiratory diseases, cardiovascular problems, and premature deaths.[7] Communities near fossil fuel extraction sites often experience higher rates of health issues due to toxic emissions and contaminated water supplies. The burden of these health risks disproportionately affects vulnerable populations, exacerbating social inequalities.
- Economic Instability: The fossil fuel market is subject to volatility, with prices fluctuating based on geopolitical tensions, supply chain disruptions, and market speculation.
- Finite Resources: Fossil fuels are non-renewable resources, meaning they will eventually deplete.[8] As extraction becomes more challenging and costly, the energy return on investment diminishes.

The drawbacks of fossil fuels in our current society are too significant to ignore. The extraction and consumption of these resources contribute significantly to climate change and ecological harm. Specifically, the increase in atmospheric greenhouse gas concentrations has significantly contributed to the ongoing warming of the planet. Figure 2 provides the visualizations of the surface air temperature for the period of

1940 to present.[1] According to data from the C3S, earth recently recorded its highest temperature in recent history. On July 22, 2024, the global daily average temperature reached a new peak of 17.16°C, surpassing the previous record of 17.08°C recorded on July 6, 2023. This new record was identified using the ERA5 dataset, indicating the continued trend of rising global temperatures.

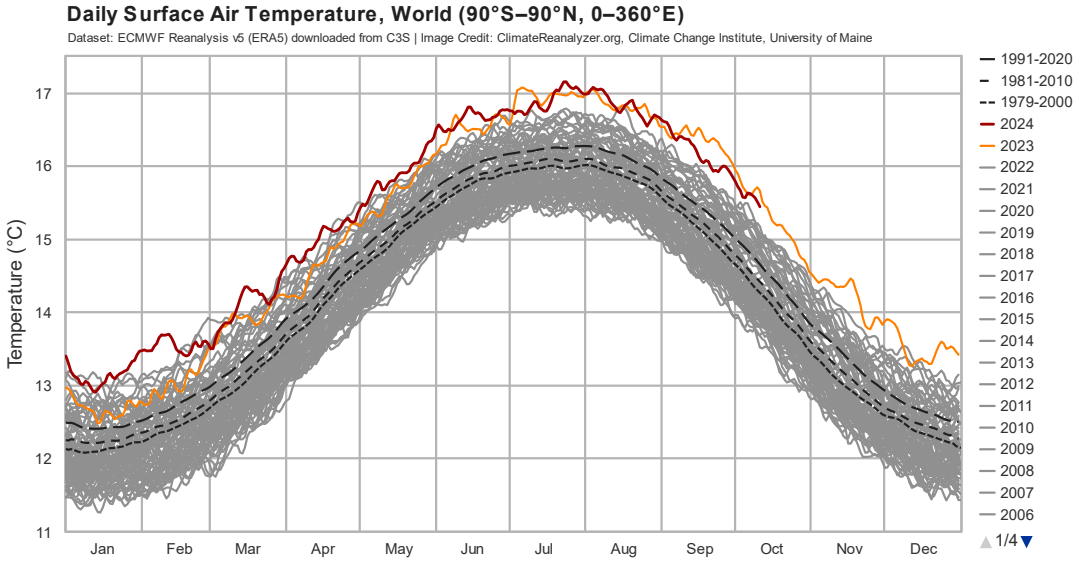

Figure 2. Daily global surface air temperature. Reproduced from Ref[10].

At this critical global juncture, two unavoidable approaches become essential: (i) the shift towards renewable energy sources for a global energy transition and (ii) the academic and social movement of *degrowth*, which serves as a critical framework for tackling these challenges. (i) Renewable energy sources, such as solar, wind, and hydroelectric power, offer a viable alternative to fossil fuels. These sources are not only environmentally friendly but also provide energy security and stability. By harnessing the power of nature, we can reduce greenhouse gas emissions, improve public health, and create a more resilient economy. The adoption and integration of renewables are crucial for transitioning to an energy model that reduces environmental impact, supports long-term ecological balance, and addresses the urgent need to combat climate change. For its part, (ii) *degrowth* promotes the intentional cut down of production and consumption, prioritizing sustainability and ecological balance over

[1] The data source is based on the Copernicus Climate Change Service (C3S) Reanalysis version 5 (ERA5).[9]

perpetual economic growth. Overall, it is essential to take action, as delaying efforts will likely lead to increasingly severe consequences in the future.

1.3 RENEWABLE ENERGY

The global emissions scenario is influenced by geopolitical events, economic developments, and energy system transformations. In this section, we will overview 2024 global report[11] from the International Energy Agency (IEA) to better understand the global situation and the urgent need for new technologies. The IEA was established within the Organisation for Economic Co-operation and Development (OECD) framework to foster international[2] cooperation on energy-related technical matters. For its statistics the IEA considers three scenarios. In the Stated Policies Scenario (STEPS) —defined as the current direction of the energy system—, emissions are expected to peak before 2030, followed by a gradual decline at about 1% per year. However, under this scenario, the projected temperature increases by the year 2100 is 2.4°C, far above the target (1.5 ºC) of the IPCC[3] needed to address climate change effectively. The Announced Pledges Scenario (APS) suggests that if all national pledges are met, the temperature rise could be limited to 1.7°C. The most optimistic scenario, Net Zero Emissions by 2050 (NZE), provides a pathway to limit global warming to 1.5°C, but it requires aggressive action and rapid declines in emissions, far beyond current efforts.

The World Energy Outlook 2024[11] of the IEA highlights that the global energy mix (Figure 3) is gradually shifting, but fossil fuels still dominate the market. In 2023, fossil fuels made up approximately 80% of global energy consumption, a slight decline from 82% in 2013. While the demand for energy has increased by 15% over the past decade, the clean energy sources[4] met about 40% of this new demand. Notably, the deployment of clean energy has been particularly prominent in emerging economies, where energy demand grew by 2.6% per year, driven by industrial growth, urban expansion, and economic development.

[2] The 31 member countries and 13 associate countries of the IEA account for approximately 75% of global energy demand.
[3] Intergovernmental Panel on Climate Change
[4] including renewables, nuclear, and low-emission fuels

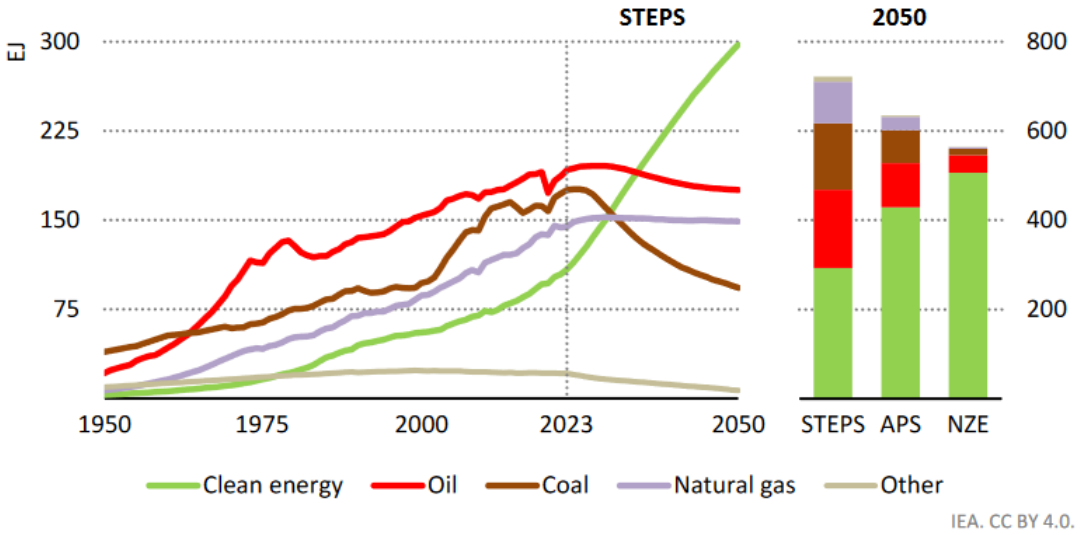

Figure 3. Global energy mix by scenario to 2050. Reproduced from *World Energy Outlook 2024*.

Despite the progress in clean energy deployment, CO_2 emissions remain a critical issue. In the STEPS, global CO_2 emissions are expected to peak before 2030, followed by a modest decline (Figure 4). However, this trajectory falls short of what is needed to meet international climate targets, as it implies an average temperature increase of 2.4°C by 2100. To meet more ambitious climate targets, including limiting temperature rise to below 1.5°C, much more aggressive reductions in emissions are required, which are outlined in the NZE scenario of the report.

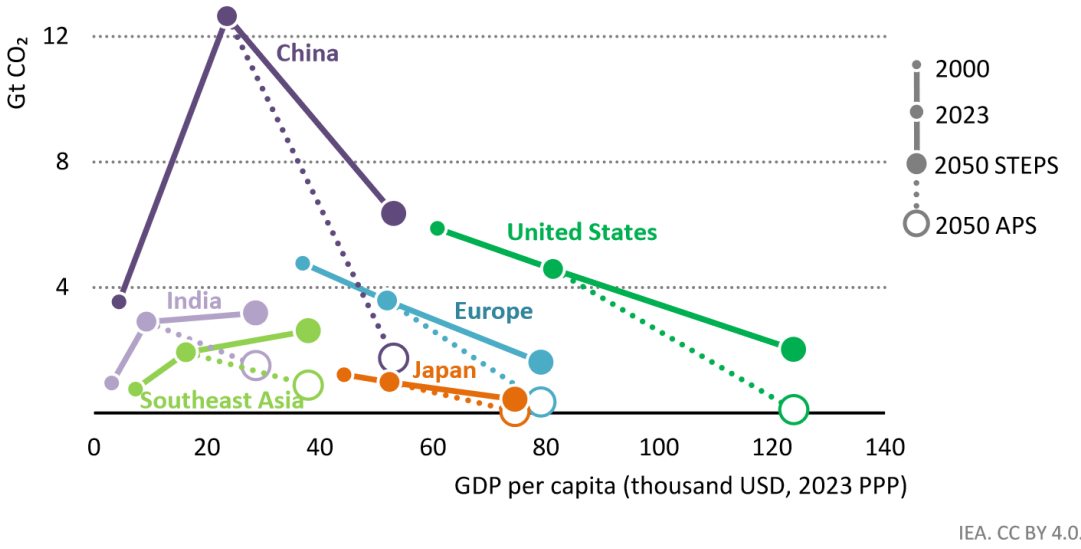

Figure 4. STEPS and APS CO_2 emissions and GPT per capita (selected countries). Reproduced from the *World Energy Outlook 2024*.

From its part, the deployment of clean power technologies has accelerated significantly. In 2023, over 560 gigawatts (GW) of new renewable capacity were added globally, nearly double the annual rate seen a decade ago (see Figure 5). Despite this progress, the expansion of clean power generation has not matched the growing global electricity demand. From 2010 to 2023, electricity output from low-emission sources[5] rose by roughly 5,000 TWh. However, clean power is not yet excelling global electricity demand as during the same period, global electricity generation increased by almost 8,500 TWh. Interestingly, since 2010, solar PV capacity has increased by a factor of 40, while wind capacity has grown sixfold. Combined, solar PV and wind energy have contributed to approximately 75% of the growth in clean power generation during this period.

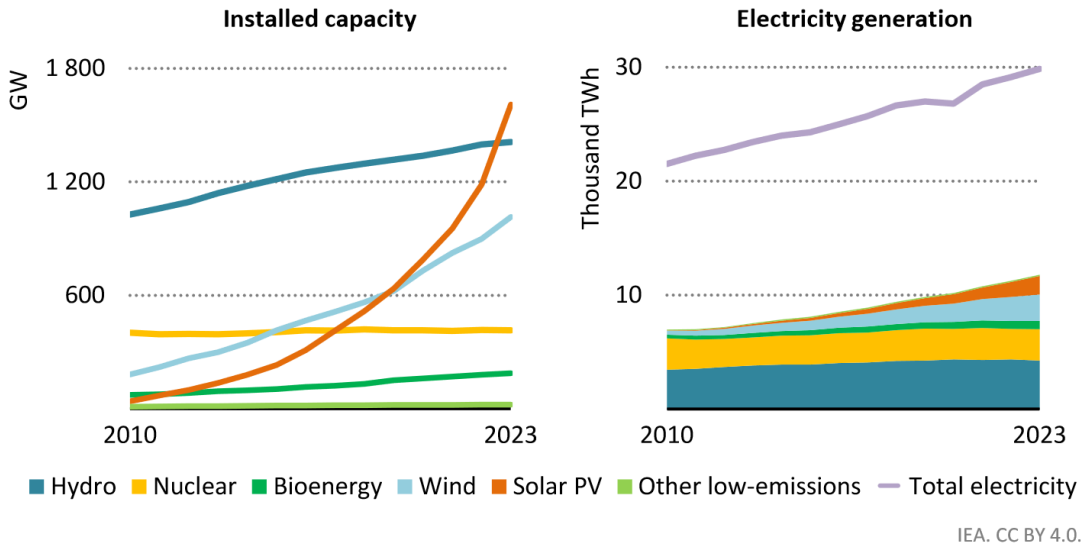

Figure 5. Global installed clean power capacity and electricity generation comparison, 2010-2023. Reproduced from *World Energy Outlook 2024*.

In this line, by 2030, the renewable power generation capacity is expected to increase from 4,250 GW to almost 10,000 GW. Low-emission energy sources, including solar, wind, and nuclear power, are set to generate over half of the world's electricity by 2030, positioning clean energy as the leading contributor to electricity generation in the coming decades (see Figure 6).

[5] including renewables, nuclear, fossil fuels with carbon capture, hydrogen, and ammonia

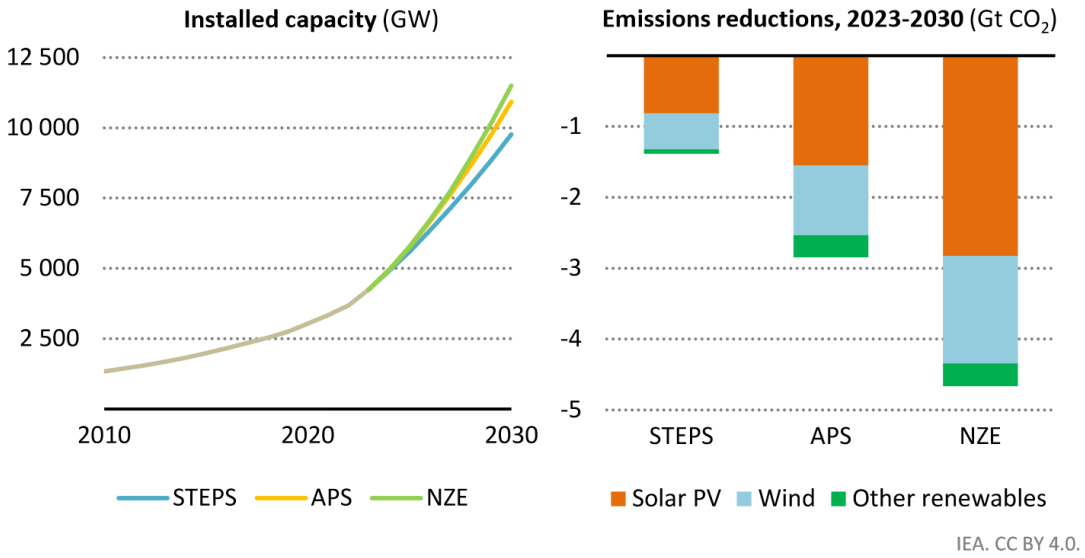

Figure 6. Global installed capacity of renewables emissions reduction by scenario. Reproduced from the *World Energy Outlook 2024*.

The transition to a cleaner energy mix is underway, but the pace is still insufficient to meet critical climate targets. The need for renewable energy technologies is more pressing than ever to curb CO_2 emissions and ensure energy security amidst geopolitical uncertainties and rising global energy demand. At this point, one might infer the IEA report to be somewhat optimistic and potentially biased, as it highlights in the same period of time the peak in installed clean power capacity while simultaneously reaching the peak in global CO_2 emissions. This apparent contradiction underscores the need for critical analysis and further emphasizes the importance of advancing the decarbonization of our economies. Thus, fostering accurate investment in renewable technologies and facilitating their adoption, especially in developing economies, is essential to achieving a sustainable energy future. To meet these goals, research into novel materials for energy solutions turns out to be a key strategy. The following section will introduce the interest in the materials investigated in this Thesis while discussing their significance in addressing the energy transition.

1.4 AIM OF THIS THESIS

On balance, the integration of renewable technologies is essential for establishing a sustainable energy model that not only reduces environmental impact

but also fosters ecological resilience. Though, achieving this requires significant effort and the development of innovative solutions.

In this context, nanocomposites represent a versatile and promising class of materials, largely due to their ability to combine the advantageous properties of their individual components while mitigating their respective limitations. These hybrid systems often exhibit synergistic effects, resulting in enhanced mechanical, optical, electronic, or chemical performance compared to their single-phase counterparts. This adaptability has made nanocomposites integral to a wide range of advanced technologies, including energy storage, catalysis, and optoelectronics. The integration of nanocomposites with perovskite materials is particularly compelling.

Perovskites, renowned for their exceptional optoelectronic properties, such as high absorption coefficients, tunable bandgaps, and long charge-carrier diffusion lengths, have garnered significant attention for their potential use in different applications. However, their inherent susceptibility to environmental stressors, such as moisture, oxygen, and thermal fluctuations, limits their stability and long-term performance. Specifically, the inherent instability of perovskite nanocrystals (PNCs), driven by their sensitive surface chemistry, aggregation, and the complex multi-step purification processes, required by conventional synthetic methods, remains a critical challenge in the field. Thus, the use of nanocomposites as hosts for perovskites offers a strategic pathway to address these challenges.

The overall aim of this research focuses on the synthesis and characterization of novel nanocomposite perovskite-based materials. Key emphasis is placed on understanding the urgent global need for these technologies, as well as the study of materials that can be easily scaled. This focus is essential for fostering implementable and versatile materials, thereby enhancing accessibility and sustainability in energy production. The Thesis will also shed light on various key synthetic aspects of the preparation of nanocomposites along with strategies to enhance their stability and processability, facilitating their integration into devices. Besides, to connect fundamental science with practical applications, most of the novel synthetic approaches described here have been tested in real-world devices such as solar cells. Lastly, the materials developed in this research have resulted in multiple patents, using nanocomposite-based strategies, for metal halide perovskites (MHPs) nanocrystals (NCs) in matrixes and stabilizing all-inorganic perovskite solar cells (PSCs).

1.5 THESIS OUTLINE

This thesis is divided into eight chapters. Chapter 1 sets the context of the topic, providing a comprehensive introduction to the global situation and setting the stage for the interest in the materials investigated throughout the work. Following this, Chapter 2 explores the fundamental background and concepts upon which the experimental techniques and results are based, while Chapter 3 provides an overview of the methodologies and techniques employed in this research. Chapters 4 and 5 present the results of a novel synthetic approach for preparing PNCs within matrixes and a detailed protocol for precise control over the final output, respectively. Chapter 6 builds on the previous results and offers a detailed crystallization and passivation mechanism for the nanocomposites, revealing their exceptional properties. Chapter 7 explores nickel acetate's role in stabilizing wide-bandgap perovskites like $CsPbI_3$ for all-inorganic PSCs. Leveraging nanocomposite materials, we demonstrate improved stability and photovoltaic (PV) performance. Finally, Chapter 8 wraps up the Thesis by underscoring the key contributions of the research. It discusses potential future directions for further exploration in this field.

Chapter 2: Chemistry and Physics background

Abstract

This chapter focuses on the key chemical and physical principles that set the basis for the diverse materials and devices explored in this Thesis. In detail, we introduce key fundamental concepts that are crucial for providing a deeper understanding of the results presented. The chapter will discuss the basic chemistry and physics of MHP semiconductors, emphasizing the main approaches and synthetic routes and how to affect their electronic properties. Understanding these concepts is crucial for following the discussions and results presented in later chapters.

2.1 METAL HALIDE PEROVSKITES BACKGROUND

This Thesis predominantly investigates the synthesis and fundamental properties of MHP semiconductors, which have emerged as promising materials in optoelectronic applications due to their exceptional photophysical characteristics. Specifically, Chapters 4, 5 and 6 focus on the preparation of MHPs NCs through a novel synthetic approach with key parameters for fine tune the final properties of the NCs. Besides, Chapter 7 introduces an innovative strategy for stabilizing wide band-gap perovskites, addressing a critical challenge in enhancing their practical usability. Given that the physical properties of MHP semiconductors differ significantly from those of established semiconductor technologies, this section aims to provide a comprehensive overview of their unique characteristics. Additionally, it offers a concise review of current state-of-the-art advancements in the field, highlighting recent breakthroughs and ongoing research trends that underscore the significance of MHPs in advancing semiconductor science.

2.1.1 Introduction

Semiconductor materials are foundational to modern technology, underpinning a vast array of applications such as PV cells, light-emitting diodes (LEDs), and integrated circuits.[12] Only by doping (introducing impurities) in different regions of a semiconductor, one can manipulate its charge carrier density and type, enabling the formation of different junctions. These junctions are critical in controlling electron flow, facilitating the operation of diodes and transistors[6]. Given the critical role that semiconductors play in technological advancement and societal infrastructure, extensive research has been devoted to synthesizing novel semiconductors for more powerful, efficient and versatile devices.

Among the emerging materials, over the past decade, MHPs have become a focal point of materials science research, driven largely by their remarkable advancements in solar cell efficiencies.[13] This surge in interest initially stemmed from the PVs community, where cost-effective devices using bulk MHP films demonstrated exceptional potential.[14] However, the appeal of MHPs soon expanded beyond solar

[6] The fundamental building blocks of electronic circuits

cells, as researchers began exploring the vast possibilities of MHPs as nanocrystals (NCs) for a wide range of optoelectronic applications.[15]

2.1.2 History and state-of-the-art

The perovskite family encompasses a wide range of materials, unified primarily by their characteristic lattice structure. The history of perovskite materials begins with their initial discovery in 1839 by German mineralogist *Gustav Rose*, who identified the mineral calcium titanium oxide ($CaTiO_3$) in the Ural Mountains and named it "perovskite" in honor of *Lev Perovski*[16], a Russian mineralogist. More than a century later, the synthesis of the first MHP semiconductor in 1978 marked a significant milestone, opening avenues for their application in electronic devices.[17] Undoubtedly, a pivotal advancement occurred in 2009 when researchers reported the use of organometal halide perovskites as light absorbers in solar cells, achieving initial power conversion efficiencies around 3.8%.[18] The materials' versatility was further showcased in 2014 with the development of the first perovskite light-emitting diode (LED), highlighting its exceptional optoelectronic properties.[19] Currently, PSCs have achieved remarkable progress, with single-junction devices reaching efficiencies exceeding 26.7%, reflecting rapid advancements and solidifying perovskites as leading materials for next-generation PV technologies.[13] To better appreciate the remarkable journey of perovskite materials over the years, Figure 7 presents a schematic timeline illustrating their key developmental milestones.

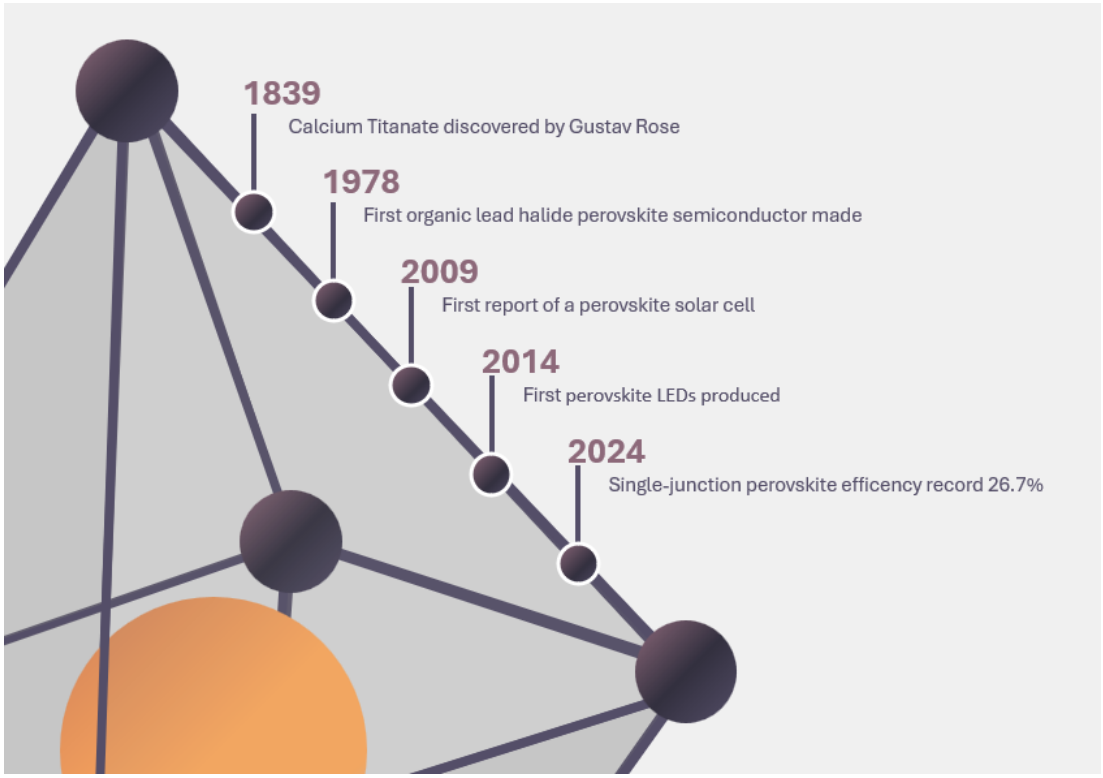

Figure 7. Perovskites timeline highlighting significant milestones.

2.1.3 The perovskite structure.

In the most widespread PV perovskite materials, the crystal structure adheres to the general formula ABX_3, where 'A' represents a large cation, 'B' is a smaller cation, and 'X' is an anion forming the lattice framework. The 'A' site can be occupied by various cations, including organic options like methylammonium (*MA*, $CH_3NH_3^+$) and formamidinium (*FA*, $HC(NH_2)_2^+$), as well as inorganic cations such as caesium (Cs^+). The 'B' site is commonly filled by lead ions (Pb^{2+}) but can also be substituted by tin ions (Sn^{2+}). The 'X' site consists of halide ions like iodide (I^-), bromide (Br^-), or chloride (Cl^-). The crystal lattice of HPs comprises a three-dimensional network of corner-sharing PbX_6^{4-} octahedra. Within this framework, A-site cations are situated in the 12-fold coordinated voids, ensuring overall charge neutrality (see Figure 8). The specific dimensions and three-dimensional geometry of the individual PbX_6^{4-} octahedra, as well as their arrangement in space, are crucial in determining the observed structural and optoelectronic properties of the perovskite. Besides, their compositional flexibility allows for fine-tuning of the perovskite's properties, making them highly suitable for optimizing performance in solar cell applications.[20]

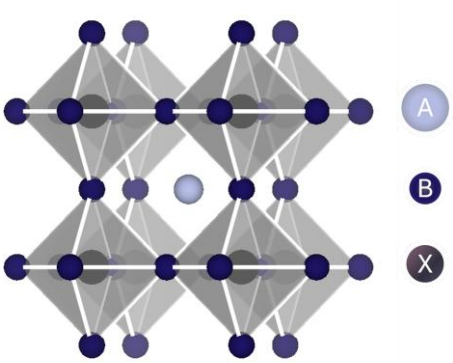

Figure 8. Perovskite crystal unit cell (ABX_3) for a Pm3m space group. *Vesta 3* Software[21] adapted from literature.[22]

An commonly used consideration for determining the stability and formability of the perovskite lattice is the Goldschmidt tolerance factor.[23] With a phenomenological origin, this size-dependent dimensionless factor, denoted by *t*, is widely used to predict whether a specific combination of ions can result in a stable perovskite structure. It is calculated using the Equation 1:

$$t = \frac{r_A + r_X}{\sqrt{2}(r_B + r_X)} \qquad 1$$

where r_A, r_B, and r_X represent the ionic radii of the A-site cation, the B-site cation, and the anion, respectively. The Goldschmidt factor is particularly important in the context of MHPs used in optoelectronic devices like solar cells and LEDs. A proper balance between the ionic radii ensures structural stability, which in turn affects the material's electronic properties and overall performance. In the field of perovskite solar cells (PSCs), the choice of A-site cations plays a pivotal role in their development and optimization.[24,25] These cations are characterized by their ionic radii and the corresponding tolerance factor (*t*), which is calculated based on the $APbX_3$ lattice framework. The value of the *t* determines the crystal structure that the perovskite material can adopt. The ideal value of the Goldschmidt *t* for a perfectly cubic perovskite structure is around 1. For values of *t* between 0.8 and 1.0, the material typically crystallizes into three-dimensional corner-sharing perovskite structures, such as cubic, tetragonal, or orthorhombic phases (see Figure 9b).[26] These structures are stable and known for their desirable electronic and optical properties, making them highly suitable for optoelectronic applications. However, if the tolerance factor falls outside this range, significant structural changes occur. When *t* is less than 0.8, which

can happen when the A-site cation is too small, the material tends to crystallize in non-perovskite phases.[27] Conversely, when the tolerance factor exceeds 1, indicating that the A-site cation is too large (Figure 9b highlights possible A-cations), the material is likely to form a hexagonal structure, which also lacks the 3D corner-sharing PbX_6^{4-} octahedral network characteristic of perovskites.[28] In some cases, the presence of larger, densely packed cations can lead to perovskite-like structures, but with reduced dimensionality. These structures can feature networks of corner-sharing PbX_6^{4-} octahedra that are confined to two-dimensional (2D) planes or even one-dimensional (1D) chains.[29] Thus, the wide range of structural variations plays a crucial role in influencing the overall performance and stability of perovskite-based devices, providing opportunities for tailoring materials to specific applications through careful selection of A-site cations. Furthermore, the inclusion of ionic shape considerations, in addition to ionic sizes, has recently extended the applicability of the Goldschmidt factor.[30] Figure 9a presents a detailed schematic highlighting the role of A-site cations in influencing the physicochemical and optoelectronic properties of MHPs.

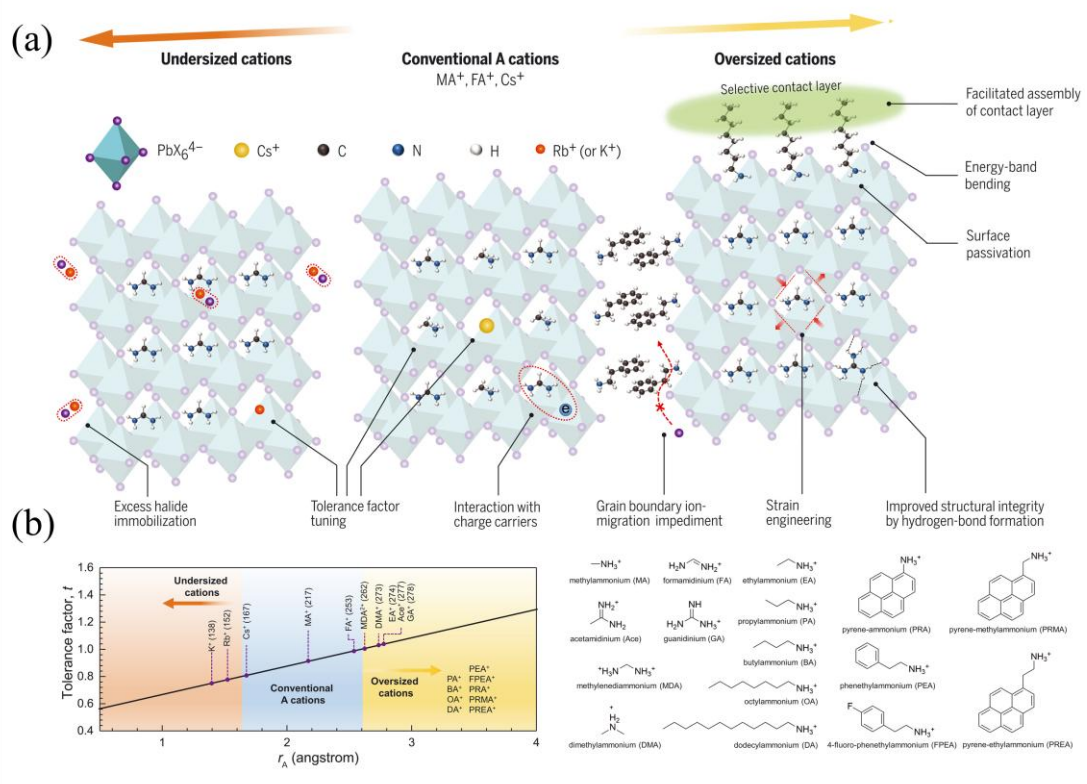

Figure 9. (a) Schematic illustration on the A cation role in tailoring physicochemical and optoelectronic properties of MHPs. (b) Most relevant A-site cations classified by

their cationic radius (in parenthesis) and corresponding tolerance factor based on the $APbI_3$ lattice framework. The right-side image shows the ammonium cation structures abbreviated in the plot. Figure adapted from Ref[26].

2.1.4 Applications and main properties of MHPs.

This subsection provides a detailed overview of the fundamental electronic properties of MHPs materials. Key topics include bandgap characteristics, spin-orbit coupling effects, electron and hole effective masses, optical absorption, defect tolerance, and the transport behavior of photoexcited carriers. Special emphasis is placed on how these properties influence slow recombination rates, carrier dynamics, and mobilities, which are crucial for optimizing device performance.

2.1.4.1 *Bandgap Characteristics*

MHP materials exhibit a direct bandgap, which is highly beneficial for PV applications due to efficient light absorption and charge carrier generation.[31] The bandgap can be tuned across the visible spectrum by altering the composition of the 'A', 'B', and 'X' sites. The cation substitution of methylammonium with formamidinium or cesium can adjust the bandgap slightly due to changes in the lattice constants and structural distortions.[26] In contrast, the halide plays a more drastic role determining the final bandgap. Halide exchange, for instance substituting iodide with bromide, or bromide by chloride, significantly widens the bandgap allowing for tunability from ~1.25 eV to over 3 eV when bulk Pb-based perovskites are considered.[32]

In the Section 2.2.2 of this chapter a more fundamental description of bandgap modification specially for semiconductor nanocrystals is provided.

2.1.4.1.1 Valence and Conduction Bands

Numerous theoretical studies have already advanced our fundamental understanding of electronic structure.[33] In the case of $MAPbI_3$ and related materials the composition of the Valence Band Maximum (VBM) is primarily derived from the antibonding interaction between the metal cation's *ns* orbitals (e.g., Pb 6s) and the halide *p* orbitals (e.g., I 5p). For its part, the Conduction Band Minimum (CBM) mainly consists of the metal cation's *np* orbitals (e.g., Pb 6p) with minor contributions from the halide orbitals (see Figure 10).[34]

Consequently, the organic molecules primarily contribute to stabilizing the perovskite structure and adjusting the lattice constant, rather than directly influencing the electronic structure. Thus $MAPbI_3$ and similar materials are characterized by strong optical absorption and luminescent properties, where the valence band maximum (VBM) and conduction band minimum (CBM) align at the same point in reciprocal space (*k*-space).[35]

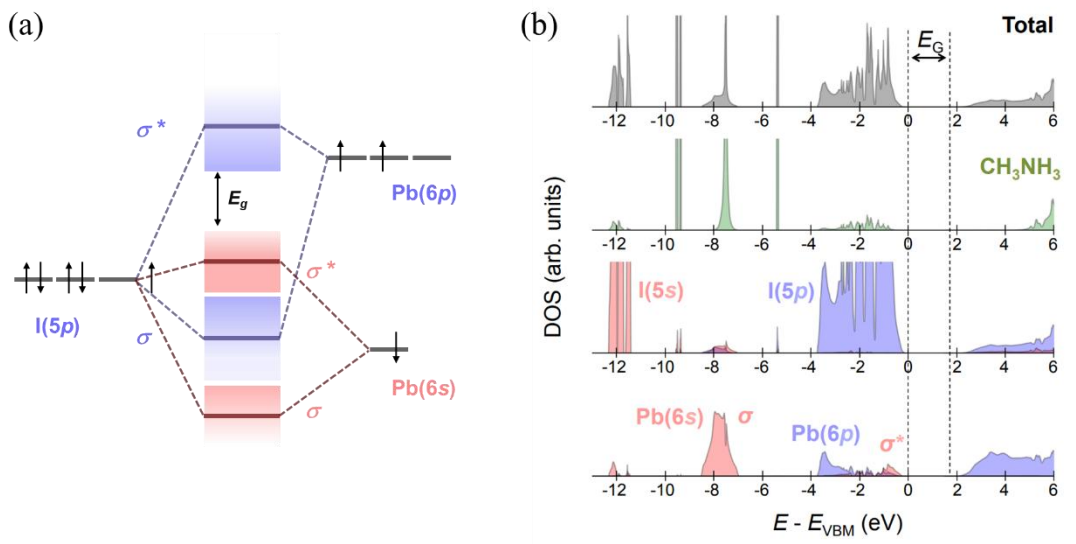

Figure 10. (a) Illustration of the bonding and antibonding orbitals in $MAPbI_3$, focusing on the $[PbI_6]^{4-}$ octahedral units relative to the energy levels of isolated s and p atomic orbitals. (b) Density of States (DOS) for $MAPbI_3$, with the individual contributions from the s and p orbitals of both cations and anions distinctly separated. Calculations were performed using the many-body GW method, incorporating Spin-Orbit Coupling (SOC) effects. Adapted from Ref[34].

2.1.4.2 *Spin-Orbit Coupling Effects*

SOC is a quantum mechanical phenomenon where a particle's spin interacts with its orbital motion around a nucleus. This interaction alters the energy levels and influences the magnetic and optical properties of materials. In perovskites, the heavy metal cations like lead (Pb^{2+}) introduce strong SOC effects due to relativistic interactions. SOC leads to significant splitting of the conduction band and affects the bandgap energy. SOC also lowers the energy of the conduction band minimum, effectively reducing the bandgap,[36] while influencing the curvature of the bands and impacting the charge carriers effective masses.[37]

2.1.4.3 *Electron and Holes Effective Masses*

The electronic structure of $MAPbI_3$ and related materials differs from that of conventional semiconductors. As mentioned before, their CBM is primarily composed of Pb *p* orbitals, while the VBM is a combination of Pb *s* and I *p* orbitals. SOC-GW calculations[7] yielded effective masses for electrons and holes of 0.19 and 0.25 times the free electron mass, which closely matched recent magnetoabsorption spectroscopy results.[38] Given that mobility is inversely proportional to effective mass of the carriers, perovskite materials exhibit well-balanced electron and hole diffusion lengths which positively impacts their efficiency when structured as solar cells.[35,39,40]

2.1.4.4 *Optical Absorption*

The electronic band structure strongly impacts the optical absorption coefficient of these materials. A key characteristic of perovskite materials is their relatively high absorption coefficient. For example, $MAPbI_3$ layers thinner than 500 nm are capable of absorbing sufficient photons to reach an efficiency exceeding 15%. In contrast, the absorber layers in first and second-generation solar cells typically measure around 300 µm and 2 mm, respectively. Specifically, perovskite materials exhibit strong optical absorption coefficients ($>10^5$ cm^{-1}) related to direct transitions and a broad absorption spectrum. The direct bandgap allows for efficient photon absorption and electron excitation without the need for phonon assistance. Meanwhile, the ability to absorb a wide range of the solar spectrum enhances the photocurrent generation in solar cells.[41]

2.1.4.5 *Charge Carrier Transport Properties*

Another interesting feature of perovskite materials is their carrier mobility. Charge carrier mobility in perovskites ranges from moderate to high, with the reported electron and hole mobilities varying between 1 to 70 $cm^2\ V^{-1}\ s^{-1}$, depending on factors such as material quality and the measurement techniques used.[42] Importantly, the transport is well-balanced for both electrons and holes, which helps minimizing charge accumulation and reduce recombination losses, enhancing overall device efficiency.[43] At the same time, MHPs also exhibit slow non-radiative recombination rates, which

[7] With the relativistic GW approximation

contribute to the extended carrier lifetimes observed, often exceeding hundreds of nanoseconds. At moderate carrier densities, bimolecular recombination dominates, consistent with the Shockley-Read-Hall recombination models, ensuring longer carrier diffusion lengths (another important feature) and better PV performance.[42]

2.1.4.6 *Defect Tolerance*

The reason for these suitable properties is strongly based on the MHPs' defect tolerance. Usually, conventional semiconductor technologies aim to produce near-perfect crystals to minimize defects, as imperfections can significantly degrade their optoelectronic performance. For instance, single-crystalline silicon is renowned for its extremely low defect densities, at a price of very restrictive and energy demanding fabrication strategies.[44] In contrast, MHP materials used in solar cells are typically synthesized through solution processing at near room temperature, which inherently leads to a higher density of defects.[45] Surprisingly, these defects do not drastically impair its performance, and the reasons behind this defect tolerance are still being explored. One key aspect of the original defect tolerance concept of $MAPbI_3$ and related MHPs materials lies in its unique electronic structure. These materials possess an antibonding upper VB and a bonding lower CB, a configuration where dangling bond defects are energetically unfavorable[8].[35] As a result, the bandgap remains clean, and only shallow defects are formed (see Figure 11), which do not trap charge carriers significantly.

[8] As they are effectively pushed into the continuum bands

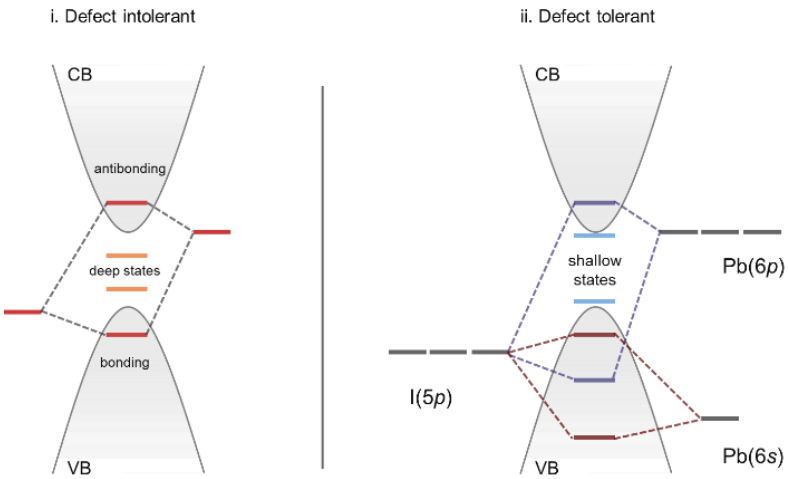

Figure 11. Band structures of an archetypical defect-intolerant semiconductor and the defect-tolerant perovskite (e.g. $MAPbI_3$). Adapted from Ref[46]

Another crucial factor is the material's ability to screen electrostatic perturbations caused by charged defects. This is quantified by the dielectric constant of the material. $MAPbI_3$ has a dielectric constant that is approximately three times higher than that of other thin-film PV materials like cadmium telluride (CdTe).[47] Higher dielectric constant can enhance the charge screening effect, thereby minimizing the influence of charged defects on charge carriers and improving defect tolerance.[48] The effective masses of charge carriers in $MAPbI_3$ also play a significant role. As mentioned before, lower effective masses mean that electrons and holes can move more freely, leading to higher carrier mobility and electrical conductivity. This mobility reduces the chance of carriers becoming localized at defect sites, which can slow down charge transport and lead to energy losses.[49] Besides, the perovskite structures like $MAPbI_3$ are composed of a framework of corner-sharing PbI_6^{3-} octahedra, forming an overall stoichiometry of PbI_3^-, with MA cations occupying the cuboctahedral voids. This framework is intrinsically soft and exhibits dynamic disorder, meaning the lattice can easily deform in response to external stimuli. Such softness facilitates the formation of large polarons, where charge carriers are surrounded by a cloud of lattice vibrations (phonons). These large polarons can significantly screen the electrostatic potential of charged defects, reducing scattering events and further enhancing charge mobility.[50]

In essence, the combination of a favorable electronic band structure, high dielectric constant, low effective mass of charge carriers, and the formation of large

polarons are proposed as the main reasons for these materials' defect tolerance. The defects present are energetically shallow and effectively screened, diminishing their impact on recombination processes that typically reduce the efficiency of PV materials. Understanding these mechanisms is crucial for the development of high-performance perovskite solar cells. It opens pathways to fabricate devices that are less sensitive to defects, potentially lowering production costs and increasing scalability.

Collectively, the unique electronic band structure and exceptional properties of perovskite materials (tunable bandgaps, strong optical absorption, high charge carrier mobilities, and remarkable defect tolerance) not only make them ideal for solar cells and LEDs but also extend their applicability to a wide array of advanced technologies. For instance, in thermoelectric applications, the ability to engineer the electronic structure and reduce lattice thermal conductivity allows perovskites to efficiently convert temperature gradients into electrical energy.[51] Their ionic conductivity and adjustable electronic states enable the emulation of synaptic functions in neuromorphic devices, making them promising candidates for artificial synapses in next-generation computing systems.[52] Furthermore, the strong absorption coefficients and excellent charge transport properties facilitate their use in photodetectors and X-ray detectors, where they can sensitively detect a broad spectrum of electromagnetic radiation from visible light to high-energy X-rays (suitable for medical imaging and security scanning applications).[53] These multifaceted features position perovskites as versatile materials with the potential to revolutionize various fields beyond traditional optoelectronics. Figure 12 combines all the previously discussed properties and illustrates the current research directions in which metal halide perovskites (MHPs) are being explored.

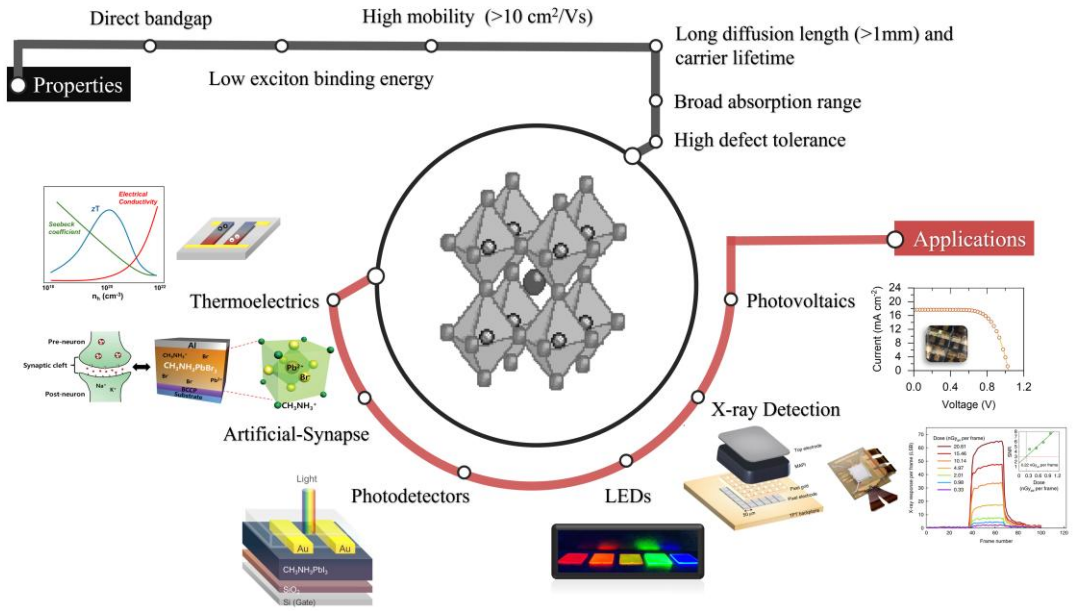

Figure 12. Schematic illustration of the main properties and research lines of MHPs.

In addition to their well-established properties, MHPs exhibit even more remarkable potential when synthesized as nanocrystals. The nanoscale dimension of these materials unlocks an entirely new range of properties and functionalities, such as enhanced high quantum yields, rapid radiative decay, and narrow emission line widths even under weak confinement conditions. In the following section, we will explore the unique advantages that arise from the nanoscale structuring of MHPs, examining how these nanocrystal properties contribute to advancements in both fundamental research and practical device applications.

2.2 MHP NANOCRYSTALS

As a significant portion of this Thesis focuses on the study of MHP NCs using a novel synthetic approach, it is relevant to review their history and background as well as their most common preparation techniques. This section serves to provide a comprehensive outline detailing the key concepts of MHP NCs that are essential for understanding the results and discussions presented in the subsequent chapters. Additionally, a general perspective will be provided on the impact of the current most used synthetic strategies and their effect on the optoelectronic properties and stability of MHP nanocrystals.

2.2.1 Brief history of colloidal MHP NCs

In the 1980s, the first theoretical models of small spherical semiconductor nanocrystals (NCs), also known as quantum dots (QDs) when their size is below the Bohr diameter, were introduced.[54] These models marked a significant milestone in understanding the properties of quantum dots, largely due to rapid advancements in synthesizing colloidal PbS and CdSe NCs.[55] However, one of the key challenges in aligning experimental data with theoretical predictions was the accurate determination of the size and shape of NCs, especially within the small size range of 1-10 nm. This limitation was overcome with the development of the transmission electron microscope (TEM), which did not achieve the necessary resolution for nanomaterial imaging until the 1970s despite its first development in the 1930s. The TEM provided direct visual evidence of NCs, bridging the gap between theory and experiment. Another major breakthrough occurred in 1993, the research group led by Moungi Bawendi, recipient of the 2023 Nobel Prize in Chemistry, developed a synthetic method that produced nearly monodisperse colloidal CdSe NCs with near-atomic precision.[56] This advancement led to the rapid growth of colloidal semiconductor NC research, expanding to materials such as PbSe, InAs, and ZnS, among others. In addition to this, a whole field was created, which began synthesizing complex binary NCs with multiple semiconductor domains offering unprecedented tunability of NC properties. As the field matured, it moved from fundamental research toward practical applications, with NCs being explored for use in LEDs, lasers, solar cells, and medical treatments.

In 2012, several studies highlighting the defect-tolerant nature of MHPs sparked significant interest in the scientific community to explore their colloidal synthesis as a new class of nanomaterials. In 2014 Schmidt et al. reported the first successful synthesis of methylammonium-based MHP NCs using the LARP method.[57] Shortly after, in 2015, Protesescu and colleagues developed monodispersed NCs through hot-injection methods, reaching a remarkable PLQY of approximately 90% without any post-synthetic treatments.[58] By adjusting the halide precursor ratios, they achieved tunable emission across the visible spectrum, with a narrow full width at half maximum (FWHM) of less than 15 nm. Around the same time, Zhang et al. synthesized $CH_3NH_3PbX_3$ NCs using a ligand-assisted reprecipitation method, yielding NCs with high PLQY at room temperature without additional surface

passivation.[59] This unexpected behavior contradicted many assumptions about traditional semiconductor QDs, highlighting the unique properties and ease of synthesis of MHP NCs. These characteristics have quickly made MHP NCs a prominent and rapidly expanding research area, with the potential to reshape established concepts in nanomaterials. The ability to precisely control the size and composition of MHP NCs has unlocked new opportunities for fine-tuning their properties, accelerating the growth of this emerging field and drawing significant attention within the scientific community.

2.2.2 Electronic Structure and Molecular Orbital Theory in Semiconductor Nanocrystals

To fully comprehend the optical and electronic properties of semiconductor nanocrystals, it is essential to first anaunderstand the behavior of electrons in single atoms and how this behavior evolves when atoms bond to form molecules or solids. In atoms, electrons occupy specific regions around the nucleus, known as atomic orbitals (AOs), which are described by the Schrödinger equation (Equation 2):

$$\hat{H}\psi = E\psi \qquad 2$$

where *H* is the Hamiltonian operator representing the total energy of the electron, and *E* is the electron's energy. The Schrödinger equation can be further refined to separate the kinetic and potential energy components (Equation 3):

$$(-\frac{\hbar}{2m}\nabla^2 + V)\psi = E\psi \qquad 3$$

Here, $\hbar$ is the reduced Planck constant, ∇ is the Laplace operator, and V is the electrostatic potential. Solving this equation provides wave functions for electrons, known as atomic orbitals, that describe the probability distribution of an electron's location.[60] The electron's likely position is expressed as a probability, proportional to ψ^2 and the arrangement of electrons in AOs follows the quantum numbers, which define their energy levels, shape, and orientation (see Figure 13). When atoms combine to form a molecule, their atomic orbitals merge through a process known as hybridization, giving rise to molecular orbitals (MOs). The formation of MOs can be described using the linear combination of atomic orbitals (LCAO) approach, which involves combining the wave functions of the individual AOs.

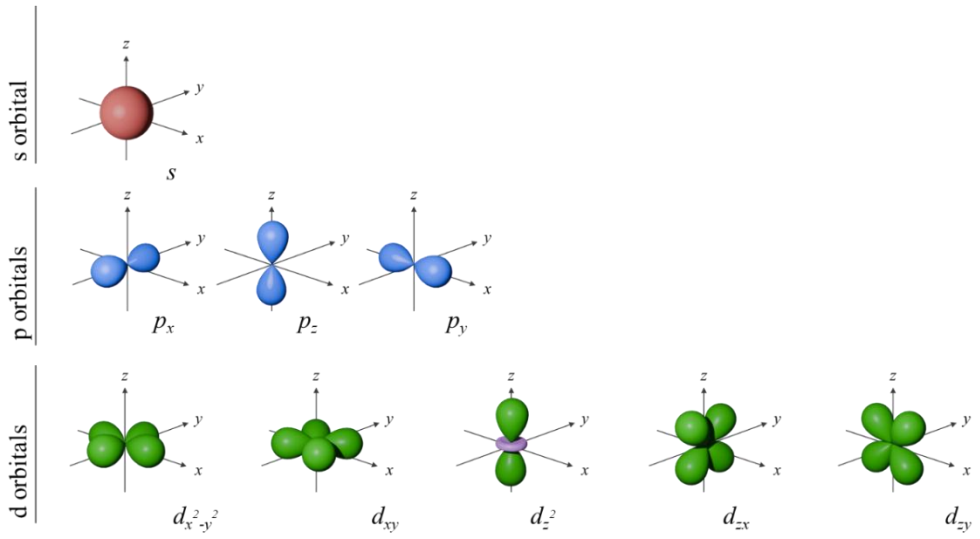

Figure 13. 3-D visualizations of hydrogen AOs.

This combination can be either constructive or destructive. Constructive overlap, where the signs of the wave functions are the same, leads to bonding orbitals, reducing the electron's energy and creating a stable interaction between atoms. Destructive overlap, where the wave functions have opposite signs, results in antibonding orbitals with higher energy and a node where the electron's presence is minimal. In a simple H_2 molecule, two hydrogen atoms' 1s orbitals combine to form a bonding molecular orbital (σ) and an antibonding molecular orbital (σ*). The two electrons occupy the bonding orbital, lowering their energy and stabilizing the molecule. More complex molecules form more intricate MOs due to the interaction of different orbitals, such as s and p orbitals, across various energy levels. In semiconductor materials, like a PbI_6^{4-} cluster, the Pb 6s and 6p orbitals hybridize with the I 5s orbitals, creating bonding and antibonding MOs. The highest energy occupied orbital is referred to as the Highest Occupied Molecular Orbital (HOMO), and the lowest energy unoccupied orbital is known as the Lowest Unoccupied Molecular Orbital (LUMO). All this has previously been discussed in this chapter in the context of the bandgap characteristics of MHP materials (see section 2.1.3).

2.2.2.1 *Size dependence*

Semiconductor NCs exhibit unique optical properties compared to bulk materials, which can be understood by treating NCs as large molecules composed of hundreds to thousands of atoms. Unlike bulk materials with quasi-continuous energy bands, NCs have discrete energy states at the band edges, explained through the linear

combination of atomic orbitals (LCAO). As the size of NCs increases, the separation between these energy states decreases, while in bulk solids, the states merge into a continuum (see Figure 14a). This transition, known as the quantum confinement effect, leads to a widening of the bandgap in smaller NCs. This widening in the energy difference between the HOMO and LUMO, leads to unique optical properties. These quantum effects, influenced by both atomic and molecular interactions, play a fundamental role in defining the electronic structure and behavior of semiconductor NCs. Understanding these principles is essential for advancing applications in optoelectronics, such as quantum dots, where the control of electron behavior at the nanoscale directly impacts the final semiconductor properties.

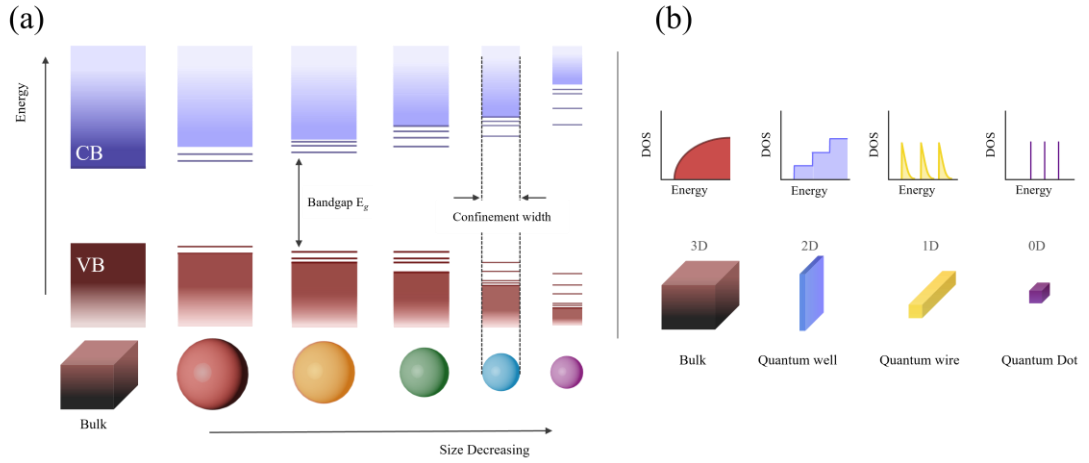

Figure 14. Schematic representation of (a) quantum confinement effect and (b) energy level structure comparing a bulk semiconductor and semiconductor nanostructures confining dimensionality. Adapted from Ref[61].

A more intuitive approach to understanding the quantum confinement effect involves examining the electron-hole pair, known as an exciton, which forms due to the Coulombic interaction between an electron in the CB and a hole in the VB. The size of the exciton is described by its Bohr radius, which is determined by the effective masses of the electron and hole and varies depending on the material. For instance, the exciton Bohr radius is approximately 5.6 nm for CdSe, while for PbSe, it is 46 nm.[62] When the NC size approaches or becomes smaller than the Bohr radius, the exciton becomes confined within the NC, increasing its energy. As the size of the NC continues to decrease, the quantum confinement effect intensifies, leading to an expansion of the bandgap. This degree of confinement is material dependent, as it is linked to the semiconductor Bohr radius.

2.2.2.2 *Shape dependence*

Spherical NCs are considered as zero-dimensional (0D) objects, with quantum confinement occurring in all three dimensions, resulting in a discontinuous density of states. When the different axes are extended, as in quantum nanorods/nanowires (1D) or nanosheets (2D) shown in Figure 14b, confinement is reduced, and the density of states becomes quasi-continuous along the unconfined axis. Though, the electronic levels are still primarily influenced by the smallest dimension.

NCs exhibit unique optical and electronic properties that are distinct from their bulk counterparts due to quantum confinement effects. These properties are governed by the behavior of electrons within the NC and how they interact with energy states at the nanoscale. As we explore the behavior of these semiconductor NCs, understanding the mechanisms of electron excitation, recombination, and the role of defects becomes essential for optimizing their performance in various applications, such as LEDs, lasers, and solar cells. In the next section, we will delve into the fundamental processes governing electrons and holes dynamics in semiconductors, focusing on how external stimuli like photons influence their energy states. We will also discuss the significance of direct and indirect bandgaps, the impact of radiative and nonradiative recombination, and the role of trap states in determining the efficiency of nanocrystal-based devices.

2.2.3 Light interaction in semiconductor NCs.

For a material to conduct electricity, electrons must be able to move through empty orbitals. In semiconductors, the bandgap separates the filled orbitals in the VB from the empty ones in the CB. Without external energy, electrons remain in the VB, unable to move to the CB where they can contribute to electrical conductivity. However, when a photon with energy greater than the bandgap is absorbed, the electron can promote to the CB, leaving behind a "hole" in the VB. This process, known as photon excitation, creates an exciton (electron-hole pair).[63] The electron can move freely through the CB, while the hole behaves like a positively charged particle moving through the VB. In semiconductors with a direct bandgap like perovskites, the electron and hole have matching momenta, allowing efficient photon absorption and emission. In contrast, indirect bandgap materials, like silicon, require a phonon to

assist in the excitation process, making the whole process less efficient. The key phenomena related to the interaction of semiconductors with photons include: photon absorption, electron excitation, and recombination processes. The interaction between light and semiconductor materials is fundamental to defining their optoelectronic properties.

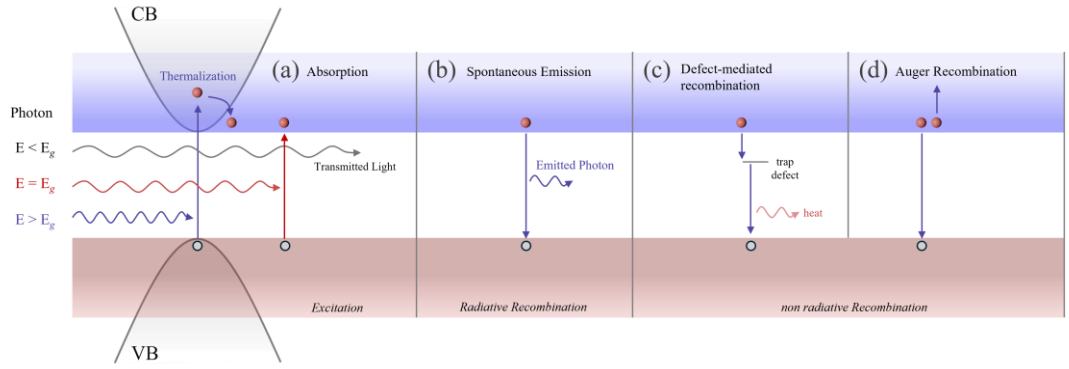

Figure 15. Diagram illustrating light interactions in semiconductor materials, showcasing: (a) the process of light absorption, (b) spontaneous emission, (c) defect-mediated recombination, and (d) Auger recombination.

When photons with energy equal to or greater than the material's bandgap strike the semiconductor, electrons are excited from the valence band to the conduction band, leaving behind holes and generating excitons (see Figure 15a). This process is critical in devices such as PV and photodetectors, where the efficient generation of charge carriers is necessary for energy conversion or detection. The efficiency of light absorption depends on the material's absorption coefficient and the energy of the incident photons. Following this excitation, radiative recombination occurs when electrons and holes recombine, resulting in the emission of a photon. This process, known as spontaneous emission (Figure 15b), is central to the operation of devices like LEDs and lasers, where precise control over the emission wavelength is essential for their functionality. The rate of spontaneous emission is influenced by several factors, including the density of states and the electronic structure of the material, both of which determine the probability of radiative transitions and the efficiency of the emission process. In the context of non-radiative recombination processes, two key mechanisms significantly impact the performance of semiconductor devices: defect-mediated recombination and Auger recombination Figure 15c and Figure 15d,

respectively. Defect-mediated recombination occurs when imperfections, such as impurities or crystallographic defects, introduce localized energy states within the bandgap.[64] These defects trap charge carriers (electrons or holes), facilitating their recombination without photon emission, dissipating energy as heat. This non-radiative pathway detrimentally affects carrier lifetimes and device efficiency, particularly in materials with high defect densities or insufficient surface passivation. Meanwhile, Auger recombination represents another non-radiative process in which the energy released from electron-hole recombination is transferred to a third carrier (electron or hole), which is subsequently excited to a higher energy state rather than emitting a photon. Auger recombination leads to efficiency losses, often observed as "efficiency drop" in LEDs, by reducing the number of radiative recombination events. [42]

Perovskite semiconductor materials, known for their high defect tolerance and superior optoelectronic properties (above discussed), are promising candidates for reducing non-radiative losses.[64] As a result of this, current research efforts are being devoted to addressing interface-related challenges by refining the composition and structure of transport layers, as well as implementing effective surface defect passivation strategies.[65] These advancements aim to mitigate non-radiative losses and improve the overall performance and longevity of perovskite-based optoelectronic devices.

Given that a significant portion of this Thesis is dedicated to investigating the emission properties of PNCs it is essential to thoroughly examine the concept of photoluminescence quantum yield (PLQY). Understanding PLQY is critical for analyzing the efficiency of light emission and thus comparing the rates of radiative and non-radiative pathways in these materials.

2.2.3.1 *Photoluminescence Quantum Yield (PLQY)*

PLQY is a key figure of merit used to assess the efficiency of light emission in semiconductor materials, particularly those employed in optoelectronic applications such as LEDs, lasers, and PSCs. PLQY reflects the material's ability to convert absorbed photons into emitted photons and is directly linked to its optical performance. In high-efficiency materials achieving a high PLQY is critical, as it signals minimal energy loss through non-radiative recombination pathways.

PLQY is formally defined as the ratio of the number of photons emitted to the number of photons absorbed by a material (see Equation 4). In an ideal scenario, a PLQY of 100% indicates that all absorbed photons result in the emission of photons, meaning that the material has no non-radiative losses.

$$PLQY = \frac{\text{Number of emitted photons}}{\text{Number of absorbed photons}} \quad 4$$

However, in real-world materials, non-radiative processes such as defect-mediated recombination and Auger recombination reduce the PLQY, limiting the efficiency of devices. The quantum yield can also be expressed in terms of the radiative (*kr*) and non-radiative (*knr*) recombination rates (Equation 5).

$$PLQY = \frac{k_r}{k_r + k_n r} \quad 5$$

When non-radiative recombination dominates (*knr* >> *kr*), the PLQY approaches zero, whereas materials with a large radiative recombination rate relative to non-radiative processes will have a high PLQY, indicating efficient photon emission. Several factors influence the PLQY of a semiconductor material, including:

- Material Purity: Defects in the crystal lattice, such as vacancies or interstitial impurities, create trap states that facilitate non-radiative recombination, thereby reducing PLQY.
- Surface Passivation: Unpassivated surfaces introduce trap states, especially in nanocrystals where surface-to-volume ratios are high. Efficient surface passivation can significantly reduce these non-radiative losses.
- Exciton Binding Energy: Materials with high exciton binding energy tend to exhibit higher PLQY due to a lower likelihood of carrier separation before radiative recombination occurs.
- Environmental Conditions: External factors, such as temperature and humidity, can influence PLQY. For instance, in perovskite materials the continuous exposure to moisture can lead to degradation, thereby decreasing the PLQY.

Thus, the PLQY of semiconductor materials serves as a crucial parameter for determining their efficiency in converting absorbed light into emitted light. It is influenced by both intrinsic material properties and external factors, and achieving a

high PLQY is essential for optimizing the performance of optoelectronic devices. In PNCs, which have shown promise in various applications, achieving a high PLQY has been a key area of research. Perovskites typically exhibit strong light absorption and can attain high PLQY values through careful control of synthesis conditions, compositional tuning, and surface passivation techniques.[66] This significant strides in enhancing PLQY have led to their growing adoption in high-efficiency applications.

2.2.4 Synthesis of PNCs

In this section of the chapter, we will review the main synthetic routes for the preparation of semiconductor NCs, focusing on how these methods allow for precise control over their size, shape, and optoelectronic properties. To fully grasp the field of PNCs, it is essential to first understand the concept of colloidal NCs, as this forms the foundation for exploring various synthesis methods and approaches.

"Colloidal" refers to particles that are dispersed in a solvent, forming a stable suspension. In the context of NCs, colloidal systems are highly valued because they allow for precise control over particle size and surface chemistry, leading to stable, uniform nanomaterials that can be easily processed in liquid form, making them ideal for scalable applications in optoelectronics and nanotechnology.[55] Commonly, colloidal semiconductor NCs (usually called Quantum Dots) consist of a nanosized inorganic semiconducting core surrounded by an organic ligand shell. This outer shell ensures colloidal stability (avoiding merging), surface passivation, and aids in controlling the size and shape of NCs during their growth.[67] The inorganic core is often composed of materials like CdE, PbE, or $CsPbX_3$ (where E = S, Se, Te and X = Cl, Br, I). More complex structures, such as hetero-NCs, feature multiple semiconductor domains. These NCs, even often depicted as spheres or cubes, are typically truncated with facets to reduce surface energy. A compact overview of NCs ligand binding motifs and the main ligand binding reactions to the surface are presented in Figure 16.

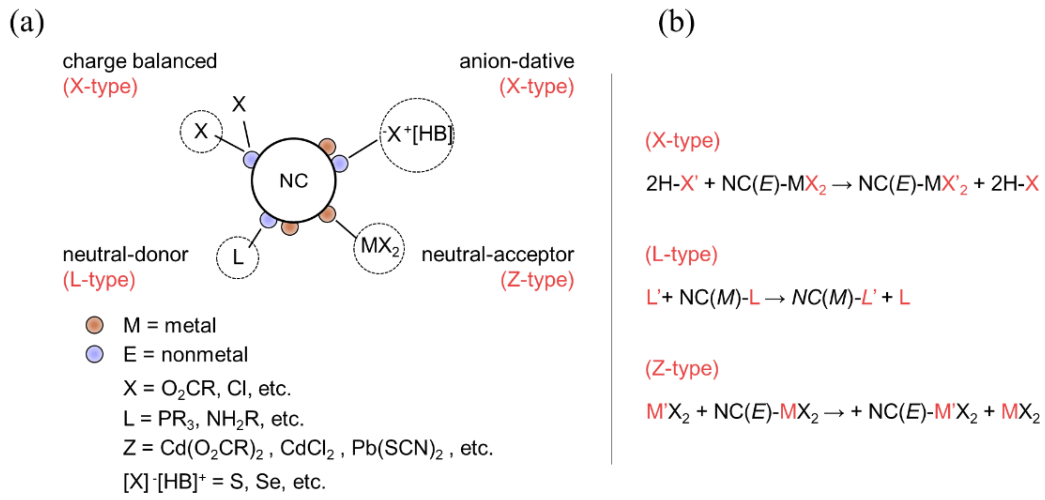

Figure 16. NCs Ligand (a) binding motifs and (b) surface exchange reactions using the L, X, Z formalism. Adapted from Ref[68].

The hot-injection method, the most widely used technique for synthesizing NCs, was first introduced by Murray et al. who demonstrated the decomposition of molecular precursors in high-temperature organic solvents.[56] This method involves rapidly injecting precursors into a hot solvent, where they decompose and release atomic monomers (the building blocks of the NCs). The rapid release of monomers creates a high degree of supersaturation, driving the growth of nanocrystals. This technique offers the advantage of a tunable reaction environment, allowing to adjust the temperature and composition of the solvent to control the kinetics of nanocrystal growth.[69] In organic solvents, the temperature and solvent composition play critical roles in determining the size, shape, and crystalline phase of the nanocrystals. For example, semiconductor NCs such as CdTe can be synthesized in different crystalline phases, such as the hexagonal wurtzite phase at higher temperatures or the cubic zinc blende phase under carefully controlled reaction conditions.[70] The solvent in these reactions serves two primary functions: solubilizing and dispersing the reactants and nanocrystals, and controlling the reaction rate. This is achieved by solvent molecules dynamically binding and unbinding from the surface of the growing nanocrystals. When a solvent molecule detaches from the nanocrystal surface, new monomers can incorporate, allowing the crystal to grow.[71,72] These solvent molecules, often referred to as surface ligands, play an important role in determining the growth dynamics of the nanocrystals. Surface ligands typically consist of a non-polar domain, often a long alkyl chain, and a polar head group (see Figure 16). The non-polar domain influences

the diffusion properties of the molecules, while the polar head group affects the binding strength to the nanocrystal surface. This balance between diffusion and binding plays a crucial role in determining the final shape and size of the nanocrystals. By carefully selecting and controlling the surface ligands, the growth process can be fine-tuned, making this an essential factor in nanocrystal synthesis.[72,73]

In more detail, the hot-injection synthesis of nanocrystals consists of three major steps. Initially, metal and non-metal precursors are complexed with organic ligands at high temperatures (100-300°C), forming the molecular building blocks for nanocrystal growth.[74] Next, one precursor solution is swiftly injected into a hot solution containing the other precursor, triggering nucleation and the controlled growth of nanocrystals. Once the desired size is reached, the reaction is stopped by cooling the solution to room temperature, often using an ice bath or cold solvent. In the final step, the nanocrystals undergo a critical purification process. This involves centrifugation to separate them from the reaction mixture, followed by washing with a low-boiling point solvent, such as toluene or hexane. The nanocrystals are often washed multiple times to remove residual ligands and high-boiling point solvents, which can hinder the conductivity of nanocrystal films.[73] This purification ensures that the nanocrystals are suitable for integration into devices like solar cells and LEDs.

Nevertheless, the intrinsic instability of colloidal NCs under environmental factors such as oxygen, UV light, temperature, and moisture, coupled with the complexity and multi-step nature of conventional synthetic routes, still represents a critical bottleneck that jeopardizes their practical application. Therefore, the development of more efficient and robust synthesis methods becomes essential to enhance their viability for real-world applications.

2.2.4.1 *Beyond the hot injection method.*

While the hot-injection method has been extensively discussed, it is important to note that NCs can be synthesized using a variety of other approaches, each depending on the materials and reaction environment involved. These methods are typically classified into "top-down" and "bottom-up" strategies. Top-down approaches involve breaking down larger solids, either mechanically, as in ball-milling with surfactants, or chemically, as in chemical exfoliation. In contrast, bottom-up methods start with individual molecules or ions, which are then assembled through chemical reactions in either the gas or liquid phase. Among these, liquid-phase synthesis has

emerged as one of the most effective bottom-up techniques for producing highly controlled colloidal MHP NCs. A comprehensive overview of the main synthetic routes, including both top-down and bottom-up methods, is provided in Table 2.

Table 2. Main synthetic routes of PNCs.

Synthetic Route	Solvent Type	Temperature	Reaction Time (scale)	Size/Shape Control	Yield	Key Features	Ref.
Hot Injection Method	Non-polar organic solvents and OAm	100-300°C	min	Good control over size and shape	High	Rapid injection of precursors into hot solvent leads to fast nucleation; tunable size by controlling temperature and time	58
Solvothermal Method	Organic solvents (OA, ODE)	80-180°C	hours	Moderate control (mostly shape)	Moderate to high	High-pressure reaction in sealed vessels enables growth of larger crystals; good for anisotropic shapes (nanorods, nanoplatelets)	75,76
Ligand-Assisted Reprecipitation (LARP)	Anti-solvent (toluene)	Room temperature	min	Limited control (mainly size)	High	Rapid precipitation by adding anti-solvent, yielding uniform small-sized NCs; often used for $CsPbX_3$ NCs	59
Microwave-Assisted Synthesis	Non-polar Organic solvents and OAm	100-150°C	min	Moderate control over size and shape	High	Microwave heating accelerates reaction kinetics and improves yield	77
Ultrasonic Synthesis	Non-polar Organic solvents and OAm	Room temperature	min	Moderate control oversize, limited shape control	Moderate	Ultrasonic waves provide energy input, resulting in rapid nucleation; mostly spherical NCs	78
Reverse Microemulsion	Mixed organic solvents (DMF and hexane)	Low temperature <130 ºC	hours	Good control over size	Moderate	Nanocrystals form in microemulsion droplets, providing precise size and shape control	79
Wet-Ball Milling	Non-polar Organic solvents and OAm	Room temperature	hours	Limited control	High to Moderate	Top-down method; bulk perovskite material is mechanically ground to produce nanocrystals; leads to irregular shapes and sizes	80
Exfoliation	Acetone	Room temperature	hours	Moderate control (layer thickness)	Low to moderate	Top-down method; bulk perovskite layered materials are exfoliated into thinner layers or nanocrystals; well-suited for 2D materials	81

2.2.5 New approaches: Nanocomposites

Despite the significant progress achieved using current synthetic approaches for PNCs, single-phase perovskites continue to face challenges in terms of stability and performance.[82] The stability and performance of colloidal QDs depend heavily on surface-protecting ligands, which often form weak ionic bonds that degrade upon film integration, negatively affecting photoluminescence (PL) and stability.[83,84] To overcome these limitations, an emerging research direction is the development of perovskite-based nanocomposites, which provide a versatile platform for tailoring material properties to meet diverse functional requirements.[82] Nanocomposite-based materials typically consist of perovskite components integrated with other substances and can adopt various structural forms, including core/shell and non-core/shell configurations.[85] Hybrid nanocomposites can be synthesized by combining different perovskite compositions or by integrating perovskites with other materials, creating intimate connections between phases .[86] As with perovskite NCs, the synthesis of perovskite nanocomposites can follow both top-down and bottom-up routes, including sol–gel synthesis, hydrothermal methods, hot injection, ligand-assisted reprecipitation (LARP), solid-state reactions, flame spray pyrolysis, chemical vapor deposition (CVD), and spin coating.[85] These approaches allow to produce various nanocomposite structures, either through simultaneous synthesis (in situ) or through separate post-processing steps.

In recent years, research in the synthesis of composite-based PNCs within matrixes/scaffolds has expanded significantly, with various groups exploring the potential of this method to enhance their stability and performance. These techniques have emerged as a promising alternative to ligand-mediated methods for synthesizing PNCs. In 2016 Dirin et al., introduced the synthesis of PNCs within mesoporous SiO_2, utilizing precisely defined pore geometries to control the crystal size and shape. This method was shown to be versatile, accommodating different cations (MA, FA, Cs) and halide anions (Br, I), resulting in tunable photoemission shifts.[87] A related study of Malgras et al., synthesized mixed halide PNCs, adjusting their size (from 3.3 to 7.1 nm) based on the pore dimensions of the SiO_2 template.[88] While these approaches offer precise control over nanocrystal size and improved stability, their granular form limits their integration into optoelectronic devices, which require laminar materials with high optical quality to minimize light scattering. By leveraging porous scaffolds, different

works have been able to prove their potential in optoelectronic applications and sensing.[89–91] Although conventional PNC synthesis methods have laid the foundation for advancements in the field, the development of nanocomposites offers a novel and less-explored path with the potential to significantly enhance the performance and stability of perovskite-based materials. Continued research into optimizing these hybrid structures may lead to breakthroughs that improve the stability and applicability of perovskite nanocomposites in a wide range of real-world applications.

In this line, the results presented in Chapters 4, 5 and 6 of this Thesis, are based on an in-situ nanocomposite-based approach. Unlike colloidal synthesis, which requires the use of structuring agents, this method controls the size and shape of the nanocrystals through the growth and confinement within a metal-organic matrix. This approach offers several key advantages. First, PNCs grow directly within the matrix, bypassing complex and additional purification processes. As a result, issues such as self-aggregation, which typically occur due to ligand detachment during washing and deposition, are avoided. Particularly the NCs synthetic method described in this Thesis, the dynamics of the crystallization of the PNCs can be controlled. Furthermore, the matrixes can be tailored in terms of their chemical composition and therefore the growing rate of the NCs, offering a flexible platform for optimizing the properties of PNCs for various applications. This synthesis approach, therefore, represents a significant advancement in the field of nanomaterials.

The next section delves into the fundamental principles and key characteristics of PSCs, providing an overview of the most widely utilized fabrication techniques.

2.3 MHP SOLAR CELLS

In the previous sections, we introduced MHPs, their structural and optoelectronic properties, followed by a discussion of nanocrystals and their relevance in modern materials science. In this section, we shift the focus toward solar cells, specifically exploring how these materials can be integrated into PV devices.

A solar cell, or PV cell, is an electronic device that converts light energy directly into electrical power through the PV effect. Currently, silicon-based solar cells (first-generation PV) dominate the market due to their continuous advancements in power conversion efficiency (PCE) and decreasing fabrication costs over the past four decades.[92] In many regions, they have achieved cost parity with traditional electricity

generation from fossil fuels.[93] However, newer solar cell technologies offer the promise of reduced material consumption and manufacturing costs, and improve large-area production.[94] These include thin-film solar cells, such as those based on CdTe, CIGS or amorphous silicon (second-generation PV) and solution-processed devices using organic semiconductors, hybrid composites, and inorganic semiconductors (third-generation PV). Second-generation PVs, though promising, have a significant drawback when considering large-scale deployment, as some of the active materials contain rare elements like tellurium and indium.[95] In contrast, third-generation PV technologies have gained substantial interest in recent years due to their potential for high efficiency and cost-effective production, as we have been repeatedly mentioning in the different sections of this current chapter.[96] Because of this, remarkable improvements in their efficiency, reproducibility, and stability have been achieved recently.

The next sections aim to establish the principles of solar energy conversion as it will serve for the description of the results from Chapter 7 of this Thesis.

2.3.1 The solar spectrum and Schockley-Queisser limit

The solar spectrum covers wavelengths from 280 to 4000 nm, with total irradiance at the Earth's surface influenced by the path length through the atmosphere, which is determined by the sun's position relative to the Earth's surface. Atmospheric filtering affects solar irradiance on Earth, scattering shorter wavelengths like blue light and absorbing certain wavelengths, particularly in the infrared range due to gases like CO_2 and water vapor. The path is quantified using the air mass (AM) coefficient, with AM1 indicating sunlight directly overhead. To standardize energy conversion processes, reference spectra are used: AM0 for extraterrestrial solar radiation and AM1.5G for sunlight passing through 1.5 times the atmospheric mass at a 48.19° angle (see Figure 17a). These standardized spectra are defined by the American Society for Testing and Materials (ASTM), with the AM0 spectrum derived from ASTM E-490 and AM1.5G from ASTM G173.[97] The irradiance spectra for AM 0, AM 1.5D, AM 1.5G, and a black body with a surface temperature of 6000 K (representing the Sun) are presented in Figure 17b.

For terrestrial semiconductor-based solar cells that interact with incoming sunlight, the Shockley-Queisser limit (Shockley and Queisser, 1961) is a key consideration.[98] This limit represents the maximum theoretical efficiency for a solar cell with a single-bandgap semiconductor, accounting for intrinsic physical losses but excluding extrinsic factors like resistive losses, reflection, or transmission. For these calculations, only unavoidable intrinsic losses are considered, such as thermalization, where photogenerated electron-hole pairs are collected at a lower energy than the incoming photons. Additionally, photons with energies below the bandgap are not absorbed. Based on approximations of the sun as a black body and refined with the AM1.5 solar spectrum, the Shockley-Queisser limit estimates the maximum efficiency for a single-gap solar cell at around 33% under standard conditions (AM1.5G), with optimal bandgap values between 1.1 and 1.6 eV.[99] Higher concentration factors can slightly increase this efficiency, but unavoidable radiative recombination and thermalization prevent cells from exceeding these fundamental limits.

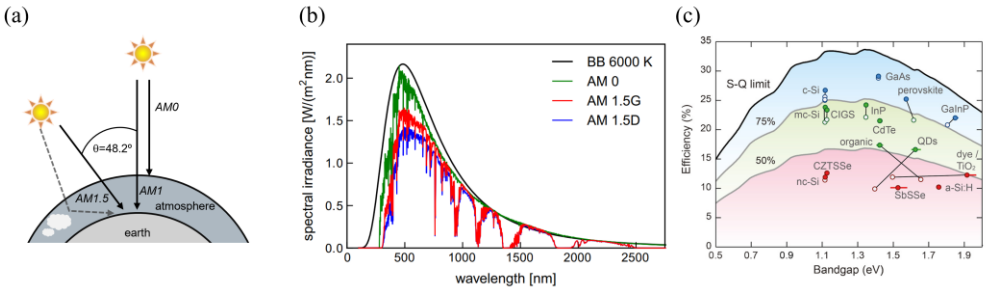

Figure 17. (a) A schematic illustration of the spectral irradiance outside Earth's atmosphere (AM0) is presented, alongside the irradiance on Earth's surface for direct sunlight (AM1.5D, solid arrow). Additionally, the figure shows the contribution from both direct sunlight and scattered atmospheric light (AM1.5G), represented by solid and dashed arrows, integrated over a hemisphere. (b) The spectral irradiance data from ASTM G173-03 is compared with the black body spectrum at a temperature of 6000 K, which was used in the Shockley-Queisser efficiency model. (c) The record efficiency of solar cells made from various materials is plotted against their respective bandgap, in comparison to the Shockley-Queisser limit (top solid line). Open symbols represent the record efficiencies as of April 2016, while solid symbols depict the updated efficiencies as of July 2020. (a,b) Reproduced from Ref[100] and (c) Reproduced from Ref[99].

2.3.2 PSCs state of the art and device configurations

In the section 2.1.4 of this chapter we have introduced the main properties of MHP materials. Besides those, these materials exhibit low formation energy and high thermal expansion coefficients.[101] The low formation energy enables the crystallization of MHP thin films through low-temperature deposition techniques, presenting both challenges and opportunities depending on the chosen synthetic route.[94] The optoelectronic properties of MHP films are highly dependent on the crystalline structure and microstructure of the film,[102] with grain size playing a crucial role both in terms of stability and performance of PSCs.[103] The phase purity of perovskite films is another critical factor. For example, secondary phases of the crystalline material can form, leading to the development of mixed grain structures when multicomponent perovskites are used.[104] While this sometimes being beneficial as passivating defects, it can also act as trap states for photoexcited carriers, promoting non-radiative recombination and accelerating degradation.[105]

Hybrid organic-inorganic and all-inorganic MHP PSCs represent a key component of third-generation PV technologies. As discussed earlier in this chapter (see in Figure 7), PSCs have made significant strides, with single-junction devices now achieving efficiencies up to 26.7%. This makes PSCs the most efficient among emerging PV technologies, rivaling the highest efficiencies reported for silicon-based PV technologies.[13] A review of the NREL's best research cell efficiency chart clearly demonstrates the significant advancements in perovskite-based technologies over the past decade, establishing perovskites as a promising material in the field of PV. Not only that but the integration of perovskites in tandem perovskite devices or with silicon PV technologies has achieved remarkable efficiencies, reaching up to 29.1 and 34.6%, respectively, as of the time of writing these lines (see Figure 18).

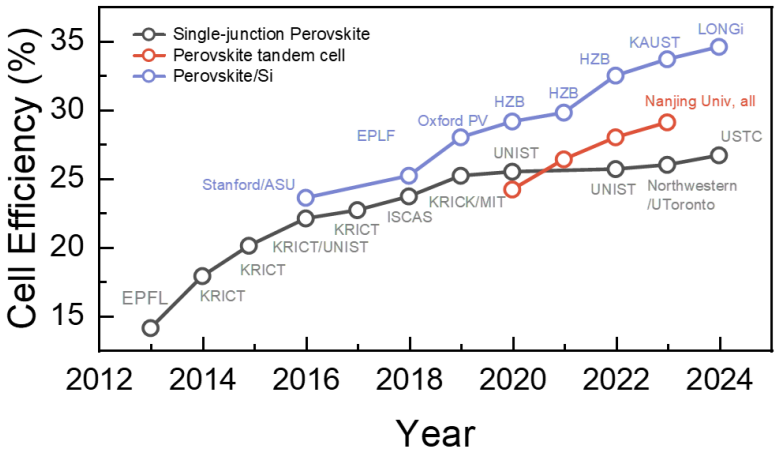

Figure 18. The progression of the highest PCE for single-junction PSCs, perovskite tandem cells, and monolithic two-terminal perovskite-silicon tandem solar cells from 2012 to 2024, along with key institutions driving these advancements.

A typical architecture of a single-junction planar PSC consists of, at least, five layers: a transparent electrode usually transparent conductive oxides (TCO), an electron transport layer (ETL), a perovskite layer, a hole transport layer (HTL), and a metal electrode. Based on their architectural configuration, the two primary categories of device architectures are classified as n-i-p and p-i-n, as illustrated in the schematic presented in Figure 19. The energy levels of the ETL and HTL are carefully chosen to match the CB and VB bands of the perovskite material, ensuring efficient extraction of photogenerated electrons and holes, which is critical for sustaining the PV effect (see detailed energy band levels of HTLs, ETLs, and typical perovskite composition in Figure 19). Factors such as non-radiative recombination at the interfaces of the perovskite and the charge transport layers (CTLs) directly affect the device's overall performance, including short circuit current density and fill factor.

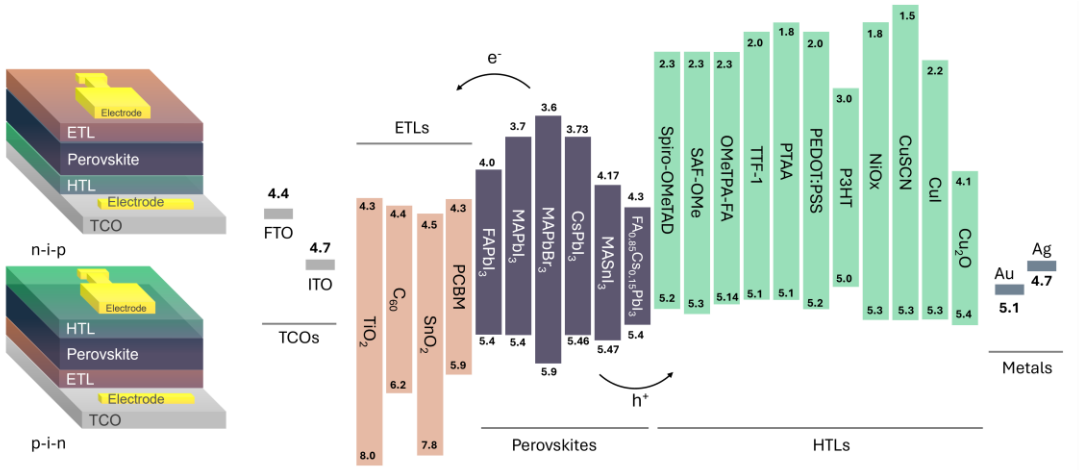

Figure 19. The left section of the image shows a schematic representation of p-i-n and n-i-p perovskite solar cell (PSC) configurations, while the right section highlights commonly used CTLs: HTLs and ETLs, and typical perovskite compositions along their corresponding energy band levels. Adapted from Ref[106].

Understanding the role of charge-selective contacts and their impact on charge extraction is fundamental for optimizing PSCs performance. In the following section, we will delve into the key parameters, governing solar cells efficiency, that are monitored when evaluating their performance.

2.3.3 Device Characterizations in Solar Cells

In the characterization of solar cell devices, a thorough understanding of the operational parameters is essential for evaluating performance under illumination. Key aspects include the behavior of photogenerated charge carriers, recombination dynamics, and the influence of voltage on current generation. Under illumination, excess electrons and holes accumulate in the CB and VB, respectively, leading to the formation of separate quasi-Fermi levels. By controlling the voltage (V) across the solar cell contacts, the balance between photogenerated carriers and recombination events can be adjusted, directly affecting the output current. At open circuit (OC) conditions, no external current is extracted, and the recombination rate of carriers equals the rate of photogeneration, establishing the OC voltage V_{OC}, a fundamental indicator of device performance. Under applied voltage ($V < V_{OC}$), the solar cell generates photocurrent, with the net current representing the differential between the photocurrent j_{ph}, recombination current j_{rec}, and dark current j_0 (Equation 6). The

resulting current-voltage (*j*–*V*) characteristic reflects the device's response under illumination.

$$j = j_{ph} - j_{rec} + j_0 \qquad 6$$

The PCE of a PV device quantifies its maximum power output relative to the incident AM 1.5G solar spectrum (1-Sun illumination at 100 mW/cm²), measured under simulated conditions at 25°C. This efficiency can be derived from current density-voltage (*j*-*V*) scans taken under 1-Sun conditions, where current density *j* is expressed in mA/cm². Key parameters extracted from the *j*-*V* curve include the short-circuit (*SC*) current density, j_{SC}, (current density at zero voltage), V_{OC}, and the fill factor (*FF*)[9], which characterizes the curve's shape. The maximum power point (MPP), defined by the product $J_{MPP} \times V_{MPP}$, indicates the optimal operating condition for power output. For calculating the PCE, the formula $PCE\ (\%) = Jsc \times Voc \times FF/100$ is applied, and FF itself is determined as $J_{MPP} \times V_{MPP} / J_{SC} \times V_{OC}$,. Additionally, a *j*-*V* curve measured in dark conditions, known as a dark *j*-*V* curve, reveals key information about the series resistance (R_s), shunt resistance (R_{sh}), and reverse saturation current density, typically with *j* shown on a logarithmic. R_S reflects the resistance that charge carriers encounter in route to the external circuit mainly from the resistances of the CTLs, interfaces, and electrodes. R_{sh} indicates the resistance to leakage current within the device, influenced by electronic defects and the internal electric field across the contacts. A high R_{sh} and low R_S are desirable for efficient PV performance. Together, these parameters (depicted in Figure 20), allow comprehensive analysis of solar cell performance, from energy conversion efficiency to current-voltage behavior under standard testing conditions.

[9] A representation of the curve's 'squareness'

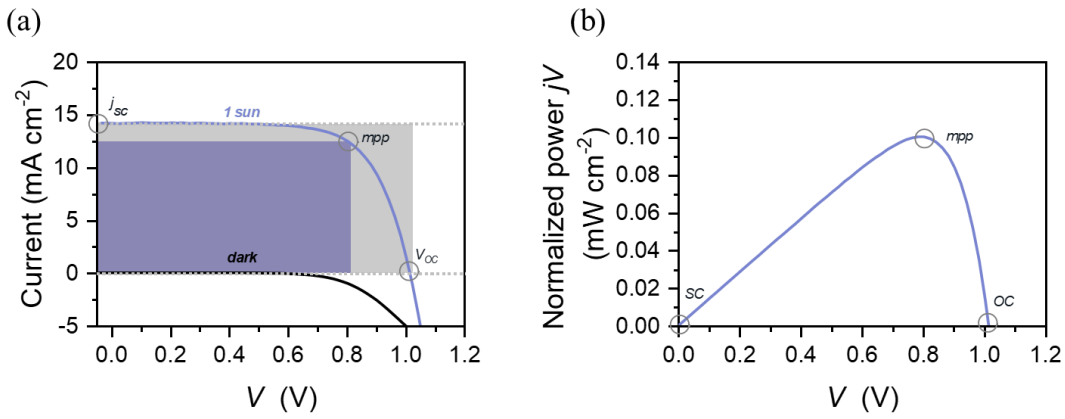

Figure 20. Diagram of *j*-*V* curves for solar cells under (a) simulated 1-Sun illumination and dark conditions. The illuminated curve (solid blue line) shows key parameters including j_{SC}, V_{OC}, *FF*. The fill factor (FF) is the ratio of the areas of the blue and grey areas. (b) The electrical power output of the solar cell as a function of voltage, normalized to a light intensity of 100 mW/cm² (equivalent to 1 sun). The *MPP* is indicated.

Beyond the conventional PV paramaters discussed above, analyzing hysteresis offers valuable insights into the performance characteristics of solar cells, particularly in MHP-based devices. Hysteresis in *j*-*V* curves occurs when the forward and reverse voltage scans (from low to high and high to low, respectively) do not produce identical results (see Figure 21a). Factors contributing to hysteresis in PSCs include absorber layer quality, device configuration, CTL materials, and scan parameters like range and rate. Hysteresis affects the FF and V_{OC} and is quantified by the hysteresis index (*HI*), calculated as $HI = PCE_{RS} + PCE_{FS} / PCE_{RS}$, where PCE_{RS} and PCE_{FS} are the efficiencies in reverse and forward scans, respectively.

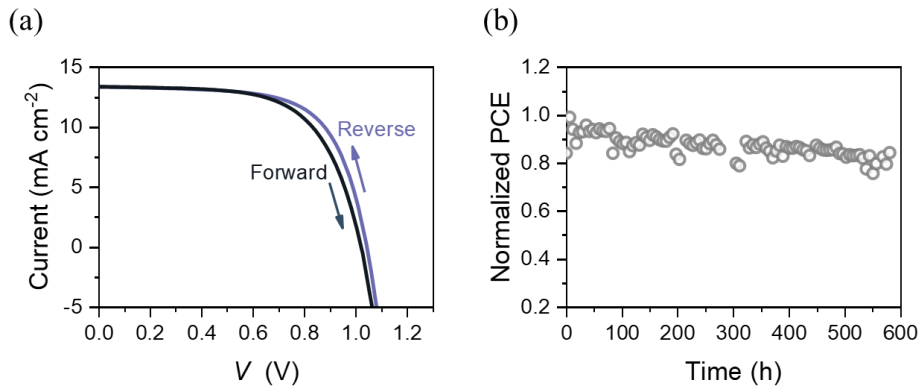

Figure 21. (a) Schematic representation of a *j*-*V* curve under 1-Sun illumination highlighting the Forward and Reverse scans (FS and RS, respectively). (b) MPP tracking, defined as the power output density (normalized PCE) of the PSCs vs. time.

Significant hysteresis in *j*-*V* curves complicates accurate PCE measurement and the determination of a PSC's maximum power output. Prolonged light exposure can elevate mobile ion concentration in the perovskite, reducing j_{SC} and the PCE; thus, MPP tracking is used for reliable power output determination (see Figure 21b). It also serves as an effective tool for assessing stability, particularly within standardized aging protocols to enable consistent data comparison across the PV research community.

2.3.4 Synthetic pathways for preparing PSCs

The synthesis of PSCs is critical to determining their scalability, efficiency and stability. In this section an overview of the wide variety of methods available is provided. The most prominent solution-based and physical deposition techniques are compared, each offering unique benefits and limitations in terms of film quality, manufacturing complexity, and cost. It is important to note that PSC fabrication encompasses not only the preparation and crystallization of the perovskite absorber layer but also the fabrication of the complete device stack, including the charge transport layers (CTLs) as well as the bottom and top electrodes.

2.3.4.1 *Solution-Based Techniques*

Solution-based methods are the most widely used for PSC fabrication due to their simplicity, lower cost, and compatibility with flexible substrates. Among them spin-coating, doctor blade coating, and slot-die coating are the most common ones, each exploiting the characteristics of solution-based processes to form high-quality perovskite layers.

Spin-coating is a popular choice for lab-scale fabrication of PSCs, wherein a perovskite precursor solution is deposited onto a substrate and then rapidly rotated to spread and thin the solution across the surface. This process leads to uniform thin films, critical for achieving high device efficiencies. The rapid drying nature of spin coating promotes crystal formation, resulting in dense, high-quality films with minimal pinholes. However, scaling up this method presents significant challenges, particularly in maintaining film uniformity over large areas, which is crucial for consistent device performance.[107] Spin coating is also sensitive to environmental conditions (humidity and temperature), which can impact film quality and reproducibility. Alternatively, *Doctor blade coating* is a simple, low-cost, scalable and versatile method for large-area applications, which makes it attractive for industrial processes. This method involves spreading the perovskite precursor solution across the substrate using a blade to achieve a controlled film thickness. In a similar way, *Slot-die coating* is a scalable deposition technique widely used for fabricating thin films in PSCs and other optoelectronic devices. In this method, a controlled amount of precursor solution is dispensed through a narrow slot onto a substrate, producing a uniform layer as the substrate moves beneath the slot. Slot-die coating offers excellent control over film thickness and material usage, making it highly efficient with minimal waste. Its compatibility with roll-to-roll processing makes it ideal for large-area applications and continuous manufacturing.[108] This technique also allows for the fine-tuning of coating parameters (such as flow rate, substrate speed, and solution concentration), enabling high-quality film formation.[109]

In short, solution-based techniques are advantageous for their low setup costs, ease of application, and compatibility with flexible substrates. However, challenges arise in scalability, uniform film thickness, and sensitivity to environmental conditions.[110] The simplicity of solution-based processing comes with trade-offs in terms of film consistency and quality, which are essential for high-efficiency devices.

2.3.4.2 *Physical Vapor Deposition Techniques*

The current most used Physical Vapor Deposition Techniques for the preparation of PSCs are pulsed laser deposition (PLD) and thermal evaporation (TE) each offering distinct advantages in terms of film quality, scalability, and cost-effectiveness.[111] Up to the present, TE stands out as the most widespread technique for the deposition of

perovskite layers. In the TE process, perovskite materials are deposited onto a substrate by heating precursor compounds under vacuum conditions. TE can be broadly classified into three approaches for PSCs: *single-source evaporation*, *co-evaporation*, and *sequential evaporation*. TE is a promising scalable approach for the fabrication of PSCs, offering unique benefits in terms of process control, material efficiency, and making it particularly advantageous for large-scale production.[110] The process is environmentally favorable, as it eliminates the need for toxic solvents like DMF or DMSO, thereby reducing both environmental and safety risks. Moreover, TE's widespread use in the electronic and optoelectronic industries facilitates the integration of PSCs production into existing manufacturing lines, a crucial factor for scaling from lab-scale cells to commercially viable modules.[112] Despite these benefits, TE also has limitations. The need for vacuum conditions adds complexity and increases operational costs, which may restrict its accessibility in some settings.[113] Additionally, the thermal stability of organic perovskite components must be carefully managed, as they can degrade at high temperatures. For multi-layer PSCs, TE can be labor-intensive, especially in sequential evaporation processes where each layer requires precise control over deposition parameters which results in high time-consuming fabrication steps. Nonetheless, recent advancements have demonstrated TE's effectiveness in creating high-performance, large-area PSCs with PCEs that are competitive with solution-processed cells.[110] Efficient mini modules with active areas spanning several square centimeters have been achieved, and ongoing research is focused on enhancing TE parameters to improve film crystallinity, reduce defect densities, curb evaporation times and increase PSC stability. Continued advancements addressing current limitations will be crucial to realizing TE's full potential in the commercial scaling of perovskite solar technology.

Over a period of fifteen years into perovskite PV research, spin-coating, and solution-based processing more broadly, continues to be the predominant method for PSC fabrication. For instance, as of the time of writing, making a query on various deposition techniques for the most common perovskite compositions (see **Error! R eference source not found.**) in the database created by Jacobsson, Unger, and colleagues[114] listed 26,029 devices. From those, 25,165 of the devices were fabricated exclusively using spin-coating techniques.

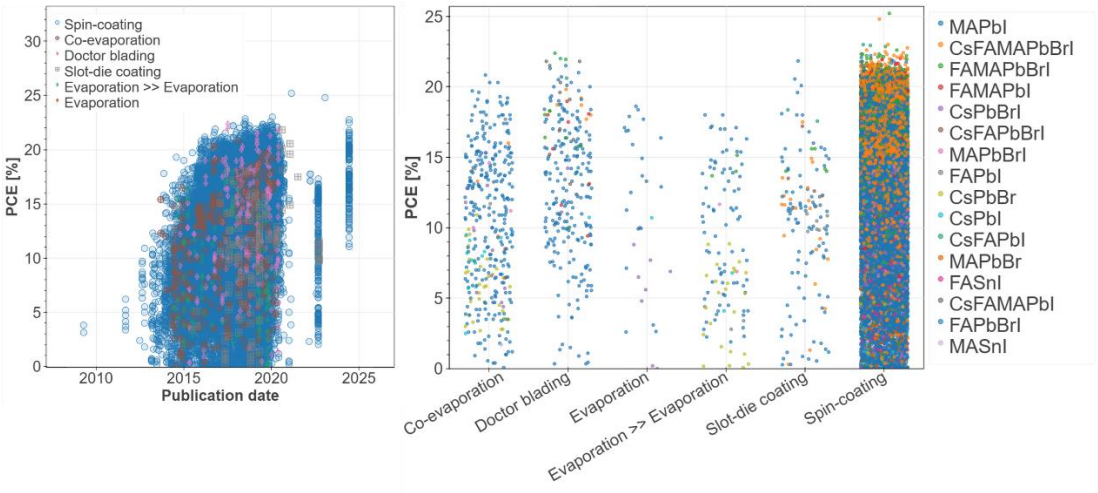

. Evolution of perovskite solar cell efficiencies in relation to deposition techniques for the perovskite layer and most common perovskite compositions in device architectures. The left panel shows PCE progression over time, while the right panel presents a histogram-style distribution of PCE, both comparing the perovskite deposition techniques. Data are sourced from the open-access database referenced in Ref.[114].

In Chapter 7 of this Thesis focused on PSC fabrication, spin-coating is the primary technique employed. While spin-coating is ideal for creating small-area devices and for investigating the properties of perovskite materials on a small scale, working with ink-based precursors allows these formulations to be readily adapted across various solution-processing techniques and substrates. The choice to use solution-based methods in this Thesis highlights their inherent versatility, offering a promising pathway for scaling up to large-area production and broadening the potential for industrial processes and applications.

The following chapter focuses on providing an overview of the synthetic and characterization methods that have been used throughout this dissertation to analyze the properties of the designed materials.

Chapter 3: Methods and Characterization Techniques

"If you wish to make an apple pie from scratch, you must first invent the universe."

Carl Sagan, *Cosmos*

This chapter provides an overview of the key fabrication methods and characterization techniques developed and employed throughout this Thesis. Rather than offering an exhaustive review of the techniques, it is intended to serve as a practical toolbox for identifying the principal techniques commonly applied in synthesis, analysis, and study of perovskite-based materials.

3.1 FABRICATION STEPS

Throughout the investigations described here all along, the novel materials were prepared using solution-processed deposition techniques. In the forthcoming chapters, the primary experimental results are obtained through fabrication processes conducted under standard laboratory conditions using conventional instrumentation. However, the inherent instability against moisture and oxygen of MHP materials presents significant challenges for their synthesis and characterization. Consequently, the next subsection will discuss the critical role of a nitrogen-filled glovebox in enabling the controlled preparation and handling of these sensitive materials.

3.1.1 Glovebox

A glovebox is a sealed enclosure that allows for the handling of sensitive materials in a controlled atmosphere, isolated from undesired agents such as oxygen, moisture, nitrogen and particulates. In PSC fabrication, gloveboxes are essential because tin-based and MHPs are highly sensitive to moisture and oxygen, which can rapidly degrade their material properties and performance. Within the glovebox, an inert atmosphere is maintained, often using nitrogen or argon to eliminate oxygen and moisture. This environment prevents any adverse reactions that could impair the quality of the perovskite films or precursor solutions. Heavy-duty gloves are attached to the walls of the box, allowing researchers to manipulate materials directly without compromising the isolated environment. Additionally, ports equipped with vacuum antechambers serve as entry and exit points, ensuring that materials can be safely transferred without contaminating the internal atmosphere (see Figure 22). The glovebox features a gas purification system that continuously filters and recirculates the inert gas, maintaining ultra-low levels of oxygen and moisture. Pressure control is also crucial; by maintaining a slight positive pressure relative to the external environment, the glovebox minimizes the risk of contaminants leaking inside. The glovebox environment is thus indispensable for multiple stages in PSC fabrication. It allows for the preparation of precursor solutions without unwanted reactions with moisture, which could lead to poor crystallinity, phase segregation or degradation. During thin film deposition and device assembly, the high-purity environment provided by the glovebox ensures consistent film quality, aiding in reproducible device performance. In the facilities where this Thesis research was conducted, the glovebox system includes an integrated evaporator. This setup enables the deposition of various

CTLs and electrodes at high-vacuum and under N_2 controlled conditions, as detailed in Chapter 7.

Figure 22. ABX_3Lab glovebox set-up for the fabrication of MHPs. The evaporator is located right behind the main antechamber (left side of the picture).

3.1.2 Spin-coating

The main features of solution-based materials (among many others mentioned in the previous subsection 2.3.4) are gathered in Table 3.

Table 3. Main features and advantages of solution-processed deposition techniques.

Feature	Description
Cost-effectiveness	Requires lower energy inputs, reducing production costs versus traditional vapor deposition.
Scalability	Supports large-area fabrication, ideal for solar cells, LEDs, and flexible electronics.
Versatility	Adaptation to a wide range of substrates, including flexible and non-rigid surfaces, opening the door to innovative applications like wearable electronics and roll-to-roll manufacturing.
Material diversity	Allows customization using various materials, including organics, hybrids, and nanomaterials allowing for customizable properties tailored to specific applications.
Low energy consumption	Operates at low temperatures, making it energy-efficient and reducing the manufacturing footprint
Simplicity of implementation	Techniques like screen-printing, roll to roll, and inkjet printing are simple and fit into existing pipelines.

Spin coating is a pivotal technique used to fabricate all the materials discussed throughout this research. However, it presents several challenges, including limitations related to substrate size. The selection of solvent, coupled with substrate wettability, plays a crucial role in determining the morphology of the resulting films. Additional limitations include the reliance on specific solvent evaporation rates, and the potential for defects due to variations in rotation speed, airborne particles or environmental conditions such as humidity. In this line, Chapter 5 will explore the crucial influence of humidity during the deposition process, presenting it as a key factor for investigating unconventional crystallization mechanisms in PNCs.

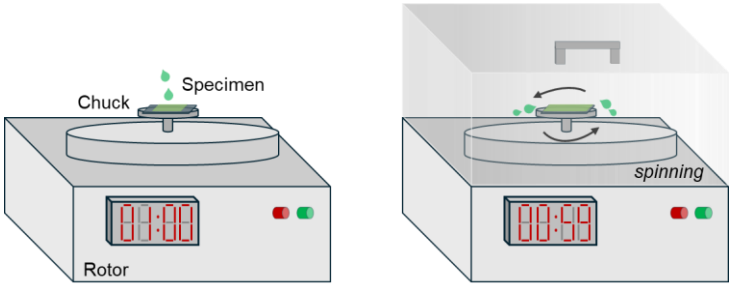

Figure 23. Schematics of a spin-coater working mechanism.

For materials such as MHPs, precursor salts are dissolved in organic solvents typically N,N-dimethylformamide (DMF) or dimethyl sulfoxide (DMSO) to the target concentration. To achieve uniformity and eliminate aggregates or undissolved particles, solutions are filtered prior to deposition. A small volume of solution (typically a few μL) is then placed on a pre-cleaned and ozone treated substrate and spin-coated at a certain speed and spinning-time (see the scheme of Figure 23). While spinning, the solution spreads evenly across the substrate, forming a thin film as the solvent evaporates. In many cases, including the preparation of PSCs in this Thesis, a post-deposition annealing step is essential to fully evaporate the solvent and dry the film. For PSCs, specifically, the annealing step also facilitates the crystallization of the perovskite precursor solution into a desired crystalline polymorph.

3.2 MATERIAL CHARACTERIZATION TECHNIQUES

3.2.1 Ultraviolet-visible spectroscopy

Ultraviolet-visible (UV-Vis) spectroscopy is an analytical technique widely employed to study the absorbance and transmission of UV and visible light in materials. In the UV-Vis region (typically 200–800 nm), this technique reveals valuable information about electronic transitions in molecules and materials, especially those with conjugated systems and chromophores. UV-Vis spectroscopy is extensively used in material science, chemistry, and biology due to its simplicity and ability to provide quantitative information about analytes in solution or solid form.

The quantitative analysis in UV-Vis spectroscopy is governed by the Lambert-Beer law:

$$A = log_{10}\left(\frac{I_o}{I}\right) = \epsilon cl$$

- Absorbance (A): A dimensionless quantity that indicates how much light a sample absorbs. It is defined as $A=-\log(I/I_0)$, where I is the intensity of light after passing through the sample and I_0 is the initial light intensity.
- Molar Absorptivity (ϵ): This constant depends on the nature of the absorbing species and the wavelength of light. It indicates how strongly a substance absorbs light at a particular wavelength and is expressed in units of $L \cdot mol^{-1} cm^{-1}$
- Concentration (c): The molar concentration of the absorbing species in the solution, typically in mol/L.
- Path Length (l): The distance the light travels through the sample, usually in cm. In most cases, standard cuvettes with a path length of 1 cm are used.

This law assumes that the absorbance is directly proportional to concentration and path length, enabling quantitative measurements. Deviations from the Lambert-Beer law can occur due to high analyte concentration, instrumental limitations, or chemical interactions that affect absorbance. The essential components of a UV-Vis spectrophotometer as depicted in Figure 24, include:

- Light Source: A UV-Vis spectrophotometer typically employs two light sources: a deuterium lamp for the ultraviolet range (200–400 nm) and a

tungsten-halogen lamp for the visible range (400–800 nm). The system switches between lamps depending on the selected wavelength range.

- Monochromator**:** A monochromator separates the light into individual wavelengths. It consists of a grating or prism that disperses the light, allowing a specific wavelength to pass through the sample. Adjustable slits control the bandwidth of the light, and high spectral resolution can be achieved by narrowing these slits.
- Sample and Reference Holders: Th sample is typically held in a transparent cuvette made of quartz (for UV measurements) or glass (for visible light measurements). In this research in particular thin-film materials were studied on quartz and glass substrates pieces.
- Detector: After passing through the sample, the transmitted light is collected by a detector, commonly a photomultiplier tube or a photodiode array (PDA). These detectors convert the light into an electrical signal proportional to the intensity of the transmitted light.

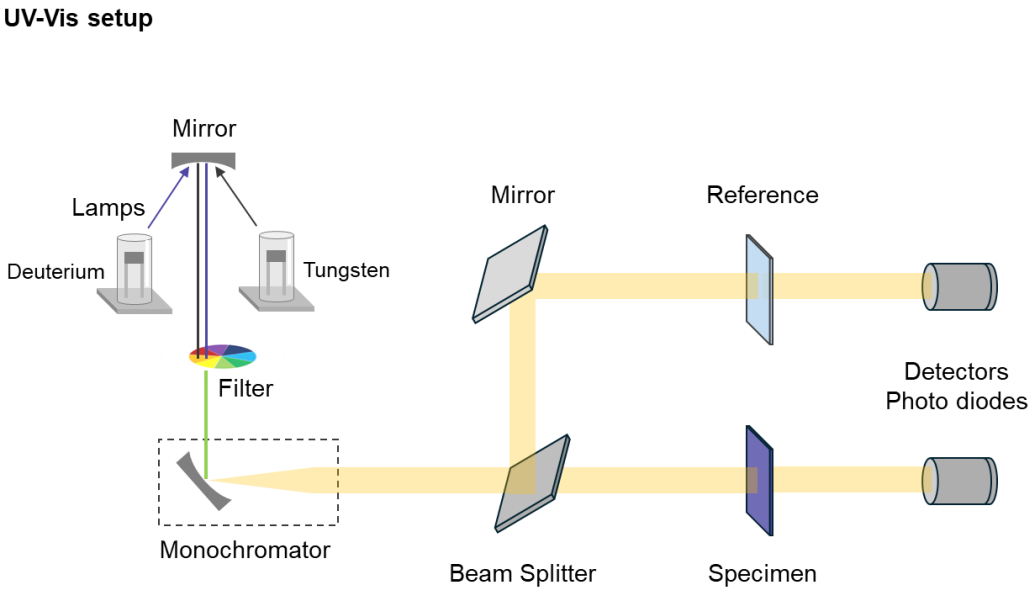

Figure 24. Schematic illustration of the commercial setup used for UV-Vis absorbance measurements. Adapted from Ref[115].

3.2.2 ATR-FTIR

Attenuated Total Reflectance Fourier Transform Infrared (ATR-FTIR) spectroscopy is an adaptation of traditional FTIR spectroscopy, specifically designed to analyze the surface of solid and liquid samples with minimal sample preparation. In ATR-FTIR, infrared light is directed into a high-refractive index crystal in contact with the sample. This configuration allows for the generation of an evanescent wave at the crystal-sample interface, enabling the measurement of absorption bands that correspond to specific molecular vibrations within the sample. ATR-FTIR is widely used in fields such as materials science, chemistry, and biochemistry for identifying chemical structures, studying molecular interactions, and characterizing surface chemistry. FTIR spectroscopy relies on the absorption of infrared light by molecules, which causes changes in their vibrational states. Each molecule has a characteristic spectrum of vibrational frequencies, allowing for identification through FTIR. ATR-FTIR differs from traditional FTIR in that it relies on an evanescent wave rather than direct transmission of light through the sample, which has several advantages:

- Evanescent Wave Interaction: When IR light enters the ATR crystal at an angle exceeding the critical angle, it undergoes total internal reflection, generating an evanescent wave that extends a few microns beyond the crystal's surface. This wave interacts with the sample in contact with the crystal, and the energy absorbed by the sample results in a characteristic FTIR spectrum.
- Enhanced Surface Sensitivity: Because only the sample surface is required to interact with the evanescent wave, ATR-FTIR can analyze opaque and strongly absorbing samples without complex preparation, unlike transmission FTIR, which requires thin films or dilutions.

An ATR-FTIR spectrometer consists of several critical components (see Figure 25) designed to facilitate infrared absorption measurements and produce high-resolution spectra:

- IR Light Source: Typically, an infrared source is used to emit a broad spectrum of IR light covering the mid-infrared range (4000–400 cm^{-1}).

- Interferometer: The interferometer allows the FTIR spectrometer to measure all IR wavelengths simultaneously, enabling rapid acquisition of spectral data.
- ATR Crystal (Internal Reflection Element): The ATR crystal is a high-refractive index material, commonly made from diamond, zinc selenide (ZnSe), or germanium, chosen based on chemical stability and desired depth of penetration. The crystal's refractive index should be significantly higher than that of the sample for total internal reflection to occur. The crystal is mounted to ensure firm contact with the sample, and its geometry, typically in the form of a trapezoid or prism, ensures multiple internal reflections.
- Detector: Detectors in ATR-FTIR are designed to convert IR radiation into electrical signals. The choice of detector depends on the required spectral range and sensitivity.
- Pressure Arm: For solid samples, an adjustable pressure arm is used to ensure optimal contact between the sample and the ATR crystal, enhancing the intensity of the evanescent wave interaction and resulting in clearer spectra.

ATR-FTIR setup

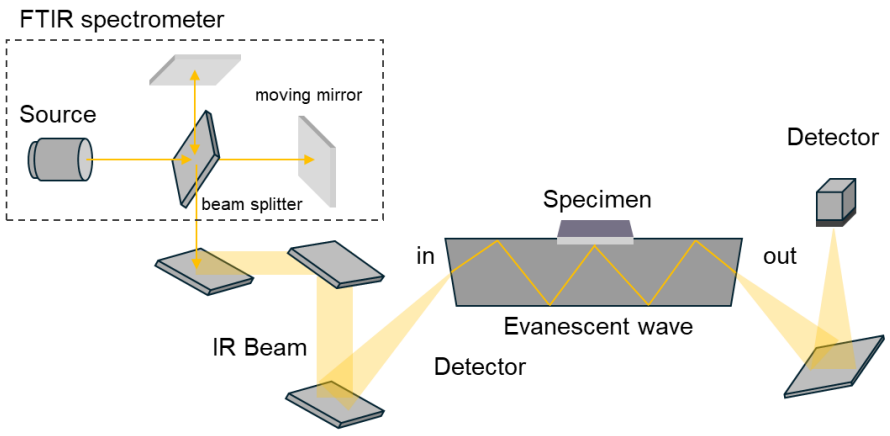

Figure 25. Schematic illustration of the commercial setup used for ATR-FTIR measurements.

3.2.3 PLQY and Time Resolved Photoluminescence (TRPL)

In the subsection 2.2.3 we have delved in the fundamentals of PLQY and its importance as a parameter for evaluating the efficiency of luminescent materials such as QDs. This is extended to semiconductors in general, as PLQY can be used as a figure of merit to assess the electrical losses of a material. A typical setup for measuring PLQY (see Figure 26) consists of the following components:

- Excitation Source: A monochromatic light source is used to excite the sample at a specific wavelength. This can be a continuous wave (CW) laser or a xenon or LED lamp equipped with filters or a monochromator to select the excitation wavelength. The chosen excitation wavelength should correspond to an absorption peak of the material to maximize photon absorption.
- Integrating Sphere: The core of the PLQY measurement setup is an integrating sphere, typically made from a reflective material that ensures that all emitted and scattered light is captured, regardless of direction, providing a comprehensive measurement of the total emitted and absorbed photons.
- Detectors: The emitted and reflected light within the integrating sphere is collected by detectors, typically photomultiplier tubes (PMTs) or photodiode arrays (PDAs), depending on the sensitivity requirements. A spectrometer coupled to the detectors can capture the full emission spectrum, while the total signal intensity is used for PLQY calculations.

To measure PLQY, the process begins with a reference (blank) measurement, where the intensity of the excitation source is recorded inside the integrating sphere without the sample. This reference measurement establishes the baseline for determining the number of incident photons. Next, the sample is introduced into the integrating sphere and excited at the same wavelength and power, allowing for the emission spectrum to be recorded. This measurement captures both the emitted light intensity and any remaining unabsorbed excitation light. As mentioned in the 2.2.3 subsection, the PLQY is then obtained as the ratio of emitted to absorbed photons.

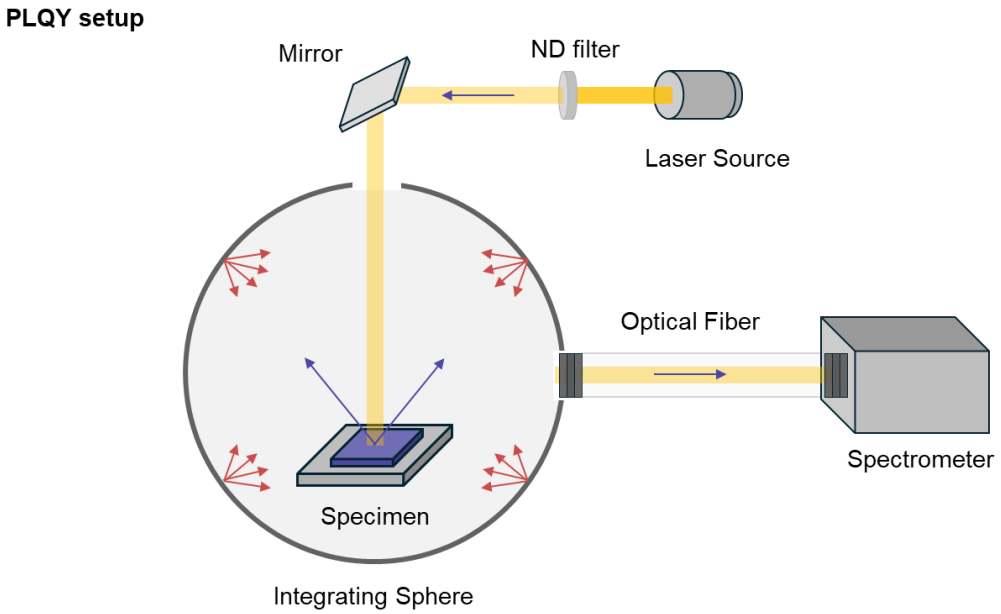

Figure 26. Schematic illustration of the home-made setup used for PL and PLQY measurements.

The TRPL measurements are based on the principle of excited-state decay following an initial excitation pulse. When a material is exposed to a short, high-intensity pulse of light, electrons are excited from the ground state to higher energy states. Over time, these electrons return to the ground state through radiative and non-radiative pathways, releasing photons in the process. The emission intensity decay follows an exponential or multi-exponential behavior, depending on the recombination dynamics present in the material. The TRPL decay profile reflects various processes, such as radiative recombination, trap-assisted recombination, and energy transfer, allowing researchers to deconvolute the contributions of each mechanism. A typical setup for measuring TRPL (see Figure 27) includes:

- Excitation Source: The sample is excited by a pulsed light source, typically a laser, that emits short pulses of high-intensity light. These lasers produce pulses with well-defined time intervals, allowing for controlled excitation of the sample and accurate measurement of decay dynamics. The excitation wavelength is usually selected to match the material's absorption band, ensuring efficient photon absorption.

- Sample Holder and Positioning System: The sample is placed on a holder, often with options for adjusting the angle and position to optimize light interaction.
- Detection System (Time-Correlated Single Photon Counting or TCSPC): The emitted PL is detected by a high-speed detection system. In TCSPC, each emitted photon is detected and time-stamped relative to the excitation pulse, building a histogram of photon arrival times to construct the decay profile.
- Spectrometer: A monochromator or spectrometer is often placed between the sample and the detector to select the emission wavelength being analyzed. This allows for decay analysis at specific emission wavelengths, providing information on the dynamics of individual transitions within complex materials.

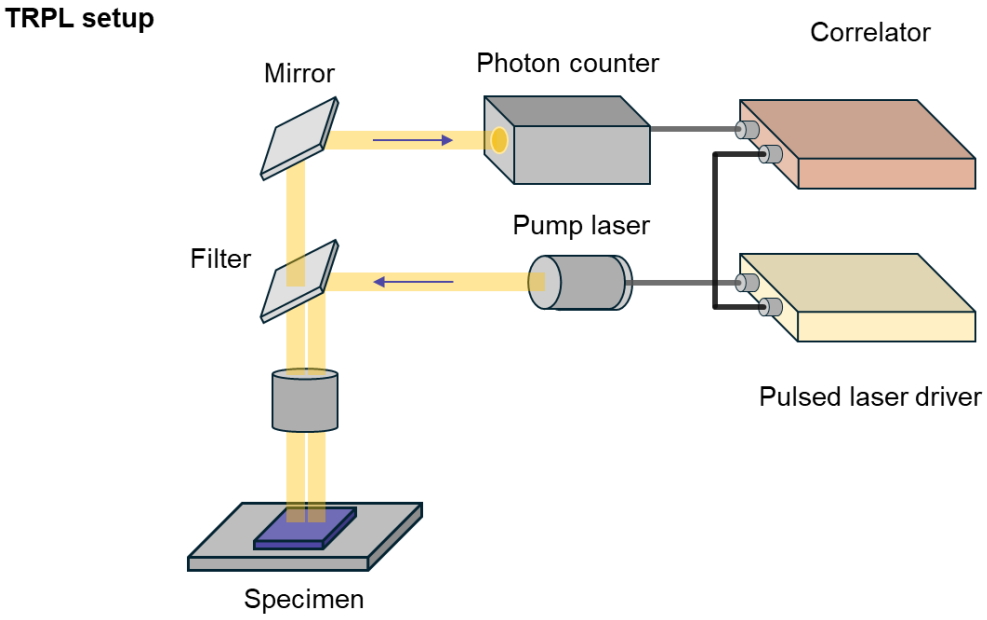

Figure 27. Schematic illustration of the setup used for TRPL measurements. Adapted from Ref[116].

3.2.4 X-ray Photoelectron Spectroscopy (XPS)

XPS is a surface-sensitive analytical technique used to identify the elemental composition, chemical state, and electronic structure of a material's surface. XPS operates on the photoelectric effect: when a material is irradiated with X-rays, core

electrons are ejected from surface atoms, and their kinetic energy is measured. The binding energy of each electron, calculated from the kinetic energy and the known X-ray photon energy, is characteristic of specific elements and oxidation states, allowing for detailed chemical analysis. The XPS spectrum plots the number of detected electrons versus their binding energy, with distinct peaks corresponding to different elements and chemical states. Surface sensitivity in XPS is of 1–10 nm depth, as only electrons from the outermost atomic layers escape the sample without energy loss. This makes XPS especially valuable for characterizing surface chemistry, thin films, and oxidation states.

A typical XPS setup (see Figure 28) consists of:

- X-ray Source: Usually an Al Kα (1486.6 eV) or Mg Kα (1253.6 eV) X-ray source to irradiate the sample surface, exciting core-level electrons.
- Ultra-High Vacuum (UHV) Chamber: The sample is placed in an ultra-high vacuum environment to prevent interference from air molecules and to ensure that emitted electrons can travel unimpeded to the detector.
- Electron Energy Analyzer: A hemispherical analyzer measures the kinetic energy of emitted electrons with high resolution, crucial for accurately determining binding energies and identifying chemical states.
- Detector and Data Processing: The analyzer transfers electron data to a detector, and a computer processes this data, producing a spectrum of binding energies. Advanced software fits peak profiles, enabling quantification and chemical state analysis of surface elements.

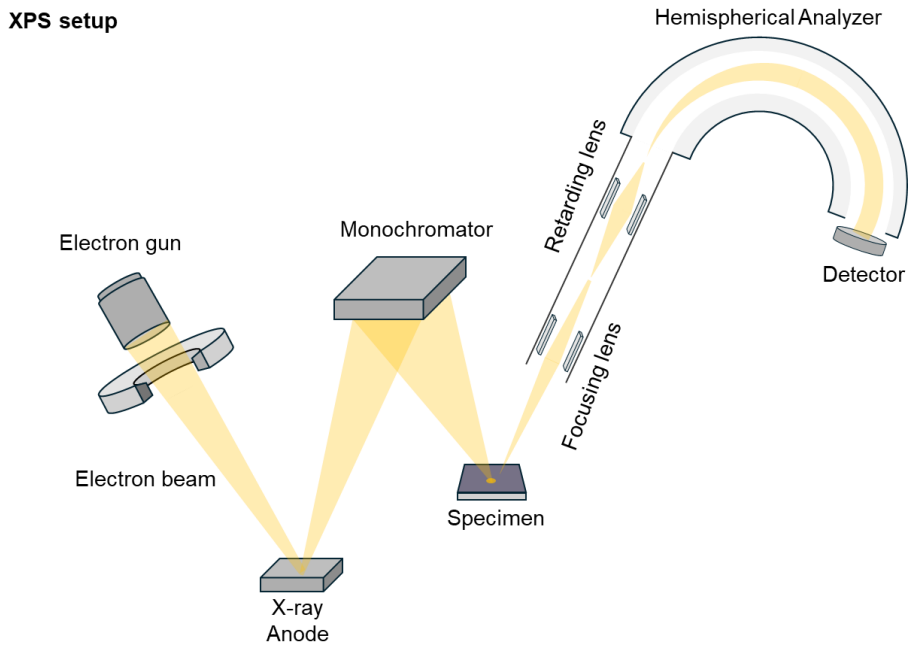

Figure 28. Schematic illustration of a XPS setup reviewing its main components and the working mechanism.

3.2.5 X-ray Diffraction (XRD)

XRD is a powerful technique used to determine the crystallographic structure, phase composition, and orientation of crystalline materials. XRD operates on the principle of Bragg's Law, where X-rays directed at a crystal lattice are diffracted by the atomic planes. When the angle of incidence satisfies the Bragg condition $n\lambda=2d\sin\theta$, constructive interference occurs, producing peaks in the diffraction pattern. These peaks correspond to specific interplanar spacings, allowing for identification of crystal structures and phases. An XRD pattern displays the intensity of diffracted X-rays as a function of 2θ, the angle between the incident and diffracted beams. The typical instrumentation for surface XRD characterization (see Figure 29) includes:

- X-ray Source: Typically, a Cu Kα source emitting X-rays at 1.54 Å, directed at the sample to generate diffraction.
- Goniometer: In XRD, there are two main configurations for the goniometer:
    - Sample Rotation Configuration: The goniometer is attached to the sample, rotating it to vary the angle of incidence (θ) while the detector remains fixed or moves along a 2θ path.

- Detector Rotation Configuration (θ-2θ Scan): In this arrangement, the sample remains fixed, and the goniometer controls the detector movement along a 2θ arc while simultaneously adjusting the angle of the incident X-ray beam to maintain the θ-2θ relationship. This setup is also widely used, particularly for thin-film and single-crystal XRD, and simplifies alignment by keeping the sample stationery.

- Detector: Measures the intensity of diffracted X-rays at different angles, generating data on the material's atomic structure.

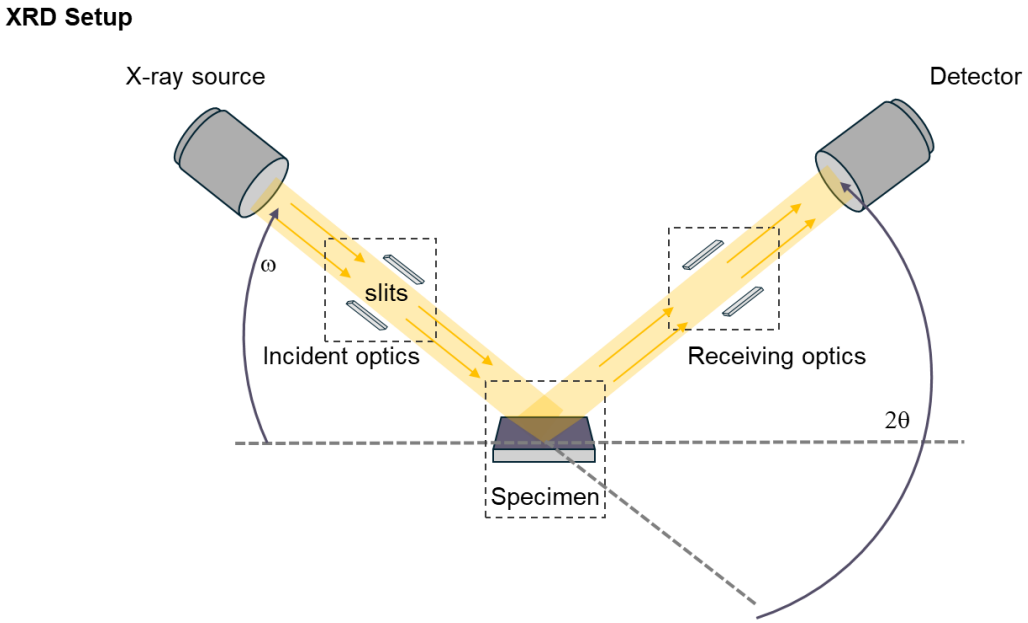

Figure 29. Schematic illustration of a XRD setup reviewing its main components and the working mechanism.

3.2.6 Scanning Electron Microscopy (SEM) and Transmission Electron Microscopy (TEM)

SEM and TEM are two essential electron microscopy techniques widely used for imaging and analyzing materials at the nanoscale (Figure 30). Both rely on electron beams rather than light to provide high-resolution images, but each has unique capabilities and applications due to differences in operation and sample interaction.

In SEM, a focused electron beam scans the surface of a sample. As electrons interact with the material, secondary and backscattered electrons are emitted and

collected to generate detailed surface images. SEM offers information on sample morphology, topography, and composition with resolutions typically ranging from nanometers to sub-nanometers, depending on the instrument's capabilities. TEM, by contrast, involves transmitting an electron beam through an ultra-thin sample (typically less than 100 nm thick). Electrons interact with the sample's internal structure and emerge to be magnified onto a screen or camera, providing high-resolution images down to atomic-scale detail. The key instrumentation of both techniques include:

- Electron Source: Both SEM and TEM use an electron gun (e.g., tungsten filament, LaB_6, or field emission gun) to generate the electron beam, with TEM often requiring higher voltages (100–300 kV) compared to SEM (1–30 kV) to penetrate the sample.
- Lenses and Beam Control: Electromagnetic lenses focus and control the electron beam in both SEM and TEM, though TEM requires more complex lens systems to achieve high magnification through sample transmission.
- Detectors: SEM uses secondary electron and backscatter detectors to capture surface details and compositional contrasts. TEM uses detectors such as fluorescent screens, CCD cameras, or direct electron detectors to capture transmitted or diffracted electrons, which provide structural and crystallographic information.

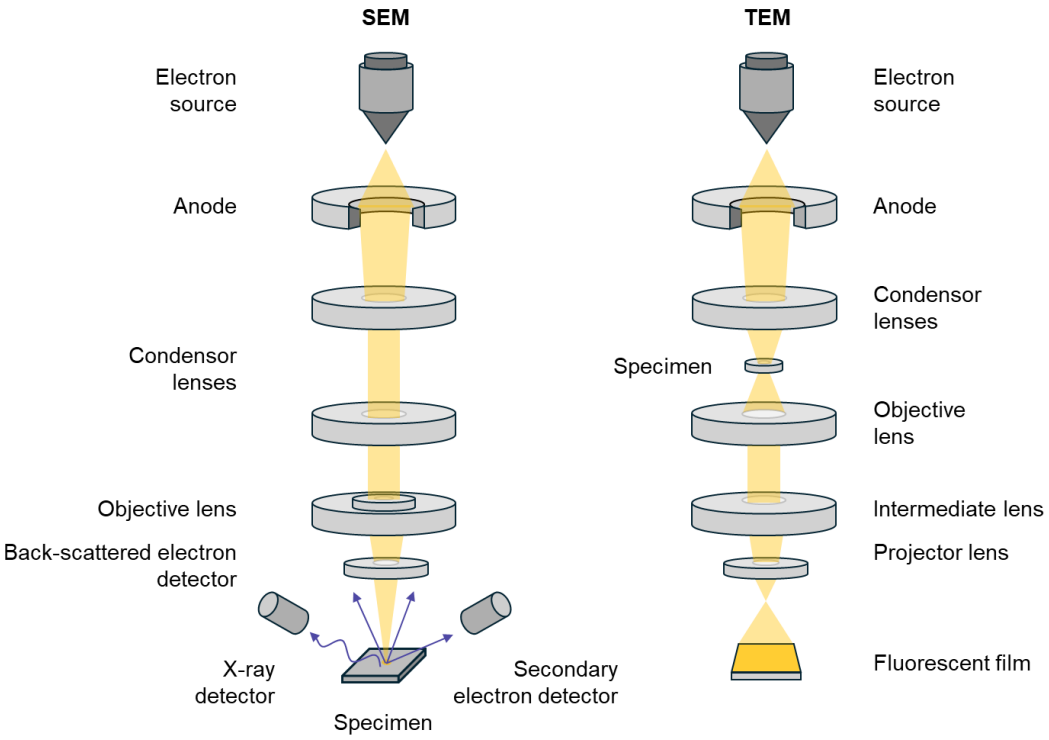

Figure 30. Schematic illustration of the commercial setups of SEM and TEM comparing their different components. Adapted from Ref[117].

Chapter 4: In situ Crystallization Method for Tunable and Stable Perovskite Nanoparticle Thin Films

Chapter 4 details all the results from the study of a novel synthetic approach for the preparation of PNCs. This *in situ* PNCs nanocomposite synthesis method could pave the way for producing large-area optoelectronic devices with enhanced performance, as well as serve as a foundation for direct band-gap tunability. The findings presented throughout this chapter are derived from and correspond to those reported in the peer-reviewed published article: Noguera-Gómez et al., Matter 5, 1–12, 2022

Everything detailed in this chapter aligns with the established data and conclusions within the original publication.

ABSTRACT

MHP NCs exhibit remarkable light-emission properties, benefiting from the broad chemical versatility within this class of materials. However, applying these properties effectively in functional films presents challenges due to issues like aggregation and material instability. By employing a metal-organic host matrix through a sol-gel approach, controlled *in situ* crystallization of PNCs can be achieved with minimal fabrication requirements. Consequently, this ambient process, which does not require annealing, produces high-performance nanocomposite thin films with PLQY exceeding 80% and offers excellent ambient and mechanical stability. The crystallization dynamics, which dictate the final nanoparticle size and, subsequently, the emission properties, can be finely tuned by adjusting ambient exposure and precursor concentrations.

4.1 INTRODUCTION

Solution-processed semiconductors have emerged as promising candidates for creating a new generation of optoelectronic devices that allow for simple, scalable mass production.[118–120] In particular, the PV performance achieved by MHPs positions them as one of the leading contenders to address the rising global energy demand.[66] These materials' unique defect physics, paired with their tunable band gaps, make them attractive for applications like lasers and LEDs.[121,122] However, bulk MHP structures often suffer from limited PL efficiency due to issues with mobile ionic defects and low exciton binding energy.[123,124] In this context, PNCs offer a new approach that can be beneficial for enhancing PL, and accessing the quantum-confinement regime to achieve an additional tool for band-gap customization. Thus, PNCs are the primary building blocks in many devices and applications.[125] The hot-injection method remains the most widely used synthesis route for producing monodisperse metal halide PNCs.[58,15] During this process, ligands in the solution prevent PNC growth and aggregation, resulting in PNCs with narrow emission linewidths (12–42 nm) and a PLQY of approximately 50%–90%.[126] However, challenges persist concerning the functionality and stability of PNCs. The hot-casting approach involves a multistep process and requires several purification steps. The synthesized PNCs often lack stability due to their sensitive surface chemistry, which is particularly problematic in solution-processed deposition where solvent effects are present. The long-term stability of PNC thin films is a major limitation, necessitating stabilization strategies to improve reproducibility and robustness for further applications.[127] To ensure sustainable use, it is essential to develop effective mechanisms to mitigate the primary sources of PNC degradation, including environmental factors like oxygen, UV light, temperature, and moisture.[128–130]

Consequently, new strategies are essential to overcome these limitations while preserving PNC optical properties. MHPs growth within pre-formed templates has been an alternative explored using various inorganic matrixes and alternative systems such as metal-organic complexes to control particle size.[131] However, this approach is often constrained by factors like host material stability, morphology, or compatibility with MHPs synthesis. In this context, the *in situ* synthesis of PNCs within a host matrix thin film is emerging as a promising alternative for next-generation solution-processed perovskites. This approach enables rapid and simple creation of nanocomposite thin

films with a uniform PNC distribution in the host matrix and precise control over nanocrystal size.[132,133] The host matrix plays a crucial role in eliminating the need for organic capping ligands to stabilize PNCs and reduce complex purification steps, while also allowing for additional control over morphology, size, and PNC distribution. Moreover, the host matrix can provide unique functionalities, such as optical and electronic properties, paving the way for multifunctional materials in fields like PV, optoelectronics, sensing, and photocatalysis. The *in situ* approach relies on formulating precursor solutions (inks) with suitable rheological properties for compatibility with standard printing and coating techniques. This strategy has been used to synthesize PNCs directly within a transparent matrix, maintaining emission efficiency and serving as a direct pathway to multifunctional PNC films.[90,91,134–136]

In this Chapter we present the *in situ* synthesis of $MAPbBr_3$ nanocrystals within a nickel acetate ($Ni(AcO)_2$) host matrix using spin coating. $Ni(AcO)_2$ is an ideal host matrix for embedding nanocrystals, due to its excellent film-forming abilities and high solubility in N,N-dimethylformamide (DMF). Additionally, $Ni(AcO)_2$ offers high transparency in the visible range (up to 95% from 400 to 800 nm for a 500 nm-thick film), which is a crucial advantage for optoelectronic applications using such materials. Unlike the hot-injection approach, no long-chain ligands are needed for PNC surface capping. As a result, functional nanocomposite thin films are produced using a straightforward process with exceptional emission properties, that can avoid antisolvent approach or even the use of glovebox. Remarkably, the MHP crystallization begins immediately after deposition without thermal annealing, resulting in mechanically and chemically stable nanocomposite thin films with a PLQY that can exceed 80%. The annealing-free nature of this solution-based method is a significant technological advancement, as it makes it directly compatible with plastic substrates, protects active device components, and simplifies its fabrication. PNC synthesis is easily regulated by controlling precursor concentration and/or relative humidity (RH) at room temperature.

4.2 EXPERIMENTAL PROCEDURES

4.2.1 Prepartion of $Ni(AcO)_2$-$MAPbBr_3$ nanocomposite thin films

The $Ni(AcO)_2$-$MAPbBr_3$ thin films are synthesized using a straightforward single-step procedure. Nickel acetate tetrahydrate ($Ni(CH_3COO)_2 \cdot 4H_2O$, 98%, Alfa Aesar) serves as the matrix precursor, while methylammonium bromide (CH_3NH_3Br, 99.5%, Ossila) and lead(II) bromide ($PbBr_2$, 98.0%, Sigma-Aldrich) act as the PNC precursors. DMF (anhydrous, 99.8%, Sigma-Aldrich) is used as the solvent. The standard $Ni(AcO)_2$ precursor solution consisted of 2 M $Ni(AcO)_2$ in DMF, prepared by dissolving 10 mmol of $Ni(AcO)_2$ in 5 mL of DMF. This solution is aged in a dry bath block at 70°C for 10 minutes, during which hydrolysis and condensation reactions of $Ni(AcO)_2$ in DMF initiated a sol-gel transition. This resulted in the formation of soluble colloidal clusters of Ni-based compounds, leading to branched metal-organic polymers that increased the solution's viscosity.

The $MAPbBr_3$ precursor solution is prepared by dissolving 5 mmol each of MABr and $PbBr_2$ in 5 mL of DMF. The $Ni(AcO)_2$ and $MAPbBr_3$ solutions are then mixed at a specified ratio and applied as ink via spin coating. Prior to deposition, the glass substrate (Sigma-Aldrich) is cleaned by ultrasonication in a 3 M HCl solution (prepared using 35% HCl, VWR Chemicals) for 10 minutes, followed by rinsing with a 3:1 mixture of isopropanol (99.5%, VWR Chemicals) and acetone (C_3H_6O, 99%, VWR Chemicals). The substrate is then rinsed with deionized water (Millipore) and dried with compressed air. Finally, an ozone treatment is performed on the substrate's deposition surface to remove any organic residues by applying UV light in an ozone chamber (Ossila Ozone Cleaner) for 10 minutes.

In this single-step synthesis process, the prepared solution is spread on glass and spin-coated at 3,000 RPM for 40 seconds. During spinning, the nanocomposite film gradually changes to a yellow color and exhibits strong PL as PNCs are formed (see Figure 31). The kinetics of *in situ* PNC synthesis depends on the concentrations of MABr, $PbBr_2$, and $Ni(AcO)_2$, as well as the relative humidity (RH). A simulated 100% RH environment is created in a closed vessel using silica gel blue saturated by adding 10 mL of H_2O.

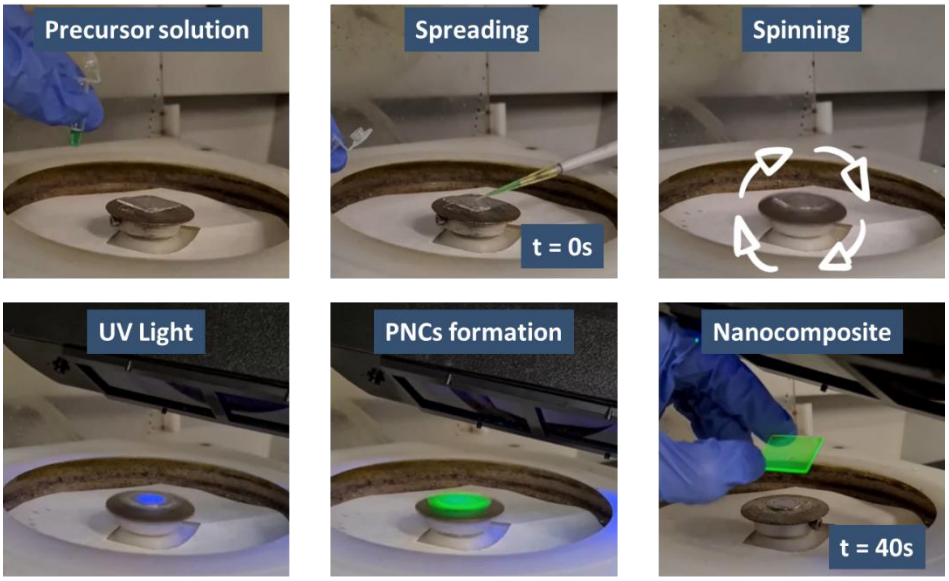

Figure 31. Nanocomposite generation through spin-coating timelapse.

4.2.2 Structural and optical characterization

Field-emission SEM is performed using a HITACHI S-4800 instrument (Tokyo, Japan) at 20 kV to analyze the sample morphology. The crystalline structure is evaluated by X-ray diffraction (XRD) on a Bruker D8 Advanced X-ray diffractometer with copper Kα radiation (λ = 1.5418 Å) at a grazing incidence of 1° and a scan rate of 5° per minute over 2θ angles ranging from 20° to 80°. Attenuated total reflectance (ATR) measurements are obtained using an Agilent Cary 630 FTIR spectrometer. TEM is performed on a JEOL JEM 1010 microscope (JEOL, Tokyo, Japan) at an acceleration voltage of 80 kV, with images captured by a Mega VIEW III camera (Olympus, Soft Imaging System, Münster, Germany). UV-visible measurements are taken with a Shimadzu UV-2501PC spectrophotometer. PL spectra are acquired using a continuous-wave GaN laser at 404 nm, while time-resolved PL (TRPL) measurements are conducted on an Edinburgh Instruments FLS 1000 fluorimeter, using 1 ns pulses at 405 nm from a diode laser.

4.2.3 Electrical characterization

The photoconductive properties of the material are assessed through the photocurrent density-voltage (*j*-*V*) characteristic curve. For photoconductivity measurements, a solution of $MAPbBr_3$:$Ni(AcO)_2$ at a 0.75:1 M ratio is spin-coated onto ITO interdigitated electrodes from Ossila (code: S161). The samples are tested

using a Gamry Interface 1010E. Measurements are conducted at a scan rate of 100 mV s^{-1} under both dark conditions and simulated sunlight with an intensity of 50 mW cm^{-2}.

4.3 RESULTS

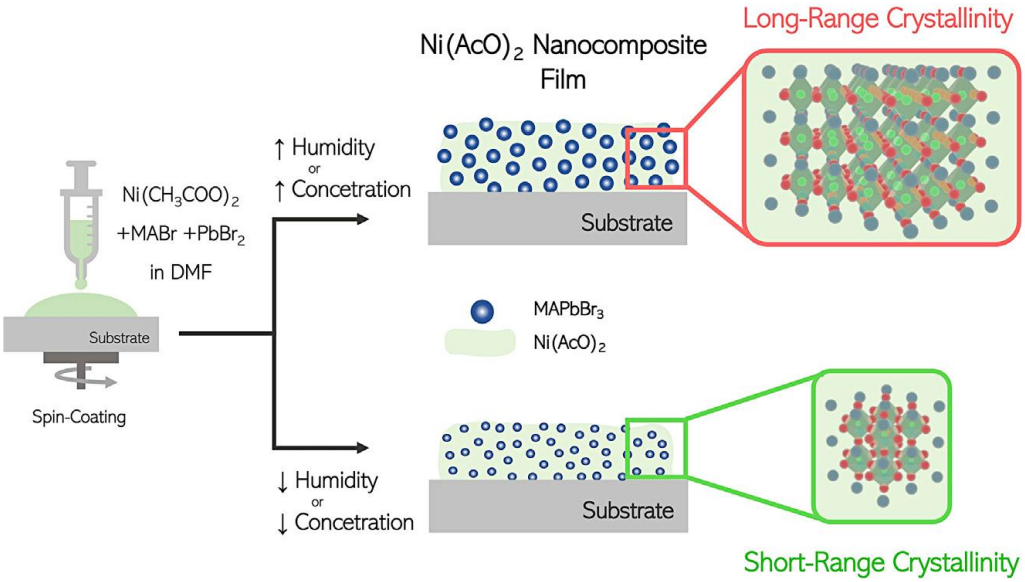

Figure 32. Schematic representation of the nanocomposite fabrication process, emphasizing how concentration and humidity affect the PNCs during crystallization through spin-coating.

The nanocomposite fabrication involves a precursor solution of MABr, $PbBr_2$, and $Ni(AcO)_2$ in DMF, which is applied onto a glass substrate and deposited via spin coating. Figure 32 outlines the general synthesis steps. At high spin rate, the excess DMF is removed, allowing the film to dry. During this spinning process, $MAPbBr_3$ nucleation spontaneously occurs within the $Ni(AcO)_2$ matrix within 30-40 seconds without requiring thermal annealing (see Figure 31). Both RH and precursor concentration significantly influence the formation, growth, and optical properties of the PNCs in the $Ni(AcO)_2$ film.

As for the matrix itself, previous studies have shown that $Ni(AcO)_2$ has excellent film-forming capabilities and can act as a host matrix for nanoparticles.[137,138] Consequently, $MAPbBr_3$:$Ni(AcO)_2$ thin films exhibit excellent optical and mechanical properties without further treatment, achieving PLQY values up to 80%, notable scratch resistance, and high stability under ambient conditions.

SEM images display the impressive morphology of the $MAPbBr_3$:$Ni(AcO)_2$ nanocomposites. The resulting PNC nanocomposite films are highly uniform and

compact (approximately 300 nm in thickness; Figure 33) with adjustable film thickness.

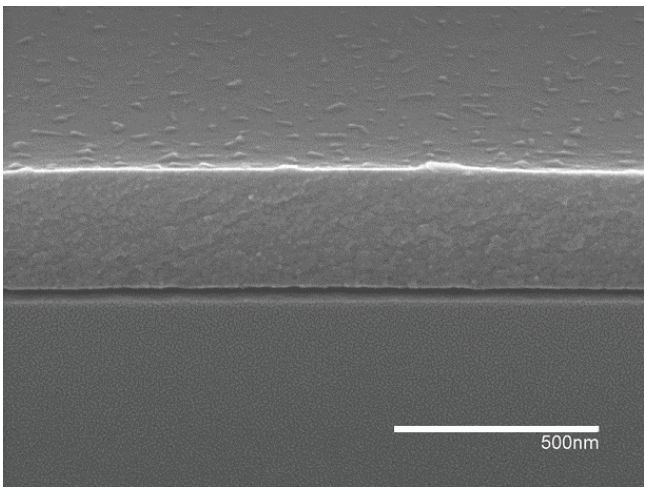

Figure 33. Cross-Sectional SEM Image of the nanocomposite $Ni(AcO)_2$-$MAPbBr_3$ coated on silicon. Thin-films image in 30º angled view.

X-ray diffraction (XRD) analysis (Figure 34a) confirms the *in situ* formation of $MAPbBr_3$ within $Ni(AcO)_2$. The diffraction peaks observed in the PNC nanocomposite correspond to the cubic Pm3m crystal structure of $MAPbBr_3$ (JCPDS no. 00-0105), with peaks at 15.05°, 21.28°, 30.13°, 33.94°, 37.07°, and 46.16° matching the (100), (110), (200), (210), (211), and (300) planes, respectively.

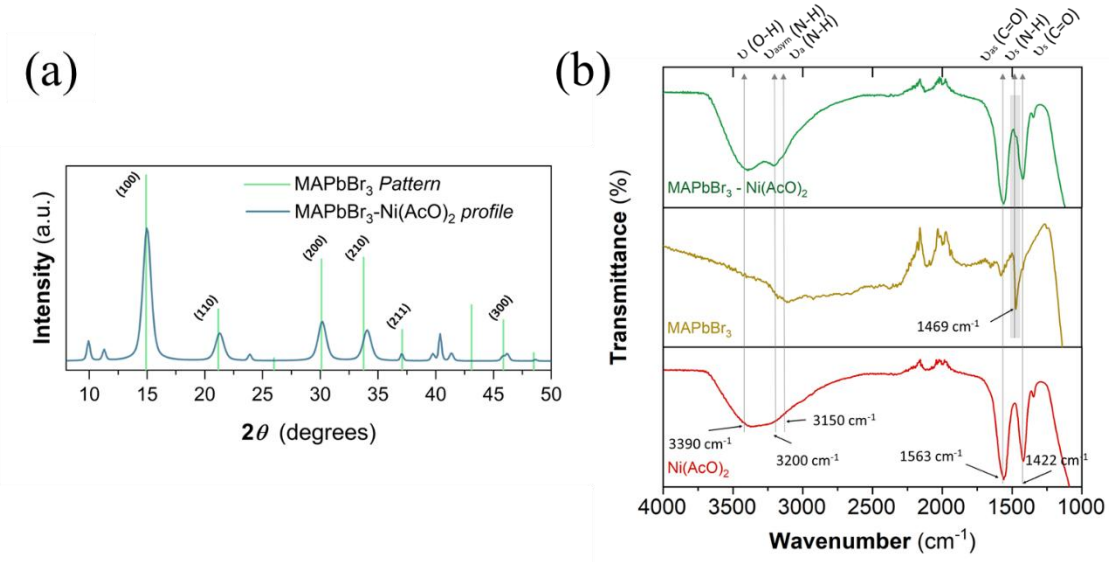

Figure 34. (A) XRD pattern of the as-synthesized $MAPbBr_3$:$Ni(AcO)_2$ nanocomposite under typical room humidity conditions. For films deposited in an ambient atmosphere (50% RH and a 0.5:1 M ratio), the estimated PNC sizes, calculated using the Scherrer

equation, are around 10 nm. (B) Comparison of ATR measurements between the $MAPbBr_3$:$Ni(AcO)_2$ nanocomposite (green) and the bare polycrystalline perovskite (yellow) and matrix (red).

Notably, films produced under RH <10% do not exhibit crystalline patterns (Figure 35a), confirming that $MAPbBr_3$ does not form at low RH levels, which aligns with the lack of optical properties observed (absorbance and PL spectra). However, when films deposited at RH <10% are exposed to an ambient environment (RH >15%), crystallization initiates. This process is marked by a gradual color change, along with increased excitonic absorption and PL (Figure 35b-e). Exposure to water vapor can significantly speed up the *in situ* synthesis of $MAPbBr_3$. These findings indicate that a minimum level of moisture is essential for PNC formation. Interestingly, unlike previous studies, no hydrate phases appear upon moisture exposure.[139]

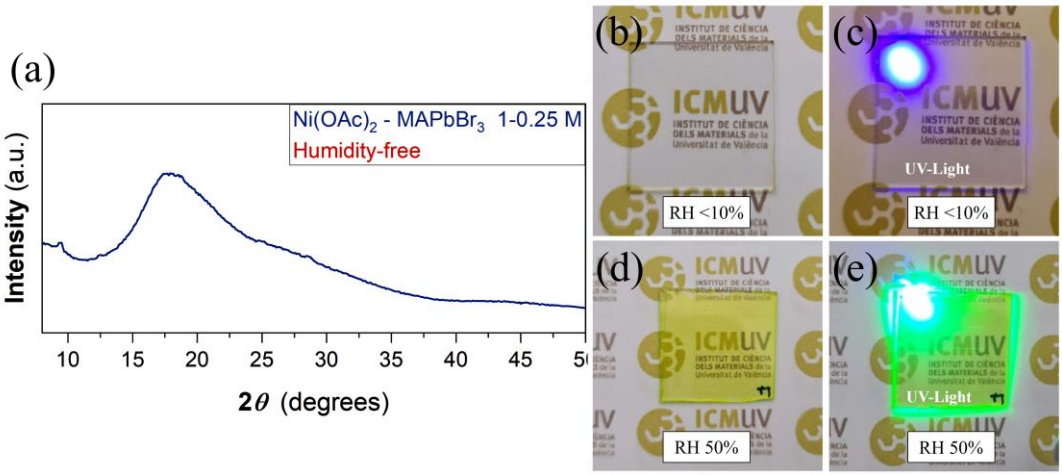

Figure 35. (a) XRD pattern of $MAPbBr_3$: $Ni(AcO)_2$ synthesized under humidity-free conditions. Images (b-e) illustrate the crystallization dynamics of samples exposed to different humidity levels. Images (b) and (c) depict as-synthesized PNC thin films (0.25:1 M) at less than 10% relative humidity (RH) under normal and UV light, respectively. Images (d) and (e) show as-synthesized PNC thin films (0.25:1 M) at over 50% RH under normal and UV light, respectively.

XRD analysis confirms the formation of $MAPbBr_3$ PNCs within the nanocomposite, though it provides limited information on the mdatrix itself. To better understand the nature of the host matrix, attenuated total reflectance Fourier transform infrared spectroscopy (ATR-FTIR) measurements are conducted to characterize the $MAPbBr_3$:$Ni(AcO)_2$ nanocomposite (Figure 34b). The ATR-FTIR spectrum of

MAPb3Br$_3$:Ni(AcO)$_2$ films (green line) reveals characteristic vibrational frequencies associated with the carboxylate group from Ni(AcO)$_2$ (red line) and N–H bonds from the $CH_3NH_3^+$ ion of MAPbBr$_3$ (yellow line). Pristine Ni(AcO)$_2$ lacks the split band centered around 3,400 cm^{-1}, indicating that this band mainly results from O–H bonds of water molecules within the coordination sphere. Both Ni(AcO)$_2$ and the MAPbBr$_3$:Ni(AcO)$_2$ nanocomposite show peaks at 1,563 and 1,422 cm^{-1} (Figure 34b), corresponding to the asymmetric and symmetric C=O stretching vibrations of Ni(AcO)$_2$, respectively.[140] Additionally, the ATR-FTIR spectrum of the nanocomposite exhibits a peak around 3,390 cm^{-1}, indicating O–H bonds likely due to ambient humidity or water in the coordination sphere of Ni(AcO)$_2$. The peaks at 3,200 and 3,150 cm^{-1} correspond to the symmetric and asymmetric stretching of N–H, confirming the presence of amines from the methylammonium cation.[141] This feature is absent in the pure matrix but is observed in both the nanocomposite and MAPbBr$_3$ spectra. Furthermore, the symmetric N–H bending mode (highlighted in gray) at 1,469 cm^{-1} in both the MAPbBr$_3$:Ni(AcO)$_2$ nanocomposite and MAPbBr$_3$ confirms the growth of MAPbBr$_3$ nanocrystals, a feature not present in pure Ni(AcO)$_2$.

To optimize the final optoelectronic performance of the PNC thin films, we focus on two primary factors influencing nanocomposite properties: (1) the dependence of PNC size on precursor concentration and the MAPbBr$_3$:Ni(AcO)$_2$ ratio, and (2) the effect of RH on activation and crystallization dynamics, which result in varying PNC sizes.

In the first scenario, Figure 36a shows the PL and absorption spectra measured for thin films fabricated under consistent conditions (RH fixed at 50%) while varying the concentration ratio of MAPbBr$_3$ to Ni(AcO)$_2$. Sixty minutes after sample preparation, using a MAPbBr$_3$ concentration of 0.5 M, a distinct excitonic absorption band appears at 518 nm, characteristic of MAPbBr$_3$ PNCs. When the MHP precursors concentration is lowered to 0.25 M, the film's absorption decreases significantly, about threefold, while its PL intensity increases nearly tenfold. As a result, these films exhibit a PLQY of 80% without additional optimization. PL decay kinetics (Figure 36b) reveal a single exponential decay with a 7.0 ns lifetime for 0.25:1 M samples, while the 0.50:1 M samples show a multiexponential decay: a primary component of 5 ns (59% weight) and two longer components at 26 ns (34%) and 250 ns (7%). This comparison suggests that the faster component primarily governs the recombination process, influencing

emission efficiency, whereas the longer-lived decay elements are likely due to shallow, non-quenching traps on nanocrystal surfaces[142] and increased light scattering in the 0.5:1 M sample. Additionally, a blue shift in the PL signal, from 525 nm (0.5:1 M sample) to 517 nm (0.25:1 M sample), suggests quantum confinement effects tied to variations in particle size: under the same RH, higher MHP precursors concentration results in larger PNC sizes.

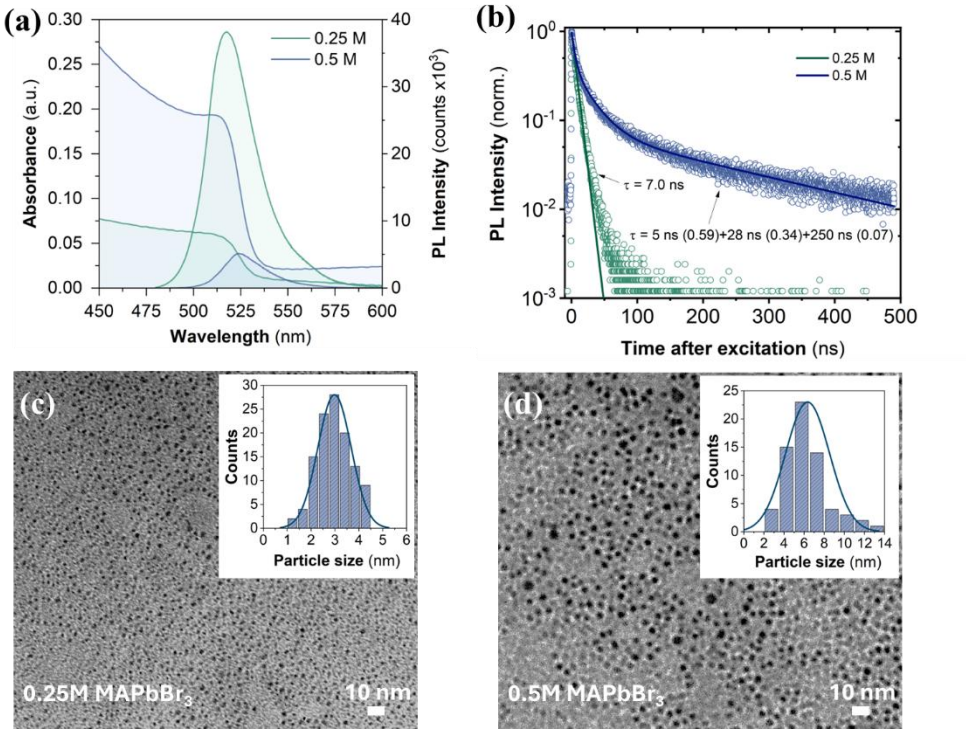

Figure 36.(a) Absorption and PL spectra of $MAPbBr_3$:$Ni(AcO)_2$ nanocomposite films, processed at molar ratios of 0.25:1 and 0.5:1 M, showing the concentration dependence.(b) PL decay kinetics for these two film samples. (c and d) TEM images and particle size distributions of PNC nanocomposites prepared at two distinct $MAPbBr_3$:$Ni(AcO)_2$ ratios, specifically 0.25:1 and 0.5:1 M.

TEM measurements (Figure 36c and Figure 36d) confirm this size variation, showing that a lower $MAPbBr_3$ concentration (0.25 M) yields smaller PNCs (approximately 2–3 nm), whereas a higher concentration (0.5 M) produces larger PNCs (around 6–7 nm). While the dependence of PL maxima on particle size (with distributions of 2–3 nm and 6–7 nm, showing PL spectra centered at 517 nm and 525 nm, respectively) is qualitatively consistent with observations for $MAPbBr_3$ NCs in suspension[143], it differs from that for similar NCs embedded in mesoporous silica.[88] It is essential to note that the position of PL spectra maxima can be influenced by factors

beyond quantum confinement. For example, with a broad size distribution and closely packed nanocrystals, the PL spectra position may shift to longer wavelengths than those predicted by the Brus equation, due to excitation funneling from smaller to larger particles (spectral diffusion[142]) or even toward the bulk phase. These findings suggest that minor amounts of larger NCs or bulk phase may exist within our systems, leading to excitation funneling that preferentially enhances the luminescence of larger particles while quenching the luminescence of smaller ones. A more detailed examination of how absorption and PL spectra maxima relate to nanocrystal size along with the impact of RH will be presented in the following chapters of this Thesis.

Although the nanocomposite matrix has inherently low conductivity, preliminary studies on indium tin oxide (ITO) interdigitated samples reveal photoconductive behavior. A nanocomposite with a $MAPbBr_3$:$Ni(AcO)_2$ ratio of 0.75:1 M exhibits a tenfold increase in current when exposed to 0.5 AM1.5G light intensity (Figure 37). This result is promising for integrating the nanocomposite into devices. Further research into matrix modifications, doping, or nanoparticle interconnections could provide valuable strategies for advancing in this area.

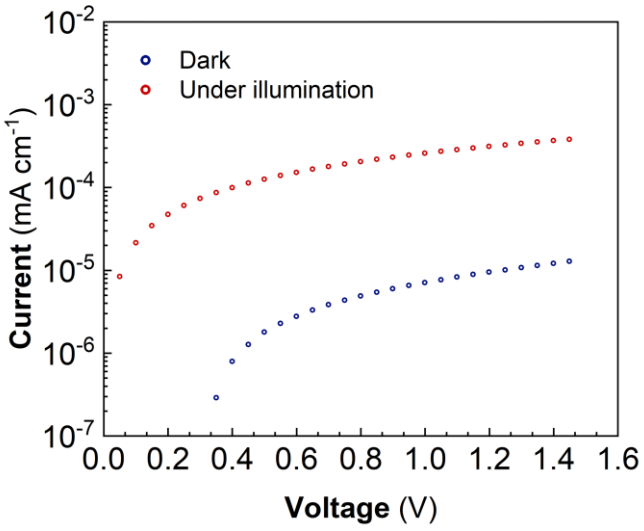

Figure 37. j-V curves under light and dark conditions for the nanocomposite $MAPbBr_3$:$Ni(AcO)_2$ with a ratio of 0.75:1 M at 50% RH.

In the second scenario, studying the RH influence on the crystallization dynamics, the MHP nanocomposite films with a $MAPbBr_3$:$Ni(AcO)_2$ ratio of 0.25:1 M are exposed to varying RH levels for 60 minutes. The PL and absorption spectra

(Figure 38) exhibit a redshift as the RH increases from 50% to 100%. Specifically, both the absorption edge and the emission peak shift to lower energies with increasing RH. The PL emission peak moves from 525 nm at 50% RH to 540 nm at 100% RH. A notable difference between the two absorption spectra is the presence of a well-defined excitonic absorption peak at 525 nm in the film exposed to 100% RH, which is absent in the film exposed to 50% RH. This is in line with a particle-size variation, similar to that noted earlier with different precursor concentrations.[143] This shift in the PL maximum suggests a particle size variation from approximately 3-5 nm at 50% RH to 11–12 nm at 100% RH. In contrast, nanocomposite films prepared under RH <10% show negligible PL emission and absorption, reinforcing that specific humidity levels are necessary for PNC crystallization, consistent with the earlier XRD results.

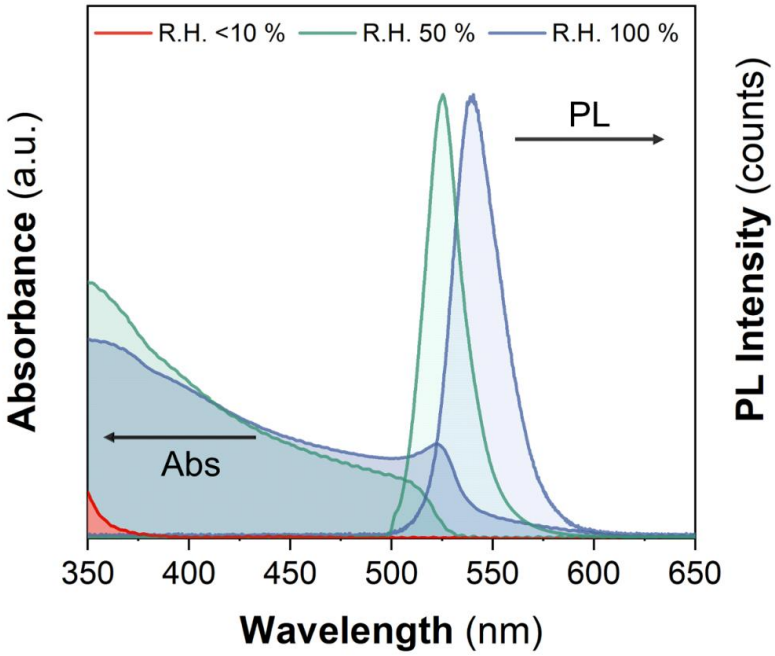

Figure 38. Absorption and PL spectra of a nanocomposite film produced with a $MAPbBr_3$:$Ni(AcO)_2$ ratio of 0.25:1 M, crystallized under varying RH conditions.

The *in situ* synthesis of PNCs within $Ni(AcO)_2$ can be tracked by observing changes in optical properties over different reaction times. To further explore the role of moisture in $MAPbBr_3$ nanocrystals crystallization, nanocomposite thin films are prepared at concentrations of 0.25 M and 0.5 M $MAPbBr_3$ under RH conditions of 50% and 100% at 25°C. Figure 39 illustrates these three conditions, where black dots indicate the intensity of the probing laser beam transmitted through the sample, blue dots represent PL intensity, and red dots show the PL peak wavelength for

$MAPbBr_3$:$Ni(AcO)_2$ nanocomposites prepared at different perovskite concentrations and RH levels.

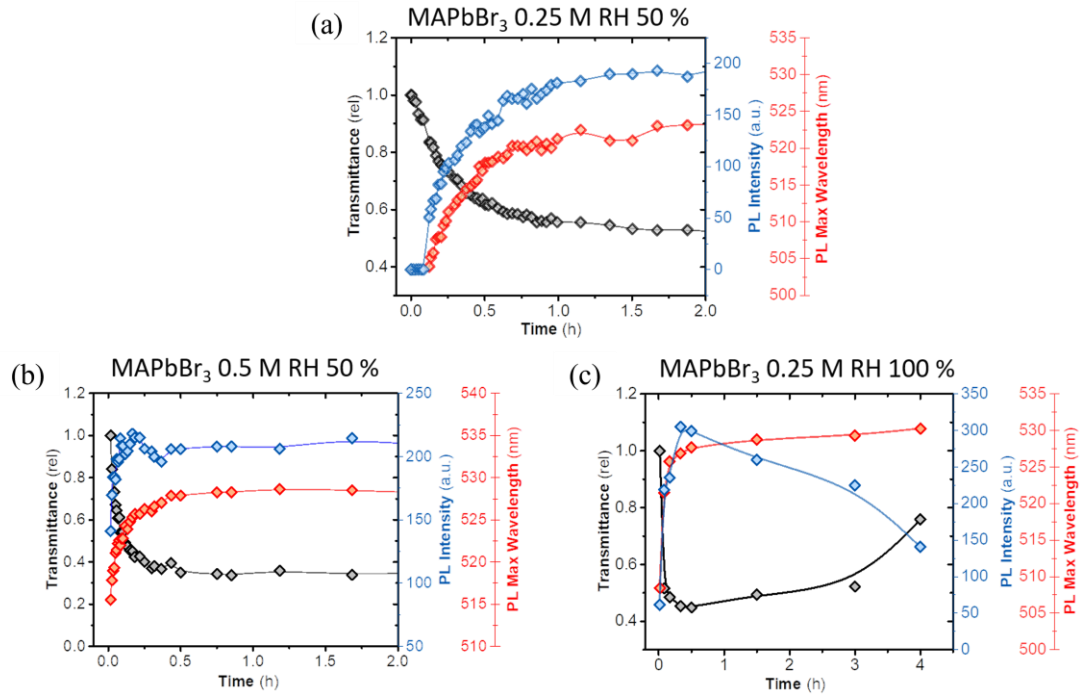

Figure 39. (a-c) Crystallization dynamics monitored through PL and Transmittance illustrating the effects of concentration and humidity on crystallization. (a) $MAPbBr_3$:$Ni(AcO)_2$ at 0.25 M and 50% RH (b) $MAPbBr_3$:$Ni(AcO)_2$ at 0.5 M and 50% RH, and (c) $MAPbBr_3$:$Ni(AcO)_2$ at 0.25 M and 100% RH.

Figure 39a illustrates the time evolution of the optical properties of a nanocomposite thin film at 50% RH with a $MAPbBr_3$:$Ni(AcO)_2$ molar ratio of 0.25:1. The process initially shows an exponential trend over the first 60 minutes, followed by a plateau lasting more than 6 hours under continuous exposure across all measured properties. During the first 30 minutes, the peak emission shifts from 502 to 520 nm. As the reaction progresses, the concentration of formed nanocrystals increases, causing the sample's transparency to decrease while simultaneously enhancing PL intensity and redshifting the PL band maximum. After one hour, the reaction stabilizes, with the PL peak fixed at 525 nm. Figure 39b displays the optical properties of a nanocomposite thin film at 50% RH but with a $MAPbBr_3$:$Ni(AcO)_2$ ratio of 0.5:1. In this case, PL intensity rapidly increases just 30 minutes post-deposition, accompanied by a decrease in sample transmittance. The changes appear sharper than those observed in the 0.25:1 M sample, with a transmittance reduction evident even at t = 0 s, suggesting that the

reaction initiates during spin coating. After about 30 minutes, the reaction is complete, resulting in a PL peak at 529–530 nm, suggesting the presence of larger particles than those in Figure 39a.

Figure 39c shows the optical properties of a nanocomposite thin film at 100% RH with a $MAPbBr_3$:$Ni(AcO)_2$ ratio of 0.25:1. The kinetics indicate an accelerated process similar to what is observed when MHP precursors concentration increases. However, noticeable degradation of the nanocomposite film properties occurs within a few hours, characterized by reduced PL intensity and increased transmittance. Despite these changes, the PL band remains centered at 530 nm, indicating that particle size remains stable despite degradation. The 5 nm blue shift observed when RH increases (Figure 39c vs. Figure 39a) suggests the formation of larger PNCs under higher humidity for the same formulations, confirming RH's significant influence on PNC size during crystallization.

Interestingly, despite the impact of ambient humidity on crystallization, once the final PNC size is reached for a given humidity and concentration condition, the nanocomposite film's optical properties remain stable. Unlike typical perovskite instability, these unencapsulated films in ambient conditions (40%–60% RH) lose less than 25% of their PL emission after 8 months (see Figure 38). This suggests an additional protective effect from the host matrix.

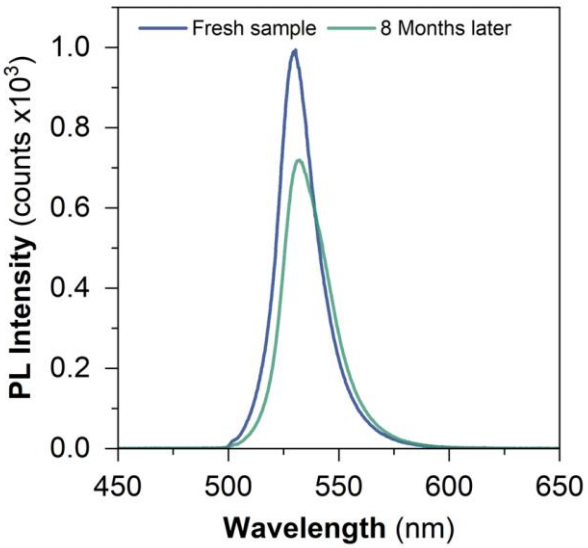

Figure 40. Evolution of PL of $MAPbBr_3$:$Ni(AcO)_2$ nanocomposite at 0.25:1 molar ratio stored under ambient conditions.

While Figure 39 provides valuable data on $MAPbBr_3$ nanocrystal formation under various conditions, absorption and luminescence spectroscopy alone are insufficient to probe the molecular mechanisms underlying nanocomposite formation. The observations suggest that the $Ni(AcO)_2$ matrix actively influences the $MAPbBr_3$ nanocrystals' optical properties, but structural analysis methods are needed to understand the nanocomposite morphology. This is exemplified by the differing excitonic absorption contributions in samples at 50% RH (weaker excitonic contribution) and 100% RH (stronger excitonic contribution). In theory, this effect could relate to changes in exciton binding energy (E_b): higher E_b would enhance excitonic contributions compared to unbound electrons and holes. However, this observation contrasts with the typical decrease in E_b as semiconductor quantum dots grow larger.[144] We hypothesize that in this nanocomposite, the surrounding matrix may affect the dielectric constant at the nanocrystal boundary, effectively altering the semiconductor's dielectric constant and thus influencing E_b.

An additional indication of the matrix's impact on $MAPbBr_3$ nanocrystal properties is the change in PL decay kinetics observed between nanocomposites with 0.25:1 M and 0.5:1 M ratios. The appearance of longer-lived decay components (see Figure 36b) could result from the formation of shallow, non-quenching traps on nanocrystal surfaces, which extend observed PL kinetics, or increased light scattering in the 0.5:1 M nanocomposite, potentially leading to multiple PL reabsorptions.

4.4 CONCLUSIONS

In summary, we have developed a simple, rapid, and cost-effective method for the *in situ* synthesis of PNCs within a metal-organic matrix, resulting in nanocomposite thin films with excellent optical properties and high stability (achieving up to 80% PLQY and durability of over one year). Despite being an annealing-free process, this approach produces uniform thin films with outstanding resistance to mechanical friction. By adjusting the precursor loading in the final thin film, we can control crystallization dynamics, allowing for tunable crystal sizes. Additionally, PNC size can be modulated by exposure to different RH conditions, as both PL and absorption spectra exhibit varied behavior under different moisture levels due to aggregation effects leading to diverse PNC sizes. Samples exposed to varying RH and precursor ratios show a shift in absorption and emission bands to longer

wavelengths, indicating an increase in PNC size. Furthermore, performing the same synthesis in a dry-air environment (without moisture) does not lead to PNC formation.

This *in situ* PNC nanocomposite synthesis approach has the potential to support the development of large-area optoelectronic devices with enhanced functionality and provides a foundation for direct bandgap tuning by controlling PNC crystallization dynamics.

In the next chapter, a detailed protocol is presented to provide insights into the crystallization dynamics and potential applications of this synthesis method. A comprehensive procedure for developing chambers, in which humidity is precisely controlled, is outlined as a critical strategy for achieving precise control over the final PNCs, thereby fully harnessing the capabilities of this approach.

Chapter 5: Controlled Crystallization of PNCs: A Comprehensive In situ Synthesis Protocol

Chapter 5 contains a full detailed protocol for the preparation PNCs developed in the previous chapter. The protocol outlined in this section corresponds to methodologies detailed in the peer-reviewed published article: Noguera-Gómez et al., STAR Protocols 4, 102507, 2023.[145] This comprehensive guide adheres closely to the established procedures presented therein, ensuring consistency with the published findings and providing a reliable foundation for replicating the results.

The protocol describes step by step the synthesis of $MAPbBr_3$ PNCs directly within a $Ni(AcO)_2$ matrix.[146] The ultimate size of the NCs, which dictates emission properties through quantum confinement, can be accurately managed by adjusting the RH during the crystallization stage (as explained in the deposition section) and by varying precursor concentrations. This synthetic approach enhances stability of PNCs, protecting them from degradation factors such as oxygen, UV exposure, temperature, and moisture.[147,148] Moreover, it enables the creation of PNCs with diverse perovskite compositions, including chloride, bromide, iodide, and their mixtures.

5.1 INTRODUCTION

The field of halide perovskites is currently challenged by the need to develop an efficient method for producing stable and highly efficient PNCs. This protocol outlines the steps for preparing precursor solutions, depositing the layers and elaborates on methods for managing key processing parameters, such as adjusting precursor concentration and creating controlled-humidity environments to achieve precise control over the final NCs size (see Figure 41). The entire protocol should be conducted with appropriate safety measures for each chemical and its by-products, including suitable laboratory facilities, personal protection, and waste management.

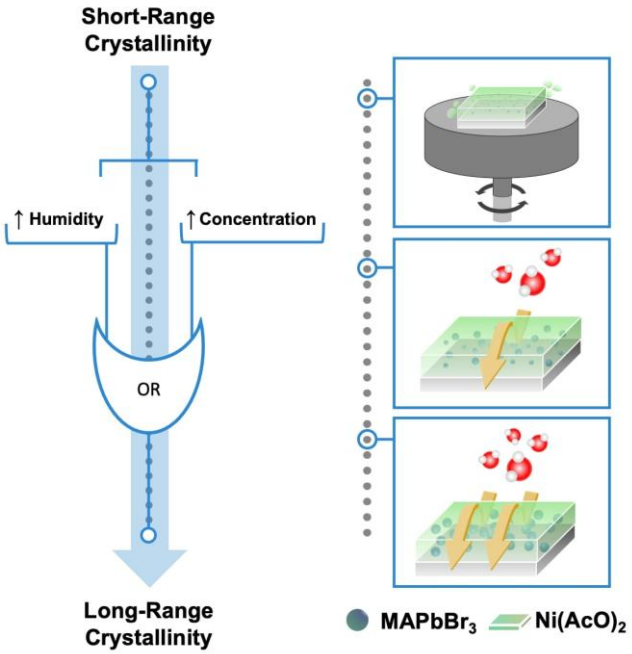

Figure 41. A schematic overview of the nanocomposite fabrication process: illustrating the influence of concentration and relative humidity (RH) on the crystallization of PNCs.

5.2 EXPERIMENTAL PROTOCOL PROCEDURES

This section is intended to present a comprehensive protocol for preparing PNCs with precise size control. This includes the description of all materials used in the synthesis process, alongside the suppliers and pertinent references, as outlined in the Key Resource Table.

5.2.1 Solutions and materials preparation

The preparation of precursor solutions is essential for the synthesis of $MAPbBr_3$:$Ni(AcO)_2$ nanocomposites, with careful mixing required to achieve a transparent solution ready for deposition. The reference scenario employs a 0.25:1 molar ratio of $MAPbBr_3$ and $Ni(AcO)_2$, respectively. For the preparation of the $Ni(AcO)_2$ matrix solution, e.g., 2 mL of a 2 M solution is prepared by dissolving 4 mmol (0.995 g) of $Ni(AcO)_2$ in 2 mL of DMF. The mixture is heated to 70°C and stirred continuously in a dry-block bath for 10 minutes. Upon completion, the solution is filtered using a 0.2 μm PVDF filter attached to a 5 mL syringe, and the resulting solution is stored at room temperature (approximately 20°C and 40% RH). The $MAPbBr_3$ precursor solution is prepared by first dissolving 1 mmol of MABr (0.112 g) in 2 mL of DMF with stirring for 20 minutes. From this initial solution, 1 mL is transferred to a second vial containing 1 mmol (0.367 g) of $PbBr_2$, and the resulting mixture is filtered through a 0.2 μm PVDF filter. The filtered solution is stored at room temperature under similar laboratory conditions. To prepare the $MAPbBr_3$:$Ni(AcO)_2$ solution, 1 mL of the $MAPbBr_3$ precursor solution is combined with 1 mL of the $Ni(AcO)_2$ solution. This mixture is stirred for 10 minutes, yielding the final precursor solution, which is then stored at approximately 20°C and 40% RH (see Figure 42). Experiments to investigate the effects of varying precursor ratios on particle size are also conducted, focusing on different $MAPbBr_3$ concentrations achieved by dilution with DMF, while maintaining a constant $Ni(AcO)_2$ matrix concentration at 1 M (see Figure 45).

When preparing solutions, undissolved reagents at the bottom of the vial may hinder optimal homogeneity; gently heating the mixture in the dry-block bath while stirring aids dissolution. When necessary, increasing the temperature up to 80°C and extending heating time by 5 minutes ensures complete solubilization. Filtration afterward removes any remaining particulates, creating a uniform solution. The matrix and perovskite solutions display considerable stability over time, with properties remaining intact for up to three months when stored under standard laboratory conditions (about 20°C and 50% RH). However, certain limitations and potential issues must be considered to ensure successful implementation. One key limitation is the long-term stability of precursor solutions, especially those with sol-gel precursors such as $Ni(AcO)_2$, which may precipitate over time. While these solutions generally

maintain stability for up to three months, occasional precipitation can occur sooner. The filtration step thus plays a crucial role in enhancing solution longevity by removing any unsolved particles that could otherwise act as nucleation centers. Aggregation, sudden aging, or clustering within the sol-gel matrix may also lead to poor dispersion and heterogeneous uniformity. If unexpected precipitation occurs even if within its expected lifespan, repreparation of the solution ensures consistency and reliability for subsequent synthesis steps.

5.2.2 Substrates cleaning

The cleaning of substrates is essential to ensure an optimal surface for film deposition, enhancing adhesion and wettability. To achieve this, substrates undergo a thorough cleaning process involving solvent treatments, rinsing, and drying to remove any unwanted particles or residues. Glass slides (approximately 25x25 mm) are sonicated in a 3 M HCl solution (35 vol%, VRW Chemicals) for 10 minutes, followed by cleaning with a toothbrush and a 2% Hellmanex solution in water. The slides are then immersed in an ultrasonic bath with 2% Hellmanex for 30 minutes, rinsed thoroughly with deionized water, and subsequently with ethanol. Afterward, they are immersed in an ultrasonic bath containing a 3:1 solution of isopropanol (IPA) and acetone for 15 minutes, and finally dried with compressed air free of moisture and dust.

During substrate preparation, inadequate wettability may sometimes occur even with meticulous cleaning, resulting in aggregation or uneven distribution of the solution on the substrate surface. Performing an ozone or plasma treatment before deposition resolves this, improving surface quality. Alternatively, spin-coating 1 mL of DMF onto the substrate before adding the nanocomposite precursor solution can help. Care must be taken with ozone, as it is a hazardous gas, and treatment should be conducted within a fume hood or a similar controlled environment.

5.2.3 Spin-coating deposition

Spin-coating deposition facilitates the controlled removal of excess solution and solvent drying while forming a thin film with desired characteristics by adjusting spinning parameters. The deposition can be performed either inside a dry glovebox with moisture-free air (see Appendixes Table 5) or under ambient conditions (approximately 40-50% RH and 20°C), as the process is highly dependent on

humidity. RH during deposition plays a critical role in determining the final PNC size, as illustrated in Figure 41. Using the aforementioned precursors solutions the resulting film thickness is generally around 300 nm (as discussed in Chapter 3:), with the thickness, which also determines the film's absorption properties, primarily influenced by the spin-rate. PNC size within the composite is strongly affected by humidity and perovskite precursor concentration.

When working within a dry box, it is crucial to place all necessary instruments inside the box at least 20 minutes prior to deposition to ensure a moisture-free environment. The single-step synthesis process involves depositing the nanocomposite precursor solution onto a glass substrate. In the spin-coating process, the glass substrate is centered in the spin-coater, which is set to 3000 rpm for 40 seconds with an acceleration ramp of 2000 rpm/s. A 70 μL drop of the precursor solution is placed at the center of the glass substrate using a micropipette, and the spin-coater program is initiated. Once the program is complete, the sample is placed within a prefabricated humidity chamber (detailed in the Humidity Chambers Building subsection) for a specified duration to induce crystallization and control PNC size.

Alternatively, the deposition can be conducted under standard laboratory conditions, which promotes PNC crystallization due to exposure to ambient humidity if there is an RH difference greater than 10% (see Figure 35b-e of previous chapter). In this case, the steps described for deposition are followed outside the dry box. Thus, the laboratory's relative humidity and temperature significantly influence the final PNC size due to the ambient moisture levels during the deposition process.

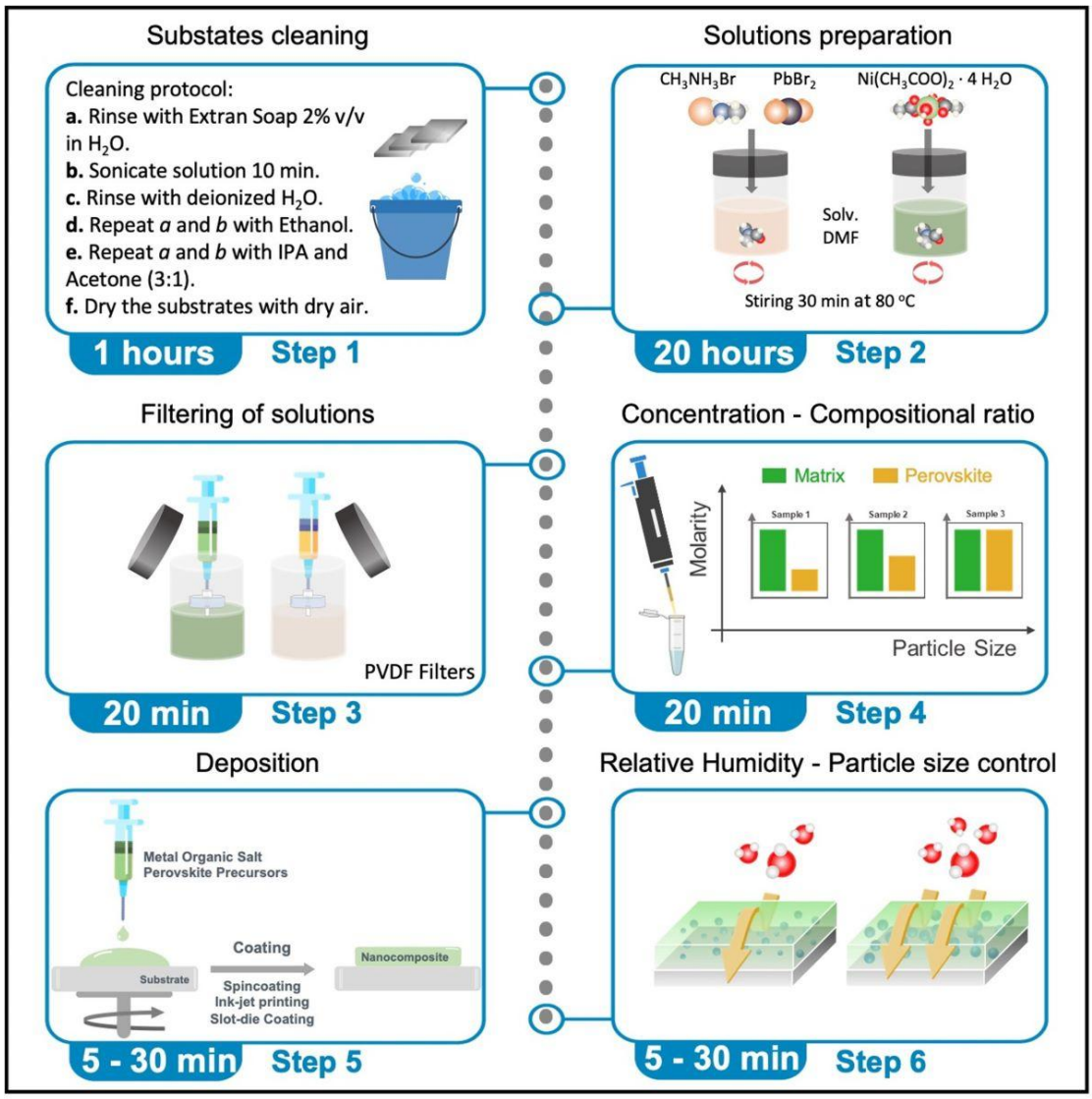

Figure 42. Schematic illustration of the primary protocol steps for preparing nanocomposite-based PNCs. Notably, steps 4 and 6 are critical in determining the final size of the nanocrystals.

5.2.4 Design and Assembly of Humidity Chambers

This section provides an overview of the design and construction of humidity chambers capable of generating controlled humidity levels between 10% and 100% RH. These chambers achieve specific RH levels by utilizing supersaturated solutions of various inorganic salts. These salt solutions are chosen for their well-defined

equilibrium vapor pressures at certain temperatures, enabling precise control of RH within the chamber.[149]

The humidity chambers are composed of four essential components (Figure 43): a polypropylene box with an airtight lid, saturated salt solutions, a sample tray holder, and a thermo-hygrometer. To ensure the desired humidity level, a supersaturated salt solution is placed inside the chamber, which is then sealed with an airtight lid. The RH is monitored with a hygrometer, and equilibrium vapor pressure is typically achieved within 30 minutes in a 10x10x10 cm box. Custom plastic trays, designed to allow sample insertion without disrupting RH equilibrium, are attached to one side wall of the chamber.[10] These trays are 3D printed using polylactic acid (PLA).

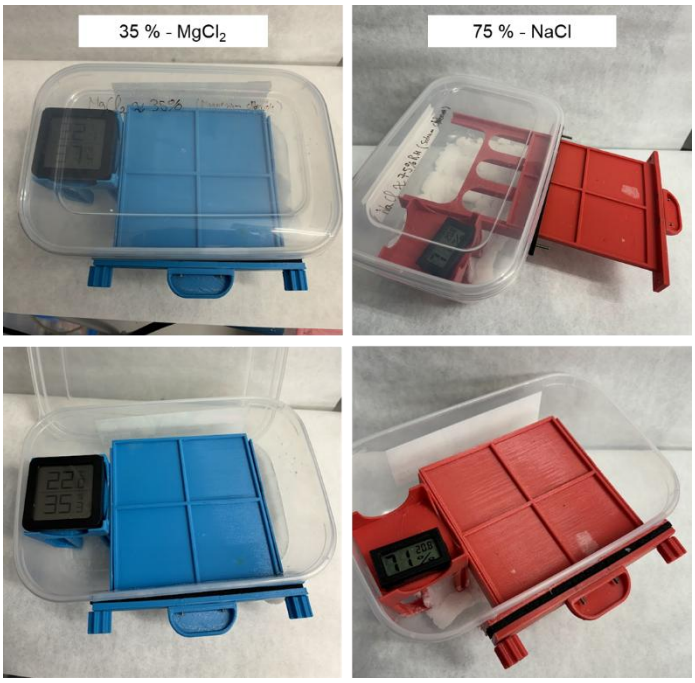

Figure 43. Custom-made humidity chambers for the crystallization of PNCs at different RHs. Sealed vessel containing a hygrometer, a tray for introducing the thin films after deposition and the saturated salts with water at the bottom.

The RH level is defined by the partial vapor pressure of the salt solution mixture at a given temperature upon reaching equilibrium. To prepare a humidity chamber,

[10] Adding multiple trays does not interfere with the chamber's equilibrium.

different inorganic salts are chosen based on the targeted RH level (see Table 5).[11] The preparation of a saturated salt solution involves selecting salts appropriate for the RH range, filling the chamber bottom with a 1 cm layer of the salt of choice, and gradually adding small amounts of distilled water while gently stirring to ensure even distribution. This process creates a slushy mixture, establishing a supersaturated salt solution. Once the solution is supersaturated, the chamber's airtight lid and tray compartments are closed, and the equilibrium is achieved within approximately 30 minutes, as confirmed by checking RH with a thermo-hygrometer.

In constructing the humidity chamber, failure to reach equilibrium within the designated timeframe may lead to incomplete humidity stabilization, which affects the crystallization process. Extending the stabilization period by 10–20 minutes often achieves vapor pressure equilibrium at the desired RH level. In cases where frequent chamber openings disrupt the RH balance, quickly closing the chamber and allowing time for the RH to restore is essential.

5.2.5 Characterization

For XRD, absorption, and PL characterization, conventional glass substrates or quartz can be used. Thin films are broken down into small pieces and sonicated in methyl acetate for subsequent deposition onto TEM grids. When preparing TEM samples, high concentrations of dispersed nanocomposite film may hinder the visualization of individual PNCs due to agglomeration on the TEM grid. To prevent this, a diluted nanocomposite solution should be used during deposition to ensure clear visualization without excessive aggregation.

5.3 RESULTS AND OUTCOMES

The main parameters to study are optical and structural characteristics. In this section a brief description of expected outcome when developing PNCs within matrixes is detailed. Most of the described results are referred to the data presented in Chapter 4.

[11] The table lists commonly used inorganic salts as viable candidates for preparing controlled humidity chambers. In a supersaturated state, these salts establish vapor equilibrium within the container, allowing for the achievement of the specific relative humidity levels at the specified temperatures.

XRD and TEM analyzes are conducted to confirm the formation of the PNC within the matrix. These techniques provide detailed insights into the existence and distribution of PNCs in the nanocomposites, as shown in Figure 44. The *in situ* synthesis of $MAPbBr_3$ in $Ni(AcO)_2$ is confirmed by the XRD diffractogram (Figure 44a), which displays peaks corresponding to the cubic Pm3m crystal phase of $MAPbBr_3$ (JCPDS no. 00-0105) in the nanocomposite. Notably, films prepared at RH levels below 10% do not exhibit crystalline patterns, indicating that $MAPbBr_3$ does not form under low humidity conditions. However, exposing films deposited at RH <10% to ambient conditions (RH above 15%) initiates crystallization, which is accompanied by a gradual color change and an increase in excitonic absorption and PL (see Figure 45a).

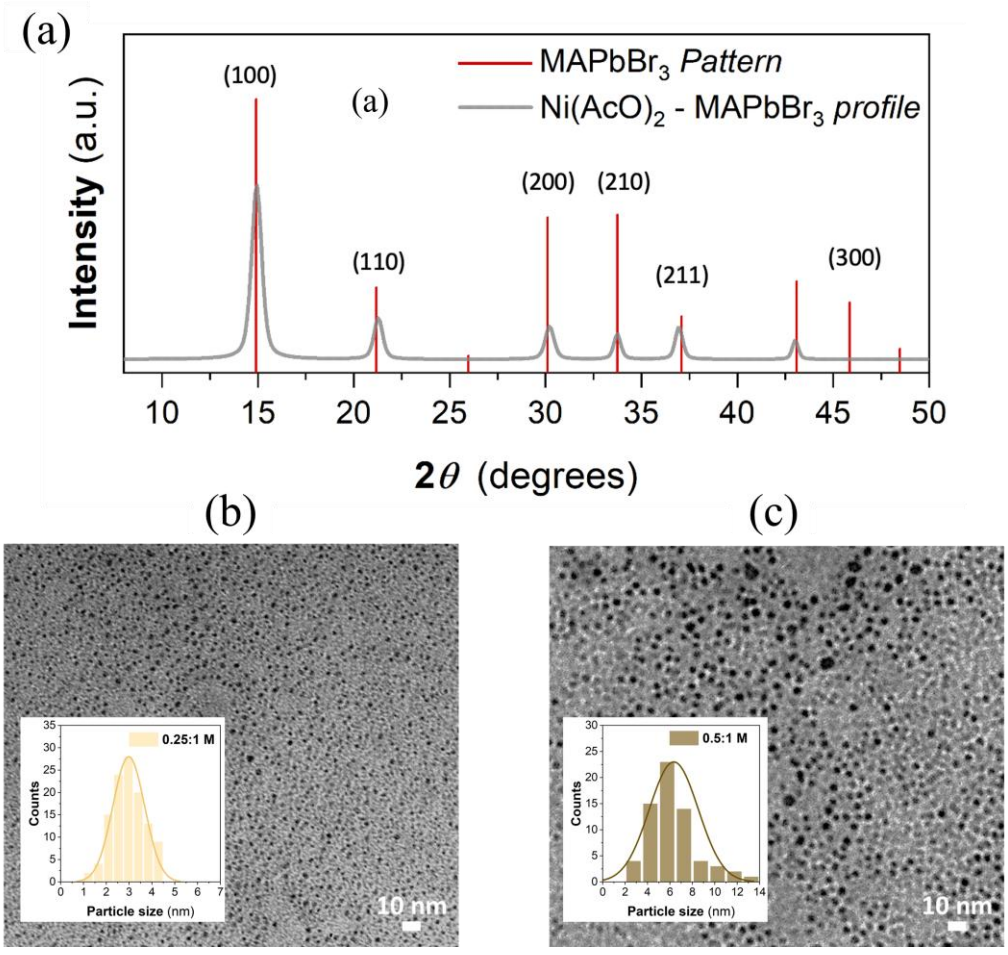

Figure 44. (a) XRD diffraction pattern of the as-synthesized $MAPbBr_3$:$Ni(AcO)_2$ nanocomposite under ambient humidity conditions (50% RH). (b and c) TEM images and particle size distributions for PNC nanocomposites at two $MAPbBr_3$:$Ni(AcO)_2$ ratios, specifically 0.25:1 and 0.5:1 M, respectively. Outcomes highlighted previously in Figure 34 and Figure 36c-d.

Under the same RH conditions, higher perovskite precursor concentrations yield larger PNCs, as TEM measurements confirm (Figure 44b-c). For instance, a lower $MAPbBr_3$ concentration (0.25 M) produces smaller PNCs with a size distribution around 2–3 nm, whereas higher $MAPbBr_3$ concentrations (0.5 M) result in larger PNCs, with sizes around 6–7 nm.[12]

The influence of precursor concentration on the formation of PNC nanocomposites is therefore critical. By varying the concentration ratio of the PNC precursor to the matrix, different outcomes can be achieved. After synthesis, the optical properties of thin films prepared at 50% RH are studied through absorption and PL, as depicted in Figure 45b-c. Detailed equipment specifications for these characterizations are provided in the Key Sources Table.

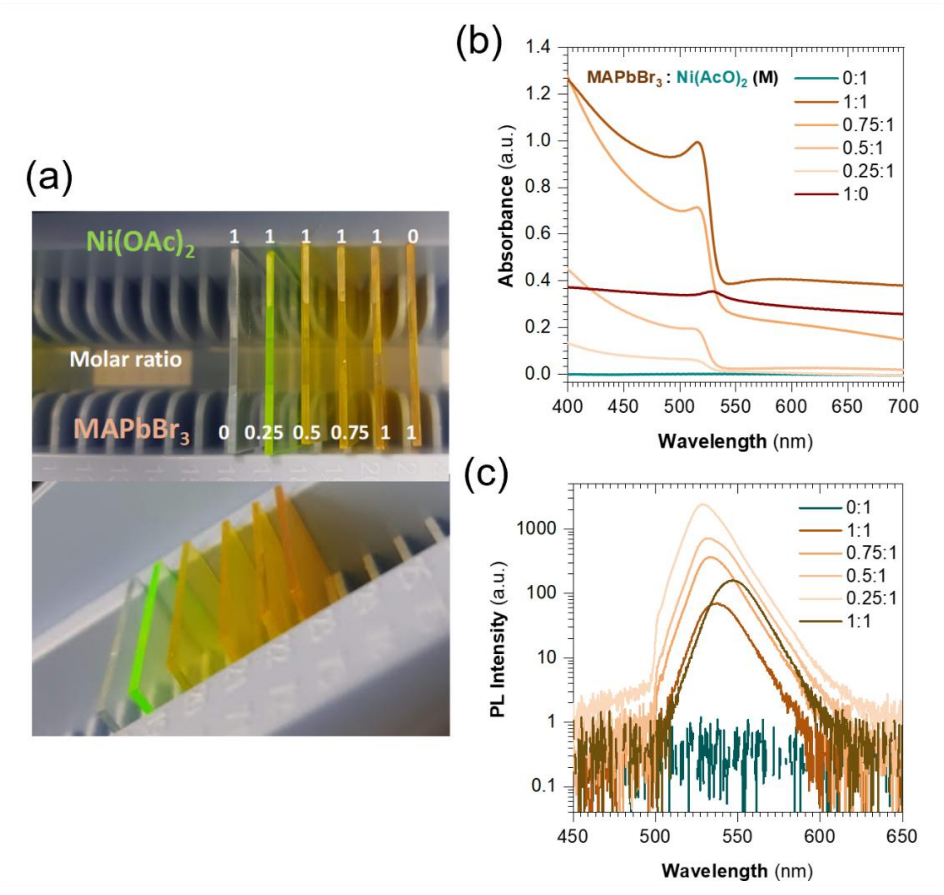

Figure 45.(a) Photograph of PNC nanocomposite thin films prepared with varying $MAPbBr_3$ concentration ratios, with $Ni(AcO)_2$ fixed at 1 M, at 50% RH. (b and c) Absorption and PL spectra of the thin films, respectively.

[12] All this previous has been extensively discussed in the previous chapter.

As shown in Figure 45a, increasing $MAPbBr_3$ concentration within the matrix, up to the bulk phase (1:0 ratio), leads to a trend of absorption peaks shifting towards lower energies, as represented in the absorption spectra (Figure 45b). Additionally, the PL response (Figure 45c) displays a redshift, with wavelengths ranging from 515 nm in samples with lower $MAPbBr_3$ concentration (0.25:1 M) to 550 nm in pure bulk $MAPbBr_3$. This shift reflects variations in average particle size within the matrix, as confirmed by TEM images (Figure 44).

Beyond precursor concentration, RH also impacts crystallization dynamics. As discussed in Figure 38 (Chapter 4), the PL and absorption spectra of nanocomposite films with a $MAPbBr_3$:$Ni(AcO)_2$ ratio of 0.25:1 M after exposure to different RH. As RH increases from 50% to 100%, both the absorption edge and emission peak redshift. As shown in Figure 38 a prominent difference between the absorption spectra is the sharply defined excitonic absorption peak at 525 nm when exposed to 100% RH, which is absent at 50% RH. Additionally, exposure to higher RH causes the PL band to shift from 525 nm at 50% RH to 540 nm at 100% RH, aligning with TEM observations. All this has been studied in detail in the Results section – Chapter 4.

It is noteworthy that, while ambient humidity influences the crystallization process, the nanocomposite film's optical properties stabilize once crystallization reaches a plateau. The stabilization period varies depending on RH and precursor concentration, but once stable, the optical characteristics remain consistent. A deep understanding of crystallization dynamics is thus essential for tuning the optoelectronic properties of perovskite thin-film nanocomposites. Higher RH expedites MHP crystallization within the matrix, while the precursor concentration also affects this process. Thus, the impact of a RH of 50% on samples with different precursor concentrations is studied immediately after preparation in a dry-glovebox environment see Figure 46. The *in situ* synthesis of PNCs within $Ni(AcO)_2$ is monitored by measuring the PL over time, as shown in Figure 46. The crystallization reaction progresses faster at higher perovskite concentrations (0.5 M) with a constant matrix concentration of 1 M, likely due to the presence of more nucleation centers associated with increased precursor concentration. Moreover, at higher concentrations (0.5 M), an emission plateau is achieved more quickly, indicating an almost complete reaction of the MHP precursors within the $Ni(AcO)_2$ matrix.

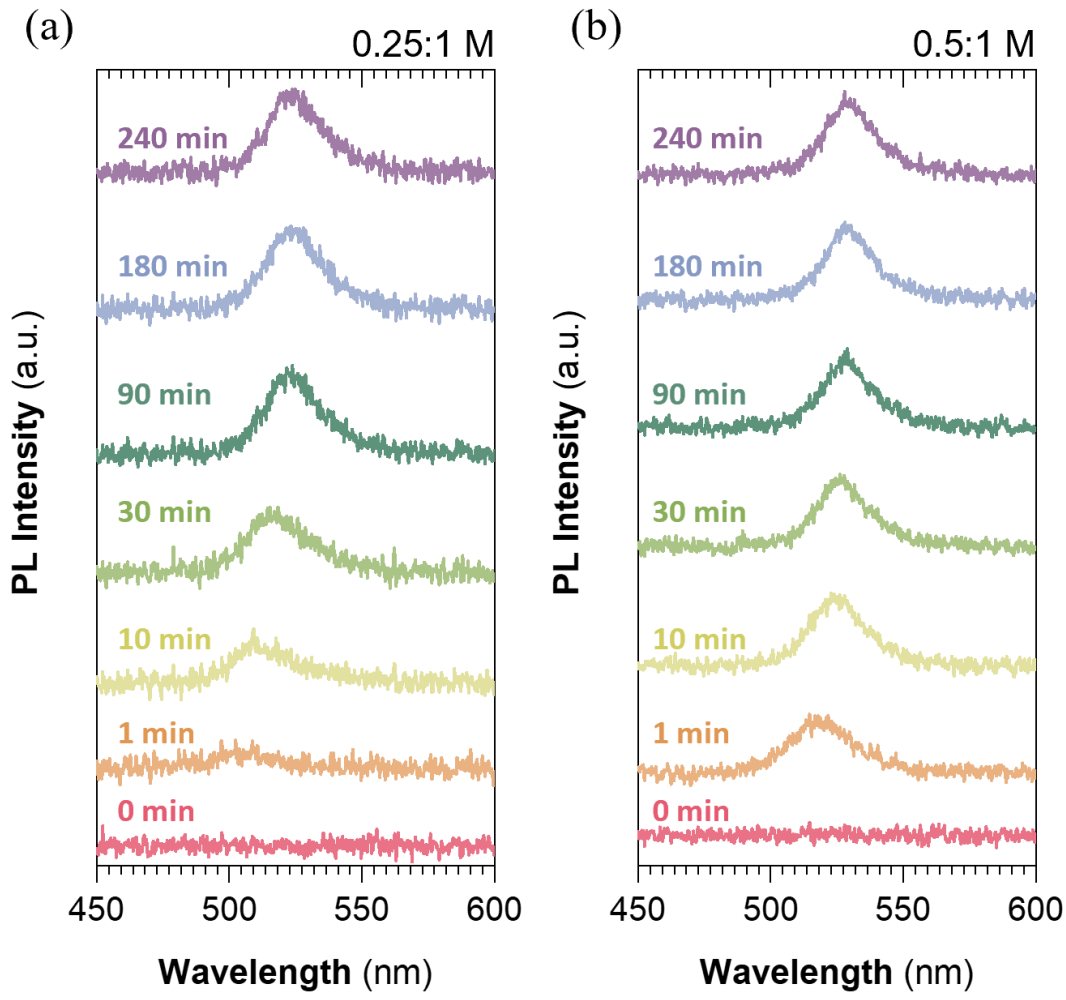

Figure 46. Crystallization dynamics monitored over time. Evolution of samples' PL depicting the impact of concentrations and humidity on the crystallization.

Besides the size control over NCs sizes with precursors concentration and RH, preliminary results demonstrate the potential of this approach for synthesizing PNCs of various halide compositions. In this sense, Figure 47 presents a series of halide variations, starting with $MAPbBr_3$ and substituting a portion of the bromine atoms with *Cl* and *I*. The introduction of alternative halides, such as *Cl* and *I* demands additional considerations on the solution chemistry. Due to different precursors solubilities, small amounts of DMSO are usually required, and hence annealing steps after spin-coating need to be incorporated to ensure proper crystallization of the PNCs. Further studies will be conducted to fully explore the potential for the bandgap tunability of the nanocomposites.

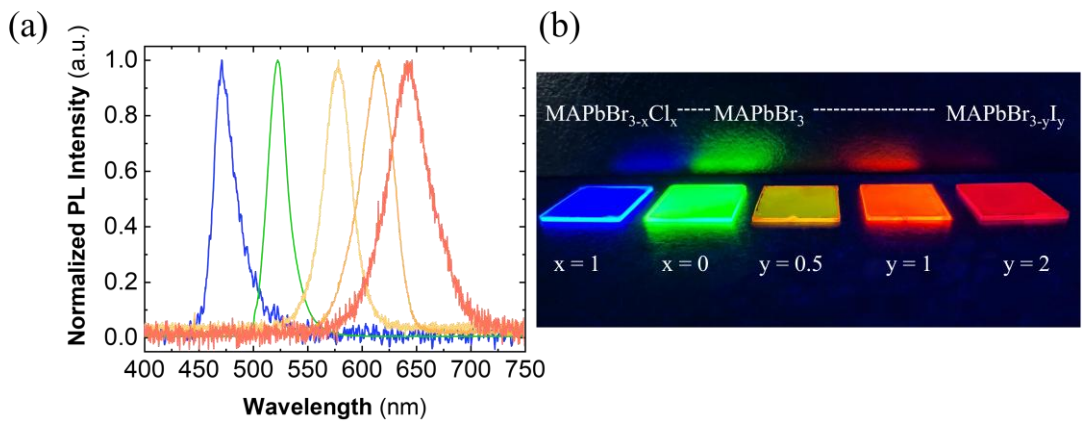

Figure 47. $MAPbBr_{3-x}Cl_x$ and $MAPbBr_{3-x}I_x$ PNC nanocomposites, showcasing various halide composition ions. (a) PL spectra and (b) films image under UV illumination.

5.4 CONCLUSIONS

This chapter provides an in-depth exploration of the crystallization process of MHP nanocomposites and presents a detailed protocol for synthesizing PNC using an in situ method. Specifically, it addresses the mechanisms of nanocomposite crystallization and offers tools for precise control over the resulting PNCs. A notable advancement in this method is the development of ambient-controlled humidity chambers, which introduce a new degree of freedom for tuning perovskite semiconductor NCs with high precision. While challenges such as solution stability and RH control persist, adherence to this protocol significantly enhances reproducibility and performance.

This method lays the groundwork for large-area, high-performance optoelectronic devices, representing a significant advancement in scalable MHP nanocomposite fabrication. Remarkably, compared with similar methods, this approach is a straightforward and cost-effective strategy that yields nanocomposites with excellent emission properties.

Building on these advancements, Chapter 6 will delve deeper into understanding the formation mechanisms, offering an extensive investigation into the crystallization process of PNCs and the resulting enhancement in their optical properties.

5.5 APPENDIXES

Table 4. Protocol - Key Resource Table

REAGENT or RESOURCE	PROVIDER	IDENTIFIER
Chemicals		
Methylammonium bromide (MABr), >99.5%	TCI	CAS 6876-37-5
Lead bromide ($PbBr_2$), >98.0%	Sigma-Aldrich	CAS 10031-22-8
N,*N*-dimethylformamide (DMF), anhydrous, 99.8%	Sigma-Aldrich	CAS 68-12-2
Nickel (II) acetate tetrahydrate ($Ni(AcO)_2$), 98%	Sigma-Aldrich	CAS 6018-89-9
Hydrochloric acid (HCl) 35%, Technical	VWR Chemicals	CAS 7647-01-0
2-Propanol (IPA) ≥99.5%	Sigma-Aldrich	CAS 67-63-0
Ethanol ≥99.5%	Sigma-Aldrich	CAS 64-17-5
Acetone, ACS reagent ≥99.5%	Sigma-Aldrich	CAS 67-64-1
Hellmanex III	Sigma-Aldrich	N/A
Inorganic Salts (Table 5)	Sigma-Aldrich or similar	N/A
0.22 µm pore size, 33 mm diameter, Millex-GV Durapore® (PVDF) membrane, hydrophilic	Sigma-Aldrich	N/A
Micropipette 20-200 µL	Thermo Fisher Scientific	11875762
Micropipette Tips 20-200 µL	Thermo Fisher Scientific	11923446
Humidity Chambers	Thermo Fisher Scientific	15889465
Carbon coated TEM grid	Sigma-Aldrich	N/A
Glass substrate – Microscope slides (76x26 mm)	VWR Chemicals	N/A

Continued		
REAGENT or RESOURCE	PROVIDER	IDENTIFIER
Other		
Ossila Ozone Cleaner	Ossila	https://www.ossila.com/en-eu/products/uv-ozone-cleaner
Spin-coater	Laurell WS-650 Model	http://www.laurell.com/spin-coater/?model=WS-650-23B
Dry-Glovebox, SICCO	SICCO	https://es.vwr.com/store/product/12566364/glove-box-sicco
Thermo-hygrometer	Thermo Fisher Scientific	15-079-679
Heating / Shaking Dry Bath	Thermo Fisher Scientific	https://www.thermofisher.com/es/es/home/life-science/lab-equipment/dry-baths/heating-shaking-dry-baths.html
Analytical balance	Waagenet	https://eu.waagenet.de/gram-
Spectrophotometer Flame-S-VIS-NIR	Ocean Insight	https://www.oceaninsight.com/blog/flame-series-general-purpose-spectrometers/
Spectrophotometer UV-2501PC, UV-Vis	Shimadzu	N/A
Blue Laser 404 nm CW GaN	Optoelectronics Tech. Co., Ltd	N/A
D8 Advanced X-ray diffractometer (XRD)	Bruker	N/A
JEOL JEM 1010 Transmission electron microscope (TEM)	JEPL, Tokyo, Japan	N/A
3D Printer – DIGILAB 3d45	Dremel	N/A
Nitrogen Glovebox	MBraun	N/A
Transmission electron microscopy (TEM)	JEOL JEM 1010	N/A

Table 5. Inorganic salts for the generation of a wide range of RH atmospheres within Humidity Chambers.

Saturated Salts	Temperature °C							
	5	10	15	20	25	30	35	40
	Relative Humidity, % over the Salt Solution							
Lithium chloride - LiCl	16	14	13	12	11	11	11	11
Potassium acetate - CH_3CO_2K	25	24	24	23	23	23	23	23
Magnesium chloride - $MgCl_2$	33	33	33	33	33	32	32	32
Potassium carbonate K_2CO_3	47	47	45	44	43	42	41	40
Magnesium nitrate - $Mg(NO_3)_2$	54	53	53	52	52	52	51	51
Sodium Chloride - NaCl	76	76	76	75	75	75	75	-
Cupric chloride - $CuCl_2$	65	68	68	68	67	67	67	67
Ammonium nitrate - NH_4NO_3	-	75	70	67	64	60	53	-
Ammonium sulfate - $(NH_4)_2SO_4$	82	82	82	81	81	81	80	80
Potassium chloride - KCl	88	87	86	85	84	84	83	82
Potassium sulfate - K_2SO_4	98	98	98	98	97	97	97	96

Chapter 6: Passivation Mechanism in Highly Luminescent Nanocomposite-based $CH_3NH_3PbBr_3$ Perovskite Nanocrystals

Chapter 6 builds upon the previous Chapters 4 and 5 by offering a deeper investigation into the crystallization and passivation mechanisms, unveiling the key stages that govern the crystallization process. The findings presented throughout this chapter are derived from and correspond to those reported in the article under revision: Noguera-Gómez et al., *Submitted*, 2024

ABSTRACT

In general, exposure to water negatively affects the structure and PL of MHPs. Nonetheless, humid conditions can also promote the *in situ* synthesis of $MAPbBr_3$ PNCs within a nickel acetate matrix, achieving PLQYs as high as 80%. In this chapter we elucidate the mechanism behind the water-driven formation and transformation of methylammonium lead bromide perovskite structures, emphasizing the key role of acetate as a mediator. By employing extensive UV-visible absorption, PL, PL excitation, Time-Resolved PL, PLQY, XRD, TEM, ATR-FTIR and X-ray Photoelectron Spectroscopy analyzes, we show that under low relative humidity (RH < 20%), the deposition results in non-emissive MA_4PbBr_6 (0D) and hydroxide species (PbBrOH, OH^-) rather than 3D crystalline $MAPbBr_3$. Increasing RH triggers a structural reorganization from 0D MA_4PbBr_6 to 3D MAPbBr through a MABr-stripping mechanism, producing NCs with enhanced PLQY. We further demonstrate that removing water quenches PL, a reversible process facilitated by hydroxide-mediated reactions controlled by the dual acid-base nature of the acetic acid/acetate system. Contrary to prior reports, our findings reveal that hydroxide ions can reversibly associate with NCs, passivating traps and enhancing stability. The basicity of acetate is critical for generating OH^-, which aids in passivation, stability, and the improved optical properties of the perovskite nanocomposites.

6.1 INTRODUCTION

Over the past decade, colloidal NCs of 3D MHP, represented by the chemical formula $APbX_3$ (where A = $CH_3NH_3^+$ (MA^+), $CH(NH_2)_2^+$ (FA^+), or Cs^+ and X = Cl^-, Br^-, or I^-), have drawn considerable interest. Typically synthesized using hot injection methods in organic solvents, these NCs display exceptional photoelectronic properties, such as high PLQY, narrow emission spectra, tunable emission wavelengths, and high defect tolerance.[15,150–153] These qualities make them promising candidates for a range of applications, including light-emitting diodes[154,155] and solar cells[156–158]. However, despite their excellent photophysical properties in solution, these colloidal NCs encounter significant issues when incorporated into functional thin films. Specifically, they suffer from reduced PL performance, which negatively impacts their optoelectronic properties and accelerates degradation. It is suggested that these functional and structural instabilities arise from the loss of passivating organic ligands in the solid-state films of perovskite NCs and their interaction with moisture. H_2O molecules infiltrate the NC lattice, forming hydrogen bonds with electronegative atoms (e.g., nitrogen and halogen), which leads to structural degradation into precursors or derivatives[159–162], ultimately affecting film quality and device performance.[161,163,164] Consequently, developing strategies for stabilization and passivation is essential to create robust materials for future applications.[66,127]

On the other hand, several studies have reported the beneficial effects of H_2O molecules in perovskite crystallization.[130,165–167] Some indicate its role in crystal reorientation[166], while others suggest that ambient water facilitates the generation of lead derivatives, such as PbBrOH.[168] Although the exact passivation mechanism in these bromide systems is not fully understood, PbBrOH is frequently proposed as a significant factor in active passivation, enhancing both stability and luminescence of 3D perovskite NCs.[169] Additionally, moisture is critical in driving a phase transition from initially formed low-dimensional 0D perovskites (A_4PbX_6) to their 3D counterparts ($APbX_3$)[170,171] via an AX-stripping mechanism facilitated by their solubility in water.[172–177] Like PbBrOH, the higher band-gap 0D phase can actively contribute to the passivation of the 3D NCs.[178]

In addition to these effects, with the results presented in chapters 4 and 5 we demonstrate that ligand-free MAPbBr3 perovskite NCs synthesized in situ within a nickel acetate ($Ni(AcO)_2$) matrix under humid conditions exhibit remarkably intense

and stable PLQY ≈ 80%.[146] A significant finding is that RH plays a crucial role in controlling the crystallization process, enabling the fine-tuning of NC formation and optimization of their optical properties. However, the mechanism behind these exceptional optical properties and the dynamics of crystallization has remained unclear.

In the study of this chapter, we show that in the aforementioned $MAPbBr_3$ nanocomposites, low humidity conditions (under 10% R.H.) initially promote the formation of 0D phase MA_4PbBr_6 NCs. These undergo two concurrent processes upon interaction with ambient humidity that determine the resulting film's properties: (a) the transition of 0D MA_4PbBr_6 to 3D $MAPbBr_3$ NCs and (b) the formation of hydroxide ions (OH^-) through an acid-base reaction with H_2O in the acetate-rich environment, which enhances passivation and optoelectronic properties of the 3D nanocrystals. Detailed studies on the PL performance of OH^--passivated NCs reveal that OH^- ions are in equilibrium with ambient humidity and can reversibly bind and unbind under vacuum and humid conditions, respectively. Consequently, the 3D $MAPbBr_3$ NCs show intense green PL with enhanced stability, attributed to the strong binding of hydroxide ions on the NC surface.

6.2 EXPERIMENTAL PROCEDURES

As emphasized throughout this Thesis, the simplicity of this method, combined with its potential applications in sensing, lasers, LEDs, PSCs, and catalysts represents a significant leap in the field. Additionally, the phenomenon of water-driven crystallization sets a foundation for further exploration of water's role in these materials.[13]

6.2.1 Preparation of $MAPbBr_3$ nanocomposites

To synthesize $Ni(AcO)_2$ -MAPbBr thin films, a single-step method is utilized, following the technique outlined in Chapters 4 and 5 and based on the work published by Noguera-Gómez et al. [146]

The synthesis process involves depositing the mixed solution onto glass and spin-coating it at 3000 rpm for 40 seconds in a humidity-free environment (Drybox).

[13] A topic that remains under active debate[179]

During spinning, the $MAPbBr_3$ nanocomposite gradually dries. The crystallization of perovskite NCs depends on concentration; however, for this work, the precursor concentrations (MABr, $PbBr_2$, and $Ni(AcO)_2$) are fixed as specified in the results section, while the relative humidity (RH) to which the samples are exposed varies.

Humidity chambers (design and preparation detailed in Chapter 5)[145] are used to create specific humidity levels, ranging from 20 to 75% RH, based on supersaturated solutions of different inorganic salts. Each $MAPbBr_3$ nanocomposite is maintained at the desired humidity level for 10 minutes to initiate the crystallization process.

6.2.2 Structural, optical and electronic characterization.

For XRD, SEM, Absorbance and ATR-FTIR measurements all the details can be found in the experimental sections of both Chapter 4 and 5.

TEM images are obtained using a Hitachi HT7800 microscope with a high-resolution LaB_6 filament, operating at an acceleration voltage of 100 kV. TEM samples have been prepared as described in Chapter 5. Crushed $MAPbBr_3$ nanocomposites are deposited onto a carbon-coated (Cu/C) TEM grids using methyl acetate as a solvent.

For X-ray Photoemission Spectroscopy (XPS) characterization, high-resolution XPS measurements are performed using a SPECS GmbH system (base pressure 1.0×10^{-10} mbar) equipped with an ASTRAIOS 190 2D-CMOS hemispherical analyzer. Photoelectrons are excited using the Al-Kα line (1486.7 eV) from a μ-FOCUS 500 monochromatic X-ray source (SPECS GmbH). Measurements are conducted at room temperature with a pass energy of 50 eV.

6.3 RESULTS

6.3.1 Crystallization mechanism

The formation of nanocomposite films via the in situ synthesis of $MAPbBr_3$ NCs within a $Ni(AcO)_2$ matrix requires water to initiate the 3D perovskite crystallization, as detailed in Chapters 4 and 5. To better understand water's specific role in the crystallization and passivation mechanisms (Figure 48), we examine the influence of RH on nanocomposites at a 0.25:1 molar ratio of $MAPbBr_3$:$Ni(AcO)_2$ as described in the experimental procedures section. RH exposure is essential not only for the growth

of perovskite NCs, as it governs their size, but more critically, for initiating structural phase transformations within the NCs, as described below.

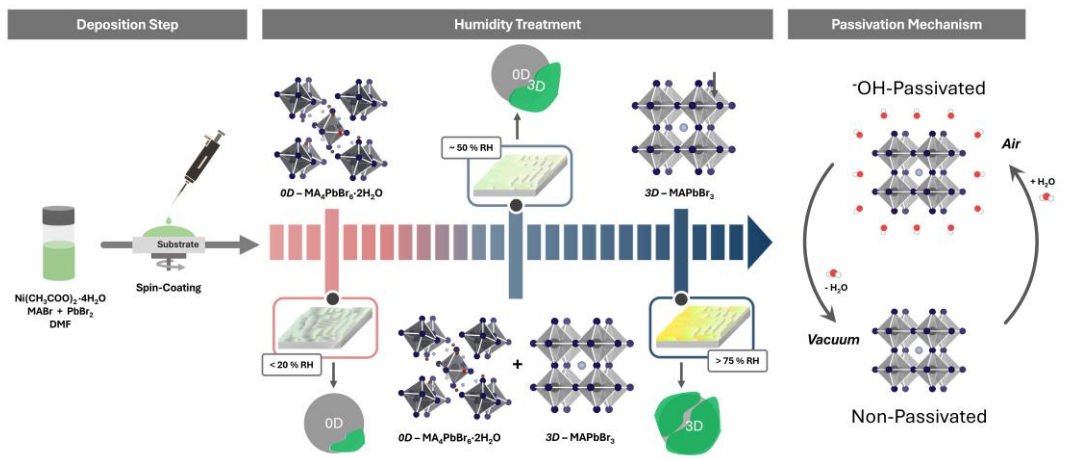

Figure 48. A schematic illustration of the crystallization process of $MAPbBr_3$ nanocomposites, emphasizing the phase transformation initiated by humidity exposure and the OH^- passivation mechanism that underpins their performance.

Films deposited under low RH conditions (< 20% RH) do not exhibit any PL response. However, upon exposure to higher RH, they display bright green luminescence. To investigate this transition, we subjected the samples to different RH levels (as detailed in the Experimental Section). Figure 49a shows the PL spectra of three samples prepared at 35%, 50%, and 75% RH, demonstrating a clear redshift in PL as humidity increases. PL, PL excitation (PLE), and 1-Transmittance (1-T) spectra for the same samples are presented in Figure 49b-d.

When both PLE and (1-T) signals stem from the same material, the spectra should approximately align for NCs, as displayed by the RH 75% sample from 375 to 530 nm (Figure 49d). In contrast, a noticeable difference between PLE and (1-T) spectra is observed for the sample generated at the lowest RH (35%) (Figure 50b). Notably, while the PLE spectrum of the 35% RH sample is qualitatively similar to those of the 50% and 75% RH samples, the (1-T) spectra differ substantially. The (1-T) spectrum of the 35% RH sample shows strong absorption bands at 225 and 320 nm, along with a weak, broad band at 400 nm. This suggests that a significant portion of the 35% RH sample is not the luminescent 3D perovskite $MAPbBr_3$, unlike the samples formed at higher RH. Instead, the 35% RH sample contains an additional phase with a distinct absorption band at 320 nm. This absorption band aligns with a dip in the PLE spectrum of the $MAPbBr_3$ nanocomposite (Figure 49d), indicating that

this additional phase is not photoactive and merely serves as a passive light absorber, screening the excitation of the luminescent 3D perovskite. The broad absorption band at 400 nm may partially correspond to the luminescent 3D perovskite.

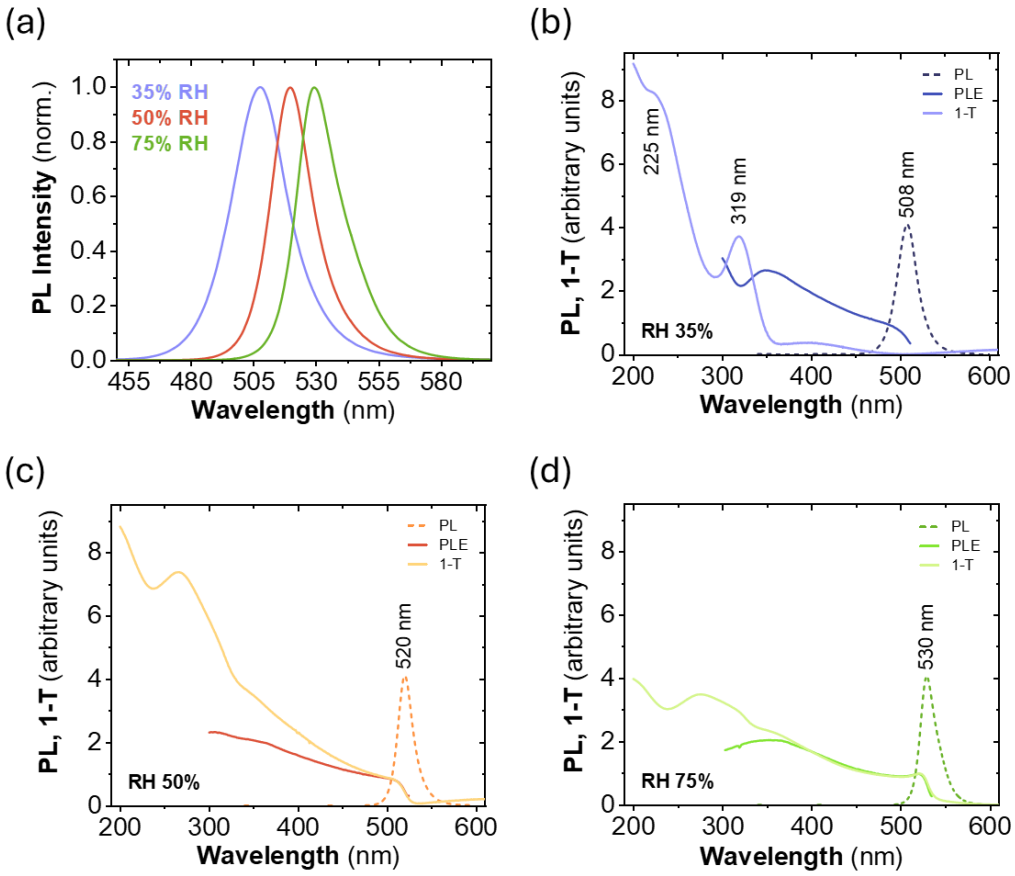

Figure 49. (a) PL spectra of $MAPbBr_3$-$Ni(AcO)_2$ nanocomposites prepared at atmospheric humidity levels of 35% (sample 508), 50% (sample 520), and 75% (sample 530). (b-d) PL, PLE, and 1-T (absorptance) spectra for these three samples.

For the $MAPbBr_3$ nanocomposite at 50% RH (Figure 49c), the PLE and (1-T) spectra coincide within the 475-520 nm range but diverge at shorter wavelengths. The shape of the (1-T) spectrum exhibits characteristics of luminescent 3D perovskite $MAPbBr_3$, although with notable contributions from other products, showing an absorption maximum at 275 nm and a shoulder at 360 nm.

To further clarify the effect of RH on the optical properties of $MAPbBr_3$-$Ni(AcO)_2$ nanocomposites, we have tracked the absorbance spectra from 200 to 700 nm across various RH levels and exposure durations. Figure 50a illustrates the progression under a 75% RH environment. Initially, only the characteristic absorption band at 320 nm is observed within the first minutes of exposure.

With prolonged exposure, a secondary absorption band emerges around 275 nm, causing an apparent blue shift of the 320 nm absorption band, as seen in the inset of Figure 50a, which will be further analyzed below. Simultaneously, the characteristic absorbance band of the 3D-$MAPbBr_3$ semiconductor at approximately 520 nm intensifies, reaching its peak after about one hour of exposure.

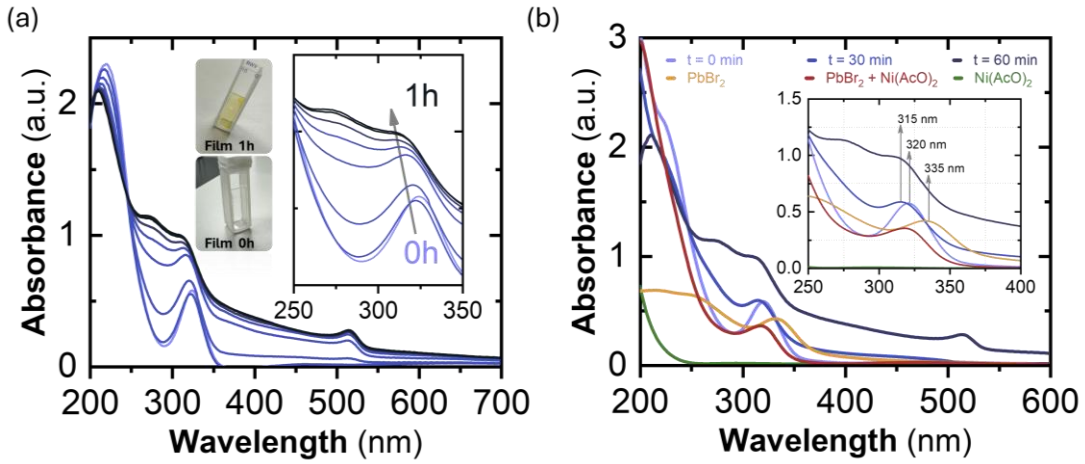

Figure 50. (a) Absorption spectrum for a $PbBr_2$+MABr+$Ni(AcO)_2$ nanocomposite film exposed to 75% RH at 25 ºC for 1 hour. (b) Absorption spectra of $PbBr_2$, $Ni(AcO)_2$, $PbBr_2$+$Ni(AcO)_2$, and $PbBr_2$+MABr+$Ni(AcO)_2$ forming the nanocomposite (75% RH, with exposure times ranging from 0 to 60 minutes).

Figure 50b displays absorbance spectra of films of $PbBr_2$, $Ni(AcO)_2$, $PbBr_2$ + $Ni(AcO)_2$, and $Ni(AcO)_2$-$MAPbBr_3$ nanocomposites exposed to 75% RH over varying times. The absorbance spectrum of a $PbBr_2$ thin film (orange line) shows a peak around 335 nm, which is absent in the other samples. Likewise, a $Ni(AcO)_2$ thin film (green line) does not show any absorption band in the studied spectral range. In contrast, a $PbBr_2$ + $Ni(AcO)_2$ film (red line) exhibits a similar absorption band as $PbBr_2$, but shifted to 320 nm. Comparing these findings with the absorbance spectra of $MAPbBr_3$ nanocomposites exposed to 75% RH at different times (Figure 50b), the 320 nm band appears as early as t = 0 min, even when no signs of 3D $MAPbBr_3$ are yet present. By t = 30 min, the absorbance spectrum still includes a band at 320 nm, but an increase in absorption within the 250-320 nm region and a tail in the 350-500 nm region are characteristic of the 3D $MAPbBr_3$ phase. Thus, we attribute the band at 320 nm, distinguishable in the $MAPbBr_3$ nanocomposites at various time intervals, to the wide band gap of PbBrOH structure.[180–183] This phenomenon is influenced by the presence of crystalline water in $Ni(AcO)_2 \cdot 4H_2O$, supported by results from co-depositing $PbBr_2$

and $Ni(AcO)_2$ (Figure 60, Step (2)), which shifts the absorption band from 335 to 320 nm, compared to the bare $PbBr_2$ sample.

A closer examination of spectral shifts in the absorption band at 315-335 nm over prolonged exposure to 75% RH (see inset of Figure 50b) indicates the presence of additional compounds in the films. Specifically, for $MAPbBr_3$-$Ni(AcO)_2$ nanocomposites at t = 0 min, the peak of the absorption band is at 320 nm, whereas at t = 30 min, it appears at 315 nm. This blue shift in the UV absorption band maximum is associated with the formation of a 0D phase in the MA-Pb-Br family, MA_4PbBr_6, which is characterized by a distinct peak at 310 nm.[175,184,185] Several studies[184,186] suggest that the transformation from 0D MA_4PbBr_6 to 3D $MAPbBr_3$ upon water interaction is facilitated by an MABr-stripping reaction (see Figure 60, Step (3)). This mechanism highlights water's role in destabilizing the 0D structure, enabling MABr removal and promoting the 3D perovskite phase formation. Thus, following deposition at low RH (< 20% RH), a nanocomposite of 0D MA_4PbBr_6 NCs embedded in $Ni(AcO)_2$ is created. When exposed to higher RH, the 0D NCs transform into 3D $MAPbBr_3$ perovskite structures, as illustrated in Figure 48. Unlike Cs_4PbBr_6, MA_4PbBr_6 is only stable as a complex with two water molecules, forming $MA_4PbBr_6{\cdot}2H_2O$.[175,184] Therefore, the waters of crystallization in the $Ni(AcO)_2{\cdot}4H_2O$ precursor is essential for forming $MA_4PbBr_6{\cdot}2H_2O$ at early crystallization stages, even at low RH. Consequently, the observed absorbance bands around 310-330 nm strongly support the coexistence of 0D $MA_4PbBr_6{\cdot}2H_2O$ and PbBrOH in the nanocomposites. Interestingly, although similar 3D/0D combinations are often described as type I heterostructures that enhance radiative recombination through funneling[146], no significant energy transfer is observed in the PLE measurements. This suggests that the 0D phase and PbBrOH primarily serve as neutral UV filters. Therefore, gaining a deeper understanding of the structural and compositional details of these coexisting phases is essential.[187,181]

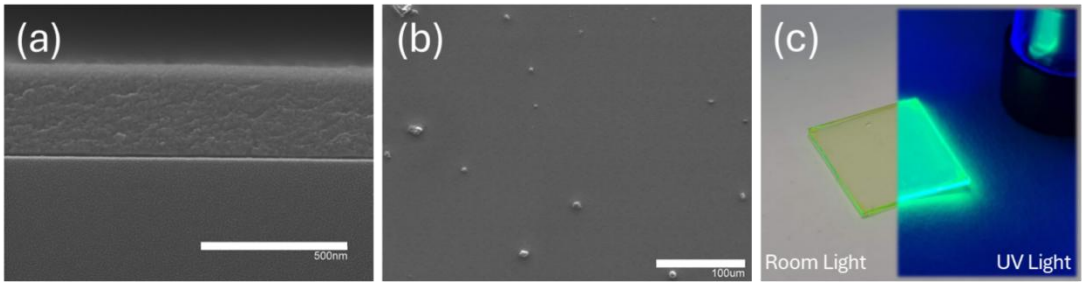

Figure 51. SEM Images (a) Cross-sectional and (b) top-view of $MAPbBr_3$ nanocomposite films. (c) Thin film photographs light comparison under UV and room light.

SEM analysis of $MAPbBr_3$-$Ni(AcO)_2$ nanocomposites reveals a uniform, dense structure with smooth surfaces, as shown in cross-sectional and top-view images (Figure 51). Regarding the morphology of the layers, SEM images show that the $Ni(AcO)_2$-$MAPbBr_3$ nanocomposites (Figure 51c) exhibit a uniform and dense structure. Cross-sectional analysis reveals a thickness of approximately 300 nm (Figure 51a), while top-view images (Figure 51b) display highly smooth surfaces for the $MAPbBr_3$ nanocomposites. Attempts to obtain TEM images of the native structures were unfruitful due to challenges in sample preparation. However, after exposure to 75% RH, TEM images revealed nanoparticles associated with 3D $MAPbBr_3$ perovskites (though no additional structures were observed). Figure 52a presents TEM images of $MAPbBr_3$ nanocomposites exposed to 75% RH. The images show black-dotted nanoparticles of various sizes, which we associate with 3D $MAPbBr_3$ perovskites. Unlike subsequent findings from absorption and XPS analyzes, the TEM images do not reveal additional structures. This discrepancy may result from sample handling or potential damage caused by the electron beam, which could obscure the observation of native multicomponent structures.

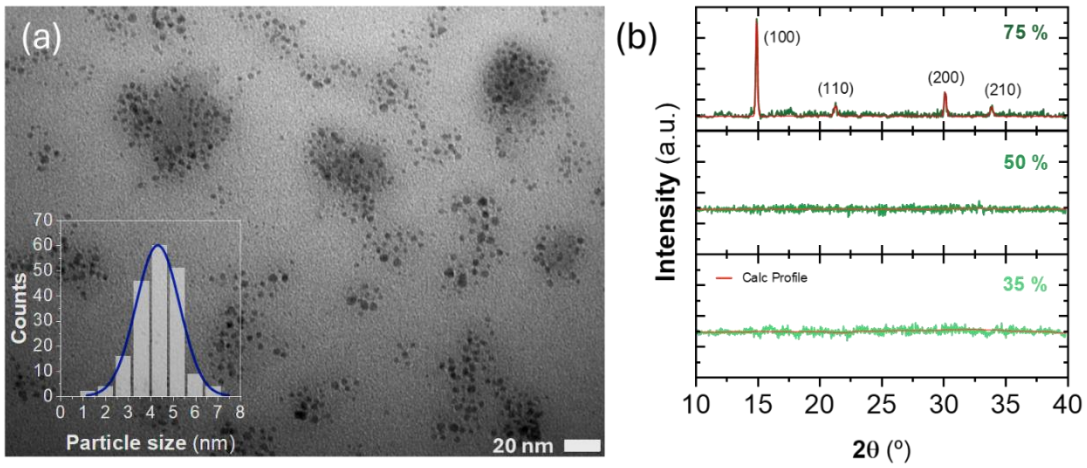

Figure 52. (a) TEM image and particle size distribution of $MAPbBr_3$ nanocomposites prepared at 75% RH. (b) XRD patterns of as-synthesized $MAPbBr_3$ nanocomposites under varying relative humidity conditions.

The XRD diffraction peaks of nanocomposites exposed to 50% and 75% RH (Figure 52b) correspond to the cubic Pm-3m crystal phase of $MAPbBr_3$ (JCPDS no. 00-0105). Specifically, peaks at 15°, 21.2°, 30.2° and 33.9º match the (100), (110), (200) and (210) crystal planes, respectively. In contrast, films prepared under < 20% RH do not show any crystalline patterns, indicating that $MAPbBr_3$ does not form at low RH. This finding aligns with the optical properties shown in Figure 49, where the formation of 3D NCs is associated with high RH conditions (> 50%). The incorporation of a relatively low concentration of MHP precursors within the amorphous matrix (in a 0.25:1 molar ratio of $MAPbBr_3$ to $Ni(AcO)_2$) presents challenges for detecting minor and poorly crystalline byproducts, such as 0D MHP and PbBrOH, during the initial stages using XRD. Additional complementary characterization techniques are thus necessary to overcome this limitation.

As a route to gain a deeper understanding of this phenomenon, attenuated total reflectance Fourier transform infrared spectroscopy (ATR-FTIR) is employed to examine the impact of humidity on the nanocomposite structure. In contrast to XRD, which identified the formation of $MAPbBr_3$ perovskite only at relative humidity levels exceeding 50%, ATR-FTIR provides detailed insights into the molecular groups present (Figure 53) even at lower RH levels exposure. The O–H vibrational band, centered between 3600 and 3250 cm^{-1}, is observed across all samples, with its intensity markedly increasing with rising humidity, eventually surpassing that of the N–H band

(~3250–3000 cm^{-1}). This trend indicates the early incorporation of OH species into the material. Moreover, the substantial enhancement of the O–H band intensity with increasing humidity supports the formation of an OH-capped configuration in the 3D perovskites. This behavior, likely linked to an OH-driven passivation mechanism (illustrated in Figure 60, Steps 4 and 5), is discussed further in the section dedicated to the OH-mediated passivation process.

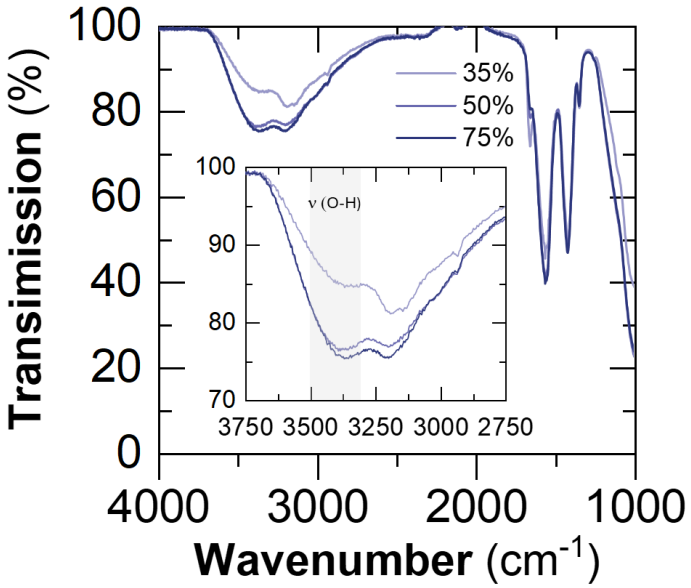

Figure 53. ATR-FTIR spectra comparing $MAPbBr_3$ nanocomposites at the different RH studied conditions.

Moreover, XPS analysis can provide additional insights to supplement the optical observations regarding the phase transformation from 0D to 3D perovskite and the OH passivation mechanism.

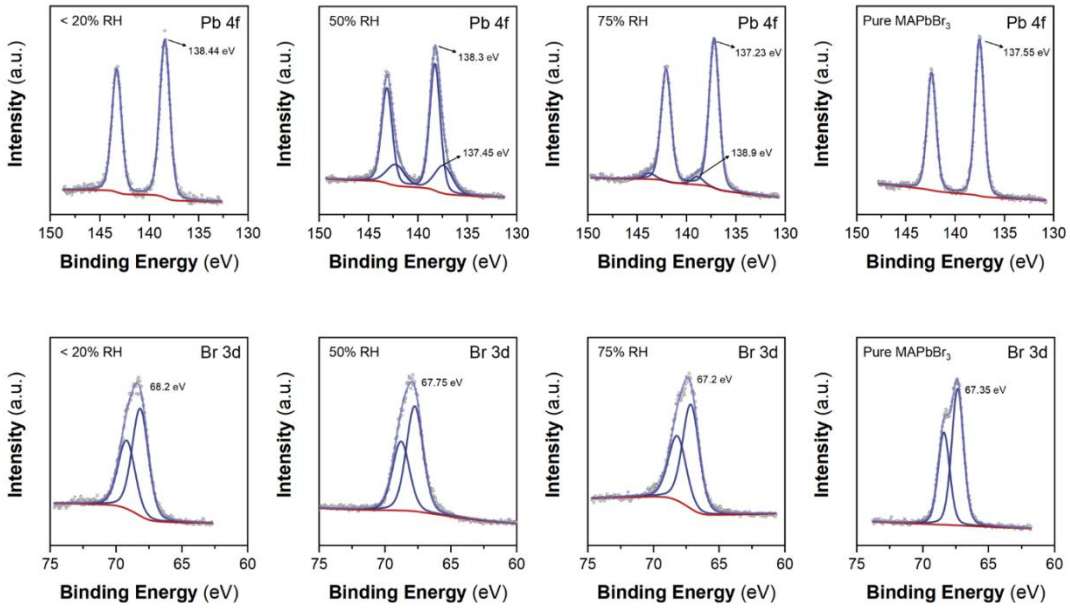

Figure 54. XPS fittings for the Pb 4f and Br 3d core levels at different RH stages for $MAPbBr_3$ nanocomposites and pure $MAPbBr_3$.

Figure 54 displays the XPS spectra of the Pb 4f and Br 3d core levels for samples prepared under <20%, 50%, and 75% RH conditions, as well as for pure $MAPbBr_3$. The spectra are deconvoluted using Voigt line shape peaks and Shirley backgrounds, with Pb 4f doublets showing a spin-orbit splitting of 4.87 eV and Br 3d doublets with a 1.04 eV split. The sample prepared at <20% RH shows a Pb 4f7/2 peak at 138.44 eV, indicating Pb-Br interactions. In the 50% RH sample, two Pb 4f doublets are identified: a lower binding energy peak at 137.45 eV attributed to Pb-O interactions[188] and a peak at 138.3 eV representing Pb-Br interactions. As noted, Pb-O interactions may be associated with species involved in crystallization, such as PbBrOH (Figure 60, Step 2). In the 75% RH sample, the deconvolution also reveals two doublets attributed to Pb-Br (137.23 eV) and Pb-OH (138.9 eV) interactions.[189] For pure $MAPbBr_3$ prepared at 50% RH, the Pb-Br bond is seen at a binding energy of 137.55 eV.

Regarding the Br 3d core levels, the Br 3d5/2 binding energy for pure $MAPbBr_3$ is 67.35 eV, while it decreases progressively from 68.2 eV in the <20% RH sample to 67.75 eV at 50% RH and finally 67.2 eV at 75% RH. This gradual reduction in binding energy in the Pb 4f and Br 3d peaks points to a weakening of the Pb-Br interaction[190,191], with the weakest Pb-Br interaction observed at 75% RH, similar to

that in pure $MAPbBr_3$. These features are consistent with the presence of $MA_4PbBr_6{\cdot}2H_2O$ (0D) perovskite in samples prepared at <20% RH, a mix of $MA_4PbBr_6{\cdot}2H_2O$ and $MAPbBr_3$ at 50% RH, and predominantly $MAPbBr_3$ at 75% RH. Further analysis and quantification of the XPS spectra reveal a direct decrease in the Br/Pb ratio in samples exposed to <20%, 50%, and 75% RH (Table 6). As RH increases, the Br/Pb ratio decreases. This observation of Pb-OH interactions in the 75% RH sample, where only the 3D perovskite phase is present, suggests an OH-capped perovskite passivation mechanism that effectively addresses Br vacancies, potentially enhancing stability and improving PL. Thus, these findings align well with the proposed transformation mechanism of nanocomposites upon water exposure, and are fully consistent with changes observed in optical properties.

Table 6. Stoichiometry parameters based on XPS Fit analyzes for the Pb 4f and Br 3d cores. Stoichiometric ratio among Br/Pb calculated from the XPS data

Sample (RH)	Peak Area		Atomic percentage		Sto. Ratio
	Pb 4f	*Br 3d*	*Pb 4f*	*Br 3d*	
< 20 %	1231.6	862.08	15.14	84.86	$Pb\ Br_{5.6}$
50%	2489.7	1349.1	18.73	81.27	$Pb\ Br_{4.33}$
75%	2781.5	1333.4	20.67	79.33	$Pb\ Br_{3.83}$
Pure $MAPbBr_3$	2132.1	937.7	22.12	77.88	$Pb\ Br_{3.52}$

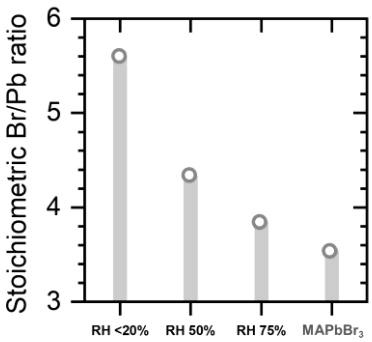

Analysis of the O1s and C1s core-level spectra (Figure 55) offers additional insights into the presence of hydroxyl (O-H) groups contributing to the passivation mechanism (Figure 60, Steps 1 and 4), though overlapping with other species, such as carbonyl groups (C=O), complicates interpretation. To clarify, we calculated the O/CC=O ratio, as derived from XPS by integrating the C 1s peak attributed to C=O (CC=O) and the main O 1s peak.

The study of the O1s and C1s core-level spectra (Figure 55) helps to identify O-H groups involved in passivation (Figure 60, Steps 1 and 4). As shown in Figure 55, the O 1s core-level peak in pure $MAPbBr_3$ perovskite is dominated by a single component at 532.3 eV, attributed to OH groups formed in humid conditions.[192] Conversely, the C 1s core-level spectra of this sample reveal a single peak at 285.0 eV,

corresponding to adventitious carbon on the surface. For NCs synthesized in acetate-rich environments, the O 1s XPS spectra shows an intense, broad peak around 532 eV, similar to that observed in bulk perovskites. Only a minor additional O 1s signal is resolved in samples prepared at 50% RH, attributed to Pb-O local environments. The O 1s peak at 532 eV in the XPS spectra from samples grown in acetate-rich environments likely indicates the incorporation of O-H groups during synthesis, though other oxidized species on the sample surface cannot be ruled out. The C 1s spectra of these samples show a prominent component attributed to carbonyl carbon (C=O) from the acetate precursors. Any O 1s XPS signal from C=O groups would overlap with that from O-H groups.

Table 7. Stoichiometric parameters from XPS Fit analyzes for C 1s and O 1s core-levels related to acetate groups.

Sample (RH)	Peak Area		Atomic percentage		O/C Atomic ratio
	C 1s (C=O)	*O 1s*	*C 1s (C=O)*	*O 1s*	
< 20 %	244.47	3374.45	17.5	82.5	4.71
50%	420.41	2165.1	36	64	1.77
75%	534.6	2975.6	34	66	1.94

To distinguish the presence of O-H in samples prepared in acetate-rich environments, we calculated the atomic O/CC=O ratio from XPS by integrating the C 1s peak attributed to C=O (CC=O) and the primary O 1s peak. The results (Table 7) show that a significant portion of the main O 1s XPS peak in samples prepared in acetate-rich environments originates from O-H, supporting the inclusion of hydroxyl (O-H) groups involved in the passivation mechanism.

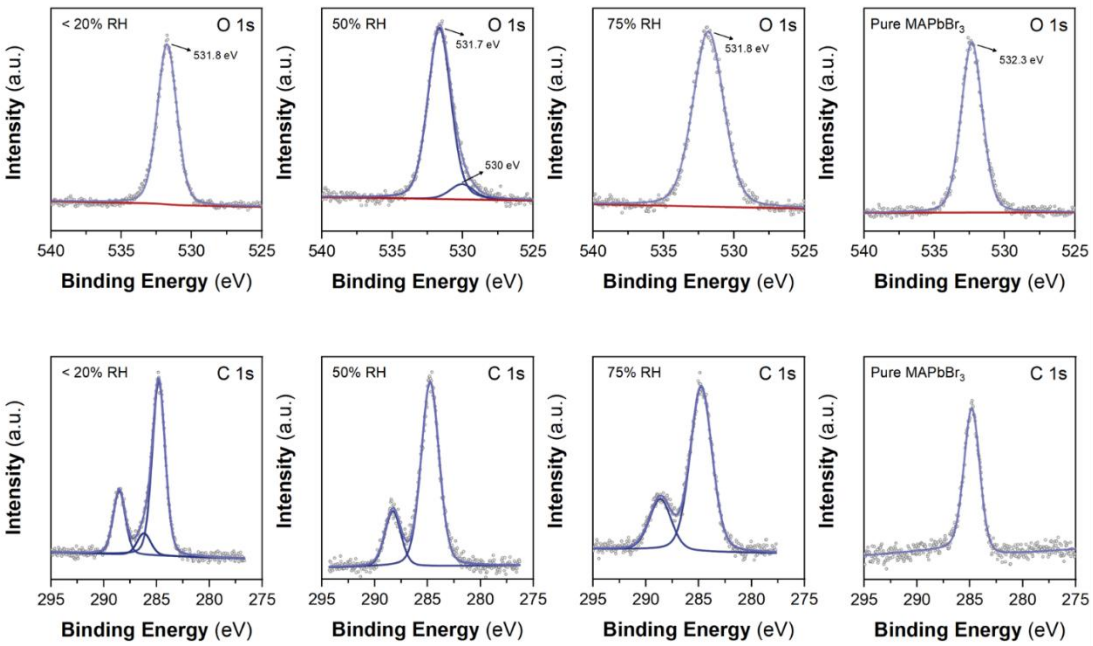

Figure 55. XPS fittings for the O 1s and C 1s core-level spectra for $MAPbBr_3$ nanocomposites and pure $MAPbBr_3$ under different RH conditions.

6.3.2 OH-mediated passivation mechanism

Given that the PL properties of in situ synthesized $MAPbBr_3$ nanocomposites are highly dependent on RH during crystallization, a key question is how different atmospheres affect the system's photophysics.

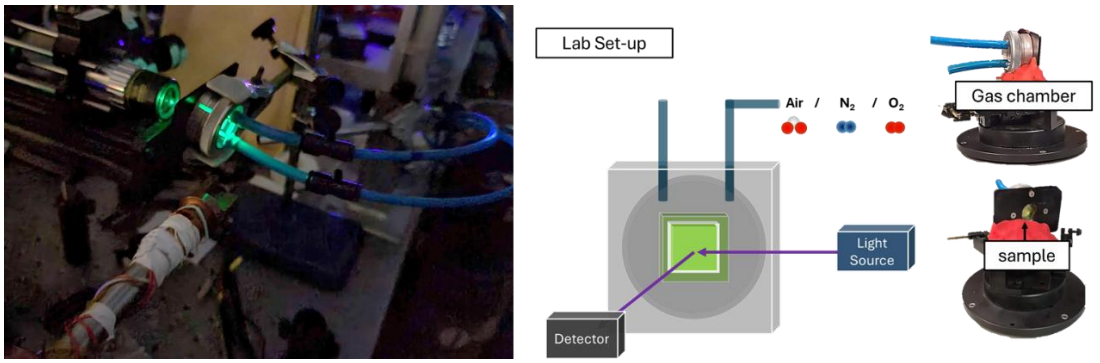

Figure 56. Illustration of the laboratory gas setup used for dynamic passivation studies. The photograph on the left shows the physical lab setup, while the schematic on the right depicts the gas flow configuration.

To investigate this, we have examined nanocomposite samples prepared under 75% RH (with a PL maximum at 532 nm) and 50% RH (with a PL maximum at 515 nm). Figure 57 shows the corresponding PL spectra and decay kinetics measured

sequentially under different atmospheres (O_2, N_2, air, and vacuum). All measurements were conducted in an optical gas flow cell (Figure 56) at atmospheric pressure with ~30-minute intervals to stabilize emission parameters.

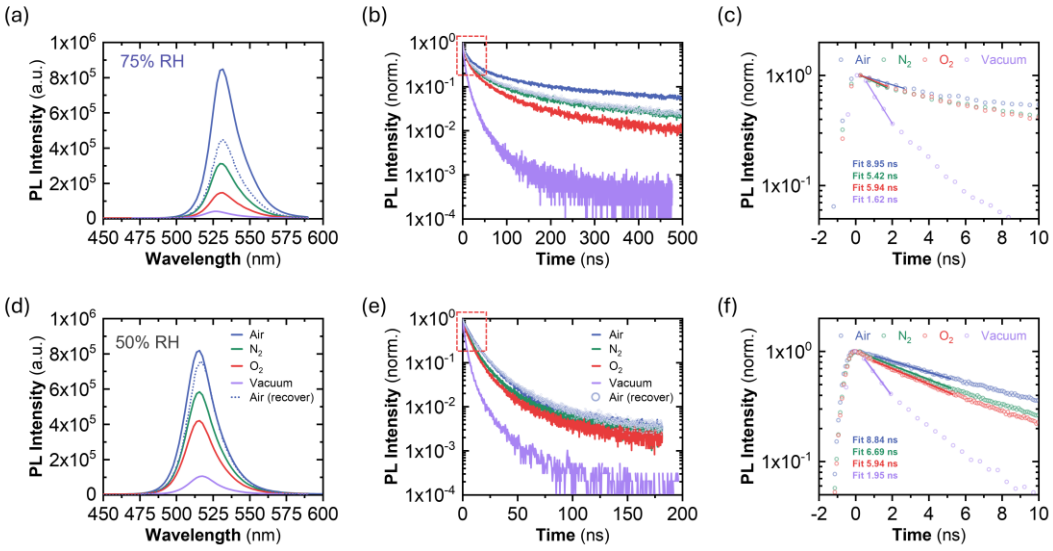

Figure 57. PL spectra (a, d), PL decay kinetics (b, e), and corresponding insights (c, f) for the $MAPbBr_3$ nanocomposite samples at 75% RH (a-c) and 50% RH (d-f), measured in an optical flow cell under various gases at atmospheric pressure (ambient air, N_2 and O_2 from a cylinder). Vacuum measurements were conducted in a metal cryostat.

For both samples, the highest PL is observed under ambient air conditions, with results indicating a strong influence of atmospheric conditions on PL parameters for both RH levels. For the 75% RH sample, Figure 6a shows that PL intensity decreases by approximately 3 and 6 times when the optical cell is filled with dry N_2 and O_2 gases, respectively. In vacuum, the PL integral intensity drops about 20-fold compared to its initial level in air, accompanied by a notable reduction in PL decay kinetics (Figure 57b). When the optical cell is filled back with air, the PL intensity is restored to approximately half of the initial value.

This partial recovery is further analyzed and attributed to the degradation process (Figure 60, Step 6), which occurs due to prolonged exposure of the 3D NCs to a high RH of 75%.[146] To investigate potential changes in absorption, we have also monitored the transmittance spectrum of the sample under both vacuum and ambient air conditions (Figure 58). The results reveal no significant variations across the cycles, indicating that the structure of the 3D NCs remains stable and does not revert to the

original 0D phase. Consequently, all observed changes must be attributed exclusively to PL quenching.

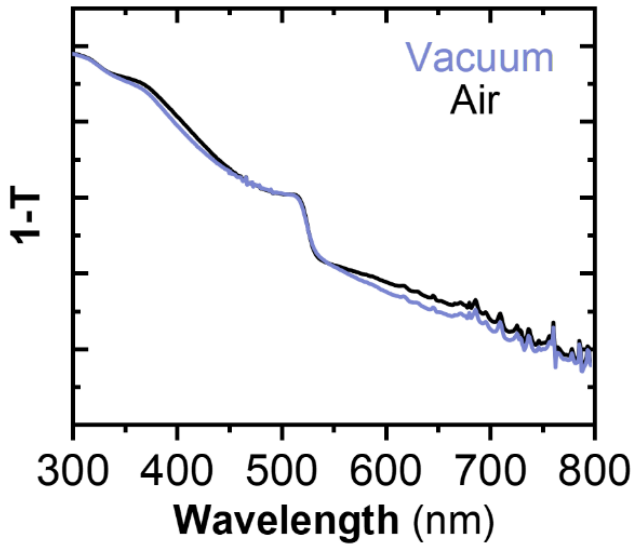

Figure 58. 1-Transmittance of a $MAPbBr_3$ nanocomposite at 75% RH at vacuum and air conditions.

The sample prepared at 50% RH shows a similar trend in PL behavior under the same atmospheric sequence. When switched from air to dry N_2 and O_2, PL intensity decreases by factors of 1.4 and 1.9, respectively (Figure 57d). Under vacuum, the integrated PL intensity further declines by approximately 6.7 times. These changes are also associated with shortened PL kinetics (Figure 57e). Upon re-exposure to atmospheric air, the PL intensity and decay kinetics nearly revert to their original values (Figure 57d and Figure 57e, dotted lines).

The decrease in PL lifetime from air to O_2, N_2, and vacuum (Figure 57b and Figure 57e) does not correlate directly with the reduction in overall PL intensity (Figure 57a and Figure 57d). For both samples, the PL decay kinetics are highly non-exponential in all atmospheres except vacuum, with long-lived components likely related to trapping-detrapping processes.[142] We therefore use the "primary lifetime" (τ_{pr}) as a parameter to characterize the charge recombination rate within the nanocomposites. This primary lifetime is obtained through mono-exponential fitting of the initial decay phase. For the 75% RH sample, the "primary lifetimes" τ_{pr} under air, N_2, O_2, and vacuum conditions are 8.95, 5.42, 5.94, and 1.62 ns, respectively (see Figure 57c and Table 8). The quenching coefficients, calculated as $\tau_{pr}(air)/\tau_{pr}(gas)$, are

1.65, 1.51, and 5.52 for O_2, N_2, and vacuum, respectively. These values are significantly lower than the 2.72, 5.74, and 22.14 obtained from the integral PL rates under these conditions. Qualitatively similar results are observed for the 50% RH sample (see Figure 57f and Table 8), indicating that PL decay kinetics do not capture all PL quenching mechanisms. To explain these findings, we suggest that in the absence of OH^- passivation, PL quenching may occur in two forms: (i) instantaneous or static (using molecular fluorescence terminology) and (ii) dynamic. Luminescent centers undergoing instantaneous quenching do not have time to emit luminescence before being quenched. Therefore, they are visible in the luminescence decay kinetics of the entire ensemble of emitters by a drop in the amplitude of the decay kinetics. In contrast, dynamic quenching results in shorter luminescence decay times without reducing amplitude. Basic kinetic measurements can help estimate the fraction of NCs affected by static quenching when passivating ligands are absent. Indeed, if TRPL measurements in air and vacuum are conducted under identical excitation and detection conditions, then the integrals under the decay kinetics should be proportional to the respective PLQY. The ratio of the decay integrals in air versus vacuum is 22.94 (Figure 59), closely matching the 22.14 ratio of steady-state PL intensities (Table 8). Furthermore, the fraction of NCs completely quenched can be derived by comparing the amplitude reduction in PL decay kinetics in vacuum relative to air, both measured under the same conditions. Figure 59 shows that the amplitude of quenched PL kinetics in vacuum is 32% of the PL signal amplitude in air, indicating that after removing adsorbed water molecules in vacuum, 68% of the NCs experience complete PL loss through static quenching.

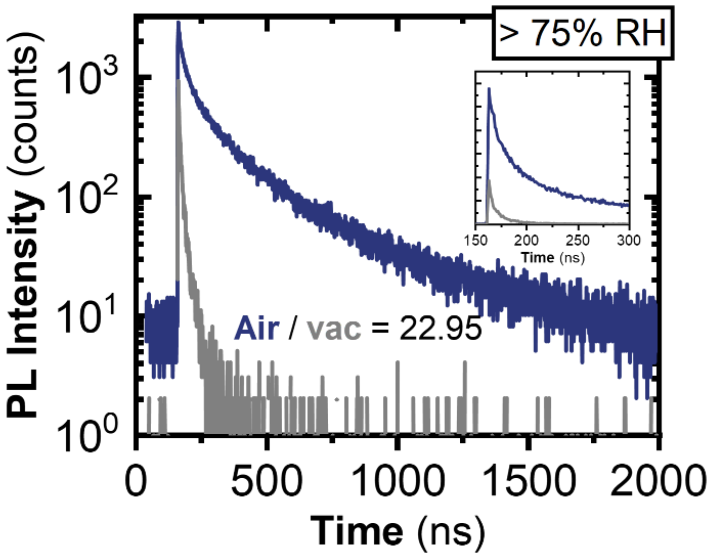

Figure 59. PL decay kinetics analysis for a sample at 75% RH at the same excitation and detection conditions.

Based on these findings, we conclude that the removal of water from $MAPbBr_3$ nanocomposites through a reduction of ambient humidity results in the loss of the passivating agent responsible for high PLQY under air and humid conditions. The most extreme case is observed in vacuum, where PL quenching is at its highest. When using gas carriers like N_2 and O_2, a less pronounced decrease in PL occurs, as these gases desorb water molecules to a lesser extent and at a slower rate than vacuum. This trend clearly suggests that adsorbed water molecules may serve as passivating agents, consistent with an OH-capped equilibrium passivation mechanism (Figure 60, Step 5).

Table 8. PL Decay monoexponential fittings and PL Integral Intensity for the nanocomposite $MAPbBr_3$ specimen. Data from Figure 57.

	Air	*N_2*	*O_2*	*Vacuum*
75% RH τ_{pr} (ns)	8.95	5.42	5.94	1.62
75% RH τ_{pr} (air)/ τ_{pr}	1	1.65	1.51	5.52
75% RH PLint(air)/PLint	1	2.72	5.74	22.14
50% RH τ_{pr} (ns)	8.84	6.69	5.94	1.95
50% RH τ_{pr} (air)/ τ_{pr}	1	1.32	1.49	4.53
50% RH PLint(air)/PLint	1	1.4	1.9	6.7

In contrast, these results cannot be explained by the formation of a type I heterostructure (with a wider bandgap 0D phase A_4BX_6 or a water-induced byproduct like lead bromide hydroxide, PbBrOH), a commonly cited explanation for the high

PLQY of 3D ABX_3 in literature.[193,194] If a type I heterostructure were responsible, an effective energy transfer from the 0D to the 3D phase would be expected, which is not observed in the PLE of the 3D phase: the 0D phase in the 0D/3D mixture acts as a neutral filter, absorbing UV radiation similarly to the wide-bandgap compound PbBrOH. Therefore, we conclude that wide-bandgap crystalline structures, such as 0D MA_4PbBr_6 and PbBrOH, do not significantly contribute to increasing the PLQY of the 3D phase through passivation. Instead, the enhanced PLQY is primarily driven by the in-situ generation of hydroxide ions, which effectively passivate the $MAPbBr_3$ nanocrystals.

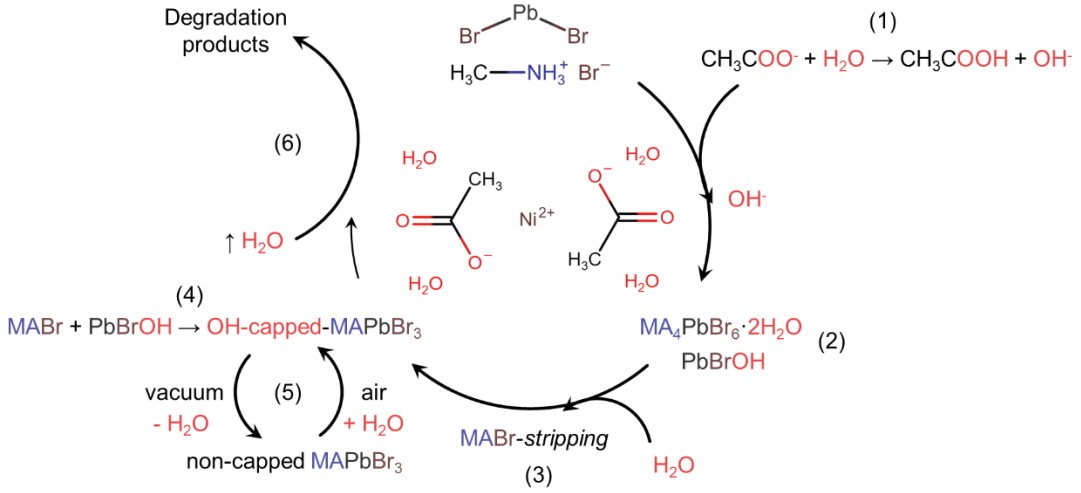

Figure 60. Schematic representation of the sequential chemical steps and reactions governing the crystallization mechanism of $MAPbBr_3$ nanocomposites within a $Ni(AcO)_2$ matrix: (1) hydrolysis of acetate ions, leading to an increase in OH^- concentration, (2) formation of the 0D perovskite phase and PbBrOH, (3) MABr-stripping mechanism triggered by water interaction, (4) phase transition from 0D to 3D (OH-capped) perovskite, (5) reversible binding and unbinding of OH-capped perovskite NCs upon water removal, and (6) excessive water exposure resulting in precursor formation and degradation products.

Based on experimental evidence and analysis, we propose the formation mechanism illustrated in Figure 60. The process begins with the emergence of the 0D $MA_4PbBr_6{\cdot}2H_2O$ structure, driven by the interaction between MABr and $PbBr_2$ in the presence of crystallization water from $Ni(AcO)_2{\cdot}4H_2O$ (Step 2). At the same time, PbBrOH forms as an intermediate due to OH^- generation via an acid-base reaction between acetates and water (Step 1). In this mechanism, acetate (CH_3COO^-) acts as a

relatively strong base, accepting H^+ from water and facilitating OH^- generation. These OH^- ions then bind with excess Pb^{2+} to form PbBrOH (Step 2), concurrent with the formation of MA_4PbBr_6. Efforts to use other nickel salts (e.g., $NiSO_4 \cdot 6H_2O$, $NiBr_2 \cdot 3H_2O$, $Ni(CH_3SO_3)_2$, $Ni(SO_3NH_2)_2 \cdot 4H_2O$, $Ni(PhSO_3)_2 \cdot 6H_2O$, $Ni(OH)_2$) did not yield similar results, as they lacked either crystallization water, suitable counterion basicity, or both.

As humidity increases, a "MABr-stripping" reaction occurs, removing methylammonium bromide (MABr) and promoting the transformation from 0D MA_4PbBr_6 to 3D $MAPbBr_3$ (Step 3) by establishing the correct stoichiometry for $MAPbBr_3$ formation. Hydroxide ions (OH^-), produced through water interactions with acetate, bind to the surface of the newly formed $MAPbBr_3$, creating an OH-capped 3D perovskite structure that enhances stability and PL performance (Step 4). The passivation process is reversible, facilitated by the dual acid-base nature of the acetic acid/acetate system, which enables the system to switch between the non-capped $MAPbBr_3$ and the OH-capped $MAPbBr_3$ configurations (Step 5). However, the transition from the 3D NCs back to the 0D phase is irreversible. The removal of water under vacuum conditions results solely in PL quenching, without inducing any changes in the sample's transmittance (Figure 58). With prolonged H_2O exposure, the 3D $MAPbBr_3$ phase eventually degrades, leading to perovskite lattice breakdown and the formation of degradation byproducts (Step 6). To validate the final step of the proposed mechanism, the evolution of PLQY and XRD patterns is monitored over time under 75% RH. The temporal progression of PLQY is presented in Figure 61a, while Figure 61b illustrates the corresponding XRD patterns at different crystallization intervals. The PLQY of the nanocomposite sample reaches a maximum of approximately 80% after 30 minutes, followed by a gradual decline with continued exposure. Over a comparable timescale, a five-fold reduction in XRD peak intensities is observed, corroborating that prolonged exposure to high RH conditions ultimately degrades the ionic structure of the perovskite.

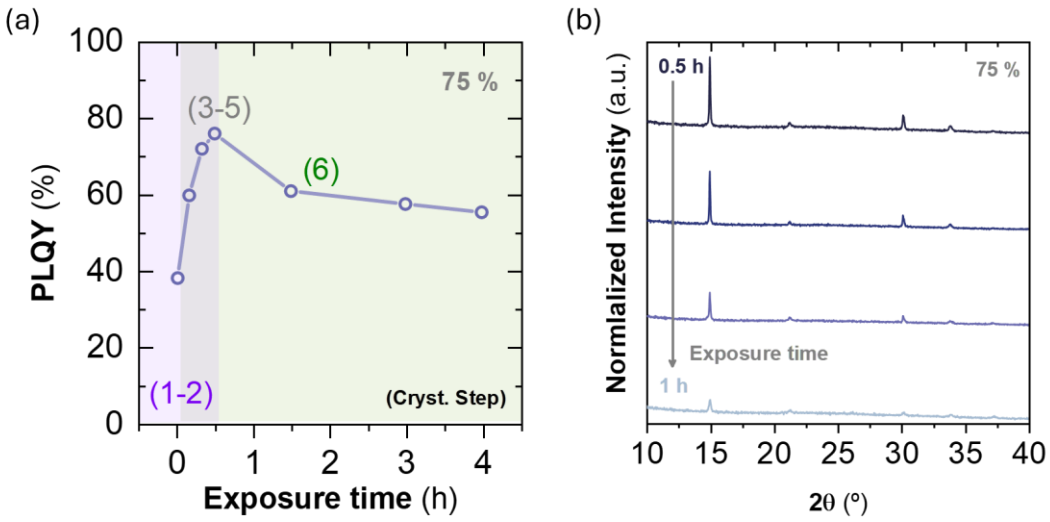

Figure 61. Monitoring the crystallization dynamics of a $MAPbBr_3$ nanocomposite at 75% RH through the evolution of PLQY and XRD profiles.

Building on the preceding analysis, acetate's basicity is critical for the passivation mechanism, as it generates OH^- in situ, which binds to the $MAPbBr_3$ nanocrystal surfaces. Its strong basic character in aqueous environments effectively promotes OH^- formation, aiding in the stabilization and passivation of the perovskite structure. This dual acid-base character of the acetic acid/acetate system is essential for driving the hydroxide-mediated reactions in the system.

6.4 CONCLUSIONS

In summary, in this chapter we present a refined understanding of the crystallization dynamics of methylammonium lead bromide perovskite NC phases through an in-situ synthesis approach under controlled humid conditions. Contrary to the typical quenching effect of H_2O on MHPs, we demonstrate that humidity, particularly above 20% RH, promotes the transformation of 0D structures into 3D perovskite NCs in the presence of acetate-rich matrix. At lower humidity levels, synthesis primarily yields non-emissive 0D perovskite and PbBrOH, while higher RH supports the formation of 3D NCs. A detailed analysis of the PLE spectrum showed no significant energy transfer, suggesting that the 0D phase and PbBrOH act as neutral UV filters. Consequently, we conclude that the wide-bandgap crystalline structures (0D MA_4PbBr_6 and PbBrOH) do not significantly contribute to increased PLQY in the

3D phase through passivation. Instead, the enhancement in PLQY is primarily due to the in-situ generation of hydroxide ions, which effectively passivate $MAPbBr_3$ nanocrystals.

Importantly, we have identified the crucial role of water and acetate basicity in controlling crystallization dynamics and producing OH^-, which acts as a passivator, enhancing the optical properties of NCs. Extensive studies on PL and PL decay kinetics of $MAPbBr_3$ nanocomposites under various gas environments confirm that the reversible removal of water molecules from NCs leads to substantial PL quenching. Our findings indicate that the in-situ-generated OH^- is essential for improving the stability and optical performance of perovskite NCs. We believe that our work will pave the way for a deeper understanding of the role of passivating agents in advancing perovskite applications in optoelectronic devices.

Chapter 7: Rapid and Straightforward Synthesis of $CsPbI_3$ PSCs via Nickel Aetate Incorporation

In this chapter, we explore the innovative use of nickel acetate in the preparation of all-inorganic PSCs. Building on the versatility, simplicity, and effectiveness of nanocomposite-based materials —examined in detail in previous chapters— in enhancing the properties of perovskite NCs, we have leveraged this approach for solar cell fabrication. Chapter 7 focuses specifically on the stabilization of wider bandgap perovskites, such as $CsPbI_3$, using nickel acetate. This method introduces a novel strategy for achieving improved material stability and evaluates the resulting performance of these perovskites in PV devices. The findings presented throughout this chapter are derived from and correspond to those reported in an article that is being prepared for submission.

ABSTRACT

Stable inorganic perovskite $CsPbI_3$ has emerged as a promising alternative to organic-inorganic hybrid perovskites, due to its thermal stability and appropriate bandgap (~1.73 eV) for single-junction and tandem solar cells in indoor and outdoor applications respectively. The formation of $CsPbI_3$ films with large grains and low trap densities are essential for high-performance and stable solar cells. In this chapter, a novel synthesis strategy is presented, incorporating varying amounts of nickel acetate ($Ni(AcO)_2$) into a pure DMSO $CsPbI_3$ precursor solution. The addition of nickel acetate results in stable γ-$CsPbI_3$ (black phase) nanocomposite perovskite films, confirmed by XRD analysis. The absence of residual PbI_2 further supports the enhanced efficiency achieved with nickel acetate compared to pure $CsPbI_3$. Using a DMA/HI-free approach, the top device with 0.1 M $Ni(AcO)_2$ concentration reached over 12% PCE in an n-i-p mesoscopic configuration, with a lifespan exceeding 600 hours at MPPT and minimal losses (<20%) without encapsulation under controlled inert conditions. Efficiencies over 15% and 17% were achieved under cool and warm white illumination, respectively, showing potential for indoor energy harvesting. Life cycle assessment (LCA) indicates a 70% reduction in GWP and the elimination of hazardous chemicals like DMF and toluene, though $Ni(AcO)_2 \cdot 4H_2O$ and PbI_2 remain in the absorbing layer.

7.1 INTRODUCTION

As detailed in Chapter 3, the interest in MHP solar cells has grown significantly within the PV community, driven by their impressive PCEs and potential for cost-effective, easy fabrication. Since their introduction in 2009, when initial efficiencies were around 3-4%,[18] advancements in this technology have rapidly increased PCE values, with the highest certified efficiency now reaching 26.1%.[13] These materials typically feature a structure composed of organic and inorganic cations such as methylammonium (MA^+), formamidinium (FA^+), and cesium (Cs^+) within a metal halide framework. However, despite their high efficiency, hybrid perovskite structures suffer from stability issues that limit their long-term viability. As a necessary requirement prior to their commercialization, solar modules must withstand various operational stresses, including temperature, light exposure (visible and UV), and electrical bias, all of which are critical concerns for their stability, as outlined in the standard ISOS stability protocols.[46,195–198]

In recent years, fully inorganic cesium lead halide perovskites, particularly $CsPbI_3$, have emerged as promising candidates due to their exceptional thermal stability.[199–203] $CsPbI_3$ is especially appealing because of its 1.73 eV bandgap, making it suitable for double-junction perovskite/silicon tandem solar cells or for single junction indoor applications.[195,204–206] Current record PCEs for lab-scale all-inorganic perovskite absorbers are around 21%.[207,208] However, $CsPbI_3$ faces significant challenges in maintaining a stable perovskite phase in ambient conditions due to its small ionic radius, leading to structural instability. This structural instability poses a significant hurdle for their practical use in long-term PV applications.[209] Moreover, the high annealing temperature required in some synthesis methods to obtain the α-$CsPbI_3$ phase (>350 ºC) restricts its compatibility with different device substrates and CTLs.[206,210,211] Therefore, low-temperature processing is crucial for improving tandem solar cell fabrication, reducing energy consumption, enhancing reproducibility, and enabling industrial scalability.[205]

Several strategies have been reported to stabilize $CsPbI_3$ black phases, including solvent engineering,[212,213] surface passivation techniques to modify surface tension,[214] dimensionality engineering (such as scaffold confinement,[215] nanocrystal colloidal methods,[202] and quasi-two-dimensional approaches with large cations[216,217]), and chemical engineering (involving small molecules[218–222] and ionic incorporation that

partially replace lead with other divalent cations ($CsPb_xM_{1-x}I_3$)[223] or substituting some iodide with bromide[224]). Currently, one of the most efficient low-temperature strategies is the addition of dimethylammonium iodide (DMAI) to form (DMA_xCs_{1-x})PbI_3. DMAI has been shown to stabilize the $CsPbI_3$ black phase, influencing crystallinity and grain size.[222] This was first reported in 2015, by the introduction of hydroiodic acid (HI) as an additive,[225] which was later identified as generating DMAI through the decomposition of DMF via acidic hydrolysis catalyzed by HI.[226] However, achieving phase transitions and fully volatilizing organic additives often requires high annealing temperatures (>330 °C) for $CsPbI_3$.[227] In contrast, high-efficiency $CsPbI_3$ perovskites with over 20% performance have been fabricated at lower temperatures using DMAI derivatives.[209] This has led to ongoing debates regarding whether DMAI-assisted $CsPbI_3$ perovskites are truly inorganic or represent $DMA_xCs_{1-x}PbI_3$ mixed-cation or "cesium-rich" systems.[227,228]

In this context, the novel approach described in the previous Chapters 4, 5 and 6 has demonstrated the significant potential of a nickel acetate-based matrix for the in-situ generation and stabilization of PNCs.[146,229] Building on these findings, we explored the matrix's applicability in the fabrication of PSCs, particularly focusing on materials that present challenges due to their metastable polymorphic nature. In this chapter, we have studied and developed a promising strategy using a DMSO-only, DMA/HI-free precursor solution that incorporates nickel acetate to crystallize the γ-$CsPbI_3$ in a nanocomposite form. In contrast to undoped $CsPbI_3$, we show a clear correlation between the concentration of $Ni(AcO)_2$ and the stabilization of the γ-$CsPbI_3$ black phase. XRD analysis confirms the role of $Ni(AcO)_2$ in the crystallization process, while Energy-dispersive X-ray (EDX) analysis shows a uniform distribution of $Ni(AcO)_2$ across the perovskite grains. SEM reveals the impact of annealing temperature on grain size in the perovskite absorber layer. JV curves analysis further identifies an optimal concentration threshold for device performance without compromising conductivity. The best device, incorporating 0.1 M of $Ni(AcO)_2$, achieves over 12% PCE in an n-i-p mesoscopic configuration, with more than 600 hours of operation at MPPT and minimal losses (<20%). Additionally, it demonstrates PCE over 15% and 17% under cool and warm white light, respectively, showcasing its potential for indoor applications. The Life cycle assessment (LCA) of this process for $CsPbI_3$ solar cell fabrication reveals a 70% reduction in global warming potential

(GWP) compared to the state-of-the-art. The results show minimized environmental impacts across most categories, despite the presence of $Ni(AcO)_2 \cdot 4H_2O$, which has low toxicity compared to PbI_2. The studied DMSO-only, DMA/HI-free method avoids hazardous substances such as DMF, toluene, and TOPO, which are used in comparative synthesis approaches. However, caution is advised as $Ni(AcO)_2 \cdot 4H_2O$ and PbI_2 remain in the absorber layer.

7.2 EXPERIMENTAL PROCEDURES

7.2.1 Chemicals and Substrate preparation

Chemicals

CsI (99.999%, Sigma-Aldrich), lead(II) iodide (PbI_2, 99.99%, TCI), dimethyl sulfoxide (DMSO, 99.9%, Sigma-Aldrich), isopropanol (IPA, 98%, Avantor), chlorobenzene (99.8%, Sigma-Aldrich), tris(2-(1H-pyrazol-1-yl)-4-tert-butylpyridine)cobalt(III) tri[bis-(trifluoromethane) sulfonimide] (FK209, Sigma Aldrich), 30 NR-D Transparent Titania Paste (GreatCell Solar Materials), bis(trifluoromethane)sulfonimide lithium salt (Li-TFSI, Sigma-Aldrich), ethanol (99.9%, Merck), spiro-OMeTAD (Lumtec), titanium diisopropoxide bis(acetylacetonate) (TIAP, 75 wt % in isopropanol, Sigma-Aldrich), 4-tert-butyl pyridine (tBP 98%, Sigma-Aldrich), nickel (II) acetate tetrahydrate (Ni(AcO)2, 99% Thermo Scientific Chemicals). All chemicals are used as received.

FTO substrates cleaning

Unpatterned FTO substrates (TEC 15, Ossila, with dimensions 2 cm × 1.5 cm) are numbered on the back side (glass side). Substrates are cleaned with 2% Extran solution with a very fine brush to clean the FTO surface, then washed with distilled water to remove soap contents. Afterwards cleaned with ethanol, acetone and isopropanol for 15 min by sonication. After drying with a nitrogen gun, the substrates are placed in a UV-ozone cleaner for 15 minutes right before the titanium oxide layer deposition.

Solution preparation

- 2% Extran solution is made by mixing 20 mL in 1000 ml distilled water.
- TiO_2 solution is prepared by adding 1000 µL TIAP into 9 mL of ethanol.

- 1.5 M CsI solution is prepared by dissolving 1.063 g of CsI solution in 2.726 ml DSMO solvent. The mixture is stirred 30 minutes until complete solubilization of CsI to get the solution.
- To get 1.3 M $CsPbI_3$ solution, 2.274 ml CsI solution is added in 1.145 g PbI_2 salt and stirred for 30 min at 80 ºC until it completely dissolved.
- To make 1.3:0.1 (molar ratio) $CsPbI_3$:$Ni(AcO)_2$ solution, 1 ml above $CsPbI_3$ solution is added to 0.025 g of $Ni(AcO)_2$ and stirred for 30 min until a clear, green-yellowish perovskite solution is formed.
- A 70 mM solution of spiro-OMeTAD is prepared by dissolving 90 mg spiro-OMeTAD in 982.26 µL chlorobenzene with 35.5 µL tBP, 20.40 µl LiTFSI with a stock solution of 520 mg/ml in acetonitrile, and 22.22 µl FK209 with a stock solution of 375 mg/ml in acetonitrile.

7.2.2 PSCs Fabrication

TiO_2 compact layer

TiO_2 compact layer is deposited by spray pyrolysis with oxygen as the carrier gas. One edge of each substrate is covered by around 5 mm using a guided-metal holder containing the substrates of conductive FTO to avoid the side being exposed. Then the substrates are heated up to 450 °C and kept at this temperature for 15 min before and 30 min after the spray of the precursor solution. The whole solution is transferred into a spray nozzle and sprayed at roughly 25 cm away from the substrates with an inclination angle of 45 degrees, with at least 20 seconds of delay between each spraying cycle. Afterward, substrates are left for cooling down to room temperature and then put in an ozone chamber for 15 minutes before perovskite film deposition.

TiO_2 mesoscopic layer

TiO_2 compact layer is deposited by spin coating. The as-prepared TiO_2 compact layers are coated using 70 mL of 30-NRD titania paste solution (150 mg mL^{-1} in ethanol). The spinning time is set at 20 s at 4000 rpm. Following the deposition step the substrates are annealed all at once starting from 100 ºC as sequentially deposited and then heated up to 450 ºC for 30 min.

Deposition of control perovskite films

After the ozone treatment, substrates are transferred into a glove box filled with nitrogen (O_2<0.1 ppm, H_2O <0.1 ppm). The substrates are placed on a hot plate at 100 °C for 5 min before perovskite deposition. 50 µL perovskite solution is added and spin-coated quickly at 4000 rpm for 40 seconds. The wet films are then annealed at 75 ºC for roughly 10 s and then transferred to a different hot plate at 200 ºC for a 10 s fast crystallization.

Hole Transport Layer (HTM) deposition

50 µl spiro-OMeTAD solution is dynamic-deposited by spin coating at 4000 rpm for 20 seconds accelerating at 800 rpm/s depositing the solution after 3 s starting the program. Afterward, all the samples are transferred into a dry air box (RH <20%) for oxygen soaking overnight.

Deposition of metal contact

Gold is evaporated using a thermal evaporator under a vacuum of approximately 10^{-6} mbar. The deposition rate is programmed at 0.02 Å/s for the first 1 nm, 0.1-0.2 Å/s for the following 5 nm, then 0.5 Å/s until 20 nm and then 1Å/s for the rest of the deposition. Overall, it takes around 25 min for the deposition of 80 nm of gold.

7.2.3 Structural and Optical Characterization

Morphological analysis has been performed using the same SEM equipment from previous chapters 4 and 6. The crystalline structure is determined through XRD using a PANalytical Empyrean diffractometer with Cu Kα radiation (λ = 1.5406 Å), covering a Bragg angle range of 4–60° with a step size of 0.026°. UV-vis absorption measurements are conducted the same instrument from Chapters 4, 5 and 6. PL spectra have been obtained using a continuous-wave (CW) GaN laser (404 nm), with PL characterization carried out on an Edinburgh Instruments FLS 1000 spectrometer, which features a double-grating Czerny-Turner monochromator for both excitation and detection. The detection system, equipped with a high-speed photomultiplier tube (PMT) housed in a cooled environment, is used to record steady-state PL spectra. XPS measurements are conducted using a Thermo Scientific K-alpha system (base pressure $4x10^{-9}$ mbar), with photoelectrons excited by the Al K-α line (1486.6 eV) from a monochromatized X-ray source. Data have been collected at room temperature with a pass energy of 20 eV and a spot size of 400 µm.

7.2.4 Electrical Characterization

J-V curve measurements are performed under ambient conditions using an Ossila class AAA solar simulator and an automated J-V measurement system (T2003B3-G2009A1). The light intensity is calibrated to 1 sun (100 mW/cm^2) using a certified Si solar cell (RERA Solutions, RQN3290, RQN001). Measurements are conducted without encapsulation at approximately 30 °C and a relative humidity (RH) of less than 10%, with the active device area defined by a mask (0.026 cm^2).

The MPPT of the solar cells is evaluated in a nitrogen (N_2) atmosphere. The stability protocol involved recording an initial J-V curve to determine the maximum power point voltage (Vmax), which is then applied to the cell for one hour under continuous illumination. After each hour, a new J-V curve has been measured to update the Vmax, which is then applied for the subsequent hour. Solar cell parameters are monitored and recorded after each J-V measurement throughout the MPPT process. Indoor illumination conditions have been achieved using the same Ossila class AAA solar simulator, selecting the "Cool White" and "Warm White" LEDs from the software.

7.3 RESULTS

To fabricate γ-$CsPbI_3$ nanocomposite films, we employ a solution-based approach similar to that used in the previous chapters. The process begins with preparing a precursor solution containing CsI, PbI_2, and $Ni(AcO)_2$ dissolved in DMSO, which is subsequently spin-coated onto a substrate. After spin-coating, the film undergoes rapid annealing to facilitate the crystallization of γ-$CsPbI_3$. Figure 62 provides a schematic of the general synthesis process for the nanocomposite, illustrating the preparation of $CsPbI_3$ and highlighting the role of the $Ni(AcO)_2$ additive in promoting the crystallization of the perovskite nanocomposite.

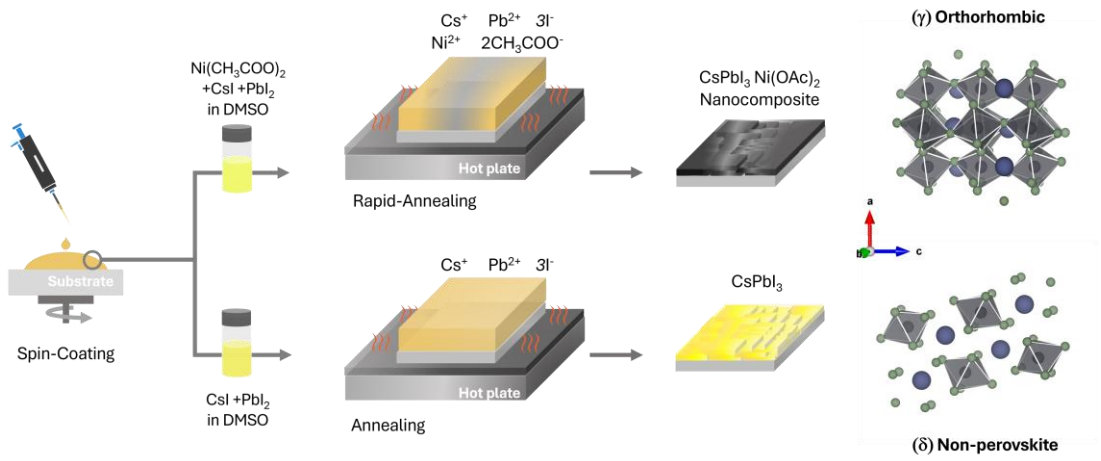

Figure 62. Synthetic approach for $CsPbI_3$ nanocomposites, emphasizing the impact of $Ni(AcO)_2$ doping on perovskite crystallization.

The effect of $Ni(AcO)_2$ concentration and annealing time on the optical properties of perovskite films is studied at an annealing temperature of 200ºC. The $CsPbI_3$ concentration is kept constant at 1.3 M for all conditions to ensure a consistent evaluation of the impact of varying nickel concentrations on the final layer properties. Annealing at 200ºC is selected due to the transition temperature for the formation of the γ-phase starting at 175ºC and to ensure the complete removal of DMSO, which has a boiling point of 189ºC. Figure 63a shows photographs of films with different $Ni(AcO)_2$ concentrations and annealing times at 200ºC.

Absorption measurements (Figure 63b) reveal that annealing times under 5 seconds (for a 0.1 M $Ni(AcO)_2$ concentration) result in inefficient conversion to the γ-phase, while annealing times exceeding 20 seconds lead to phase degradation from γ-$CsPbI_3$ to the non-perovskite yellow phase (δ-$CsPbI_3$), as shown by decreased absorption. With lower $Ni(AcO)_2$ concentrations (less than 0.1 M), incomplete transformation to γ-$CsPbI_3$ is observed, which is confirmed by XRD analysis (discussed in the next section). Based on these findings, we selected a set of conditions for the control and target samples. The control sample consists of pure 1.3 M $CsPbI_3$, and the target sample is a 0.1:1.3 M $CsPbI_3$:$Ni(AcO)_2$ nanocomposite. The optimal annealing conditions (OAC) for both samples are set at 200ºC for 10 seconds. A comparison of their optical properties is shown in Figure 63c. The control sample does not show PL, whereas the target sample exhibits a PL peak centered around 720 nm. The 0.1 M $Ni(AcO)_2$ concentration, corresponding to less than 10 wt.%, is identified

as the critical threshold for maintaining both crystallinity and optimal current densities (as shown in the J-V curves in Figure 69b). Beyond this threshold, current density significantly decreases, likely due to reduced charge carrier mobility caused by excessive nickel content. This excess nickel reduces grain interconnectivity, which impairs the suitability of the material for PV applications, as detailed in subsequent sections.

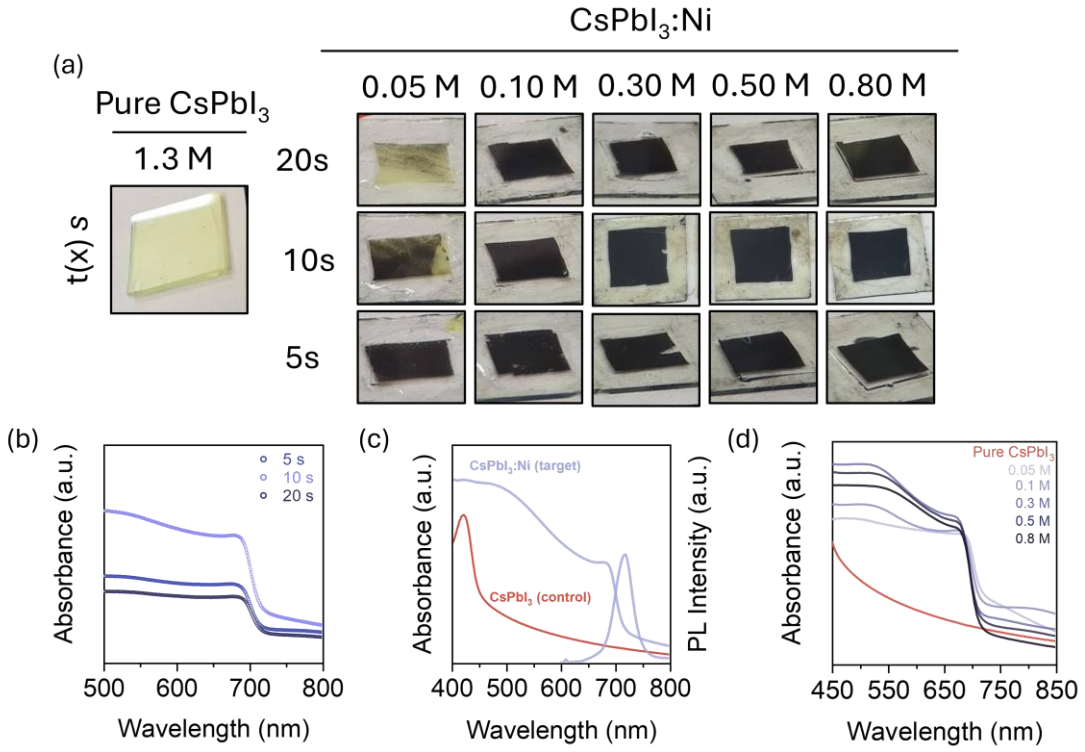

Figure 63. Impact of annealing time and concentration on $CsPbI_3$ films (a) Photographic images of pure undoped and $Ni(AcO)_2$ doped $CsPbI_3$ films annealed at 200 ºC at different times and for increasing Ni concentrations. (b) Annealing time dependency in absorbance spectra for the target concentration at OAC. (c) Absorbance and PL spectra comparison for the control and the target nanocomposite. (d) Nanocomposites absorbance spectra vs. $Ni(AcO)_2$ concentration at OAC.

Figure 63d displays the absorption measurements of the nanocomposite at different concentrations under the same annealing conditions. The bandgap of the $CsPbI_3$:$Ni(AcO)_2$ thin films (Table 9) is calculated from the absorption spectra shown in Figure 63d. To determine the bandgap, we have simulated the spectra near the band-edge of the absorption curve (Figure 64) according to Elliott's formula[230]:

$$\alpha(\hbar\omega) = P_{cv}\left[\Theta(\hbar\omega - E_g)\cdot\left(\frac{\pi e^{x}}{\sinh(\pi x)}\right) + R_{ex}\sum_{n=1}^{\infty}\left(\frac{4\pi}{n^3}\cdot\delta\left(\hbar\omega - E_g + \frac{R_{ex}}{n^2}\right)\right)\right] \quad 7$$

In this expression, $\hbar\omega$ is the photon energy, the term P_{cv} is a constant related to the transition matrix element, θ and δ are the Heaviside and Dirac delta functions, respectively, R_{ex} is the exciton binding energy, n is the principal quantum number and x is defined as $x = \sqrt{\frac{R_{ex}}{(\hbar\omega - E_g)}}$

The first and second terms correspond to the continuum and excitonic absorption band, respectively. Each of those terms are convolved with gaussian functions to account for inhomogeneous broadening.

Table 9. Concentration dependency for the bandgap of $CsPbI_3$ nanocomposites estimated by Elliot's Formula.

$Ni(AcO)_2$ (M)	Bandgap (eV)
0.05	1.703
0.1	1.704
0.3	1.719
0.5	1.731
0.8	1.732

The calculations reveal a clear trend in the absorption spectra, where increasing the concentration of $Ni(AcO)_2$ leads to a shift in the optical bandgap toward higher energies. We attribute these findings to the presence of significant random-disturbed microstrain across the perovskite grains.[231] This strain, indicated by the broadening of XRD peaks (discussed in the following section), plays a critical role in enhancing the stability of the γ-$CsPbI_3$ phase.

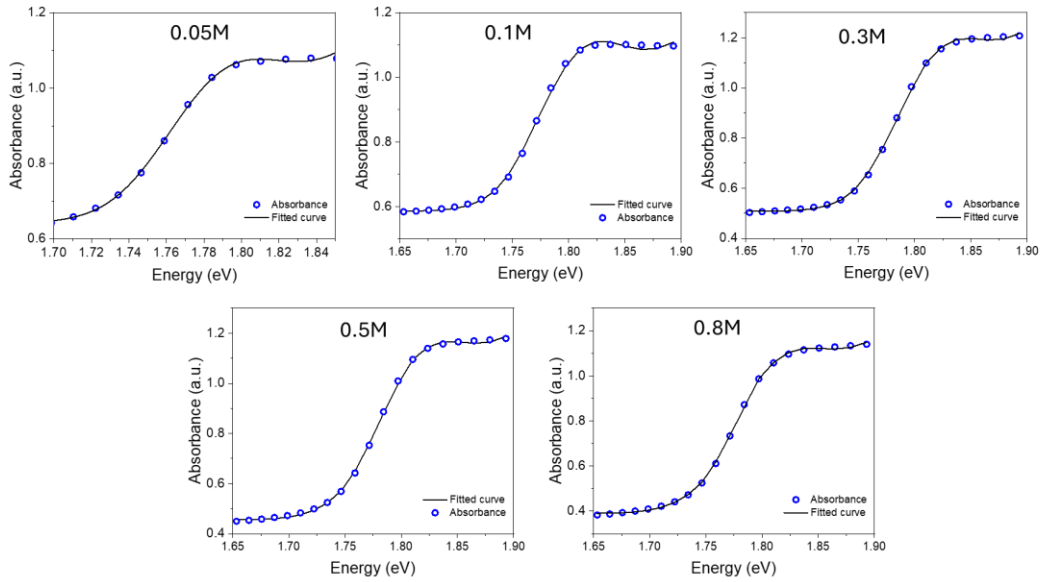

Figure 64. Absorbance spectra of the $CsPbI_3$-$Ni(AcO)_2$ nanocomposite thin-films and the fitting curve obtained by Elliott's formula.

To investigate the structural impact of incorporating varying concentrations of $Ni(AcO)_2$ into a 1.3 M $CsPbI_3$ perovskite precursor solution, we have performed XRD studies on the resulting nanocomposites. The XRD analysis is conducted at different annealing temperatures (using the OAC time of 10 s) and $Ni(AcO)_2$ concentrations to confirm the optimal formation of the γ-$CsPbI_3$ phase. The results are summarized in Figure 65.

XRD patterns, consistent with optical characterization results, confirm that the selected OAC maximizes the crystallinity of the γ-$CsPbI_3$ phase while avoiding the formation of the non-perovskite δ-phase (Figure 65a). Dominant diffraction peaks for the orthorhombic γ-phase appear at 14.3º, 20.8º, and 28.9º, corresponding to the (020), (002), and (202) crystal planes, respectively (ICSD nº 434338). Peaks characteristic of the δ-phase, observed at 13.1º, 26.5º, and 37.7º (associated with the (102), (105), and (020) planes; ICSD nº 250744), emerge only at annealing temperatures exceeding 200 ºC (Figure 65b). While higher annealing temperatures improve crystallinity and peak intensity, we identify 200 ºC as optimal, achieving the desired γ-phase without inducing a phase transition. SEM imaging corroborates these findings, showing larger grain morphology at 200 ºC, which enhances carrier mobility and device performance.[103]

Additionally, consistent with prior studies by Duan et al. (2022), we observe the transient presence of a 0D Cs_4PbI_6 intermediate phase during the annealing process. XRD patterns reveal discernible peaks for Cs_4PbI_6 at 11.9º and 28.6º at temperatures below 150 ºC, which disappear by 200 ºC (Figure 65c). This indicates that Cs_4PbI_6 serves as a template for the transformation to γ-$CsPbI_3$, fully disappearing at higher annealing temperatures. These findings align with our earlier results from Chapter 6, which demonstrates how acetate groups and waters of crystallization in the matrix facilitate bypassing this 0D intermediate phase, streamlining the crystallization process.

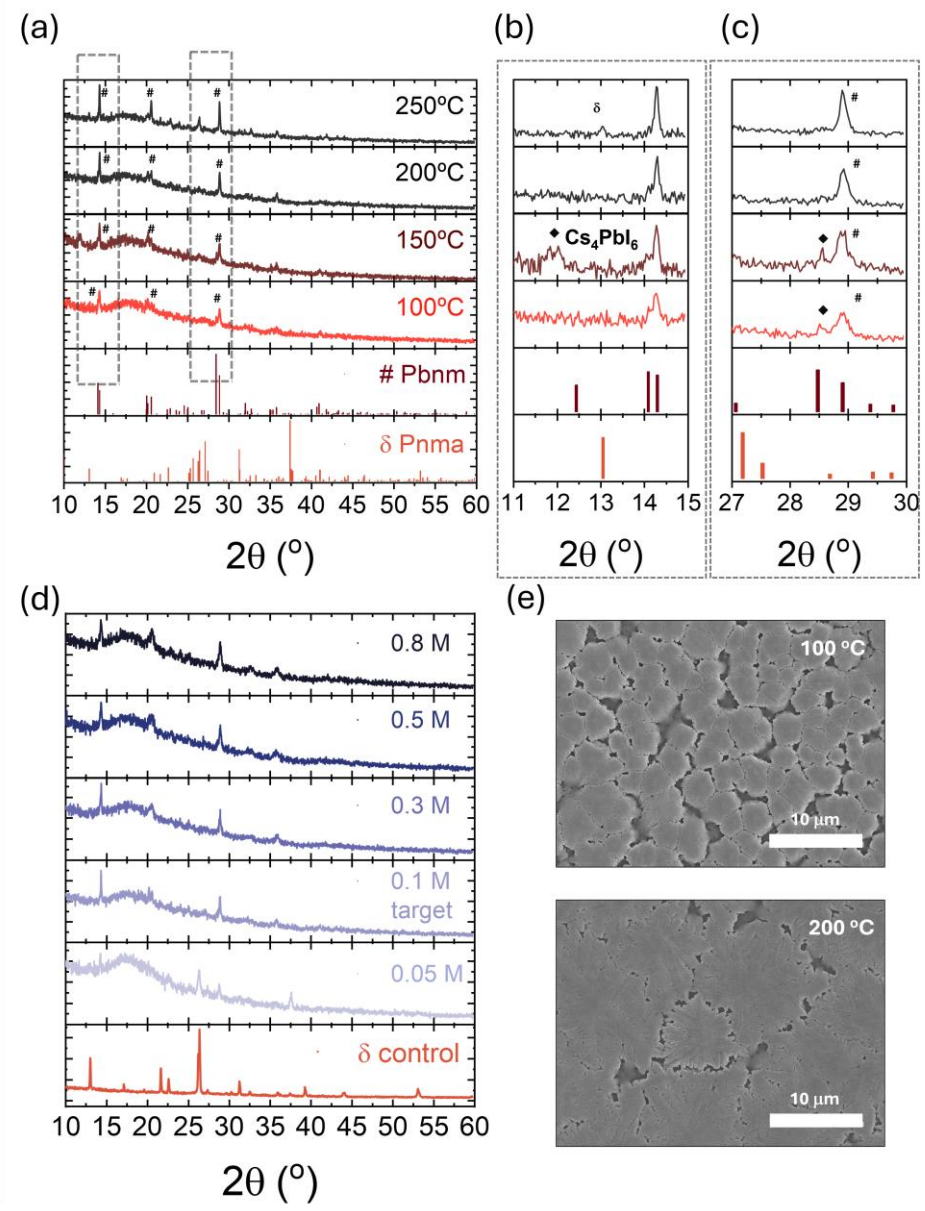

Figure 65. XRD patterns of $CsPbI_3$ nanocomposites. (a) Annealing temperatures impact on target's concentration for 10 s (b-c) insights at different angles from (a) and

(d) nickel acetate concentration at OAC. (e) SEM images of *target* nanocomposite at two different temperatures.

The effect of $Ni(AcO)_2$ concentration is another key factor to analyze. XRD patterns for samples prepared under OAC with $Ni(AcO)_2$ concentrations below 0.1 M reveal residual peaks associated with the δ-phase, indicating either incomplete phase transition or insufficient stabilization of the γ-$CsPbI_3$ phase (Figure 65d). These findings confirm that the formation and stabilization of the γ-$CsPbI_3$ phase depend not only on annealing temperature but also significantly on the $Ni(AcO)_2$ concentration in the $CsPbI_3$ precursor solution. At concentrations exceeding 0.1 M, the orthorhombic peaks exhibit increased intensity and sharper profiles, indicating enhanced crystallinity (Figure 65d). Additionally, partial substitution of Pb^{2+} ions (~120 pm) with smaller Ni^{2+} ions (~72 pm) causes contraction of the crystalline lattice, leading to a shift in the XRD peaks toward higher 2θ values. However, the absence of a substantial shift suggests that only a small fraction of Ni^{2+} ions occupy interstitial sites within the $CsPbI_3$ lattice.[232] This hypothesis is consistent with the structural stability trends observed.

To further analyze the structural effects, we evaluate peak broadening (Figure 66a) at different $Ni(AcO)_2$ concentrations using Williamson-Hall plots to calculate the crystallite size (D) and microstrain (ε) within the perovskite grains (Figure 66b). The results indicate that as $Ni(AcO)_2$ concentration increases, microstrain within the grains also rises, correlating with a slight reduction in grain domain size.[231] This finding aligns with the Elliott bandgap calculations, which show a shift toward higher energy levels as microstrain increases.

While higher $Ni(AcO)_2$ concentrations improve the stability of the orthorhombic phase, they also introduce excessive acetate, which hampers charge mobility within the lattice. This effect is evident in PV device studies (Figure 69b), where current density drops significantly with excessive nickel, ultimately compromising the nanocomposite's performance as a PV material.

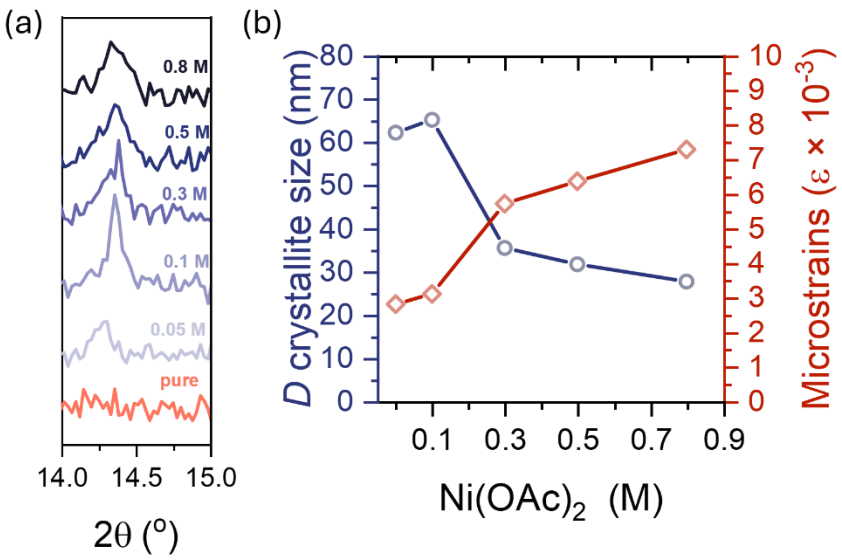

Figure 66. (a) XRD patterns of the control $CsPbI_3$ and samples with increasing concentrations of Ni $(AcO)_2$, highlighting the peak broadening at 14.3º. (b) Crystallite size (*D*) and Microstrain (ε) calculated from XRD data across various diffraction angles.

SEM images of the target $CsPbI_3$ films reveal a pronounced dependence on annealing temperature. SEM micrographs (Figure 65e) show significant microstructural differences when comparing films annealed at 100°C and 200°C. At 200°C, the films exhibit larger, more compact grains, in contrast to the smaller, less defined grains observed at 100°C. The reduced grain size at lower temperatures is attributed to incomplete chemical reactions or inefficient DMSO removal, both of which negatively impact the overall crystallinity of the perovskite layer. The larger and more compact grains formed at 200°C are advantageous for device performance, as they reduce grain boundary defects, minimize recombination centers, and enhance charge carrier mobility.[103]

Energy-dispersive X-ray (EDX) analysis (Figure 67) confirms the uniform distribution of $Ni(AcO)_2$ across the perovskite grains. Elemental mapping highlights the consistent presence of nickel throughout the grain structure without signs of aggregation or phase separation. This homogeneity suggests an effective incorporation of $Ni(AcO)_2$ across the perovskite grains during synthesis, which is essential for maintaining uniform electronic properties and ensuring reliable and reproducible device performance.

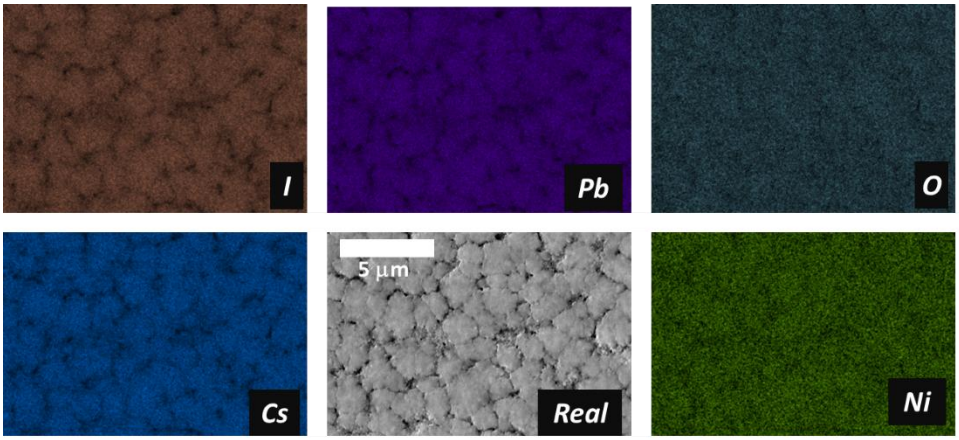

Figure 67. EDX Maps from SEM Images of the target $CsPbI_3$ nanocomposite.

XPS analysis has been performed to investigate how the lattice binding energy of $CsPbI_3$ varies with increasing $Ni(AcO)_2$ content (Figure 68). In the Cs 3d spectra of the control sample, two distinct peaks are observed at 723.5 eV and 737.2 eV, corresponding to the Cs $3d_{5/2}$ and Cs $3d_{3/2}$ binding energies, respectively. In the target sample, these peaks shift slightly to 723.99 eV and 737.95 eV. Similarly, the Pb 4f spectra for the control sample exhibit peaks at 137.94 eV and 142.81 eV, corresponding to Pb $4f_{7/2}$ and Pb $4f_{5/2}$, respectively, which shift to 137.61 eV and 142.49 eV in the target samples. The I 3d spectra show peaks at 618.89 eV and 630.37 eV for the control sample, while these shift to 618.41 eV and 629.90 eV in the target sample, corresponding to I $3d_{5/2}$ and I $3d_{3/2}$, respectively. Furthermore, the Ni 2p peaks detected in the target samples confirm the successful incorporation of $Ni(AcO)_2$ into the perovskite lattice.

As shown in Figure 68, the Cs 3d, Pb 4f, and I 3d peaks consistently shift to lower binding energies with the addition of $Ni(AcO)_2$. This shift is attributed to an increase in electron density on the surface of $CsPbI_3$, likely resulting from electron transfer from Ni atoms to the perovskite lattice. The increased surface charge density induced by $Ni(AcO)_2$ reduces the surface tension of $CsPbI_3$, thereby lowering the surface free energy.[218] This modification plays a pivotal role in stabilizing the γ-$CsPbI_3$ phase at relatively low annealing temperatures.

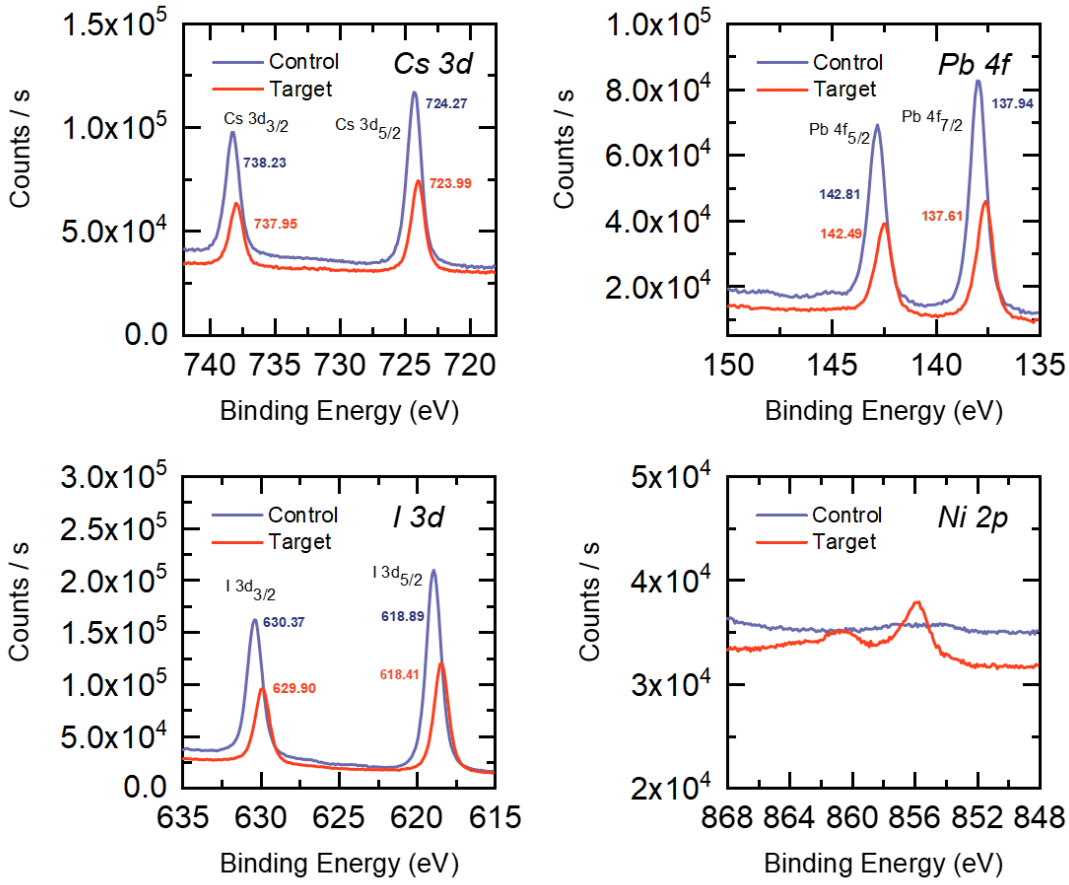

Figure 68. XPS Fittings for Cs 3d, Pb 4f, I 3d and Ni 2p cores for control and target $CsPbI_3$ nanocomposite films.

Our primary objective is to evaluate the device performance of $CsPbI_3$ nanocomposite films as PSCs, which is a bit challenging given the isolating nature of the $Ni(AcO)_2$. The studied PSCs feature a device architecture of FTO/c-TiO_2/m-TiO_2/perovskite/Spiro-OMeTAD/Au, as illustrated in Figure 69a. A cross-sectional view of the complete device stack is provided in Figure 70. Figure 69b presents statistical data of devices fabricated under varying conditions (10 each condition), with $Ni(AcO)_2$ concentrations ranging from 0.05 M to 0.8 M. The champion SC for the target $CsPbI_3$ nanocomposite achieves a Jsc of 17.6 mA/cm², an Voc of 1.03 V, and a FF of 68.13%, corresponding to a PCE of 12.43%. The J-V curve and statistical data are shown in Figure 69c.

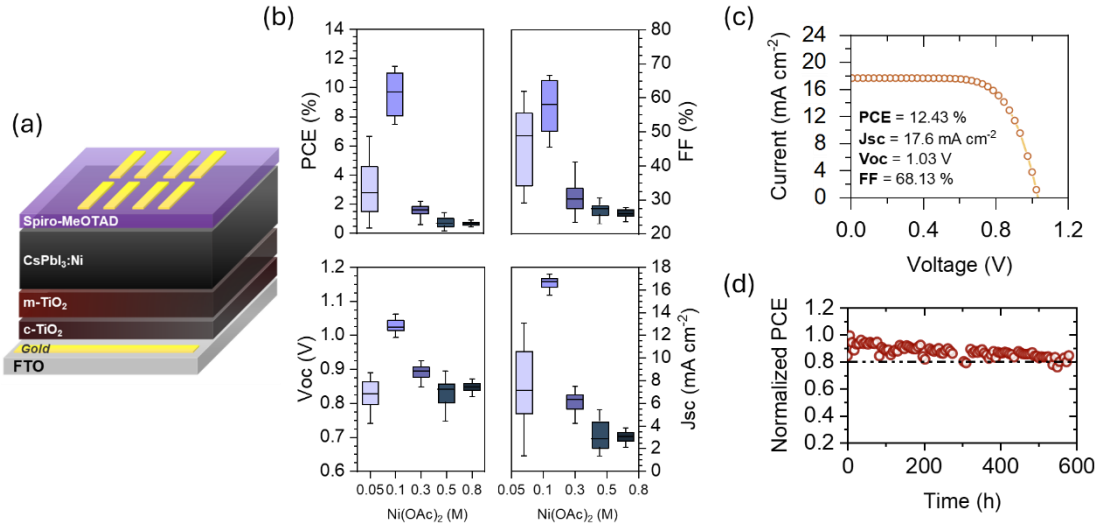

Figure 69. (a) Device structure: FTO/c-TiO_2/m-TiO_2/$CsPbI_3$/Spiro-OMeTAD/Au. (b) Statistical data of devices with different $CsPbI_3$:Ni ratios. (c) J-V curve of the champion device. (d) Light stability test on unencapsulated devices under N_2 conditions, with constant 1-sun illumination at 30 ºC.

Device performance exhibits a volcano-shaped dependency on additive concentration. An optimal concentration of 0.1 M is associated with the highest current density, in agreement with XRD results. At $Ni(AcO)_2$ concentrations below 0.1 M, the coexistence of both perovskite and non-perovskite phases is observed, impeding effective charge transport within the absorber and resulting in suboptimal electrical performance. Conversely, higher concentrations of $Ni(AcO)_2$ lead to a significant decline in current density, attributed to its insulating nature, which disrupts grain connectivity. This observation aligns with previous studies showing that excess $Ni(AcO)_2$ can act as a matrix separating perovskite grains, compromising electrical interconnection.[145]

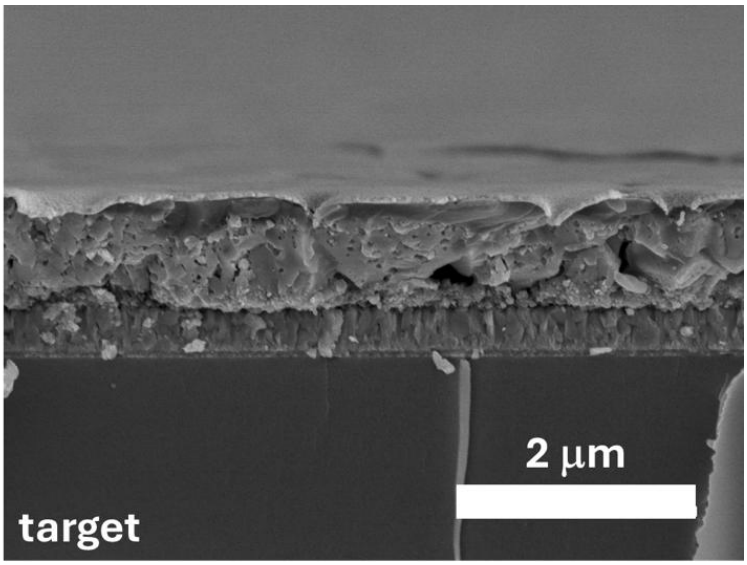

Figure 70. Cross-Sectional Image of one of the best-performing devices using the target conditions for the nanocomposite fabrication.

To gain deeper insights into the dominant recombination mechanisms affecting device performance, we analyze the ideality factor (n_{id}) of the solar cells. The ideality factor is derived from the relationship between the Voc and light intensity, as shown in Figure 71.[233]

The fitted ideality factor for the $CsPbI_3$:$Ni(AcO)_2$ solar cell is 1.76, suggesting that Shockley-Read-Hall (SRH) recombination within the bulk is the primary loss mechanism. This observation aligns with findings reported in previous studies on $CsPbI_3$-based solar cells.[233–235] Such recombination behavior highlights the need for strategies to mitigate bulk defects, which could further improve the performance and stability of these devices.

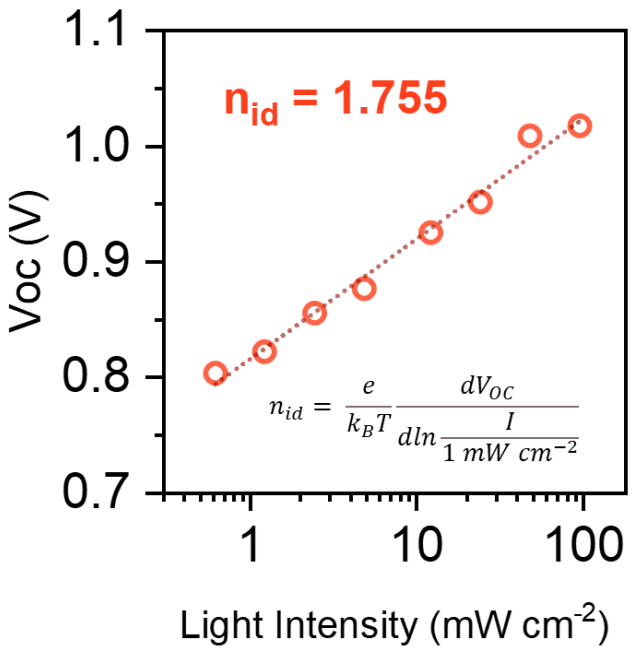

Figure 71. Light intensity dependence of J-V characteristics of the target PSC fo the open-circuit voltage V_{oc} parameter and extracted ideality factor.

Moreover, we conducted stability tests on unencapsulated devices under ambient conditions in an inert nitrogen atmosphere with continuous 1-sun illumination. The target $CsPbI_3$-based device retains approximately 80% of its initial efficiency after 600 hours of light exposure, measured at a fixed voltage near the MPPT (Figure 69d).

7.3.1 Indoor Studies

The increasing demand for efficient energy-harvesting systems to power indoor electronic devices has driven substantial interest in indoor PV. Unlike natural sunlight, indoor lighting possesses unique spectral characteristics, requiring specialized PV materials optimized for artificial illumination. By adapting the Shockley-Queisser limit to varying irradiation spectra, the maximum theoretical efficiency under specific light conditions can be determined.[98] Remarkably, this efficiency limit increases from 33% under solar illumination to 57% under indoor lighting conditions.[236]

Indoor light sources, such as warm white and cool white illumination (Figure 72a), achieve peak efficiencies with semiconductor materials having bandgaps between 1.7 and 1.8 eV (Figure 72b), contrasting with the optimal 1.4 eV bandgap for

solar illumination. $CsPbI_3$ perovskite, with an ideal bandgap of approximately 1.72 eV, stands out as a promising material for indoor PV applications.

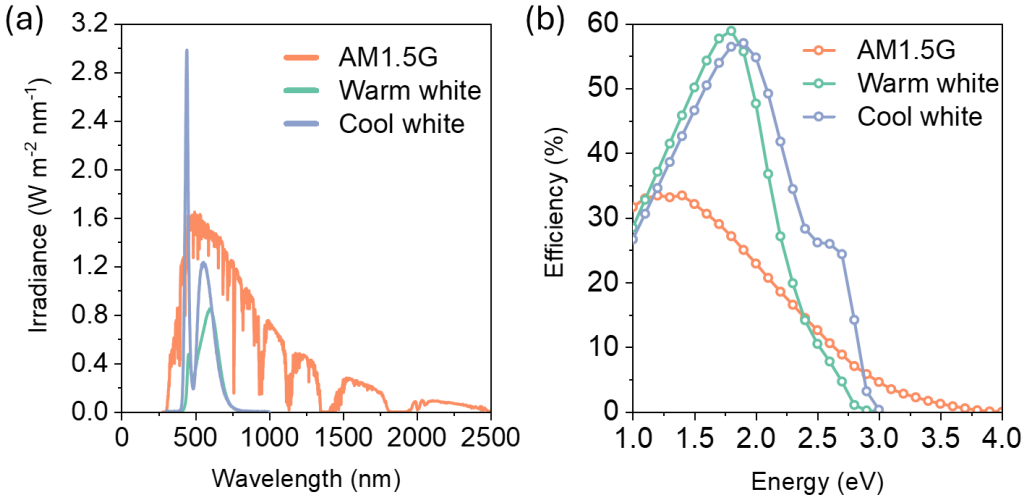

Figure 72. Irradiance of AM1.5G solar spectrum, warm white and cool white illuminations used in the experiments (left). Maximum efficiencies calculated according to Shockley-Queisser limit for the different illuminations (right).

To assess this potential, performance measurements are conducted on the target $CsPbI_3$:$Ni(AcO)_2$ solar cell under both cool white and warm white lighting. The device achieves notable efficiencies of 15.4% under cool white lighting and 17.6% under warm white lighting. Detailed statistics and J-V curves for indoor measurements are presented in Table 10. These results confirm the suitability of all-inorganic $CsPbI_3$-based perovskites for indoor applications, demonstrating a strong correlation with theoretical efficiency predictions.

Table 10. Performance statistics derived from J-V curves for the target condition under various indoor lighting conditions.

Condition	PCE (%)	FF (%)	J_{sc} (mA cm^{-2})	V_{oc} (V)
1 Sun 100 mW cm^{-2}	10.0	70	14.2	1.02
Cool White 23 mW cm^{-2}	15.4	71	5.3	0.96
Warm White 13 mW cm^{-2}	17.6	76	3.2	0.94

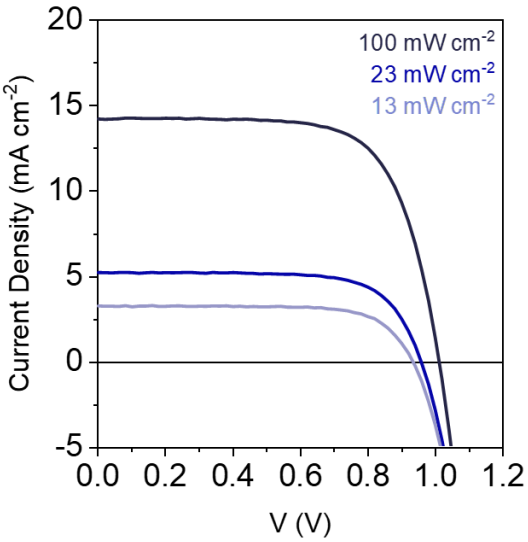

7.3.2 LCA

The environmental impacts associated with the synthesis and deposition of $CsPbI_3$ with nickel acetate are evaluated using the LCA methodology, following EN-ISO standards (14040/14044) and IEA PVPS guidelines.[237] This analysis is compared to the synthesis and deposition of $CsPbI_3$ using DMAI.[238] The functional unit for both methods is 1 cm^2. The evaluation focuses solely on the absorber layer in the indoor solar cell, excluding transport layers, electrodes, and substrates, which are identical for both methods. Life cycle inventories include raw materials, energy consumption for heating, annealing, and spin coating, air emissions, and treatment of spin-coating wastes. Detailed inventories and impact evaluations using the method Environmental Footprint (EF) 3.0[239] are provided in the Appendixes of this chapter.

The addition of nickel acetate to the $CsPbI_3$ precursor simplifies the process by eliminating substances such as DMAI, MACl, OAI, and TOPO, reducing spin coating steps from four to one. This modification shortens precursor formation heating times and lowers annealing times and temperatures. Energy consumption with DMAI is 2.6 times higher than with nickel acetate. However, the $Ni(AcO)_2$ method slightly increases metal usage (ratio of 0.8) due to higher consumption of nickel, lead, and cesium. Relative differences between the two methods are illustrated in Figure 73a.

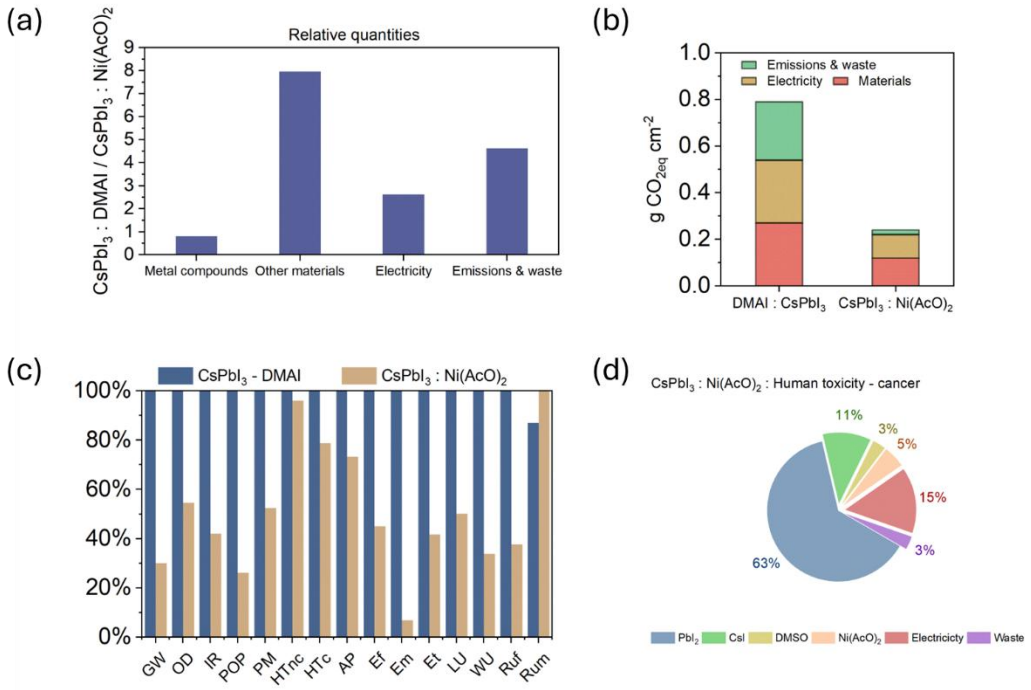

Figure 73. a) Relative quantities of materials, energy and wastes for 1 cm^2 of $CsPbI_3$ synthesized with DMAI respect the one synthesized with $Ni(Ac)_2{\cdot}4H_2O$. b) Comparison of absolute climate change impacts broken down in materials, electricity and emissions and waste. c) Relative impacts for the two methods to synthesize $CsPbI_3$ (absolute values and meaning of the abbreviations are in the Table 20**)**. d) Breakdown of the potential human toxicity-cancer impact for $CsPbI_3$ obtained with nickel acetate tetrahydrate and whose contribution is only 5% of the total.

This reduction in materials and energy usage significantly lowers the climate change impact, as shown in Figure 73b. It also decreases waste, which in spin coating accounts for 98% of the initial mass and has a high global warming impact due to incineration of organic-rich waste liquids. Reductions in the carbon footprint are 57%, 62%, and 93% for materials, electricity, and waste, respectively, yielding an overall reduction of 70%.

Environmental impact reductions are not limited to the climate change category but extend to most impact categories (Figure 73c), with an average reduction of 52%. The only exception is mineral resource and metal use (Rum), which slightly increases due to higher metal consumption. The impacts considered are cradle-to-gate, but greater stability and efficiency achieved with the new method could further reduce the environmental impact over the product's life cycle.

Human toxicity impacts are also lower with the nickel acetate method, though less pronounced. Reductions of 4% and 21% are observed in non-carcinogenic (HTnc) and carcinogenic human toxicity (HTc) categories, respectively. Key contributors to HTc impacts include PbI_2 synthesis (63%), energy consumption during deposition (15%), and CsI synthesis (11%) (Figure 73d). Nickel acetate tetrahydrate contributes minimally, accounting for only 5% of HTc and 2% of HTnc impacts.

Finally, the study also considers properties of concern based on harmonized classification and labeling (CLH) and the CLP regulation (EC No. 1272/2008). Lead iodide, classified as "toxic for reproduction" (CLH), is a common concern in both methods. The method with DMAI also includes DMF, “toxic for reproduction” (CLH) and included in “the candidate list of substances of very high concern” (SVHC); toluene, “suspected to be toxic for reproduction” (CLH); and TOPO, “most of the data submitters agree that this substance is a skin sensitizer” (CLP). In the nickel acetate method, these three substances are not included, although a new substance with properties of concern, $Ni(AcO)_2.4H_2O$, is added, “most data submitters agree that this substance is a skin sensitizer and a respiratory sensitizer” (CLP).

7.4 CONCLUSIONS

Our synthetic approach provides a rapid-crystallization (<10 s), low-temperature (<250°C), and environmentally friendly (antisolvent- and DMF-free) method to enhance the performance of $CsPbI_3$ perovskite solar cells (PSCs). Using this strategy, the champion device, incorporating 7.7 mol% $Ni(AcO)_2$, achieves a PCE exceeding 12% in an n-i-p mesoscopic configuration with a stability of over 600 hours at maximum power point tracking (MPPT) and minimal performance loss (<20%). Furthermore, under cool and warm white illumination, the devices demonstrate promising efficiencies exceeding 15% and 17%, respectively, showcasing the potential of $Ni(AcO)_2$-$CsPbI_3$ PSCs for efficient energy harvesting in indoor environments.

In addition to performance improvements, the new synthesis method employing nickel acetate tetrahydrate significantly reduces environmental impact. The method achieves a 70% reduction in greenhouse gas emissions (GW) and reductions across most impact categories. While the addition of $Ni(AcO)_2{\cdot}4H_2O$ introduces potential risks as a skin and respiratory sensitizer, its contribution to human toxicity categories

is minimal compared to the substantial impacts of lead iodide. Importantly, our DMSO-only, DMA/HI-free synthesis eliminates the need for substances with concerning properties, such as DMF, toluene, and TOPO.

Despite these advances, the persistence of hazardous materials, including $Ni(AcO)_2 \cdot 4H_2O$ and PbI_2, in the absorber layer warrants careful consideration. Nonetheless, we believe this straightforward, DMSO-only, and antisolvent-free approach represents a significant step toward the development of highly efficient, stable, and environmentally conscious all-inorganic perovskite materials for PV applications.

7.5 APPENDIXES

Life Cycle Assessment Appendixes

This study encompasses the environmental impacts associated with the production of raw materials, the synthesis of $CsPbI_3$ perovskite, its deposition, and the annealing process. It also accounts for emissions, wastewater treatment, and the management of waste generated during the synthesis, deposition, and annealing of $CsPbI_3$ on glass substrates. The $CsPbI_3$ perovskite is synthesized using the DMAI and $Ni(AcO)_2$ methods, as outlined in Table 11 and Table 12, respectively. The quantities of precursors and solvents are calculated based on the amount required to produce $CsPbI_3$ for a single solar cell.

Environmental data from Ecoinvent 3.8 is utilized for the LCA, where available. For PbI_2, inventory data is adapted from the literature.[240] Specific inventories developed for this research are detailed in Table 13-19.

Electricity consumption during synthesis, deposition, and annealing is monitored using a CIRCUTOR MYeBOX 1500 Network Analyzer. Measurements are taken at one-second intervals with a sampling rate of 2 kHz. The synthesis and annealing steps are monitored using an IKA C-MAG HS 7 hotplate and a Harry Gestigkeit Präzitherm PZ28-2 heating mantle, respectively. Energy consumption for deposition is measured using a Laurel WS-650-23 Spin Coater paired with a VWR VP 100 C vacuum pump. Two clamps with a measurement range of 0.05 to 5 A are used, providing an accuracy of 0.2% for current intensity and ±0.5% or 1 W for power. Measurements were conducted under the maximum operational capacity of each device and experimental

conditions. In cases where direct measurement of electricity consumption is not feasible, thermodynamic equations are applied for estimation.[241]

Life cycle inventories (LCI) for spin coating waste are assumed to undergo incineration, with the resulting slags being disposed of in landfills. These processes were modeled using Doka[242] tools and subsequently integrated into SimaPro software to evaluate the environmental impacts associated with these end-of-life scenarios.

Environmental impacts are assessed using the Environmental Footprint 3.0 method, with the results presented in Table 20.

Inventory for $CsPbI_3$ Perovskite Synthesis Using the DMAI Method

To fabricate a $CsPbI_3$ perovskite cell using the DMAI method, a solution of perovskite precursors is spin-coated onto a pre-heated substrate. Subsequently, an MACl solution is spin-coated over the perovskite layer, followed by an annealing process. An OAI solution is then applied via spin coating, with annealing performed afterward. Finally, a TOPO solution is deposited by spin coating as the top layer, without any additional annealing step.

Table 11. Inventory for the synthesis of $CsPbI_3$ with the DMAI method.

Functional unit	**1**	**cm²**		**$CsPbI_3$ - DMAI**
	Step	**Flow**	**Unit**	**Quantity**
Input	Perovskite solution preparation	PbI_2	g	0.0059
		DMF	g	0.0115
		CsI	g	0.0029
		DMAI	g	0.0020
	MACl solution preparation	MACl	g	0.0002
		IPA	g	0.0439
	OAI solution preparation	OAI	g	0.0000
		IPA	g	0.0126
	TOPO solution preparation	TOPO	g	0.0002
		Toluene	g	0.0277
	Solutions preparation	Electricity	J	697.9
	Deposition	Electricity	J	1947.2
	Annealing of $CsPbI_3$	Electricity	J	47.3
	Annealing of $CsPbI_3$ - OAI	Electricity	J	71.6
Output	Deposition	Waste	g	0.1047
	Annealing	Emission to air, DMF	g	0.0002
		Emission to air, IPA	g	0.0011

Inventory for $CsPbI_3$ Perovskite Synthesis Using the $Ni(AcO)_2 \cdot 4H_2O$ Method

In the fabrication of a $CsPbI_3$ perovskite cell using the $Ni(AcO)_2 \cdot 4H_2O$ method, a solution of perovskite precursors is spin-coated onto a pre-heated substrate. The deposited layer is then subjected to a two-step annealing process.

Table 12. Inventory for the synthesis of $CsPbI_3$ with the $Ni(AcO)_2$ method.

Functional unit		**1**	**cm^2**		**$CsPbI_3$:$Ni(AcO)_2$**
	Step		**Flow**	**Unit**	**Quantity**
Input	Perovskite solution preparation		PbI_2	g	0.0061
			CsI	g	0.0044
			DMSO	g	0.0123
			$Ni(AcO)_2 \cdot 4H_2O$	g	0.0003
	Solution preparation		Electricity	J	84.5
	Deposition		Electricity	J	958.7
	Annealing		Electricity	J	8.6
Output	Deposition		Waste	g	0.0227
	Annealing		Emission to air, DMSO	g	0.0002

Inventory for Octylammonium Iodide (OAI) Production

The production inventory for OAI is derived from the reaction between hydroiodic acid and octylamine, achieving a yield of 76%.[243] Hydroiodic acid is synthesized in situ using formic acid and iodine in ethanol, with carbon dioxide (CO_2) generated as a by-product. The reaction mixture is stirred at 80 °C for 2 hours. Ethanol is utilized for crystallization, while diethyl ether is employed for purification. Recovery rates are assumed to be 95% for ethanol and 90% for diethyl ether, accounting for losses to the air during processing.

Table 13. Inventory for production of 1 kg of OAI.

Functional Unit	**1**	**kg**	**OAI**
	Flow	**Unit**	**Quantity**
Input	Iodine	kg	0.5087
	Formic acid	kg	0.0895
	Octylamine	kg	0.6736
	Ethanol	kg	0.2544
	Diethyl ether	kg	0.0688
	Chemical plant	p	0.0000
	Electricity	MJ	7.4096
Output	Emission to air, carbon dioxide	kg	0.0856
	Emission to air, ethanol	kg	0.2544
	Emission to air, diethyl ether	kg	0.0688
	Waste	kg	0.1863

Inventory for Octylamine (OA) Production

OA is synthesized through the amination of octanoic acid with ammonia at 200 °C for 7 hours, followed by hydrogenation of the resulting amide at 200 °C for 6.5 hours, achieving a yield of 76%.[244] Cyclopentyl methyl ether is used as the solvent, and a ruthenium–tungsten oxide catalyst facilitated the reaction. For the life cycle assessment, methyl tert-butyl ether and crude tall oil were used as proxies for cyclopentyl methyl ether and octanoic acid, respectively.

Table 14. Inventory for production of 1 kg of OA.

Functional Unit	**1**	**kg**	**OA**
	Flow	**Unit**	**Quantity**
Input	Octanoic Acid	kg	1.4682
	Ammonia	kg	0.1734
	Hydrogen	kg	0.0410
	Ru-WO_x catalyst	kg	0.0235
	Cyclopentyl methyl ether	kg	0.0876
	Chemical plant	p	4.00E-10
	Electricity	kWh	0.6295
Output	Emission to air, water	kg	0.2788
	Residues	kg	0.4038

Inventory for Ruthenium-Tungsten Oxide (Ru-WO_x) Catalyst Production

The inventory for the ruthenium-tungsten oxide (Ru-WO_x) catalyst is based on the reaction of ruthenium chloride, magnesium aluminate, and tungsten oxide.[245] Precursors included tungsten oxide,[246] ruthenium, chlorine, magnesium oxide, and alumina.

Table 15. Inventory for production of 1 kg of Ruthenium-Tungsten Oxide (Ru-WO_x) Catalyst.

Functional Unit	**1**	**kg**	**Ru-WO_x catalyst**
	Flow	**Unit**	**Quantity**
Input	Tungsten oxide	kg	0.0126
	Ruthenium	kg	0.0400
	Chlorine	kg	0.0421
	Magnesium oxide	kg	0.2565
	Aluminum oxide	kg	0.6488
	Chemical plant	p	4.00E-10
	Electricity	kWh	0.5149

Inventory for Dimethylammonium Iodide (DMAI) Production

The production inventory for DMAI is established based on the reaction between hydroiodic acid and dimethylamine, achieving a yield of 88%.[243] Hydroiodic acid is synthesized in situ from formic acid and iodine in ethanol, with carbon dioxide (CO_2) as a by-product. The reaction is conducted at 80 °C for 1 hour with constant stirring. Ethanol is employed for crystallization, and diethyl ether is used for purification. Recovery rates are estimated at 95% for ethanol and 90% for diethyl ether, accounting for losses to the atmosphere.

Table 16. Inventory for production of 1 kg of DMAI.

Functional Unit	**1**	**kg**	**DMAI**
	Flow	**Unit**	**Quantity**
Input	Iodine	kg	0.7562
	Formic acid	kg	0.1330
	Dimethylamine	kg	0.3492
	Ethanol	kg	0.3781
	Diethyl ether	kg	0.0481
	Chemical plant	p	4E-10
	Electricity	MJ	10.7424
Output	Emission to air, Carbon dioxide	kg	0.1272
	Emission to air, Diethyl ether	kg	0.0481
	Emission to air, ethanol	kg	0.3781
	Wastewater	kg	0.1113

Inventory for Dimethylamine (DMA) Production

The production inventory for DMA is based on its synthesis through the reaction of methanol with ammonia, achieving a yield of 59.6%. The reaction is conducted at 400 °C and 14.52 atm for 20 hours, using zeolite powder as a catalyst. By-products included methylammonium (36.4%), trimethylammonium (3.9%), and water. Residual materials from the reaction are treated as wastewater.

Table 17. Inventory for production of 1 kg of DMA.

Functional unit	**1**	**kg**	**DMAI**
	Flow	**Unit**	**Quantity**
Input	CH_3OH	kg	1.3398
	NH_3	kg	0.4542
	Catalyst: Zeolite	kg	0.0098
	Electricity	MJ	11.8253
Output	Wastewater	kg	0.7631

Inventory for Nickel Acetate Tetrahydrate ($Ni(AcO)_2 \cdot 4H_2O$) Production

The production inventory for nickel acetate tetrahydrate ($Ni(AcO)_2 \cdot 4H_2O$) is based on the reaction between nickel sulfate heptahydrate and acetic acid. The reaction generates sulfuric acid and water as by-products, with sulfuric acid considered an avoided product. Residual materials from the reaction are managed as wastewater.

Table 18. Inventory for production of 1 kg of Nickel Acetate tetrahydrate.

Functional unit	**1**	**kg**	**$Ni(AcO)_2 \cdot 4H_2O$**
	Flow	**Unit**	**Quantity**
Input	CH_3COOH	kg	0.4826
	$NiSO_4 \cdot 7H_2O$	kg	1.1285
	Electricity	MJ	0.6176
Output	H_2SO_4	kg	0.3941
	H_2O	kg	0.2172

Inventory for Methylammonium Chloride (MACl) Production

The production inventory for MACl is derived from the reaction between methylamine and hydrochloric acid, with ethanol serving as the solvent.

Table 19. Inventory for production of 1 kg of methylammonium chloride.

Functional unit	**1**	**kg**	**MACl**
	Flow	**Unit**	**Quantity**
Input	Methylamine	kg	0.4600
	HCl 30%	kg	0.5400
	Ethanol	kg	0.0619
	Chemical plant	p	4.00E-10
	Electricity	MJ	6.3682
Output	Emission to air, Water	kg	0.0017
	Emission to air, Ethanol	kg	0.0619
	Emission to water, Water	kg	1.2583

Environmental Impacts

The results of the comparative life cycle assessment (LCA) for the synthesis and deposition of 1 cm² of $CsPbI_3$ are presented in Table S11. All impact categories from the EF 3.0 method are considered, except for ecotoxicity,[247] due to significant discrepancies with the USETox method.[248]

Table 20. Results of the environmental impacts with the method EF 3.0 from cradle to gate for 1 cm^2 of $CsPI_3$ synthesized with DMAI and $Ni(AcO)_2$.

Impact categorý	**Unit**		**$CsPbI_3$ - DMAI**	**$CsPbI_3$ $Ni(AcO)_2$**
Climate change	kg CO_2 eq	GW	7.98E-04	2.39E-04
Ozone depletion	kg CFC11 eq	OD	2.03E-11	1.11E-11
Ionising radiation	kBq U-235 eq	IR	2.02E-04	8.49E-05
Photochemical ozone formation	kg NMVOC eq	POP	2.69E-06	7.03E-07
Particulate matter	disease inc.	PM	1.65E-11	8.65E-12
Human toxicity, non-cancer	CTUh	HTnc	1.60E-11	1.54E-11
Human toxicity, cancer	CTUh	HTc	2.67E-13	2.11E-13
Acidification	mol H^+ eq	AP	3.32E-06	2.43E-06
Eutrophication, freshwater	kg P eq	Ef	3.04E-07	1.37E-07
Eutrophication, marine	kg N eq	Em	2.78E-06	1.92E-07
Eutrophication, terrestrial	mol N eq	Et	4.60E-06	1.91E-06
Land use	Pt	LU	1.44E-03	7.20E-04
Water use	m^3 depriv.	WU	8.18E-03	2.77E-03
Resource use, fossils	MJ	Ruf	1.11E-02	4.17E-03
Resource use, minerals and metals	kg Sb eq	Rum	9.51E-09	1.09E-08

Chapter 8: Conclusions

This Thesis, titled *"Synthesis and Characterization of Multifunctional Nanocomposite-Based Materials for Next-Generation Energy Solutions"*, explores the development of innovative nanocomposite-based materials as a cornerstone for addressing critical challenges in energy technologies. The research highlights the immense potential of these materials in enabling the formation of perovskite structures, paving the way for advancements in crystallization dynamics in perovskite-based materials, scalable emission technologies, and PVs.

The overarching objective of this work is to synthesize and characterize novel nanocomposite systems that combine scalability, cost-effectiveness, and enhanced stability. Central to this Thesis is the investigation of key synthetic methodologies, offering insights into the formation, stabilization, and processability of nanocomposites. Emphasis is placed on strategies to improve material robustness and compatibility with device fabrication processes. Furthermore, to ensure the practical relevance of the findings, many of the synthetic approaches have been validated through integration into functional devices, such as PSCs (**Chapter 7**).

In summary, the work from **Chapter 4** introduces a streamlined, rapid, and cost-efficient methodology for the in situ synthesis of PNCs embedded within a metal-organic matrix, yielding nanocomposite thin films with exceptional optical properties and remarkable stability. Achieving PLQY as high as 80% and durability exceeding one year, the method stands out for its annealing-free nature, producing uniform thin films with notable resistance to mechanical wear. By fine-tuning the precursor loading in the final thin film, precise control over crystallization dynamics is achieved, enabling tunable crystal sizes. Furthermore, the size of PNCs can be effectively modulated by exposure to varying RH conditions, with both PL and absorption spectra showing diverse responses to moisture levels. This phenomenon is furhter studied in **Chapter 6** and attributed to aggregation effects that influence the resulting PNC size. This nanocomposite synthesis approach lays a robust foundation for the advancement of large-area optoelectronic devices with superior functionality. It offers a viable route for direct band-gap tuning through precise manipulation of PNC crystallization

dynamics, highlighting its potential for integration into next-generation optoelectronic applications.

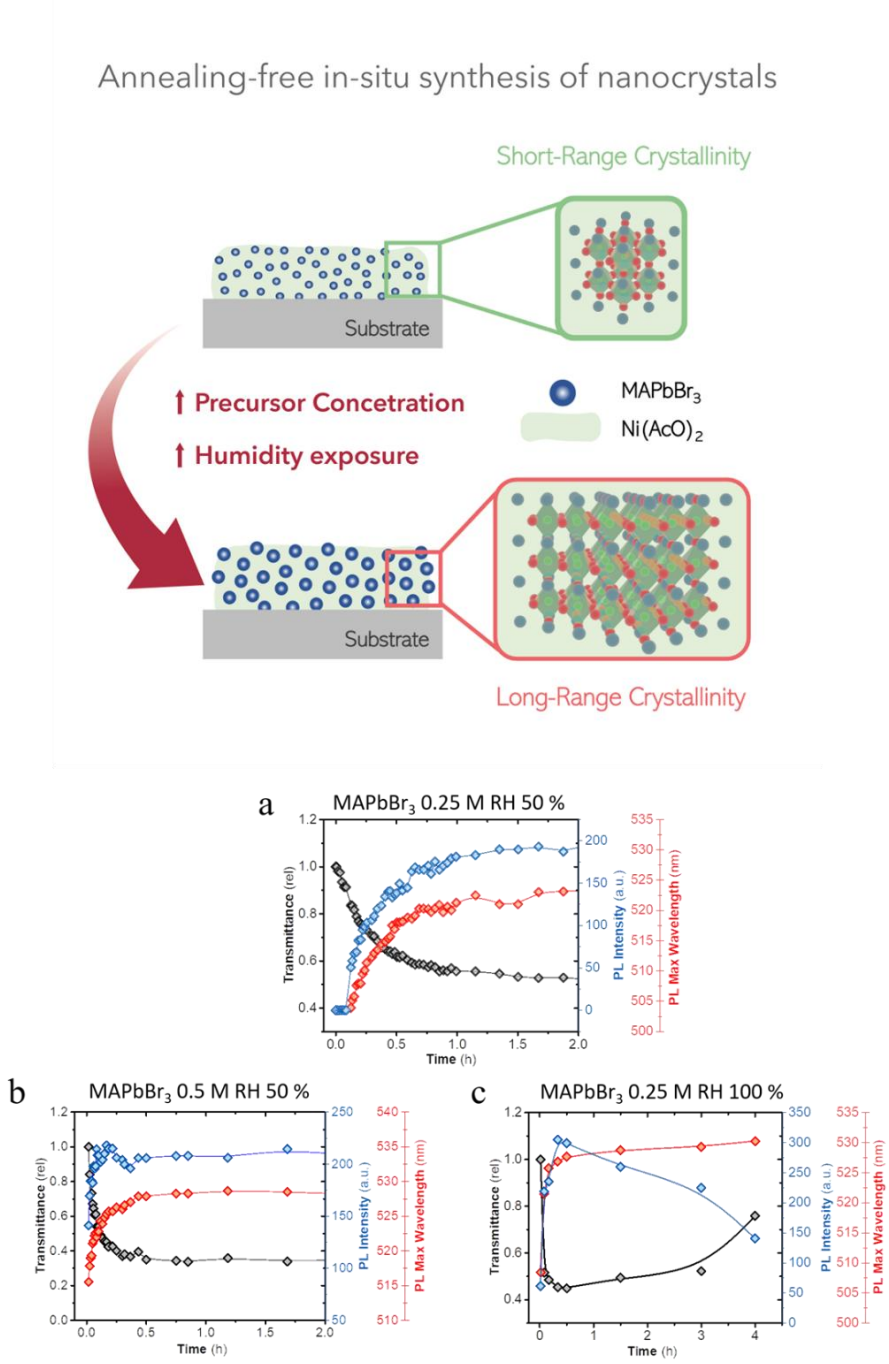

Figure 74. Summary and highlights of the main findings from Chapter 4.

In the work of **Chapter 5** a comprehensive protocol is designed to offer deeper insights into the crystallization dynamics of PNCs and the broad potential of this synthesis technique. A critical aspect of this exploration involves the development and utilization of specialized humidity-controlled chambers, a key strategy for ensuring

precise control over the final PNC properties and fully exploiting the versatility of this approach.

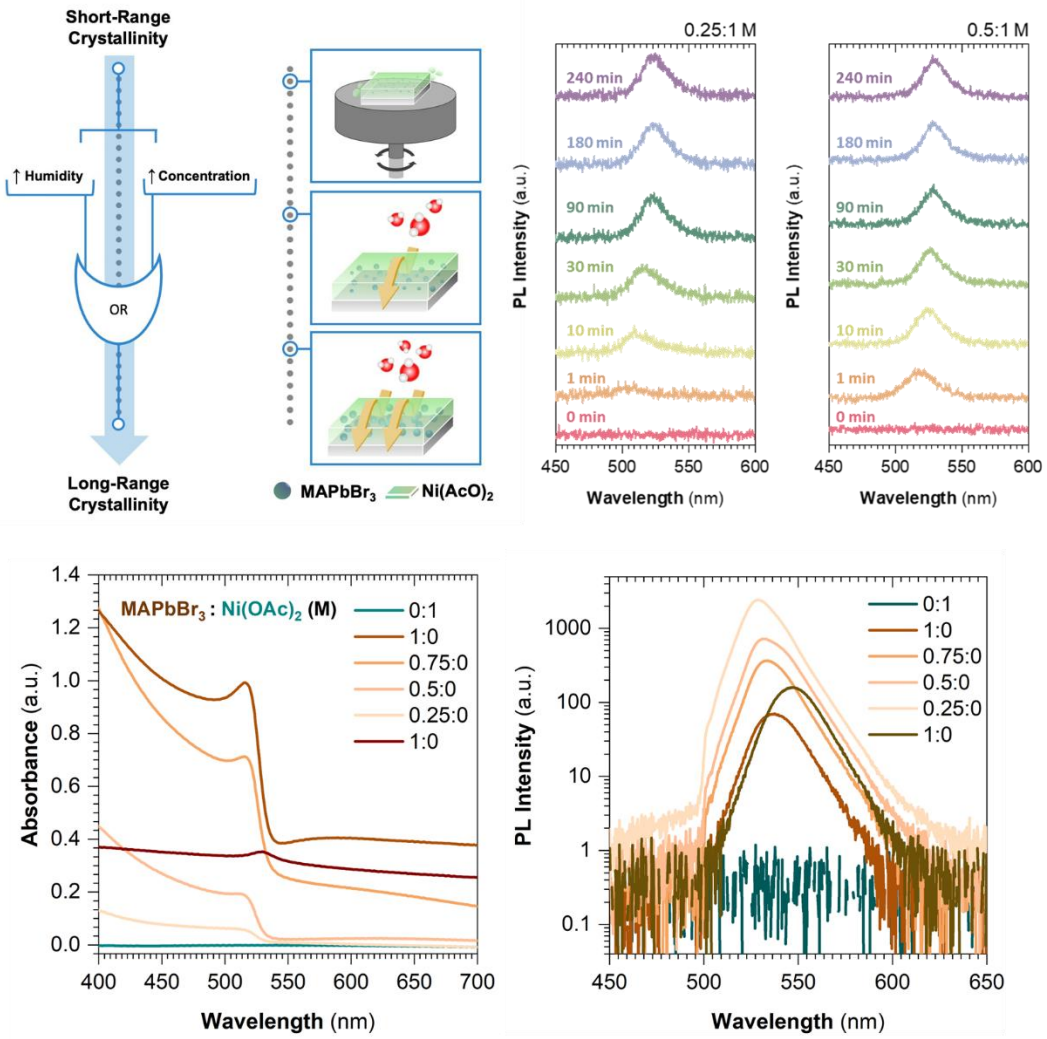

Figure 75. Summary and highlights of the main findings from Chapter 5.

In **Chapter 6** we further explored the underlying formation mechanisms of PNCs, presenting an in-depth analysis of the crystallization processes and their direct impact on enhancing the optical properties of the nanocomposites. This study presents a meaningful understanding of the crystallization dynamics of the PNC system studied in **Chapters 4** and **5**. Contrary to the commonly observed quenching effects of water MHPs, we demonstrate that RH levels above 20% play a pivotal role in promoting the transformation of 0D structures into 3D perovskite NCs within an acetate-rich matrix. At lower humidity levels, the synthesis predominantly yields non-emissive 0D phases, including MA_4PbBr_6 and PbBrOH, whereas higher RH favors the formation of luminescent 3D NCs. PLE analysis reveal that these wide-bandgap materials (0D and

PbBrOH) act as neutral UV filters rather than contributors to PLQY. Instead, the enhanced PLQY is primarily due to the *in situ* generation of OH^-, which effectively passivate defects in the 3D NCs and improve their optical properties. Investigations into the PL and decay kinetics of the $MAPbBr_3$ nanocomposites under varying gas environments and vacuum confirm that water removal from NCs results in significant PL quenching. This underscores the reversible nature of water-induced passivation. These findings underscore the transformative potential of the developed synthesis strategy, establishing it as a cornerstone for future advancements in the field of perovskite-based materials and technologies.

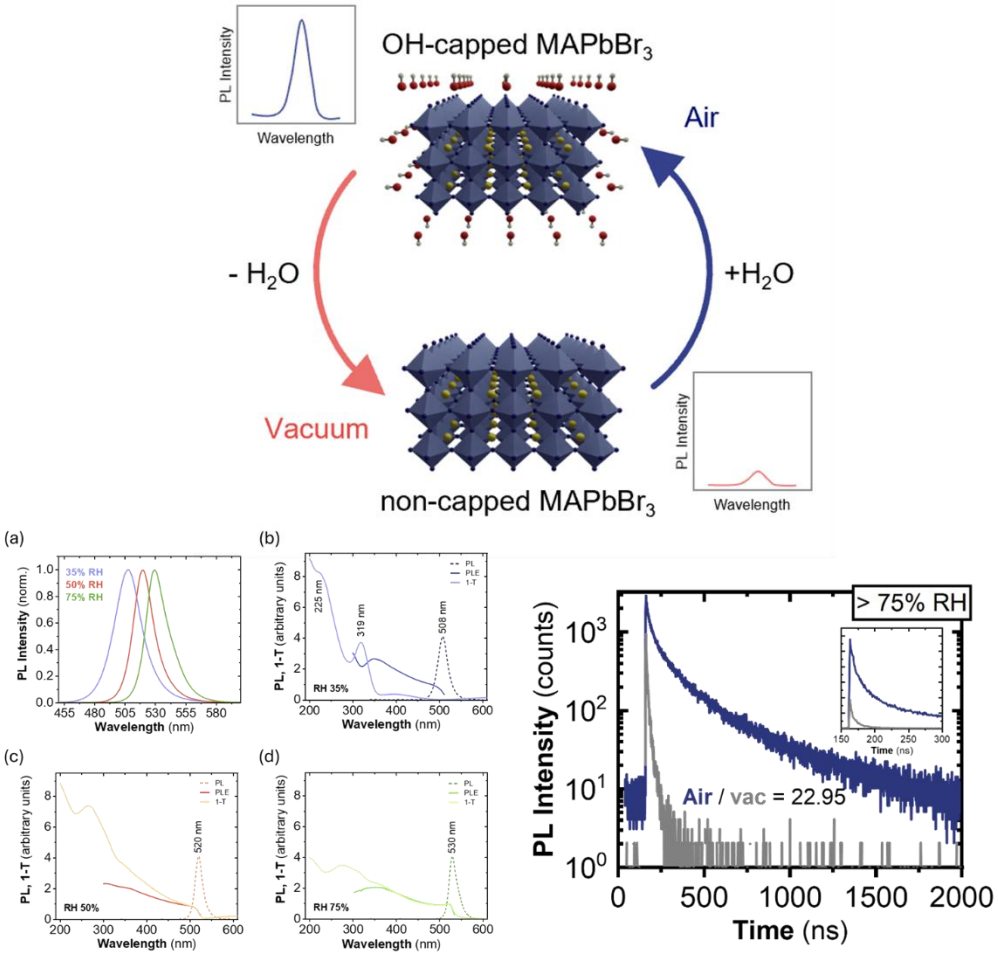

Figure 76. Summary and highlights of the main findings from Chapter 6.

Finally in **Chapter 7** we explore the innovative use of nickel acetate in the synthesis of all-inorganic PSCs, presenting a novel strategy for stabilizing wide-bandgap perovskites such as $CsPbI_3$. Building on the versatile and effective nanocomposite-based methodologies described in the aforementioned chapters, we

demonstrate a significant advancement in material stability and device performance. The synthesis method involves incorporating $Ni(AcO)_2$ into a pure DMSO precursor solution to create a $CsPbI_3$ solution. The addition of $Ni(AcO)_2$ promotes the formation of stable γ-$CsPbI_3$ (black phase) nanocomposites, as confirmed by XRD analysis, and eliminates residual PbI_2, enhancing device efficiency compared to unmodified $CsPbI_3$. Using a rapid (<10 s), low-temperature (<250°C), and environmentally friendly antisolvent- and DMA/HI-free process, we have achieved PCEs exceeding 12% in an n-i-p mesoscopic configuration. The champion device, incorporating a concentration of 0.1 M (7.7 mol%) $Ni(AcO)_2$, demonstrated remarkable stability, maintaining over 80% of its initial performance after 600 hours of MPPT in inert conditions. Additionally, calculations assessing the suitability of the bandgap under various lighting conditions are also presented, highlighting the significant potential of these materials. Indoor light sources, such as warm white and cool white illumination achieve peak efficiencies with semiconductor materials having bandgaps between 1.7 and 1.8 eV. Under indoor lighting conditions, the efficiencies exceeded 15% with cool white illumination and 17% with warm white illumination, showcasing the materials' strong potential for indoor energy harvesting. Environmental sustainability is a core focus of this synthesis approach. By eliminating harmful solvents like DMF and toluene, the method reduces greenhouse gas emissions by 70% and lowers most impact categories in a LCA study. This straightforward and scalable method represents a significant step toward the development of stable, efficient, and environmentally responsible all-inorganic PSCs.

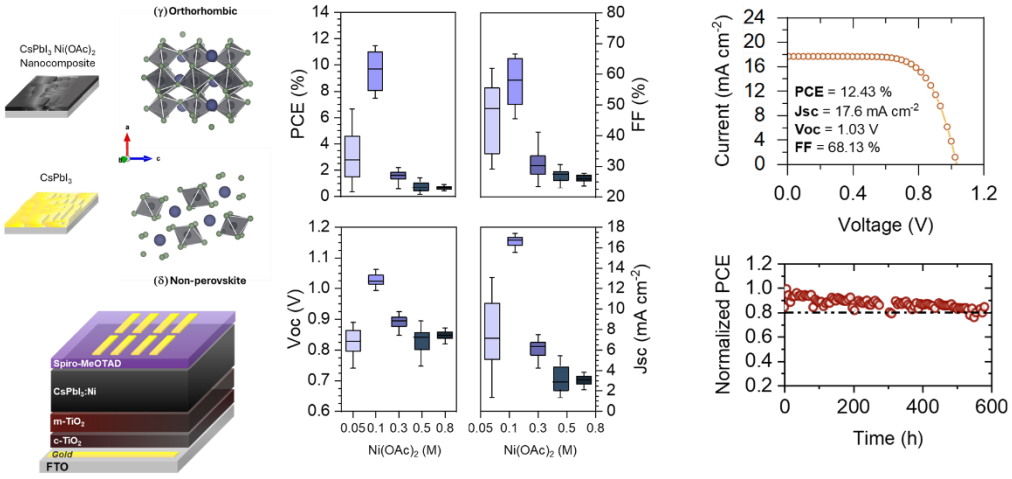

Figure 77. Summary and highlights of the main findings from Chapter 7.

Outlook

- The streamlined synthesis method introduced in Chapter 4 enables the rapid, in situ formation of PNCs embedded within a metal-organic matrix, demonstrating exceptional optical properties with PLQY reaching 80% and durability exceeding one year. Future work should focus on optimizing scalability for large-area applications and assessing long-term stability under different light intensities, particularly for integration into down-converter devices.

- Controlling PNC size and optical properties through humidity modulation offers significant potential for material customization. Future research should explore how this approach can be scaled for industrial applications and leveraged to design devices with tunable optical and electronic properties, focusing on the effects of RH on crystallization dynamics.

- The humidity-controlled chambers developed in Chapter 5 are valuable tools for achieving precise and reproducible PNC synthesis. Expanding this technique to enable real-time monitoring of crystallization under diverse environmental conditions could further improve material control and allow for tailored PNCs in advanced optoelectronic applications.

- Chapter 6 highlights the role of RH in transforming 0D structures into luminescent 3D PNCs and further passivating them with OH groups enhancing their PLQY. Future studies should explore in greater depth the in situ passivation mechanisms induced by water, focusing on developing strategies to mitigate long-term degradation effects, including advanced encapsulation techniques and their influence on optical properties.

- Density functional theory (DFT) calculations on crystallization dynamics and OH^- passivation mechanisms offer valuable insights. Further computational studies could expand our understanding of these phenomena, guiding experimental optimization for improved material performance.

- The incorporation of $Ni(AcO)_2$ in $CsPbI_3$ perovskite films has shown significant improvements in efficiency and stability under controlled conditions. Scaling this approach for large-area solar cell production requires addressing challenges in film uniformity, long-term stability, and passivation strategies suitable for practical environments.

- In indoor PVs, $CsPbI_3$ emerges as a promising material, with a suitable bandgap. Further investigation integrating them into multi-junction solar cells could enhance performance under low-light conditions.

- Environmental sustainability remains a priority. The DMSO-only, nickel acetate-based synthesis method reduces harmful solvent use and greenhouse gas emissions, but addressing residual materials like PbI_2 and $Ni(AcO)_2 \cdot 4H_2O$ in absorber layers is essential. Research into non-toxic alternatives, such as $Mg(AcO)_2$, should be prioritized to balance sustainability with high performance and also explore its use for the fabrication of lead-free perovskite materials.

- While stability under inert conditions is promising, long-term testing under varied environmental conditions, including humidity, temperature fluctuations, and UV exposure, is necessary. Future work should also investigate the role of advanced passivating agents in mitigating degradation mechanisms and optimizing the optical and electronic properties of perovskites for next-generation PV devices.

Implications of the Thesis

The materials developed in this thesis have not only advanced knowledge about perovskites and their derivatives but have also demonstrated significant potential for technological applications. As a result, several patents have arisen from the research work carried out in this thesis:

1. Rafael Abargues López, Pedro Javier Rodríguez Cantó, Juan P. Martínez Pastor, Jaume Noguera, Sixto Giménez Juliá, Miguel García Tecedor. *Catalytic nickel oxide film, procedure for its production, and its uses*. Priority date: June 19, 2019. Intenanomat S.L. (10 %), University of Valencia (55 %), Universitat Jaume I (35 %). Application number: **P201930558**.

2. Jaume Noguera Gómez, Pablo Pérez Boix, Rafael Abargues

   Method for preparing layers of metal halide perovskite nanocrystals, nanocomposite in the form of a nanometric film composed of perovskite nanocrystals, layers of metal halide perovskite nanocrystals, and their uses. Priority date: July 23, 2021. University of Valencia**.** Application number: **P202130716**.

3. Jaume Noguera Gómez, Pablo Pérez Boix, Noemí Farinós, Alejandro Saura, Juan Martínez Pastor, Rafael Abargues.

   Method for preparing non-stoichiometric palladium oxide layers. Priority date: June 8, 2023. University of Valencia. Application number: **P202330481**.

4. Jaume Noguera Gómez, Rafael Abargues, Pablo P. Boix, Teresa Ripollés, Víctor Sagra, Marta Vallés, Sandy Sánchez.

   Procedure for obtaining a composite perovskite coating, composite perovskite, and its applications. Priority date: June 12, 2024. University of Valencia (90%) and École Polytechnique Fédérale de Lausanne (EPFL) (10%). Application number: **P202430479**.

The first patent describes a method to obtain nanocomposites from nickel acetate for various applications, notably water electrolysis for hydrogen production. The second patent outlines a method for producing perovskite nanocrystals in the form of nanocomposites for use in optoelectronic devices. The third patent describes a method for preparing palladium oxide layers. The fourth patent presents a method for

stabilizing the active phase of $CsPbI_3$ using transition metal acetates for various applications, with a particular focus on photovoltaics.

These contributions pave promising paths toward the development of new technologies with potential social impact.

Resum en valencià

Ja vos ho vaig dir: No se n'aneu!

JNM a MBS

Aquesta tesi doctoral, amb títol **"Síntesi i caracterització de materials basats en nanocompòsits multifuncionals per a solucions energètiques de nova generació"**, aprofundeix en el desenvolupament de materials innovadors basats en nanocompòsits, considerats peces clau per afrontar reptes crucials en la ciència de materials aplicada a tecnologies d'emissió i solucions energètiques.

L'estudi destaca el potencial d'aquestos materials per a diverses aplicacions d'avantguarda. En particular, la recerca es centra, per una banda, en l'anàlisi de les dinàmiques de cristal·lització de nanocristalls de perovskites a l'interior de matrius i per altra en l'estabilització d'un dels polimorfs inestables de perovskita ($CsPbI_3$) per al seu ús en aplicacions fotovoltaiques. Aquestes troballes obrin noves perspectives per al seu ús com a materials en dispositius com les cèl·lules solars o LEDs (de l'anglès *light-emitting diodes*), marcant un pas endavant cap a solucions sostenibles i d'alt rendiment.

OBJECTIUS DE LA TESI

L'objectiu principal d'aquesta tesi doctoral és la síntesi i caracterització de materials innovadors basats en nanocompòsits de perovskites, caracteritzats per una fàcil implementació en processos de producció industrials i cost reduït fabricació. La investigació posa un èmfasi especial en donar resposta a la necessitat global d'adoptar tecnologies d'emissió i captació d'energia que siguen més eficients, sostenibles i fàcilment escalables.

Els objectius específics de la recerca per capítols engloben:

Capítol 1: Introducció i context global.

- Establir el marc global del tema d'estudi.
- Proporcionar una introducció completa sobre el panorama global actual i la rellevància dels materials investigats.

Capítol 2: Fonaments en química i física.

- Explorar els fonaments científics i tècnics relacionats amb la recerca desenvolupada.
- Presentar els conceptes clau emprats en les tècniques experimentals i l'anàlisi de resultats.

Capítol 3: Mètodes i tècniques de caracterització experimentals.

- Descriure detalladament les metodologies emprades en la recerca.
- Proporcionar una visió general de les tècniques experimentals utilitzades per assolir els objectius de la tesi.

Capítol 4: Mètode de cristal·lització *in situ* de nanopartícules de perovskita a l'interior de matrius. Control dimensional i de l'estabilitat de les nanopartícules.

- Presentar un nou mètode sintètic per a la preparació de nanocristalls de perovskita a l'interior de matrius.
- Demostrar el potencial del mètode per aconseguir un control precís de la mida final dels nanocristalls.

Capítol 5: Protocol detallat per a la fabricació de nanocristalls de perovskita.

- Estudi de la influència de les dissolucions precursores i l'ambient de cristal·lització en les propietats optoelectròniques finals.
- Fabricació i optimització de cambres d'ambient controlat per facilitar la cristal·lització de les nanopartícules (control de la humitat relativa de l'ambient).

Capítol 6: Mecanisme de passivació en nanocristalls de perovskita $CH_3NH_3PbBr_3$ altament luminescents basats en nanocompòsits.

- Estudi del mecanisme químic subjacent en el procés de cristal·lització.
- Anàlisi del paper de la humitat relativa i de les diferents espècies presents durant la cristal·lització per establir el mecanisme de passivació que confereix una alta eficiència a l'emissió dels nanocristalls a l'interior de matrius.

Capítol 7: Síntesi ràpida i senzilla de $CsPbI_3$ per al seu ús en cèl·lules solars mitjançant la incorporació d'acetat de níquel.

- Explorar l'ús de l'acetat de níquel per estabilitzar la fase activa de perovskites com el $CsPbI_3$ i preparar dispositius eficients.
- Establir, mitjançant comparació, l'adequació d'aquest mètode per estabilitzar el polimorf gamma de $CsPbI_3$ en comparació amb la ruta clàssica utilitzant DMAI.
- Analitzar el potencial d'aquest tipus de sistemes per a la seua utilització en aplicacions de fotovoltaica d'interiors.

Capítol 8: Conclusions i perspectives futures

- Resumir les contribucions clau de la recerca.
- Discutir les possibles direccions futures per a l'exploració i el desenvolupament del camp d'estudi.

RESUM PER CAPÍTOLS

Capítol 1: Introducció.

L'any 2023, la humanitat havia traspassat sis dels nou límits planetaris proposats, l'any 2009, per l'acadèmic suec Johan Rockström i un equip de 28 investigadors. Aquest fet posa de manifest la necessitat d'una acció urgent per garantir un futur sostenible. Els límits planetaris estan interconnectats, i això implica que per abordar problemes globals com l'escalfament climàtic, cal actuar simultàniament en tots ells. Tot i l'aclaparadora complexitat del repte, aquest també presenta oportunitats per avançar cap a un model de desenvolupament més resilient i sostenible.

Una de les qüestions clau és assegurar una transició efectiva que permeta superar l'actual dependència dels combustibles fòssils, que han estat el pilar de la indústria, el transport i les llars des de la revolució industrial. Malgrat el paper fonamental que han jugat, els seus efectes negatius s'han tornat insostenibles. La dependència dels combustibles fòssils està associada a problemes com la contaminació ambiental, l'emissió de gasos d'efecte hivernacle i els riscos per a la salut humana. A més, els recursos fòssils són finits, i la seua extracció i ús contribueixen a la pèrdua de biodiversitat i a fenòmens climàtics extrems.

El 22 de juliol de 2024, la temperatura mitjana global va assolir un màxim històric de 17.16°C, fet que evidencia la gravetat de la situació. En aquest context, les dues vessants d'acció més directes son: d'una banda, accelerar la transició cap a energies renovables, que són més netes i sostenibles; de l'altra, avançar cap al decreixement, que proposa reduir la producció i el consum per prioritzar la sostenibilitat ecològica. Aquest darrer model busca un equilibri entre les necessitats humanes i els límits del planeta, promovent un canvi de paradigma basat en l'ús eficient dels recursors.

Tot i els progressos recents en matèria de renovables, els combustibles fòssils encara representaven el 80% del consum energètic global el 2023. Encara que les fonts renovables han crescut de manera significativa –especialment la solar i l'eòlica, que han liderat el 75% de l'augment en energia neta durant l'última dècada–, la demanda energètica mundial continua superant la capacitat de generació renovable. En aquesta línia, per al 2030, s'espera una expansió notable de la capacitat renovable, que posicionarà aquestes fonts com a protagonistes en la generació d'electricitat. Però, no obstant, el ritme d'aquesta transició és encara insuficient per assolir els objectius climàtics.

Afrontar aquest desafiament implica accelerar l'adopció de tecnologies renovables, invertir en investigació i desenvolupament, i promoure polítiques que incentiven tant la producció d'energia neta com un consum responsable. Només amb una resposta global coordinada s'hi podrà revertir la crisi climàtica i garantir un futur sostenible per a les generacions vinents.

Capítol 2: Fonaments en física i química.

Els materials semiconductors són imprescindibles per a la tecnologia moderna, ja que sustenten aplicacions clau com les cèl·lules fotovoltaiques, els LEDs i els circuits integrats. Amb una conductivitat elèctrica intermèdia entre conductors i aïllants, les propietats dels semiconductors es poden ajustar amb tècniques com el dopatge, que modifiquen la densitat i el tipus de portadors de càrrega. Això permet configurar dispositius com díodes i transistors, essencials per al control del flux d'electrons. La recerca constant en aquest camp ha permès desenvolupar materials més eficients i versàtils, adaptats a les necessitats d'una societat en evolució.

Entre els materials emergents, les perovskites halur metàl·lic (de l'anglès *metal halide* perovskites, MHP) han esdevingut protagonistes gràcies als avanços en l'eficiència de les cèl·lules solars. Inicialment, les MHP van destacar pel seu baix cost i gran potencial fotovoltaic, però posteriorment es van explorar les seues aplicacions en altres dispositius optoelectrònics, com LEDs. Amb una estructura cristal·lina de fórmula general ABX_3, aquestes perovskites ofereixen una gran flexibilitat compositiva. Els ions de les posicions A, B i X, que poden ser orgànics o inorgànics, determinen les propietats estructurals i optoelectròniques del material, obrint la porta a innovacions tecnològiques. Des del descobriment de la perovskita natural $CaTiO_3$ el 1839 fins a l'ús de les perovskites en cèl·lules solars amb eficiències del 26.7%, aquests materials han redefinit el camp de la ciència de materials. La seua versatilitat i el seu alt rendiment els posicionen com a pilars de les tecnologies energètiques del futur.

Les perovskites han despertat gran interès en l'àmbit científic gràcies a un conjunt de propietats úniques que les fan ideals per a diverses aplicacions optoelectròniques, com ara cèl·lules solars i LEDs. D'una banda, la seua capacitat d'ajustar la banda prohibida (de l'anglès *bandgap*) segons la composició química permet adaptar-les a diferents aplicacions. Per a cèl·lules solars, un *bandgap* de 1,1 a 1,6 eV és òptim, mentre que per a LEDs es pot ajustar per cobrir tot l'espectre visible, l'infraroig i l'ultraviolat, millorant l'emissió de llum. A més, les perovskites tenen un alt coeficient d'absorció òptica, cosa que permet fer capes actives molt fines, reduint el cost de materials i salvaguardant-ne l'òptima absorció de llum. Una altra propietat destacada és la mobilitat alta dels portadors de càrrega, que assegura un transport eficient en cèl·lules solars i una emissió ràpida en LEDs, millorant el rendiment de tots dos dispositius. Les perovskites també presenten una gran tolerància als defectes, a diferència d'altres semiconductors, mantenint altes eficiències tot i els defectes cristal·lins, ja que aquests no generen trampes electròniques profundes que afecten el rendiment dels dispositius. A més, la seua producció és econòmica gràcies a tècniques de processat per dissolució, que permeten la fabricació de capes primes a baixes temperatures, facilitant la producció a gran escala. A més, les perovskites ofereixen una gran flexibilitat composicional, ja que és possible substituir-ne totalment o parcialment els ions de la seua estructura per ajustar-les per a diferents aplicacions. Malgrat les preocupacions per l'ús de plom en la seua composició, les quantitats

utilitzades són molt petites, i la recerca actual en alternatives, com l'estany, és prometedora.

Aquest conjunt de característiques fa que les perovskites siguin una opció destacada i competitiva per a aplicacions optoelectròniques sostenibles i de gran rendiment, amb un gran potencial per transformar diversos sectors.

Capítol 3: Mètodes i tècniques de caracterització.

El capítol 3 d'aquesta tesi ofereix una anàlisi exhaustiva de les tècniques de fabricació i caracterització emprades per al desenvolupament dels materials. Aquest capítol aborda els mètodes de síntesi i dipòsit de materials, destacant el paper central del *spin coating*. Aquesta tècnica, apreciada per la seua senzillesa i versatilitat, és fonamental per a la formació de pel·lícules primes homogènies, tot i que presenta reptes inherents. Es detalla també la importància de paràmetres com l'elecció de dissolvents i les condicions ambientals, amb èmfasi en la humitat relativa de fabricació, un factor que s'explora en els capítols posteriors. En el sentit de les condicions de fabricació, es ressalta la utilitat de les caixes de guants, que permeten operar sota atmosferes controlades amb nivells ultrabaixos d'oxigen i humitat. Aquestes condicions són d'ús comú per a la fabricació de dispositius fotovoltaics basats en perovskites amb la finalitat d'evitar, en molts casos, la degradació dels materials i assegurar la consistència i estabilitat dels dispositius fabricats.

Quant a les tècniques de caracterització, el capítol aprofundeix en una àmplia gamma de metodologies experimentals. La difracció de raigs X (XRD) s'utilitza per determinar l'estructura cristal·lina i les fases presents, mentre que l'espectroscòpia UV-Vis proporciona informació sobre les propietats òptiques. També s'utilitzen tècniques com l'espectroscòpia ATR-FTIR, per analitzar la química superficial, i l'espectroscòpia XPS, per caracteritzar la composició elemental i l'estat químic a nivell superficial. Pel que fa a l'estudi de la morfologia i estructura a escala nanomètrica dels materials, aquesta s'adreça mitjançant l'ús de tècniques de microscòpia electrònica d'escombratge (SEM de l'anglès *scanning electron microscopy*) i de transmissió (TEM de l'anglès *tranmission electron microscopy*).

En conjunt, aquest capítol no només proporciona una descripció detallada de les tècniques utilitzades, sinó que també subratlla la seua rellevància per a l'optimització

i el disseny de dispositius optoelectrònics avançats, posicionant aquest treball en la frontera de la investigació en materials de perovskita.

Capítol 4: Mètode de cristal·lització *in situ* de pel·lícules primes de nanopartícules de perovskita ajustables i estables.

El Capítol 4 introdueix una metodologia simplificada, ràpida i rendible per a la síntesi *in situ* de nanocristalls de perovskita a l'interior d'una matriu organometàl·lica, produint pel·lícules de nanocompòsits amb propietats òptiques excepcionals i una estabilitat notable. Amb un PLQY que arriba al 80% i una durabilitat superior a un any, el mètode destaca per no requerir recuit, produint pel·lícules primes uniformes amb una gran resistència al desgast mecànic. Ajustant la càrrega de precursors al film final, s'aconsegueix un control precís de la dinàmica de cristal·lització, que permet ajustar la mida final dels cristalls. A més, la mida dels cristalls de perovskita s'hi pot modular exposant-los a diferents condicions d'humitat relativa, amb els espectres de PL i d'absorció mostrant respostes diverses als nivells d'humitat. Aquesta influència de la humitat s'estudia més a fons al Capítol 6, on s'atribueix, a efectes d'agregació i transicions d'estructura cristal·lina, l'augment de la mida resultant dels nanocristalls. Aquesta metodologia de síntesi de nanocompòsits de perovskita estableix una base sòlida per al desenvolupament de dispositius optoelectrònics de gran àrea amb funcionalitats superiors. A més estableix una via senzilla per ajustar directament el *bandgap* mitjançant la manipulació precisa de la dinàmica de cristal·lització dels nanocristalls, ressaltant el seu potencial per a aplicacions optoelectròniques de nova generació.

Capítol 5: Cristal·lització controlada de nanocristalls de perovskita: Un protocol de síntesi *in situ* comprensiu.

En el Capítol 5, es dissenya un protocol complet per oferir una comprensió més profunda de la dinàmica de cristal·lització dels nanocristalls de perovskita i el gran potencial d'aquesta tècnica de síntesi. Un aspecte crític d'aquesta exploració implica el desenvolupament i ús de cambres especialitzades en el control d'humitat, una estratègia clau per garantir un control precís sobre les propietats finals dels nanocristalls i explotar completament la versatilitat d'aquesta nova metodologia.

Capítol 6: Mecanisme de passivació en nanocristalls de perovskita $CH_3NH_3PbBr_3$ basats en nanocompòsits altament luminescents.

Al Capítol 6, s'exploren en profunditat els mecanismes de formació i passivació de nanocristalls de perovskita a l'interior de matrius. A més, s'hi presenta una anàlisi detallada dels diferents processos al llarg de la cristal·lització i el seu impacte directe en la millora de les propietats òptiques dels nanocompòsits. Aquest estudi proporciona una comprensió significativa de la dinàmica de cristal·lització del sistema de nanocristalls estudiat als Capítols 4 i 5. Contràriament als efectes de degradació i *quenching* habituals de l'aigua en les perovskites, es demostra que nivells d'humitat relativa superiors al 20% són essencials per promoure la transformació d'estructures 0D en nanocristalls de perovskita 3D dins de la matriu d'acetat. Quan els nivells d'humitat relativa son baixos (< 20%), la síntesi produeix predominantment fases cristal·lines no emissives, com MA_4PbBr_6 i PbBrOH, mentre que una humitat més alta afavoreix la formació de nanocristalls de perovskita 3D luminescents. Els estudis de PLE mostren que aquests materials amb major *bandgap* (0D i PbBrOH) actuen com a filtres UV neutres en lloc de contribuir al PLQY. En canvi, l'increment del PLQY es deu principalment a la generació d'ions OH^-, que passiven de manera efectiva els defectes en els nanocristalls 3D i milloren les seues propietats òptiques. Investigacions sobre la fotoluminescència dels nanocompòsits $MAPbBr_3$ sota entorns de gas variables i en absència d'aire confirmen que l'eliminació d'aigua dels nanocristalls comporta un *quenching* significatiu de la PL, subratllant la naturalesa reversible de la passivació induïda per l'aigua. Aquestes troballes posen en relleu el potencial transformador de l'estratègia de síntesi desenvolupada, establint-la com a base per a futurs avanços en el camp dels materials i tecnologies basats en perovskites.

Capítol 7: Síntesi ràpida i senzilla de cèl·lules solars de perovskita CsPbI3 mitjançant la incorporació d'acetat de niquel

En el Capítol 7, es presenta una metodologia sintètica innovadora per a la fabricació de cèl·lules solars de perovskita de $CsPbI_3$ que destaca per ser ràpid (cristal·lització en 10 segons), a baixa temperatura (per sota de 250°C) i més respectuós amb el medi ambient, comparant amb rutes de síntesi clàssiques, ja que no

fa servir *antisolvents* ni DMF. Aquesta nova metodologia permet obtenir cèl·lules solars, amb una eficiència de conversió de potència (PCE de l'anglès *power converion efficiency*) superior al 12% en una configuració mesoscòpica n-i-p, amb una estabilitat superior a les 600 hores en seguiment del punt de màxima potència (MPPT de l'anglès *maximum power point tracking*) i una pèrdua de rendiment de menys del 20%. A més, sota il·luminació blanca freda i càlida, els dispositius aconsegueixen eficiències destacables de més del 15% i 17%, respectivament, mostrant el gran potencial de les cèl·lules solars de perovskita $CsPbI_3$ amb $Ni(AcO)_2$ per a la captació eficient d'energia en ambients interiors. A banda de les millores en el rendiment, el mètode de síntesi que incorpora l'acetat de níquel té un impacte ambiental reduït, amb una disminució del 70% en les emissions de gasos d'efecte hivernacle en comparació amb les rutes clàssiques de síntesi d'aquest material. Aquest enfocament senzill, representa un pas significatiu cap al desenvolupament de materials de perovskita purament inorgànics, eficients i estables per a aplicacions fotovoltaiques.

Capítol 8: Conclusions.

El mètode de síntesi desenvolupat al Capítol 4 permet formar ràpidament nanocristalls de perovskita amb una eficiència de fotoluminescència del 80% i una durabilitat superior a un any. Els esforços futurs haurien de centrar-se en l'escalabilitat per a aplicacions de gran àrea i en l'avaluació de l'estabilitat dels materials sota diverses intensitats d'il·luminació (per a aplicacions en LEDs com *down-converters*).

La modulació de la humitat com a eina per controlar les propietats dels nanocristalls de perovskita ofereix un gran potencial per personalitzar materials per a aplicacions industrials. Una possible ampliació d'aquesta síntesi inclouria el monitoratge en temps real de la cristal·lització sota diverses condicions ambientals, millorant així el control sobre els materials. La humitat juga un paper clau en la passivació, amb grups OH, i millora de les propietats òptiques dels nanocristalls generats, però, tot i això, calen estudis per desenvolupar estratègies que mitiguen la degradació a llarg termini, com encapsulacions avançades. A més, càlculs basats en teoria funcional de densitat (DFT de l'anglès *Density Functional Theory*) podrien guiar noves estratègies per optimitzar els materials.

Pel que fa a la síntesi desenvolupada al capítol 7, la incorporació de $Ni(AcO)_2$ en films de $CsPbI_3$ ha demostrat ser una estratègia prometedora per millorar l'eficiència i estabilitat de les cèl·lules solars. D'esta manera, la seua escalabilitat requereix abordar desafiaments com l'estabilitat en condicions ambientals així com la possibilitat d'adaptar aquest tipus de síntesi a un procés a escala industrial tot sense comprometre'n les seues propietats. A banda, la sostenibilitat ambiental continua sent un repte clau. Tot i que el mètode basat en DMSO i acetat de níquel redueix l'ús de dissolvents tòxics i les emissions de gasos d'efecte hivernacle, cal abordar la gestió de residus com PbI_2 i $Ni(AcO)_2{\cdot}4H_2O$ en les capes absorbents. La recerca en alternatives no tòxiques, com $Mg(AcO)_2$, podria ajudar a equilibrar la sostenibilitat amb un alt rendiment, a més d'explorar materials de perovskita lliures de plom.

IMPLICACIONS DE LA TESI

Els materials desenvolupats en aquesta tesi no només han avançat el coneixement sobre les perovskites i els seus derivats, sinó que també han demostrat un gran potencial per a aplicacions tecnològiques. D'aquesta forma, a partir de les tasques de recerca d'aquesta tesi han sorgit diverses patents:

1. Rafael Abargues López, Pedro Javier Rodríguez Cantó, Juan P. Martínez Pastor, Jaume Noguera, Sixto Giménez Juliá, Miguel García Tecedor

   Pel·lícula catalítica d'òxid de níquel, procediment per a la seua obtenció i els seus usos. Data de prioritat: 19 de juny de 2019. Intenanomat S.L. (10 %), Universitat de València (55 %), Universitat Jaume I (35 %). Nº de sol·licitud **P201930558**.

2. Jaume Noguera Gómez, Pablo Pérez Boix, Rafael Abargues

   Mètode de preparació de capes de nanocristalls de perovskites d'halur metàl·lic, nanocompòsit en forma de pel·lícula nanomètrica format per nanocristalls de perovskites, capes de nanocristalls de perovskites d'halurs metàl·lics i usos de les capes. Data de prioritat: 23 de juliol de 2021. Universitat de València. Nº **P202130716**.

3. Jaume Noguera Gómez, Pablo Pérez Boix, Noemí Farinós, Alejandro Saura, Juan Martínez Pastor, Rafael Abargues

Mètode de preparació de capes d'òxid de pal·ladi no estequiomètric. Data de prioritat: 8 de juny de 2023. Universitat de València. Nº de sol·licitud **P202330481**.

4. Jaume Noguera Gómez, Rafael Abargues, Pablo P. Boix, Teresa Ripollés, Víctor Sagra, Marta Vallés, Sandy Sánchez.

   Procediment per a l'obtenció d'un recobriment de perovskita composta, perovskita composta i les seves aplicacions. Data de prioritat: 12 de juny de 2024. Universitat de València (90 %) i Escola Politècnica Federal de Lausana (EPFL) (10 %). Nº de sol·licitud **P202430479**.

La primera patent descriu un mètode per obtenir nanocompòsits a partir d'acetat de níquel per a diferents aplicacions, on destaca l'electròlisi de l'aigua per a la producció d'hidrogen. La segona descriu un mètode per a l'obtenció de nanocristalls de perovskites en forma de nanocompòsits, per al seu ús en dispositius optoelectrònics. La tercera descriu un mètode per al a preparació de capes d'òxid de paladi. La quarta patent descriu un mètode per a l'estabilització de la fase activa de $CsPbI_3$ mitjançant d'acetats de metalls de transició per a diferents aplicacions, on hi destaca la fotovoltaica.

Aquestes contribucions obrin camins prometedors cap a la generació de noves tecnologies amb potencial impacte social.

Bibliography

(1) Rockström, J.; Steffen, W.; Noone, K.; Persson, Å.; Chapin, F. S.; Lambin, E. F.; Lenton, T. M.; Scheffer, M.; Folke, C.; Schellnhuber, H. J.; Nykvist, B.; de Wit, C. A.; Hughes, T.; van der Leeuw, S.; Rodhe, H.; Sörlin, S.; Snyder, P. K.; Costanza, R.; Svedin, U.; Falkenmark, M.; Karlberg, L.; Corell, R. W.; Fabry, V. J.; Hansen, J.; Walker, B.; Liverman, D.; Richardson, K.; Crutzen, P.; Foley, J. A. A Safe Operating Space for Humanity. *Nature* **2009**, *461* (7263), 472–475. https://doi.org/10.1038/461472a.

(2) Rockström, J.; Steffen, W.; Noone, K.; Persson, Å.; Chapin, F. S. I.; Lambin, E.; Lenton, T.; Scheffer, M.; Folke, C.; Schellnhuber, H. J.; Nykvist, B.; de Wit, C.; Hughes, T.; van der Leeuw, S.; Rodhe, H.; Sörlin, S.; Snyder, P.; Costanza, R.; Svedin, U.; Falkenmark, M.; Karlberg, L.; Corell, R.; Fabry, V.; Hansen, J.; Walker, B.; Liverman, D.; Richardson, K.; Crutzen, P.; Foley, J. Planetary Boundaries: Exploring the Safe Operating Space for Humanity. *Ecol. Soc.* **2009**, *14* (2). https://doi.org/10.5751/ES-03180-140232.

(3) Richardson, K.; Steffen, W.; Lucht, W.; Bendtsen, J.; Cornell, S. E.; Donges, J. F.; Drüke, M.; Fetzer, I.; Bala, G.; Von Bloh, W.; Feulner, G.; Fiedler, S.; Gerten, D.; Gleeson, T.; Hofmann, M.; Huiskamp, W.; Kummu, M.; Mohan, C.; Nogués-Bravo, D.; Petri, S.; Porkka, M.; Rahmstorf, S.; Schaphoff, S.; Thonicke, K.; Tobian, A.; Virkki, V.; Wang-Erlandsson, L.; Weber, L.; Rockström, J. Earth beyond Six of Nine Planetary Boundaries. *Sci. Adv.* **2023**, *9* (37), eadh2458. https://doi.org/10.1126/sciadv.adh2458.

(4) Stern, D. I.; Kander, A. The Role of Energy in the Industrial Revolution and Modern Economic Growth. *Energy J.* **2012**, *33* (3), 125–152. https://doi.org/10.5547/01956574.33.3.5.

(5) Nepstad, D. C.; Stickler, C. M.; Filho, B. S.-; Merry, F. Interactions among Amazon Land Use, Forests and Climate: Prospects for a near-Term Forest Tipping Point. *Philos. Trans. R. Soc. B Biol. Sci.* **2008**, *363* (1498), 1737–1746. https://doi.org/10.1098/rstb.2007.0036.

(6) N. T., S.; M., V.; B., L.; Nadaf, S. Biodiversity Loss Due to Mining Activities. In *Impact of Societal Development and Infrastructure on Biodiversity Decline*; Rathoure, A. K., Ed.; IGI Global: Hershey, PA, USA, 2024; pp 166–191. https://doi.org/10.4018/979-8-3693-6950-0.ch011.

(7) Lelieveld, J.; Klingmüller, K.; Pozzer, A.; Burnett, R. T.; Haines, A.; Ramanathan, V. Effects of Fossil Fuel and Total Anthropogenic Emission Removal on Public Health and Climate. *Proc. Natl. Acad. Sci.* **2019**, *116* (15), 7192–7197. https://doi.org/10.1073/pnas.1819989116.

(8) Valero, A.; Valero, A.; Calvo, G. *The Material Limits of Energy Transition: Thanatia*; Springer International Publishing: Cham, 2021. https://doi.org/10.1007/978-3-030-78533-8.

(9) Hersbach, H.; Bell, B.; Berrisford, P.; Hirahara, S.; Horányi, A.; Muñoz-Sabater, J.; Nicolas, J.; Peubey, C.; Radu, R.; Schepers, D.; Simmons, A.; Soci, C.; Abdalla, S.; Abellan, X.; Balsamo, G.; Bechtold, P.; Biavati, G.; Bidlot, J.; Bonavita, M.; De Chiara, G.; Dahlgren, P.; Dee, D.; Diamantakis, M.; Dragani, R.; Flemming, J.; Forbes, R.; Fuentes, M.; Geer, A.; Haimberger, L.; Healy, S.; Hogan, R. J.; Hólm, E.; Janisková, M.; Keeley, S.; Laloyaux, P.;

Lopez, P.; Lupu, C.; Radnoti, G.; de Rosnay, P.; Rozum, I.; Vamborg, F.; Villaume, S.; Thépaut, J.-N. The ERA5 Global Reanalysis. *Q. J. R. Meteorol. Soc.* **2020**, *146* (730), 1999–2049. https://doi.org/10.1002/qj.3803.
(10) C3S. ERA5 Hourly Data on Single Levels from 1940 to Present, 2018. https://doi.org/10.24381/CDS.ADBB2D47.
(11) World Energy Outlook 2024. World Energy Outlook 2024. **2024**.
(12) Grundmann, M. *The Physics of Semiconductors: An Introduction Including Nanophysics and Applications*; Graduate Texts in Physics; Springer International Publishing: Cham, 2016. https://doi.org/10.1007/978-3-319-23880-7.
(13) *Best Research-Cell Efficiency Chart*. https://www.nrel.gov/pv/cell-efficiency.html (accessed 2024-10-16).
(14) Ahmad, S. *Perovskite Solar Cells*; Ahmad, S., Kazim, S., Grätzel, M., Eds.; Blackwell Verlag: Berlin, Germany, 2021. https://doi.org/10.1002/9783527825790.
(15) Akkerman, Q. A.; Rainò, G.; Kovalenko, M. V.; Manna, L. Genesis, Challenges and Opportunities for Colloidal Lead Halide Perovskite Nanocrystals. *Nat. Mater.* **2018**, *17* (5), 394–405. https://doi.org/10.1038/s41563-018-0018-4.
(16) A Stand out Family. *Nat. Mater.* **2021**, *20* (10), 1303–1303. https://doi.org/10.1038/s41563-021-01127-8.
(17) Weber, D. CH3NH3PbX3, Ein Pb(II)-System Mit Kubischer Perowskitstruktur / CH3NH3PbX3, a Pb(II)-System with Cubic Perovskite Structure. *Z. Für Naturforschung B* **1978**, *33* (12), 1443–1445. https://doi.org/10.1515/znb-1978-1214.
(18) Kojima, A.; Teshima, K.; Shirai, Y.; Miyasaka, T. Organometal Halide Perovskites as Visible-Light Sensitizers for Photovoltaic Cells. *J. Am. Chem. Soc.* **2009**, *131* (17), 6050–6051. https://doi.org/10.1021/ja809598r.
(19) Tan, Z.-K.; Moghaddam, R. S.; Lai, M. L.; Docampo, P.; Higler, R.; Deschler, F.; Price, M.; Sadhanala, A.; Pazos, L. M.; Credgington, D.; Hanusch, F.; Bein, T.; Snaith, H. J.; Friend, R. H. Bright Light-Emitting Diodes Based on Organometal Halide Perovskite. *Nat. Nanotechnol.* **2014**, *9* (9), 687–692. https://doi.org/10.1038/nnano.2014.149.
(20) Zhang, H.; Pfeifer, L.; Zakeeruddin, S. M.; Chu, J.; Grätzel, M. Tailoring Passivators for Highly Efficient and Stable Perovskite Solar Cells. *Nat. Rev. Chem.* **2023**, *7* (9), 632–652. https://doi.org/10.1038/s41570-023-00510-0.
(21) Momma, K.; Izumi, F. VESTA 3 for Three-Dimensional Visualization of Crystal, Volumetric and Morphology Data. *J. Appl. Crystallogr.* **2011**, *44* (6), 1272–1276. https://doi.org/10.1107/S0021889811038970.
(22) López, C. A.; Abia, C.; Alvarez-Galván, M. C.; Hong, B.-K.; Martínez-Huerta, M. V.; Serrano-Sánchez, F.; Carrascoso, F.; Castellanos-Gómez, A.; Fernández-Díaz, M. T.; Alonso, J. A. Crystal Structure Features of CsPbBr3 Perovskite Prepared by Mechanochemical Synthesis. *ACS Omega* **2020**, *5* (11), 5931–5938. https://doi.org/10.1021/acsomega.9b04248.
(23) Goldschmidt, V. M. Die Gesetze der Krystallochemie. *Naturwissenschaften* **1926**, *14* (21), 477–485. https://doi.org/10.1007/BF01507527.
(24) Kieslich, G.; Sun, S.; Cheetham, A. K. An Extended Tolerance Factor Approach for Organic–Inorganic Perovskites. *Chem. Sci.* **2015**, *6* (6), 3430–3433. https://doi.org/10.1039/C5SC00961H.

(25) Hautzinger, M. P.; Mihalyi-Koch, W.; Jin, S. A-Site Cation Chemistry in Halide Perovskites. *Chem. Mater.* **2024**. https://doi.org/10.1021/acs.chemmater.4c02043.
(26) Lee, J.-W.; Tan, S.; Seok, S. I.; Yang, Y.; Park, N.-G. Rethinking the A Cation in Halide Perovskites. *Science* **2022**, *375* (6583), eabj1186. https://doi.org/10.1126/science.abj1186.
(27) Bartel, C. J.; Sutton, C.; Goldsmith, B. R.; Ouyang, R.; Musgrave, C. B.; Ghiringhelli, L. M.; Scheffler, M. New Tolerance Factor to Predict the Stability of Perovskite Oxides and Halides. *Sci. Adv.* **2019**, *5* (2), eaav0693. https://doi.org/10.1126/sciadv.aav0693.
(28) Li, Z.; Yang, M.; Park, J.-S.; Wei, S.-H.; Berry, J. J.; Zhu, K. Stabilizing Perovskite Structures by Tuning Tolerance Factor: Formation of Formamidinium and Cesium Lead Iodide Solid-State Alloys. *Chem. Mater.* **2016**, *28* (1), 284–292. https://doi.org/10.1021/acs.chemmater.5b04107.
(29) Fu, Y.; Hautzinger, M. P.; Luo, Z.; Wang, F.; Pan, D.; Aristov, M. M.; Guzei, I. A.; Pan, A.; Zhu, X.; Jin, S. Incorporating Large A Cations into Lead Iodide Perovskite Cages: Relaxed Goldschmidt Tolerance Factor and Impact on Exciton–Phonon Interaction. *ACS Cent. Sci.* **2019**, *5* (8), 1377–1386. https://doi.org/10.1021/acscentsci.9b00367.
(30) Gholipour, S.; Ali, A. M.; Correa-Baena, J.-P.; Turren-Cruz, S.-H.; Tajabadi, F.; Tress, W.; Taghavinia, N.; Grätzel, M.; Abate, A.; De Angelis, F.; Gaggioli, C. A.; Mosconi, E.; Hagfeldt, A.; Saliba, M. Globularity-Selected Large Molecules for a New Generation of Multication Perovskites. *Adv. Mater.* **2017**, *29* (38), 1702005. https://doi.org/10.1002/adma.201702005.
(31) Gholipour, S.; Saliba, M. Chapter 1 - Bandgap Tuning and Compositional Exchange for Lead Halide Perovskite Materials. In *Characterization Techniques for Perovskite Solar Cell Materials*; Pazoki, M., Hagfeldt, A., Edvinsson, T., Eds.; Micro and Nano Technologies; Elsevier, 2020; pp 1–22. https://doi.org/10.1016/B978-0-12-814727-6.00001-3.
(32) Tao, S.; Schmidt, I.; Brocks, G.; Jiang, J.; Tranca, I.; Meerholz, K.; Olthof, S. Absolute Energy Level Positions in Tin- and Lead-Based Halide Perovskites. *Nat. Commun.* **2019**, *10* (1), 2560. https://doi.org/10.1038/s41467-019-10468-7.
(33) Prasanna, R.; Gold-Parker, A.; Leijtens, T.; Conings, B.; Babayigit, A.; Boyen, H.-G.; Toney, M. F.; McGehee, M. D. Band Gap Tuning via Lattice Contraction and Octahedral Tilting in Perovskite Materials for Photovoltaics. *J. Am. Chem. Soc.* **2017**, *139* (32), 11117–11124. https://doi.org/10.1021/jacs.7b04981.
(34) Brandt, R. E.; Stevanović, V.; Ginley, D. S.; Buonassisi, T. Identifying Defect-Tolerant Semiconductors with High Minority-Carrier Lifetimes: Beyond Hybrid Lead Halide Perovskites. *MRS Commun.* **2015**, *5* (2), 265–275. https://doi.org/10.1557/mrc.2015.26.
(35) Park, N.-G. *Multifunctional Organic-Inorganic Halide Perovskite: Applications in Solar Cells, Light-Emitting Diodes, and Resistive Memory*; 2022.
(36) Das, T.; Di Liberto, G.; Pacchioni, G. Density Functional Theory Estimate of Halide Perovskite Band Gap: When Spin Orbit Coupling Helps. *J. Phys. Chem. C* **2022**, *126* (4), 2184–2198. https://doi.org/10.1021/acs.jpcc.1c09594.
(37) Even, J.; Pedesseau, L.; Katan, C.; Kepenekian, M.; Lauret, J.-S.; Sapori, D.; Deleporte, E. Solid-State Physics Perspective on Hybrid Perovskite

Semiconductors. *J. Phys. Chem. C* **2015**, *119* (19), 10161–10177. https://doi.org/10.1021/acs.jpcc.5b00695.
(38) Miyata, A.; Mitioglu, A.; Plochocka, P.; Portugall, O.; Wang, J. T.-W.; Stranks, S. D.; Snaith, H. J.; Nicholas, R. J. Direct Measurement of the Exciton Binding Energy and Effective Masses for Charge Carriers in Organic–Inorganic Tri-Halide Perovskites. *Nat. Phys.* **2015**, *11* (7), 582–587. https://doi.org/10.1038/nphys3357.
(39) Chen, Y.; Peng, J.; Su, D.; Chen, X.; Liang, Z. Efficient and Balanced Charge Transport Revealed in Planar Perovskite Solar Cells. *ACS Appl. Mater. Interfaces* **2015**, *7* (8), 4471–4475. https://doi.org/10.1021/acsami.5b00077.
(40) Stranks, S. D.; Eperon, G. E.; Grancini, G.; Menelaou, C.; Alcocer, M. J. P.; Leijtens, T.; Herz, L. M.; Petrozza, A.; Snaith, H. J. Electron-Hole Diffusion Lengths Exceeding 1 Micrometer in an Organometal Trihalide Perovskite Absorber. *Science* **2013**, *342* (6156), 341–344. https://doi.org/10.1126/science.1243982.
(41) Adjokatse, S.; Fang, H.-H.; Loi, M. A. Broadly Tunable Metal Halide Perovskites for Solid-State Light-Emission Applications. *Mater. Today* **2017**, *20* (8), 413–424. https://doi.org/10.1016/j.mattod.2017.03.021.
(42) Herz, L. M. Charge-Carrier Dynamics in Organic-Inorganic Metal Halide Perovskites. *Annu. Rev. Phys. Chem.* **2016**, *67* (Volume 67, 2016), 65–89. https://doi.org/10.1146/annurev-physchem-040215-112222.
(43) Janker, L.; Tong, Y.; Polavarapu, L.; Feldmann, J.; Urban, A. S.; Krenner, H. J. Real-Time Electron and Hole Transport Dynamics in Halide Perovskite Nanowires. *Nano Lett.* **2019**, *19* (12), 8701–8707. https://doi.org/10.1021/acs.nanolett.9b03396.
(44) *Solar Silicon Processes: Technologies, Challenges, and Opportunities*; Ceccaroli, B., Ovrelid, E., Pizzini, S., Eds.; CRC Press: Boca Raton, 2016. https://doi.org/10.1201/9781315369075.
(45) Jena, A. K.; Kulkarni, A.; Miyasaka, T. Halide Perovskite Photovoltaics: Background, Status, and Future Prospects. *Chem. Rev.* **2019**, *119* (5), 3036–3103. https://doi.org/10.1021/acs.chemrev.8b00539.
(46) Ahn, N.; Choi, M. Towards Long-Term Stable Perovskite Solar Cells: Degradation Mechanisms and Stabilization Techniques. *Adv. Sci.* **2024**, *11* (4), 2306110. https://doi.org/10.1002/advs.202306110.
(47) Löper, P.; Stuckelberger, M.; Niesen, B.; Werner, J.; Filipič, M.; Moon, S.-J.; Yum, J.-H.; Topič, M.; De Wolf, S.; Ballif, C. Complex Refractive Index Spectra of CH3NH3PbI3 Perovskite Thin Films Determined by Spectroscopic Ellipsometry and Spectrophotometry. *J. Phys. Chem. Lett.* **2015**, *6* (1), 66–71. https://doi.org/10.1021/jz502471h.
(48) Juarez-Perez, E. J.; Sanchez, R. S.; Badia, L.; Garcia-Belmonte, G.; Kang, Y. S.; Mora-Sero, I.; Bisquert, J. Photoinduced Giant Dielectric Constant in Lead Halide Perovskite Solar Cells. *J. Phys. Chem. Lett.* **2014**, *5* (13), 2390–2394. https://doi.org/10.1021/jz5011169.
(49) Herz, L. M. Charge-Carrier Mobilities in Metal Halide Perovskites: Fundamental Mechanisms and Limits. *ACS Energy Lett.* **2017**, *2* (7), 1539–1548. https://doi.org/10.1021/acsenergylett.7b00276.
(50) Miyata, K.; Meggiolaro, D.; Trinh, M. T.; Joshi, P. P.; Mosconi, E.; Jones, S. C.; De Angelis, F.; Zhu, X.-Y. Large Polarons in Lead Halide Perovskites. *Sci. Adv.* **2017**, *3* (8), e1701217. https://doi.org/10.1126/sciadv.1701217.

(51) Hu, S.; Ren, Z.; Djurišić, A. B.; Rogach, A. L. Metal Halide Perovskites as Emerging Thermoelectric Materials. *ACS Energy Lett.* **2021**, *6* (11), 3882–3905. https://doi.org/10.1021/acsenergylett.1c02015.
(52) Fernandez-Guillen, I.; Aranda, C. A.; Betancur, P. F.; Vallés-Pelarda, M.; Momblona, C.; Ripolles, T. S.; Abargues, R.; Boix, P. P. Perovskite Thin Single Crystal for a High Performance and Long Endurance Memristor. *Adv. Electron. Mater.* **2024**, *10* (5), 2300475. https://doi.org/10.1002/aelm.202300475.
(53) Sakhatskyi, K.; Turedi, B.; Matt, G. J.; Wu, E.; Sakhatska, A.; Bartosh, V.; Lintangpradipto, M. N.; Naphade, R.; Shorubalko, I.; Mohammed, O. F.; Yakunin, S.; Bakr, O. M.; Kovalenko, M. V. Stable Perovskite Single-Crystal X-Ray Imaging Detectors with Single-Photon Sensitivity. *Nat. Photonics* **2023**, *17* (6), 510–517. https://doi.org/10.1038/s41566-023-01207-y.
(54) Quantum Dots Still Shining Strong 30 Years On. *ACS Nano* **2014**, *8* (7), 6511–6512. https://doi.org/10.1021/nn5036922.
(55) Meng, H. *Colloidal Quantum Dot Light Emitting Diodes*; Blackwell Verlag: Berlin, Germany, 2023.
(56) Murray, C. B.; Norris, D. J.; Bawendi, M. G. Synthesis and Characterization of Nearly Monodisperse CdE (E = Sulfur, Selenium, Tellurium) Semiconductor Nanocrystallites. *J. Am. Chem. Soc.* **1993**, *115* (19), 8706–8715. https://doi.org/10.1021/ja00072a025.
(57) Schmidt, L. C.; Pertegás, A.; González-Carrero, S.; Malinkiewicz, O.; Agouram, S.; Mínguez Espallargas, G.; Bolink, H. J.; Galian, R. E.; Pérez-Prieto, J. Nontemplate Synthesis of CH3NH3PbBr3 Perovskite Nanoparticles. *J. Am. Chem. Soc.* **2014**, *136* (3), 850–853. https://doi.org/10.1021/ja4109209.
(58) Protesescu, L.; Yakunin, S.; Bodnarchuk, M. I.; Krieg, F.; Caputo, R.; Hendon, C. H.; Yang, R. X.; Walsh, A.; Kovalenko, M. V. Nanocrystals of Cesium Lead Halide Perovskites (CsPbX3, X = Cl, Br, and I): Novel Optoelectronic Materials Showing Bright Emission with Wide Color Gamut. *Nano Lett.* **2015**, *15* (6), 3692–3696. https://doi.org/10.1021/nl5048779.
(59) Zhang, F.; Chen, C.; Wu, X.; Hu, X.; Huang, H.; Han, J.; Zou, B.; Dong, Y.; Zhong, H. Brightly-Luminescent and Color-Tunable Colloidal CH3NH3PbX3 (X=Br, I, Cl) Quantum Dots: Potential Alternatives for Display Technology.
(60) Pfennig, B. W. (Author). *Principles of Inorganic Chemistry*.
(61) Busatto, S.; de Mello Donega, C. Magic-Size Semiconductor Nanostructures: Where Does the Magic Come From? *ACS Mater. Au* **2022**, *2* (3), 237–249. https://doi.org/10.1021/acsmaterialsau.1c00075.
(62) Sanmartín-Matalobos, J.; Bermejo-Barrera, P.; Aboal-Somoza, M.; Fondo, M.; García-Deibe, A. M.; Corredoira-Vázquez, J.; Alves-Iglesias, Y. Semiconductor Quantum Dots as Target Analytes: Properties, Surface Chemistry and Detection. *Nanomaterials* **2022**, *12* (14), 2501. https://doi.org/10.3390/nano12142501.
(63) Bisquert, J. *The Physics of Solar Cells: Perovskites, Organics, and Photovoltaic Fundamentals*, 1st ed.; CRC Press: Boca Raton, FL : CRC Press, Taylor & Francis Group, [2018], 2017. https://doi.org/10.1201/b22380.
(64) Yuan, Y.; Yan, G.; Dreessen, C.; Rudolph, T.; Hülsbeck, M.; Klingebiel, B.; Ye, J.; Rau, U.; Kirchartz, T. Shallow Defects and Variable Photoluminescence Decay Times up to 280 Ms in Triple-Cation Perovskites. *Nat. Mater.* **2024**, *23* (3), 391–397. https://doi.org/10.1038/s41563-023-01771-2.

(65) Shen, X.; Kang, K.; Yu, Z.; Jeong, W. H.; Choi, H.; Park, S. H.; Stranks, S. D.; Snaith, H. J.; Friend, R. H.; Lee, B. R. Passivation Strategies for Mitigating Defect Challenges in Halide Perovskite Light-Emitting Diodes. *Joule* **2023**, *7* (2), 272–308. https://doi.org/10.1016/j.joule.2023.01.008.
(66) Dey, A.; Ye, J.; De, A.; Debroye, E.; Ha, S. K.; Bladt, E.; Kshirsagar, A. S.; Wang, Z.; Yin, J.; Wang, Y.; Quan, L. N.; Yan, F.; Gao, M.; Li, X.; Shamsi, J.; Debnath, T.; Cao, M.; Scheel, M. A.; Kumar, S.; Steele, J. A.; Gerhard, M.; Chouhan, L.; Xu, K.; Wu, X. G.; Li, Y.; Zhang, Y.; Dutta, A.; Han, C.; Vincon, I.; Rogach, A. L.; Nag, A.; Samanta, A.; Korgel, B. A.; Shih, C. J.; Gamelin, D. R.; Son, D. H.; Zeng, H.; Zhong, H.; Sun, H.; Demir, H. V.; Scheblykin, I. G.; Mora-Seró, I.; Stolarczyk, J. K.; Zhang, J. Z.; Feldmann, J.; Hofkens, J.; Luther, J. M.; Pérez-Prieto, J.; Li, L.; Manna, L.; Bodnarchuk, M. I.; Kovalenko, M. V.; Roeffaers, M. B. J.; Pradhan, N.; Mohammed, O. F.; Bakr, O. M.; Yang, P.; Müller-Buschbaum, P.; Kamat, P. V.; Bao, Q.; Zhang, Q.; Krahne, R.; Galian, R. E.; Stranks, S. D.; Bals, S.; Biju, V.; Tisdale, W. A.; Yan, Y.; Hoye, R. L. Z.; Polavarapu, L. State of the Art and Prospects for Halide Perovskite Nanocrystals. *ACS Nano* **2021**, *15* (7), 10775–10981. https://doi.org/10.1021/acsnano.0c08903.
(67) Jung, D.; Park, J. W.; Min, S.; Lee, H. J.; Park, J. S.; Kim, G.-M.; Shin, D.; Im, S.; Lim, J.; Kim, K. H.; Chae, J. A.; Lee, D. C.; Pugin, R.; Bulliard, X.; Hwang, E.; Park, J.-S.; Park, Y.-S.; Bae, W. K. Strain-Graded Quantum Dots with Spectrally Pure, Stable and Polarized Emission. *Nat. Commun.* **2024**, *15* (1), 5561. https://doi.org/10.1038/s41467-024-49791-z.
(68) Anderson, N. C.; Hendricks, M. P.; Choi, J. J.; Owen, J. S. Ligand Exchange and the Stoichiometry of Metal Chalcogenide Nanocrystals: Spectroscopic Observation of Facile Metal-Carboxylate Displacement and Binding. *J. Am. Chem. Soc.* **2013**, *135* (49), 18536–18548. https://doi.org/10.1021/ja4086758.
(69) de Mello Donegá, C.; Liljeroth, P.; Vanmaekelbergh, D. Physicochemical Evaluation of the Hot-Injection Method, a Synthesis Route for Monodisperse Nanocrystals. *Small Weinh. Bergstr. Ger.* **2005**, *1* (12), 1152–1162. https://doi.org/10.1002/smll.200500239.
(70) Yamçiçier, Ç.; Kürkçü, C.; Merdan, Z. A Study of Structural, Electronic, Elastic, Phonon Properties, and Transition Mechanism of Wurtzite CdTe under High Pressure. *Solid State Sci.* **2020**, *105*, 106209. https://doi.org/10.1016/j.solidstatesciences.2020.106209.
(71) Li, H.; Zhao, G.; Song, B.; Mao, Z.; Qian, Y.; Dong, W.; Han, G. Evolution of Perovskite Nanocrystals in Hot Injection Process with Various Ligand-Rich Systems. *J. Sol-Gel Sci. Technol.* **2024**. https://doi.org/10.1007/s10971-024-06507-5.
(72) Soni, A. K.; Joshi, R.; Ningthoujam, R. S. Hot Injection Method for Nanoparticle Synthesis: Basic Concepts, Examples and Applications. In *Handbook on Synthesis Strategies for Advanced Materials : Volume-I: Techniques and Fundamentals*; Tyagi, A. K., Ningthoujam, R. S., Eds.; Springer Singapore: Singapore, 2021; pp 383–434. https://doi.org/10.1007/978-981-16-1807-9_13.
(73) Vighnesh, K.; Wang, S.; Liu, H.; Rogach, A. L. Hot-Injection Synthesis Protocol for Green-Emitting Cesium Lead Bromide Perovskite Nanocrystals. *ACS Nano* **2022**, *16* (12), 19618–19625. https://doi.org/10.1021/acsnano.2c11689.

(74) Nugraha, M. I.; Indriyati, I.; Primadona, I.; Gedda, M.; Timuda, G. E.; Iskandar, F.; Anthopoulos, T. D. Recent Progress in Colloidal Quantum Dot Thermoelectrics. *Adv. Mater.* **2023**, *35* (38), 2210683. https://doi.org/10.1002/adma.202210683.
(75) Zhang, D.; Yu, M.; Xu, Y.; Li, D.; Huang, Y.; Yu, C.; Tang, C.; Lin, J. Solvothermal Synthesis of Perovskite CsPbCl3 Nanoplates and Improved Photoluminescence Performance through Postsynthetic Treatment. *Opt. Mater.* **2022**, *127*, 112257. https://doi.org/10.1016/j.optmat.2022.112257.
(76) Chen, M.; Zou, Y.; Wu, L.; Pan, Q.; Yang, D.; Hu, H.; Tan, Y.; Zhong, Q.; Xu, Y.; Liu, H.; Sun, B.; Zhang, Q. Solvothermal Synthesis of High-Quality All-Inorganic Cesium Lead Halide Perovskite Nanocrystals: From Nanocube to Ultrathin Nanowire. *Adv. Funct. Mater.* **2017**, *27* (23), 1701121. https://doi.org/10.1002/adfm.201701121.
(77) Long, Z.; Ren, H.; Sun, J.; Ouyang, J.; Na, N. High-Throughput and Tunable Synthesis of Colloidal CsPbX3 Perovskite Nanocrystals in a Heterogeneous System by Microwave Irradiation. *Chem. Commun.* **2017**, *53* (71), 9914–9917. https://doi.org/10.1039/C7CC04862A.
(78) Jang, D. M.; Kim, D. H.; Park, K.; Park, J.; Lee, J. W.; Song, J. K. Ultrasound Synthesis of Lead Halide Perovskite Nanocrystals. *J. Mater. Chem. C* **2016**, *4* (45), 10625–10629. https://doi.org/10.1039/C6TC04213A.
(79) Zhang, Y.; Saidaminov, M. I.; Dursun, I.; Yang, H.; Murali, B.; Alarousu, E.; Yengel, E.; Alshankiti, B. A.; Bakr, O. M.; Mohammed, O. F. Zero-Dimensional Cs $_4$ PbBr $_6$ Perovskite Nanocrystals. *J. Phys. Chem. Lett.* **2017**, *8* (5), 961–965. https://doi.org/10.1021/acs.jpclett.7b00105.
(80) Protesescu, L.; Yakunin, S.; Nazarenko, O.; Dirin, D. N.; Kovalenko, M. V. Low-Cost Synthesis of Highly Luminescent Colloidal Lead Halide Perovskite Nanocrystals by Wet Ball Milling. *ACS Appl. Nano Mater.* **2018**, *1* (3), 1300–1308. https://doi.org/10.1021/acsanm.8b00038.
(81) Dhanabalan, B.; Castelli, A.; Palei, M.; Spirito, D.; Manna, L.; Krahne, R.; Arciniegas, M. Simple Fabrication of Layered Halide Perovskite Platelets and Enhanced Photoluminescence from Mechanically Exfoliated Flakes. *Nanoscale* **2019**, *11* (17), 8334–8342. https://doi.org/10.1039/C9NR00638A.
(82) Soosaimanickam, A.; Rodríguez-Cantó, P. J.; Martínez-Pastor, J. P.; Abargues, R. 2 - Preparation and Processing of Nanocomposites of All-Inorganic Lead Halide Perovskite Nanocrystals. In *Hybrid Perovskite Composite Materials*; Khan, I., Khan, A., Khan, M. M. A., Khan, S., Verpoort, F., Umar, A., Eds.; Woodhead Publishing Series in Composites Science and Engineering; Woodhead Publishing, 2021; pp 19–93. https://doi.org/10.1016/B978-0-12-819977-0.00002-0.
(83) Collantes, C.; Teixeira, W.; González Pedro, V.; Bañuls, M.-J.; Maquieira, Á. Designing Stable Lead Halide Perovskite Nanocrystals: From a Single Particle to Nanocomposites. *Appl. Mater. Today* **2023**, *31*, 101775. https://doi.org/10.1016/j.apmt.2023.101775.
(84) Wu, Y.; Li, X.; Zeng, H. Highly Luminescent and Stable Halide Perovskite Nanocrystals. *ACS Energy Lett.* **2019**, *4* (3), 673–681. https://doi.org/10.1021/acsenergylett.8b02100.
(85) Choi, Y.; Han, S.; Park, B.-I.; Xu, Z.; Huang, Q.; Bae, S.; Kim, J. S.; Kim, S. O.; Meng, Y.; Kim, S.; Moon, J.; Roh, I.; Park, J.-W.; Bae, S. Perovskite Nanocomposites: Synthesis, Properties, and Applications from Renewable

Energy to Optoelectronics. *Nano Converg.* **2024**, *11* (1), 36. https://doi.org/10.1186/s40580-024-00440-7.
(86) Qin, J.; Chen, Y.; Guo, X.; Yang, H.; Qin, Y.; Yao, C.; Lv, B.; Bai, Y.; Zhan, Y. A Polymer Strategy toward High-Performance Multifunctional Perovskite Optoelectronics: From Polymer Matrix to Device Applications. *Adv. Opt. Mater.* **2023**, *11* (7), 2202809. https://doi.org/10.1002/adom.202202809.
(87) Dirin, D. N.; Protesescu, L.; Trummer, D.; Kochetygov, I. V.; Yakunin, S.; Krumeich, F.; Stadie, N. P.; Kovalenko, M. V. Harnessing Defect-Tolerance at the Nanoscale: Highly Luminescent Lead Halide Perovskite Nanocrystals in Mesoporous Silica Matrixes. *Nano Lett.* **2016**, *16* (9), 5866–5874. https://doi.org/10.1021/acs.nanolett.6b02688.
(88) Malgras, V.; Tominaka, S.; Ryan, J. W.; Henzie, J.; Takei, T.; Ohara, K.; Yamauchi, Y. Observation of Quantum Confinement in Monodisperse Methylammonium Lead Halide Perovskite Nanocrystals Embedded in Mesoporous Silica. *J. Am. Chem. Soc.* **2016**, *138* (42), 13874–13881. https://doi.org/10.1021/JACS.6B05608/SUPPL_FILE/JA6B05608_SI_001.PDF.
(89) Romero-Pérez, C.; Zanetta, A.; Fernández-Delgado, N.; Herrera-Collado, M.; Hernández-Saz, J.; Molina, S. I.; Caliò, L.; Calvo, M. E.; Míguez, H. Responsive Optical Materials Based on Ligand-Free Perovskite Quantum Dots Embedded in Mesoporous Scaffolds. *ACS Appl. Mater. Interfaces* **2023**, *15* (1), 1808–1816. https://doi.org/10.1021/acsami.2c16867.
(90) Rubino, A.; Caliò, L.; García-Bennett, A.; Calvo, M. E.; Míguez, H. Mesoporous Matrices as Hosts for Metal Halide Perovskite Nanocrystals. *Adv. Opt. Mater.* **2020**, *8* (9), 1–14. https://doi.org/10.1002/adom.201901868.
(91) Rubino, A.; Anaya, M.; Galisteo-López, J. F.; Rojas, T. C.; Calvo, M. E.; Míguez, H. Highly Efficient and Environmentally Stable Flexible Color Converters Based on Confined CH 3 NH 3 PbBr 3 Nanocrystals. *ACS Appl. Mater. Interfaces* **2018**, *10* (44), 38334–38340. https://doi.org/10.1021/acsami.8b11706.
(92) Golroudbary, S. R.; Lundström, M.; Wilson, B. P. Analogical Environmental Cost Assessment of Silicon Flows Used in Solar Panels by the US and China. *Sci. Rep.* **2024**, *14* (1), 9538. https://doi.org/10.1038/s41598-024-60270-9.
(93) Renewable Power Generation Costs in 2022. **2022**.
(94) Li, Z.; Klein, T. R.; Kim, D. H.; Yang, M.; Berry, J. J.; van Hest, M. F. A. M.; Zhu, K. Scalable Fabrication of Perovskite Solar Cells. *Nat. Rev. Mater.* **2018**, *3* (4), 1–20. https://doi.org/10.1038/natrevmats.2018.17.
(95) Candelise, C.; Speirs, J. F.; Gross, R. J. K. Materials Availability for Thin Film (TF) PV Technologies Development: A Real Concern? *Renew. Sustain. Energy Rev.* **2011**, *15* (9), 4972–4981. https://doi.org/10.1016/j.rser.2011.06.012.
(96) Krebs-Moberg, M.; Pitz, M.; Dorsette, T. L.; Gheewala, S. H. Third Generation of Photovoltaic Panels: A Life Cycle Assessment. *Renew. Energy* **2021**, *164*, 556–565. https://doi.org/10.1016/j.renene.2020.09.054.
(97) *Reference Air Mass 1.5 Spectra*. https://www.nrel.gov/grid/solar-resource/spectra-am1.5.html (accessed 2024-11-05).
(98) Shockley, W.; Queisser, H. J. Detailed Balance Limit of Efficiency of P-n Junction Solar Cells. *J. Appl. Phys.* **1961**, *32* (3), 510–519. https://doi.org/10.1063/1.1736034.

(99) Ehrler, B.; Alarcón-Lladó, E.; Tabernig, S. W.; Veeken, T.; Garnett, E. C.; Polman, A. Photovoltaics Reaching for the Shockley–Queisser Limit. *ACS Energy Lett.* **2020**, *5* (9), 3029–3033. https://doi.org/10.1021/acsenergylett.0c01790.
(100) Rühle, S. Tabulated Values of the Shockley–Queisser Limit for Single Junction Solar Cells. *Sol. Energy* **2016**, *130*, 139–147. https://doi.org/10.1016/j.solener.2016.02.015.
(101) Rosales, B. A.; Schutt, K.; Berry, J. J.; Wheeler, L. M. Leveraging Low-Energy Structural Thermodynamics in Halide Perovskites. *ACS Energy Lett.* **2023**, *8* (4), 1705–1715. https://doi.org/10.1021/acsenergylett.2c02698.
(102) Khassaf, H.; Yadavalli, S. K.; Zhou, Y.; Padture, N. P.; Kingon, A. I. Effect of Grain Boundaries on Charge Transport in Methylammonium Lead Iodide Perovskite Thin Films. *J. Phys. Chem. C* **2019**, *123* (9), 5321–5325. https://doi.org/10.1021/acs.jpcc.9b00538.
(103) McGovern, L.; Koschany, I.; Grimaldi, G.; Muscarella, L. A.; Ehrler, B. Grain Size Influences Activation Energy and Migration Pathways in MAPbBr3 Perovskite Solar Cells. *J. Phys. Chem. Lett.* **2021**, *12* (9), 2423–2428. https://doi.org/10.1021/acs.jpclett.1c00205.
(104) Hidalgo, J.; Atourki, L.; Li, R.; Castro-Méndez, A.-F.; Kim, S.; Sherman, E. A.; Bieber, A. S.; Sher, M.; Nienhaus, L.; Perini, C. A. R.; Correa-Baena, J.-P. Bulky Cation Hinders Undesired Secondary Phases in FAPbI3 Perovskite Solar Cells. *Mater. Today* **2023**, *68*, 13–21. https://doi.org/10.1016/j.mattod.2023.06.010.
(105) Castro-Méndez, A.-F.; Perini, C. A. R.; Hidalgo, J.; Ranke, D.; Vagott, J. N.; An, Y.; Lai, B.; Luo, Y.; Li, R.; Correa-Baena, J.-P. Formation of a Secondary Phase in Thermally Evaporated MAPbI3 and Its Effects on Solar Cell Performance. *ACS Appl. Mater. Interfaces* **2022**, *14* (30), 34269–34280. https://doi.org/10.1021/acsami.2c02036.
(106) Nie, T.; Fang, Z.; Ren, X.; Duan, Y.; Liu, S. Recent Advances in Wide-Bandgap Organic–Inorganic Halide Perovskite Solar Cells and Tandem Application. *Nano-Micro Lett.* **2023**, *15* (1), 70. https://doi.org/10.1007/s40820-023-01040-6.
(107) Pathak, C. S.; Choi, H.; Kim, H.; Lim, J.; Cho, S.-K.; Ham, D. S.; Song, S. Recent Progress in Coating Methods for Large-Area Perovskite Solar Module Fabrication. *Sol. RRL* **2024**, *8* (4), 2300860. https://doi.org/10.1002/solr.202300860.
(108) Sangale, S. S.; Mann, D. S.; Lee, H.-J.; Kwon, S.-N.; Na, S.-I. Influence of Interfacial Roughness on Slot-Die Coatings for Scaling-up High-Performance Perovskite Solar Cells. *Commun. Mater.* **2024**, *5* (1), 1–10. https://doi.org/10.1038/s43246-024-00645-7.
(109) Matondo, J. T.; Hu, H.; Ding, Y.; Mateen, M.; Cheng, G.; Ding, J. Slot-Die Coating for Scalable Fabrication of Perovskite Solar Cells and Modules. *Adv. Mater. Technol.* **2024**, *9* (10), 2302082. https://doi.org/10.1002/admt.202302082.
(110) Kosasih, F. U.; Erdenebileg, E.; Mathews, N.; Mhaisalkar, S. G.; Bruno, A. Thermal Evaporation and Hybrid Deposition of Perovskite Solar Cells and Mini-Modules. *Joule* **2022**, *6* (12), 2692–2734. https://doi.org/10.1016/j.joule.2022.11.004.

(111) Soto-Montero, T.; Morales-Masis, M. Laser Deposition of Metal Halide Perovskites. *ACS Energy Lett.* **2024**, *9* (8), 4199–4208. https://doi.org/10.1021/acsenergylett.4c01466.
(112) Bae, S.-R.; Heo, D. Y.; Kim, S. Y. Recent Progress of Perovskite Devices Fabricated Using Thermal Evaporation Method: Perspective and Outlook. *Mater. Today Adv.* **2022**, *14*, 100232. https://doi.org/10.1016/j.mtadv.2022.100232.
(113) Vaynzof, Y. The Future of Perovskite Photovoltaics—Thermal Evaporation or Solution Processing? *Adv. Energy Mater.* **2020**, *10* (48), 2003073. https://doi.org/10.1002/aenm.202003073.
(114) Jacobsson, T. J.; Hultqvist, A.; García-Fernández, A.; Anand, A.; Al-Ashouri, A.; Hagfeldt, A.; Crovetto, A.; Abate, A.; Ricciardulli, A. G.; Vijayan, A.; Kulkarni, A.; Anderson, A. Y.; Darwich, B. P.; Yang, B.; Coles, B. L.; Perini, C. A. R.; Rehermann, C.; Ramirez, D.; Fairen-Jimenez, D.; Di Girolamo, D.; Jia, D.; Avila, E.; Juarez-Perez, E. J.; Baumann, F.; Mathies, F.; González, G. S. A.; Boschloo, G.; Nasti, G.; Paramasivam, G.; Martínez-Denegri, G.; Näsström, H.; Michaels, H.; Köbler, H.; Wu, H.; Benesperi, I.; Dar, M. I.; Bayrak Pehlivan, I.; Gould, I. E.; Vagott, J. N.; Dagar, J.; Kettle, J.; Yang, J.; Li, J.; Smith, J. A.; Pascual, J.; Jerónimo-Rendón, J. J.; Montoya, J. F.; Correa-Baena, J.-P.; Qiu, J.; Wang, J.; Sveinbjörnsson, K.; Hirselandt, K.; Dey, K.; Frohna, K.; Mathies, L.; Castriotta, L. A.; Aldamasy, M. H.; Vasquez-Montoya, M.; Ruiz-Preciado, M. A.; Flatken, M. A.; Khenkin, M. V.; Grischek, M.; Kedia, M.; Saliba, M.; Anaya, M.; Veldhoen, M.; Arora, N.; Shargaieva, O.; Maus, O.; Game, O. S.; Yudilevich, O.; Fassl, P.; Zhou, Q.; Betancur, R.; Munir, R.; Patidar, R.; Stranks, S. D.; Alam, S.; Kar, S.; Unold, T.; Abzieher, T.; Edvinsson, T.; David, T. W.; Paetzold, U. W.; Zia, W.; Fu, W.; Zuo, W.; Schröder, V. R. F.; Tress, W.; Zhang, X.; Chiang, Y.-H.; Iqbal, Z.; Xie, Z.; Unger, E. An Open-Access Database and Analysis Tool for Perovskite Solar Cells Based on the FAIR Data Principles. *Nat. Energy* **2022**, *7* (1), 107–115. https://doi.org/10.1038/s41560-021-00941-3.
(115) *Nanomaterials and Nanocomposites: Characterization, Processing, and Applications*; Babu, B. S., Kumar, K., Eds.; CRC Press: Boca Raton, 2021. https://doi.org/10.1201/9781003160946.
(116) Han, Y.; Kim, U. J.; Nugera, F. A.; Kim, S. I.; Park, Y.; Cheon, M.; Kim, G. C.; Gutiérrez, H. R.; Lee, M.; Son, H. Photo-Carrier Lifetime in Binary and Ternary Heterostructures of Transition Metal Dichalcogenides. *Phys. Status Solidi B* **2023**, *260* (5), 2200501. https://doi.org/10.1002/pssb.202200501.
(117) *SEM vs TEM*. Analysis & Separations from Technology Networks. http://www.technologynetworks.com/analysis/articles/sem-vs-tem-331262 (accessed 2024-10-30).
(118) Saki, Z.; Byranvand, M. M.; Taghavinia, N.; Kedia, M.; Saliba, M. Solution-Processed Perovskite Thin-Films: The Journey from Lab- to Large-Scale Solar Cells. *Energy Environ. Sci.* **2021**, *14*, 5690. https://doi.org/10.1039/D1EE02018H.
(119) Kulkarni, S. A.; Mhaisalkar, S. G.; Mathews, N.; Boix, P. P. Perovskite Nanoparticles: Synthesis, Properties, and Novel Applications in Photovoltaics and LEDs. *Small Methods* **2019**, *3* (1), 1800231. https://doi.org/10.1002/SMTD.201800231.

(120) Meredith, P.; Armin, A. Scaling of next Generation Solution Processed Organic and Perovskite Solar Cells. *Nat. Commun.* **2018**, *9* (1), 5261. https://doi.org/10.1038/S41467-018-05514-9.
(121) Gualdrón-Reyes, A. F.; Yoon, S. J.; Barea, E. M.; Agouram, S.; Muñoz-Sanjosé, V.; Meléndez, Á. M.; Niño-Gómez, M. E.; Mora-Seró, I. Controlling the Phase Segregation in Mixed Halide Perovskites through Nanocrystal Size. *ACS Energy Lett.* **2019**, *4* (1), 54–62. https://doi.org/10.1021/acsenergylett.8b02207.
(122) Clasen Hames, B.; Sánchez Sánchez, R.; Fakharuddin, A.; Mora-Seró, I. A Comparative Study of Light-Emitting Diodes Based on All-Inorganic Perovskite Nanoparticles (CsPbBr3) Synthesized at Room Temperature and by a Hot-Injection Method. *ChemPlusChem* **2018**, *83* (4), 294–299. https://doi.org/10.1002/cplu.201800014.
(123) Reichert, S.; An, Q.; Woo, Y.-W.; Walsh, A.; Vaynzof, Y.; Deibel, C. Probing the Ionic Defect Landscape in Halide Perovskite Solar Cells. *Nat. Commun.* **2020**, *11*, 6098. https://doi.org/10.5281/ZENODO.4049791.
(124) Meggiolaro, D.; Mosconi, E.; Angelis, F. D. Formation of Surface Defects Dominates Ion Migration in Lead-Halide Perovskites. *ACS Energy Lett.* **2019**, *4* (3), 779–785. https://doi.org/10.1021/ACSENERGYLETT.9B00247.
(125) Aina, S.; Villacampa, B.; Bernechea, M. Earth-Abundant Non-Toxic Perovskite Nanocrystals for Solution Processed Solar Cells. *Mater. Adv.* **2021**, *2* (13), 4140–4151. https://doi.org/10.1039/D1MA00245G.
(126) Shamsi, J.; Urban, A. S.; Imran, M.; De Trizio, L.; Manna, L. Metal Halide Perovskite Nanocrystals: Synthesis, Post-Synthesis Modifications, and Their Optical Properties. *Chem. Rev.* **2019**, *119* (5), 3296–3348. https://doi.org/10.1021/acs.chemrev.8b00644.
(127) Kar, M. R.; Ray, S.; Patra, B. K.; Bhaumik, S. State of the Art and Prospects of Metal Halide Perovskite Core@shell Nanocrystals and Nanocomposites. *Mater. Today Chem.* **2021**, *20*, 100424. https://doi.org/10.1016/j.mtchem.2021.100424.
(128) Huang, H.; Polavarapu, L.; Sichert, J. A.; Susha, A. S.; Urban, A. S.; Rogach, A. L. Colloidal Lead Halide Perovskite Nanocrystals: Synthesis, Optical Properties and Applications. *NPG Asia Mater.* **2016**, *8* (11). https://doi.org/10.1038/am.2016.167.
(129) Bederak, D.; Sukharevska, N.; Kahmann, S.; Abdu-Aguye, M.; Duim, H.; Dirin, D. N.; Kovalenko, M. V.; Portale, G.; Loi, M. A. On the Colloidal Stability of PbS Quantum Dots Capped with Methylammonium Lead Iodide Ligands. *ACS Appl. Mater. Interfaces* **2020**, *12* (47), 52959–52966. https://doi.org/10.1021/acsami.0c16646.
(130) Contreras-Bernal, L.; Aranda, C.; Valles-Pelarda, M.; Ngo, T. T.; Ramos-Terrón, S.; Gallardo, J. J.; Navas, J.; Guerrero, A.; Mora-Seró, I.; Idígoras, J.; Anta, J. A. Homeopathic Perovskite Solar Cells: Effect of Humidity during Fabrication on the Performance and Stability of the Device. *J. Phys. Chem. C* **2018**, *122* (10), 5341–5348. https://doi.org/10.1021/acs.jpcc.8b01558.
(131) Tsai, H.; Shrestha, S.; Vilá, R. A.; Huang, W.; Liu, C.; Hou, C.-H.; Huang, H.-H.; Wen, X.; Li, M.; Wiederrecht, G.; Cui, Y.; Cotlet, M.; Zhang, X.; Ma, X.; Nie, W. Bright and Stable Light-Emitting Diodes Made with Perovskite Nanocrystals Stabilized in Metal–Organic Frameworks. *Nat. Photonics 2021 1511* **2021**, *15* (11), 843–849. https://doi.org/10.1038/s41566-021-00857-0.

(132) Abargues, R.; Marqués-Hueso, J.; Canet-Ferrer, J.; Pedrueza, E.; Valdés, J. L.; Jiménez, E.; Martínez-Pastor, J. P. High-Resolution Electron-Beam Patternable Nanocomposite Containing Metal Nanoparticles for Plasmonics. *Nanotechnology* **2008**. https://doi.org/10.1088/0957-4484/19/35/355308.
(133) Aznar-Gadea, E.; Rodríguez-Canto, P. J.; Martínez-Pastor, J. P.; Lopatynskyi, A.; Chegel, V.; Abargues, R. Molecularly Imprinted Silver Nanocomposites for Explosive Taggant Sensing. *ACS Appl. Polym. Mater.* **2021**, *3* (6), 2960–2970. https://doi.org/10.1021/acsapm.1c00116.
(134) Tiede, D. O.; Rubino, A.; Calvo, M. E.; Galisteo-López, J. F.; Míguez, H. Monitoring, Modeling, and Optimization of Lead Halide Perovskite Nanocrystal Growth within Porous Matrices. *J. Phys. Chem. C* **2020**, *124* (14), 8041–8046. https://doi.org/10.1021/acs.jpcc.0c01750.
(135) Anaya, M.; Rubino, A.; Cristina Rojas, T.; Francisco Galisteo-López, J.; Ernesto Calvo, M.; Míguez, H.; Anaya, M.; Rubino, A.; Rojas, T. C.; Galisteo-López, J. F.; Calvo, M. E.; Míguez, H. Strong Quantum Confinement and Fast Photoemission Activation in CH 3 NH 3 PbI 3 Perovskite Nanocrystals Grown within Periodically Mesostructured Films. **2017**, *5*, 1601087. https://doi.org/10.1002/adom.201601087.
(136) Romero-Pérez, C.; Rubino, A.; Caliò, L.; Calvo, M. E.; Míguez, H. Optoelectronic Devices Based on Scaffold Stabilized Black-Phase CsPbI3 Nanocrystals. *Adv. Opt. Mater.* **2022**, *10* (6), 2102112. https://doi.org/10.1002/adom.202102112.
(137) Noguera-Gómez, J.; García-Tecedor, M.; Sánchez-Royo, J. F.; Liñán, L. M. V.; Mata, M. de la; Herrera-Collado, M.; Molina, S. I.; Abargues, R.; Giménez, S. Solution-Processed Ni-Based Nanocomposite Electrocatalysts: An Approach to Highly Efficient Electrochemical Water Splitting. *ACS Appl. Energy Mater.* **2021**, *4* (5), 5255–5264. https://doi.org/10.1021/ACSAEM.1C00776.
(138) Fragua, D.; Noguera-Gomez, J.; Rodríguez Cantó, P. J.; Valencia, L. M.; de la Mata, M.; Herrera, M.; Molina, S.; Abargues, R. Au–NiOx Nanocomposite for Hot Electron-Assisted Plasmonic Photocatalysis. *J. Mater. Chem. C* **2020**, *9*, 2394. https://doi.org/10.1039/D0TC01507E.
(139) Zhang, W.; Xiong, J.; Li, J.; Daoud, W. A. Mechanism of Water Effect on Enhancing the Photovoltaic Performance of Triple-Cation Hybrid Perovskite Solar Cells. *ACS Appl. Mater. Interfaces* **2019**, *11* (13), 12699–12708. https://doi.org/10.1021/acsami.8b20264.
(140) Hussein, G. A. M.; Nohman, A. K. H.; Attyia, K. M. A. Characterization of the Decomposition Course of Nickel Acetate Tetrahydrate in Air. *J. Therm. Anal. 1994 426* **1994**, *42* (6), 1155–1165. https://doi.org/10.1007/BF02546925.
(141) Acik, M.; Alam, T. M.; Guo, F.; Ren, Y.; Lee, B.; Rosenberg, R. A.; Mitchell, J. F.; Park, I. K.; Lee, G.; Darling, S. B. Substitutional Growth of Methylammonium Lead Iodide Perovskites in Alcohols. *Adv. Energy Mater.* **2018**, *8* (5), 1701726. https://doi.org/10.1002/AENM.201701726.
(142) Chirvony, V. S.; González-Carrero, S.; Suárez, I.; Galian, R. E.; Sessolo, M.; Bolink, H. J.; Martínez-Pastor, J. P.; Pérez-Prieto, J. Delayed Luminescence in Lead Halide Perovskite Nanocrystals. *J. Phys. Chem. C* **2017**, *121* (24), 13381–13390. https://doi.org/10.1021/acs.jpcc.7b03771.
(143) Li, F.; Cao, L.; Shi, S.; Gao, H.; Song, L.; Geng, C.; Bi, W.; Xu, S. Controlled Growth of CH 3 NH 3 PbBr 3 Perovskite Nanocrystals via a Water–Oil

Interfacial Synthesis Method. *Angew. Chem.* **2019**, *131* (49), 17795–17799. https://doi.org/10.1002/ANGE.201910225.
(144) Elward, J. M.; Chakraborty, A. Effect of Dot Size on Exciton Binding Energy and Electron-Hole Recombination Probability in CdSe Quantum Dots. *J. Chem. Theory Comput.* **2013**, *9* (10), 4351–4359. https://doi.org/10.1021/ct400485s.
(145) Noguera-Gómez, J.; Boix, P. P.; Abargues, R. Protocol for the Synthesis of Perovskite Nanocrystal Thin Films via in Situ Crystallization Method. *STAR Protoc.* **2023**, *4* (4), 102507. https://doi.org/10.1016/j.xpro.2023.102507.
(146) Noguera-Gómez, J.; Fernández-Guillen, I.; Betancur, P. F.; Chirvony, V. S.; Boix, P. P.; Abargues, R. Low-Demanding in Situ Crystallization Method for Tunable and Stable Perovskite Nanoparticle Thin Films. *Matter* **2022**. https://doi.org/10.1016/J.MATT.2022.07.017.
(147) Ansari, M. I. H.; Qurashi, A.; Nazeeruddin, M. K. Frontiers, Opportunities, and Challenges in Perovskite Solar Cells: A Critical Review. *J. Photochem. Photobiol. C Photochem. Rev.* **2018**, *35*, 1–24. https://doi.org/10.1016/J.JPHOTOCHEMREV.2017.11.002.
(148) Correa-Baena, J. P.; Saliba, M.; Buonassisi, T.; Grätzel, M.; Abate, A.; Tress, W.; Hagfeldt, A. Promises and Challenges of Perovskite Solar Cells. *Science* **2017**, *358* (6364), 739–744. https://doi.org/10.1126/SCIENCE.AAM6323/SUPPL_FILE/AAM6323_CORREA-BAENA_SM.PDF.
(149) Rockland, L. B. Saturated Salt Solutions for Static Control of Relative Humidity between 5° and 40° C. *Anal. Chem.* **1960**, *32* (10), 1375–1376. https://doi.org/10.1021/AC60166A055/ASSET/AC60166A055.FP.PNG_V03.
(150) Bai, Y.; Hao, M.; Ding, S.; Chen, P.; Wang, L. Surface Chemistry Engineering of Perovskite Quantum Dots: Strategies, Applications, and Perspectives. *Adv. Mater.* **2022**, *34* (4), 2105958. https://doi.org/10.1002/adma.202105958.
(151) Qu, R.; Gao, M.; Li, H.; Qi, X.; Liu, C.; Zhao, W.; Yan, J.; Zhang, Z. Hydrobromic Acid-Assisted Size Control of Formamidinium Lead Bromide Perovskite Quantum Dots at Room Temperature. *Opt. Mater.* **2021**, *113* (August 2020), 110776. https://doi.org/10.1016/j.optmat.2020.110776.
(152) R, S.; Nayak, V.; Jyothi, M. S.; Geetha Balakrishna, R. Review on Recent Advances of Core-Shell Structured Lead Halide Perovskites Quantum Dots. *J. Alloys Compd.* **2020**, *834*, 155246. https://doi.org/10.1016/j.jallcom.2020.155246.
(153) Wei, Y.; Cheng, Z.; Lin, J. An Overview on Enhancing the Stability of Lead Halide Perovskite Quantum Dots and Their Applications in Phosphor-Converted LEDs. *Chem. Soc. Rev.* **2019**, *48* (1), 310–350. https://doi.org/10.1039/C8CS00740C.
(154) Kim, Y.-H.; Park, J.; Kim, S.; Kim, J. S.; Xu, H.; Jeong, S.-H.; Hu, B.; Lee, T.-W. Exploiting the Full Advantages of Colloidal Perovskite Nanocrystals for Large-Area Efficient Light-Emitting Diodes. *Nat. Nanotechnol.* **2022**, *17* (6), 590–597. https://doi.org/10.1038/s41565-022-01113-4.
(155) Zhang, L.; Yuan, F.; Jiao, B.; Dong, H.; Li, J.; Wu, Z. Exploiting a Multiphase Pure Formamidinium Lead Perovskite for Efficient Green-Light-Emitting Diodes. *ACS Appl. Mater. Interfaces* **2021**, *13* (19), 23067–23073. https://doi.org/10.1021/acsami.1c00116.
(156) Benas, J.-S.; Liang, F.-C.; Chen, W.-C.; Hung, C.-W.; Chen, J.-Y.; Zhou, Y.; Han, S.-T.; Borsali, R.; Kuo, C.-C. Lewis Adduct Approach for Self-

Assembled Block Copolymer Perovskite Quantum Dots Composite toward Optoelectronic Application: Challenges and Prospects. *Chem. Eng. J.* **2022**, *431*, 133701. https://doi.org/10.1016/j.cej.2021.133701.
(157) Chen, S.; Zhang, Y.; Zhang, X.; Zhao, J.; Zhao, Z.; Su, X.; Hua, Z.; Zhang, J.; Cao, J.; Feng, J.; Wang, X.; Li, X.; Qi, J.; Li, J.; Gao, P. General Decomposition Pathway of Organic–Inorganic Hybrid Perovskites through an Intermediate Superstructure and Its Suppression Mechanism. *Adv. Mater.* **2020**, *32* (29), 2001107. https://doi.org/10.1002/adma.202001107.
(158) Zhou, F.; Li, Z.; Chen, H.; Wang, Q.; Ding, L.; Jin, Z. Application of Perovskite Nanocrystals (NCs)/Quantum Dots (QDs) in Solar Cells. *Nano Energy* **2020**, *73*, 104757. https://doi.org/10.1016/j.nanoen.2020.104757.
(159) Cao, J.; Zeng, X.; Yang, S.; Li, W.; Yan, C.; Huang, H.; Wang, Q.; Lu, J.; Yang, W. Water-Induced Nucleation Growth Kinetics Enhancement of Cesium Lead Bromide Perovskite Nanocrystals. *Cell Rep. Phys. Sci.* **2023**, *4* (3), 101305. https://doi.org/10.1016/j.xcrp.2023.101305.
(160) Gao, Y.; Lin, D.; Liu, P.; Shi, T.; Xie, W. Interaction Mechanism between Water Molecules and Perovskites. *Mater. Chem. Front.* **2024**, *8* (3), 785–799. https://doi.org/10.1039/D3QM00969F.
(161) Chen, B.; Wang, S.; Song, Y.; Li, C.; Hao, F. A Critical Review on the Moisture Stability of Halide Perovskite Films and Solar Cells. *Chem. Eng. J.* **2022**, *430*, 132701. https://doi.org/10.1016/j.cej.2021.132701.
(162) Zhou, C.; Tarasov, A. B.; Goodilin, E. A.; Chen, P.; Wang, H.; Chen, Q. Recent Strategies to Improve Moisture Stability in Metal Halide Perovskites Materials and Devices. *J. Energy Chem.* **2022**, *65*, 219–235. https://doi.org/10.1016/j.jechem.2021.05.035.
(163) Huang, J.; Tan, S.; Lund, P. D.; Zhou, H. Impact of H2O on Organic-Inorganic Hybrid Perovskite Solar Cells. *Energy Environ. Sci.* **2017**, *10* (11), 2284–2311. https://doi.org/10.1039/c7ee01674c.
(164) Zhang, C.-X.; Shen, T.; Guo, D.; Tang, L.-M.; Yang, K.; Deng, H.-X. Reviewing and Understanding the Stability Mechanism of Halide Perovskite Solar Cells. *InfoMat* **2020**, *2* (6), 1034–1056. https://doi.org/10.1002/inf2.12104.
(165) Wang, M.; Sun, H.; Cao, F.; Tian, W.; Li, L. Moisture-Triggered Self-Healing Flexible Perovskite Photodetectors with Excellent Mechanical Stability. *Adv. Mater.* **2021**, *33* (16), 2100625. https://doi.org/10.1002/adma.202100625.
(166) Hidalgo, J.; Perini, C. A. R.; Castro-Mendez, A.-F.; Jones, D.; Köbler, H.; Lai, B.; Li, R.; Sun, S.; Abate, A.; Correa-Baena, J.-P. Moisture-Induced Crystallographic Reorientations and Effects on Charge Carrier Extraction in Metal Halide Perovskite Solar Cells. *ACS Energy Lett.* **2020**, *5* (11), 3526–3534. https://doi.org/10.1021/acsenergylett.0c01964.
(167) Liu, K.; Luo, Y.; Jin, Y.; Liu, T.; Liang, Y.; Yang, L.; Song, P.; Liu, Z.; Tian, C.; Xie, L.; Wei, Z. Moisture-Triggered Fast Crystallization Enables Efficient and Stable Perovskite Solar Cells. *Nat. Commun.* **2022**, *13* (1), 4891. https://doi.org/10.1038/s41467-022-32482-y.
(168) Guan, J.; Yang, D.; Ma, J.; Shen, Y.; Xu, Q.; Hu, X. Ultra-Stable $CsPbBr_3$@PbBrOH Nanorods for Fluorescence Labeling Application Based on Methylimidazole-Assisted Synthesis. *J. Mater. Chem. B* **2023**, *11* (8), 1705–1712. https://doi.org/10.1039/D2TB02502G.
(169) Liu, K. K.; Liu, Q.; Yang, D. W.; Liang, Y. C.; Sui, L. Z.; Wei, J. Y.; Xue, G. W.; Zhao, W. B.; Wu, X. Y.; Dong, L.; Shan, C. X. Water-Induced

MAPbBr3@PbBr(OH) with Enhanced Luminescence and Stability. *Light Sci. Appl.* **2020**, *9* (1). https://doi.org/10.1038/S41377-020-0283-2.
(170) Palazon, F.; Urso, C.; De Trizio, L.; Akkerman, Q.; Marras, S.; Locardi, F.; Nelli, I.; Ferretti, M.; Prato, M.; Manna, L. Postsynthesis Transformation of Insulating Cs4PbBr6 Nanocrystals into Bright Perovskite CsPbBr3 through Physical and Chemical Extraction of CsBr. *ACS Energy Lett.* **2017**, *2* (10), 2445–2448. https://doi.org/10.1021/acsenergylett.7b00842.
(171) Sun, S.; Lu, M.; Guo, J.; Zhang, F.; Lu, P.; Fu, Y.; Bai, X.; Shi, Z.; Wu, Z.; Yu, W. W.; Zhang, Y. ZnBr2 Mediated Transformation from Nonluminescent Cs4PbBr6 to Green-Emitting Zn-Doped CsPbBr3/Cs4PbBr6 Nanocrystals for Electroluminescent Light-Emitting Diodes. *Chem. Eng. J.* **2022**, *433*, 133556. https://doi.org/10.1016/j.cej.2021.133556.
(172) Wu, L.; Hu, H.; Xu, Y.; Jiang, S.; Chen, M.; Zhong, Q.; Yang, D.; Liu, Q.; Zhao, Y.; Sun, B.; Zhang, Q.; Yin, Y. From Nonluminescent Cs4PbX6 (X = Cl, Br, I) Nanocrystals to Highly Luminescent CsPbX3 Nanocrystals: Water-Triggered Transformation through a CsX-Stripping Mechanism. *Nano Lett.* **2017**, *17* (9), 5799–5804. https://doi.org/10.1021/acs.nanolett.7b02896.
(173) Chen, M.; Hu, H.; Tan, Y.; Yao, N.; Zhong, Q.; Sun, B.; Cao, M.; Zhang, Q.; Yin, Y. Controlled Growth of Dodecapod-Branched CsPbBr3 Nanocrystals and Their Application in White Light Emitting Diodes. *Nano Energy* **2018**, *53*, 559–566. https://doi.org/10.1016/j.nanoen.2018.09.020.
(174) Rao, L.; Ding, X.; Du, X.; Liang, G.; Tang, Y.; Tang, K.; Zhang, J. Z. Ultrasonication-Assisted Synthesis of $CsPbBr_3$ and Cs_4PbBr_6 Perovskite Nanocrystals and Their Reversible Transformation. *Beilstein J. Nanotechnol.* **2019**, *10*, 666–676. https://doi.org/10.3762/bjnano.10.66.
(175) Huisman, B. A. H.; Palazon, F.; Bolink, H. J. Zero-Dimensional Hybrid Organic-Inorganic Lead Halides and Their Post-Synthesis Reversible Transformation into Three-Dimensional Perovskites. *Inorg. Chem.* **2021**, *60* (7), 5212–5216. https://doi.org/10.1021/acs.inorgchem.1c00212.
(176) Christians, J. A.; Miranda Herrera, P. A.; Kamat, P. V. Transformation of the Excited State and Photovoltaic Efficiency of CH3NH3PbI3 Perovskite upon Controlled Exposure to Humidified Air. *J. Am. Chem. Soc.* **2015**, *137* (4), 1530–1538. https://doi.org/10.1021/ja511132a.
(177) Zhang, L.; Ju, M.-G.; Liang, W. The Effect of Moisture on the Structures and Properties of Lead Halide Perovskites: A First-Principles Theoretical Investigation. *Phys. Chem. Chem. Phys.* **2016**, *18* (33), 23174–23183. https://doi.org/10.1039/C6CP01994C.
(178) Zhuang, L.; Zhai, L.; Li, Y.; Ren, H.; Li, M.; Lau, S. P. Mixed Dimensional 0D/3D Perovskite Heterostructure for Efficient Green Light-Emitting Diodes. *J. Mater. Chem. C* **2021**, *9* (40), 14318–14326. https://doi.org/10.1039/D1TC03611D.
(179) Cheng, S.; Zhong, H. What Happens When Halide Perovskites Meet with Water? *J. Phys. Chem. Lett.* **2022**, *13* (10), 2281–2290. https://doi.org/10.1021/acs.jpclett.2c00166.
(180) Tavakoli, F.; Salavati-Niasari, M.; Mohandes, F. Sonochemical Synthesis and Characterization of Lead Iodide Hydroxide Micro/Nanostructures. *Ultrason. Sonochem.* **2014**, *21* (1), 234–241. https://doi.org/10.1016/j.ultsonch.2013.05.007.
(181) Xu, Y.; Yu, L.; Peng, K.; Deng, Y.; Zhao, Y.; Zeng, X.; Yu, Y. Ultra-Stable Perovskite Quantum Dot Composites Encapsulated with Mesoporous SiO2

and PbBr(OH) for White Light-Emitting Diodes. *Luminescence* **2023**, *38* (5), 536–545. https://doi.org/10.1002/bio.4491.
(182) Liu, G.; Zhou, H.; Che, Q.; Liu, B.; Li, J.; Cao, B.; Liu, Z. A Novel Phosphor of Cu^{+} -Doped PbBrOH: Preparation, Luminescence Mechanism, and Outstanding Properties. *J. Mater. Chem. C* **2021**, *9* (29), 9178–9187. https://doi.org/10.1039/D1TC01855H.
(183) Xue, G.-W.; Liu, K.-K.; Lv, C.-F.; Chang, Y.; Zhao, W.-B.; Song, S.-Y.; Liang, Y.; Shan, C.-X. MAPbBrxCl3-x Quantum Dots in Pb(OH)Br for Stable Blue Light-Emitting Devices. *J. Lumin.* **2021**, *236*, 118158. https://doi.org/10.1016/j.jlumin.2021.118158.
(184) Sharma, S. K.; Phadnis, C.; Das, T. K.; Kumar, A.; Kavaipatti, B.; Chowdhury, A.; Yella, A. Reversible Dimensionality Tuning of Hybrid Perovskites with Humidity: Visualization and Application to Stable Solar Cells. *Chem. Mater.* **2019**, *31* (9), 3111–3117. https://doi.org/10.1021/acs.chemmater.8b04115.
(185) Akkerman, Q. A.; Park, S.; Radicchi, E.; Nunzi, F.; Mosconi, E.; De Angelis, F.; Brescia, R.; Rastogi, P.; Prato, M.; Manna, L. Nearly Monodisperse Insulator Cs4PbX6 (X = Cl, Br, I) Nanocrystals, Their Mixed Halide Compositions, and Their Transformation into CsPbX3 Nanocrystals. *Nano Lett.* **2017**, *17* (3), 1924–1930. https://doi.org/10.1021/acs.nanolett.6b05262.
(186) Liu, Z.; Bekenstein, Y.; Ye, X.; Nguyen, S. C.; Swabeck, J.; Zhang, D.; Lee, S.-T.; Yang, P.; Ma, W.; Alivisatos, A. P. Ligand Mediated Transformation of Cesium Lead Bromide Perovskite Nanocrystals to Lead Depleted Cs4PbBr6 Nanocrystals. *J. Am. Chem. Soc.* **2017**, *139* (15), 5309–5312. https://doi.org/10.1021/jacs.7b01409.
(187) Cao, F.; Yu, D.; Xu, X.; Han, Z.; Zeng, H. CsPbBr3@Cs4PbBr6 Emitter-in-Host Composite: Fluorescence Origin and Interphase Energy Transfer. *J. Phys. Chem. C* **2021**, *125* (1), 3–19. https://doi.org/10.1021/acs.jpcc.0c08100.
(188) Kim, K. S.; O'Leary, T. J.; Winograd, Nicholas. X-Ray Photoelectron Spectra of Lead Oxides. *Anal. Chem.* **1973**, *45* (13), 2214–2218. https://doi.org/10.1021/ac60335a009.
(189) Yang, X.; Mu, Y.; Liu, S. The Interaction between Iron Cyanide and Lead Ions in Pyrite Flotation. *Molecules* **2024**, *29* (11), 2517. https://doi.org/10.3390/molecules29112517.
(190) Yun, R.; Yang, H.; Li, Y.; Liu, Y.; Chu, Y.; Wu, S.; Liu, X.; Zhang, X.; Zhang, L.; Li, X. Inorganic Ligand Triggered Transformation from Cs4PbBr6 Nanocrystals to Blue-Emitting CsPbBr3 Nanoplatelets. *Chem. Mater.* **2023**, *35* (2), 424–431. https://doi.org/10.1021/acs.chemmater.2c02794.
(191) Li, X.-B.; Huang, W.-T.; Zhang, R.-R.; Guo, Y.; Yang, H.-J.; He, X.-Y.; Yu, M.-X.; Wang, L.-X.; Zhang, Q.-T. Synthesis and Luminescence of Ultrasmall CsPbBr3 Nanocrystals and CsPbBr3/Cs4PbBr6 Composites by One-Pot Method. *Rare Met.* **2022**, *41* (4), 1230–1238. https://doi.org/10.1007/s12598-021-01856-4.
(192) Kang, S.; Mauchauffé, R.; You, Y. S.; Moon, S. Y. Insights into the Role of Plasma in Atmospheric Pressure Chemical Vapor Deposition of Titanium Dioxide Thin Films. *Sci. Rep.* **2018**, *8* (1), 16684. https://doi.org/10.1038/s41598-018-35154-4.
(193) Rao, L.; Zhang, Q.; Sun, B.; Wen, M.; Zhang, J.; Yu, S.; Fu, T.; Niu, X. CsPbBr3/Cs4PbBr6 Heterostructure Solids with High Stability and

Photoluminescence for White Light-Emitting Diodes. *J. Alloys Compd.* **2022**, *919*, 165857. https://doi.org/10.1016/j.jallcom.2022.165857.
(194) Li, J.; Liu, G.; Lu, Y.; Liu, Z. Greatly Enhanced Stability of $CsPbBr_3$@PbBrOH through Water Induction. *J. Mater. Chem. C* **2022**, *10* (42), 15843–15850. https://doi.org/10.1039/D2TC03322D.
(195) Meheretu, G. M.; Worku, A. K.; Yihunie, M. T.; Koech, R. K.; Wubetu, G. A. The Recent Advancement of Outdoor Performance of Perovskite Photovoltaic Cells Technology. *Heliyon* **2024**, *10* (17), e36710. https://doi.org/10.1016/j.heliyon.2024.e36710.
(196) Zhao, J.; Deng, Y.; Wei, H.; Zheng, X.; Yu, Z.; Shao, Y.; Shield, J. E.; Huang, J. Strained Hybrid Perovskite Thin Films and Their Impact on the Intrinsic Stability of Perovskite Solar Cells. *Sci. Adv.* **2017**, *3* (11), eaao5616. https://doi.org/10.1126/sciadv.aao5616.
(197) Khatoon, S.; Kumar Yadav, S.; Chakravorty, V.; Singh, J.; Bahadur Singh, R.; Hasnain, M. S.; Hasnain, S. M. M. Perovskite Solar Cell's Efficiency, Stability and Scalability: A Review. *Mater. Sci. Energy Technol.* **2023**, *6*, 437–459. https://doi.org/10.1016/j.mset.2023.04.007.
(198) Zhang, D.; Li, D.; Hu, Y.; Mei, A.; Han, H. Degradation Pathways in Perovskite Solar Cells and How to Meet International Standards. *Commun. Mater.* **2022**, *3* (1), 1–14. https://doi.org/10.1038/s43246-022-00281-z.
(199) Sutton, R. J.; Filip, M. R.; Haghighirad, A. A.; Sakai, N.; Wenger, B.; Giustino, F.; Snaith, H. J. Cubic or Orthorhombic? Revealing the Crystal Structure of Metastable Black-Phase CsPbI3 by Theory and Experiment. *ACS Energy Lett.* **2018**, *3* (8), 1787–1794. https://doi.org/10.1021/acsenergylett.8b00672.
(200) Marronnier, A.; Roma, G.; Boyer-Richard, S.; Pedesseau, L.; Jancu, J.-M.; Bonnassieux, Y.; Katan, C.; Stoumpos, C. C.; Kanatzidis, M. G.; Even, J. Anharmonicity and Disorder in the Black Phases of Cesium Lead Iodide Used for Stable Inorganic Perovskite Solar Cells. *ACS Nano* **2018**, *12* (4), 3477–3486. https://doi.org/10.1021/acsnano.8b00267.
(201) Jiang, Y.; Yuan, J.; Ni, Y.; Yang, J.; Wang, Y.; Jiu, T.; Yuan, M.; Chen, J. Reduced-Dimensional α-CsPbX3 Perovskites for Efficient and Stable Photovoltaics. *Joule* **2018**, *2* (7), 1356–1368. https://doi.org/10.1016/j.joule.2018.05.004.
(202) Swarnkar, A.; Marshall, A. R.; Sanehira, E. M.; Chernomordik, B. D.; Moore, D. T.; Christians, J. A.; Chakrabarti, T.; Luther, J. M. Quantum Dot–Induced Phase Stabilization of α-$CsPbI_3$ Perovskite for High-Efficiency Photovoltaics. *Science* **2016**, *354* (6308), 92–95. https://doi.org/10.1126/science.aag2700.
(203) Hu, S.; Tapa, A. R.; Zhou, X.; Pang, S.; Lira-Cantu, M.; Xie, H. Formation and Stabilization of Metastable Halide Perovskite Phases for Photovoltaics. *Cell Rep. Phys. Sci.* **2024**, *5* (2). https://doi.org/10.1016/j.xcrp.2024.101825.
(204) Shah, S.-F.-A.; Jeong, I.; Park, J.; Shin, D.; Hwang, I.; Tsvetkov, N.; Kim, D.; Gwak, J.; Park, J. H.; Seok, S. I.; Kim, K.; Min, H. Efficient and Stable CsPbI3 Perovskite Solar Cells with Spontaneously Formed 2D-Cs2PbI2Cl2 at the Buried Interface. *Cell Rep. Phys. Sci.* **2024**, *5* (5), 101935. https://doi.org/10.1016/j.xcrp.2024.101935.
(205) Al-Ashouri, A.; Köhnen, E.; Li, B.; Magomedov, A.; Hempel, H.; Caprioglio, P.; Márquez, J. A.; Morales Vilches, A. B.; Kasparavicius, E.; Smith, J. A.; Phung, N.; Menzel, D.; Grischek, M.; Kegelmann, L.; Skroblin, D.; Gollwitzer, C.; Malinauskas, T.; Jošt, M.; Matič, G.; Rech, B.; Schlatmann, R.;

Topič, M.; Korte, L.; Abate, A.; Stannowski, B.; Neher, D.; Stolterfoht, M.; Unold, T.; Getautis, V.; Albrecht, S. Monolithic Perovskite/Silicon Tandem Solar Cell with >29% Efficiency by Enhanced Hole Extraction. *Science* **2020**, *370* (6522), 1300–1309. https://doi.org/10.1126/science.abd4016.
(206) Li, H.; Zhang, W. Perovskite Tandem Solar Cells: From Fundamentals to Commercial Deployment. *Chem. Rev.* **2020**, *120* (18), 9835–9950. https://doi.org/10.1021/acs.chemrev.9b00780.
(207) Xu, D.; Wu, M.; Bai, Y.; Wang, B.; Zhou, H.; Fan, Z.; Zhang, N.; Tan, J.; Li, H.; Bian, H.; Liu, Z. Record-Efficiency Inverted CsPbI3 Perovskite Solar Cells Enabled by Rearrangement and Hydrophilic Modification of SAMs. *Adv. Funct. Mater. n/a* (n/a), 2412946. https://doi.org/10.1002/adfm.202412946.
(208) Qiu, J.; Mei, X.; Zhang, M.; Wang, G.; Zou, S.; Wen, L.; Huang, J.; Hua, Y.; Zhang, X. Dipolar Chemical Bridge Induced CsPbI3 Perovskite Solar Cells with 21.86 % Efficiency. *Angew. Chem. Int. Ed.* **2024**, *63* (18), e202401751. https://doi.org/10.1002/anie.202401751.
(209) Tan, X.; Wang, S.; Zhang, Q.; Liu, H.; Li, W.; Zhu, L.; Chen, H. Stabilizing CsPbI3 Perovskite for Photovoltaic Applications. *Matter* **2023**, *6* (3), 691–727. https://doi.org/10.1016/j.matt.2022.12.012.
(210) Wright, M.; Stefani, B. V.; Jones, T. W.; Hallam, B.; Soeriyadi, A.; Wang, L.; Altermatt, P.; Snaith, H. J.; Wilson, G. J.; Bonilla, R. S. Design Considerations for the Bottom Cell in Perovskite/Silicon Tandems: A Terawatt Scalability Perspective. *Energy Environ. Sci.* **2023**, *16* (10), 4164–4190. https://doi.org/10.1039/D3EE00952A.
(211) Montecucco, R.; Pica, G.; Romano, V.; De Boni, F.; Cavalli, S.; Bruni, G.; Quadrivi, E.; De Bastiani, M.; Prato, M.; Po, R.; Grancini, G. The Stabilization of CsPbI3−Br Phase by Lowering Annealing Temperature for Efficient All-Inorganic Perovskite Solar Cells. *Sol. RRL* **2023**, *7* (20), 2300358. https://doi.org/10.1002/solr.202300358.
(212) Haque, F.; Wright, M.; Mahmud, M. A.; Yi, H.; Wang, D.; Duan, L.; Xu, C.; Upama, M. B.; Uddin, A. Effects of Hydroiodic Acid Concentration on the Properties of CsPbI3 Perovskite Solar Cells. *ACS Omega* **2018**, *3* (9), 11937–11944. https://doi.org/10.1021/acsomega.8b01589.
(213) Gao, Y.; Xu, W.; He, F.; Fan, T.; Cai, W.; Zhang, X.; Wei, G. Boosting Performance of CsPbI3 Perovskite Solar Cells via the Synergy of Hydroiodic Acid and Deionized Water. *Adv. Energy Sustain. Res.* **2022**, *3* (2), 2100149. https://doi.org/10.1002/aesr.202100149.
(214) Li, B.; Zhang, Y.; Fu, L.; Yu, T.; Zhou, S.; Zhang, L.; Yin, L. Surface Passivation Engineering Strategy to Fully-Inorganic Cubic CsPbI3 Perovskites for High-Performance Solar Cells. *Nat. Commun.* **2018**, *9* (1), 1076. https://doi.org/10.1038/s41467-018-03169-0.
(215) Chakrabarti, A.; Lefler, B. M.; Fafarman, A. T. Scaffold-Enforced Nanoscale Crystalline Order Supersedes Interfacial Interactions in Driving CsPbI3 Perovskite Phase Stability. *J. Phys. Chem. C* **2022**, *126* (51), 21708–21715. https://doi.org/10.1021/acs.jpcc.2c05794.
(216) Shpatz Dayan, A.; Cohen, B.-E.; Aharon, S.; Tenailleau, C.; Wierzbowska, M.; Etgar, L. Enhancing Stability and Photostability of CsPbI3 by Reducing Its Dimensionality. *Chem. Mater.* **2018**, *30* (21), 8017–8024. https://doi.org/10.1021/acs.chemmater.8b03709.
(217) Li, F.; Pei, Y.; Xiao, F.; Zeng, T.; Yang, Z.; Xu, J.; Sun, J.; Peng, B.; Liu, M. Tailored Dimensionality to Regulate the Phase Stability of Inorganic Cesium

Lead Iodide Perovskites. *Nanoscale* **2018**, *10* (14), 6318–6322. https://doi.org/10.1039/C8NR00758F.
(218) Zhang, Y.; Yang, Y.; Zhang, X.; Wang, T.; Nian, L.; Rong, Q.; Zhou, G.; Li, N. Low Temperature Preparation of All-Inorganic CsPbI 3 Perovskite Solar Cells with Ethanediamine as Additive. *Org. Electron.* **2020**, *87*, 105940. https://doi.org/10.1016/j.orgel.2020.105940.
(219) Li, T.; Wu, Y.; Liu, Z.; Yang, Y.; Luo, H.; Li, L.; Chen, P.; Gao, X.; Tan, H. Cesium Acetate-Assisted Crystallization for High-Performance Inverted CsPbI 3 Perovskite Solar Cells. *Nanotechnology* **2022**, *33* (37), 375205. https://doi.org/10.1088/1361-6528/ac76d5.
(220) Chang, X.; Fang, J.; Fan, Y.; Luo, T.; Su, H.; Zhang, Y.; Lu, J.; Tsetseris, L.; Anthopoulos, T. D.; Liu, S. (Frank); Zhao, K. Printable CsPbI3 Perovskite Solar Cells with PCE of 19% via an Additive Strategy. *Adv. Mater.* **2020**, *32* (40), 2001243. https://doi.org/10.1002/adma.202001243.
(221) Duan, L.; Zhang, H.; Liu, M.; Grätzel, M.; Luo, J. Phase-Pure γ-CsPbI3 for Efficient Inorganic Perovskite Solar Cells. *ACS Energy Lett.* **2022**, *7* (9), 2911–2918. https://doi.org/10.1021/acsenergylett.2c01219.
(222) Wang, Y.; Liu, X.; Zhang, T.; Wang, X.; Kan, M.; Shi, J.; Zhao, Y. The Role of Dimethylammonium Iodide in CsPbI3 Perovskite Fabrication: Additive or Dopant? *Angew. Chem. Int. Ed.* **2019**, *58* (46), 16691–16696. https://doi.org/10.1002/anie.201910800.
(223) Shekarnoush, M.; Aguirre-Tostado, F. S.; López, M. Q. Stability of CsPbI 3 with Divalent Cations Incorporated *via* Mechanochemical Alloying. *Mater. Adv.* **2024**, *5* (9), 3742–3750. https://doi.org/10.1039/D4MA00034J.
(224) Li, Z.; Xu, J.; Zhou, S.; Zhang, B.; Liu, X.; Dai, S.; Yao, J. CsBr-Induced Stable CsPbI3–xBrx (x < 1) Perovskite Films at Low Temperature for Highly Efficient Planar Heterojunction Solar Cells. *ACS Appl. Mater. Interfaces* **2018**, *10* (44), 38183–38192. https://doi.org/10.1021/acsami.8b11474.
(225) Eperon, G. E.; Paternò, G. M.; Sutton, R. J.; Zampetti, A.; Haghighirad, A. A.; Cacialli, F.; Snaith, H. J. Inorganic Caesium Lead Iodide Perovskite Solar Cells. *J. Mater. Chem. A* **2015**, *3* (39), 19688–19695. https://doi.org/10.1039/C5TA06398A.
(226) Ke, W.; Spanopoulos, I.; Stoumpos, C. C.; Kanatzidis, M. G. Myths and Reality of HPbI3 in Halide Perovskite Solar Cells. *Nat. Commun. 2018 91* **2018**, *9* (1), 1–9. https://doi.org/10.1038/s41467-018-07204-y.
(227) Marshall, A. R.; Sansom, H. C.; McCarthy, M. M.; Warby, J. H.; Ashton, O. J.; Wenger, B.; Snaith, H. J. Dimethylammonium: An A-Site Cation for Modifying CsPbI3. *Sol. RRL* **2021**, *5* (1), 2000599. https://doi.org/10.1002/solr.202000599.
(228) Bian, H.; Wang, H.; Li, Z.; Zhou, F.; Xu, Y.; Zhang, H.; Wang, Q.; Ding, L.; Liu, S. (Frank); Jin, Z. Unveiling the Effects of Hydrolysis-Derived DMAI/DMAPbI Intermediate Compound on the Performance of CsPbI3 Solar Cells. *Adv. Sci.* **2020**, *7* (9), 1902868. https://doi.org/10.1002/advs.201902868.
(229) Minguez-Avellan, M.; Farinós-Navajas, N.; Noguera-Gómez, J.; Sagra Rodríguez, V.; Vallés-Pelarda, M.; Momblona, C.; Ripolles, T. S.; Boix, P. P.; Abargues, R. Perovskite Nanocomposite: A Step Toward Photocatalytic Degradation of Organic Dyes. *Sol. RRL* **2024**, *8* (19), 2400449. https://doi.org/10.1002/solr.202400449.
(230) Elliott, R. J. Intensity of Optical Absorption by Excitons. *Phys. Rev.* **1957**, *108* (6), 1384–1389. https://doi.org/10.1103/PhysRev.108.1384.

(231) Wang, J. T.-W.; Wang, Z.; Pathak, S.; Zhang, W.; deQuilettes, D. W.; Wisnivesky-Rocca-Rivarola, F.; Huang, J.; Nayak, P. K.; Patel, J. B.; Mohd Yusof, H. A.; Vaynzof, Y.; Zhu, R.; Ramirez, I.; Zhang, J.; Ducati, C.; Grovenor, C.; Johnston, M. B.; Ginger, D. S.; Nicholas, R. J.; Snaith, H. J. Efficient Perovskite Solar Cells by Metal Ion Doping. *Energy Environ. Sci.* **2016**, *9* (9), 2892–2901. https://doi.org/10.1039/C6EE01969B.
(232) Zhao, H.; Xu, Z.; Che, Y.; Han, Y.; Yang, S.; Duan, C.; Cui, J.; Dai, S.; Liu, Z.; Liu, S. (Frank). Simultaneous Dual-Interface and Bulk Defect Passivation for High-Efficiency and Stable CsPbI2Br Perovskite Solar Cells. *J. Power Sources* **2021**, *492*, 229580. https://doi.org/10.1016/j.jpowsour.2021.229580.
(233) Tress, W.; Yavari, M.; Domanski, K.; Yadav, P.; Niesen, B.; Baena, J. P. C.; Hagfeldt, A.; Graetzel, M. Interpretation and Evolution of Open-Circuit Voltage, Recombination, Ideality Factor and Subgap Defect States during Reversible Light-Soaking and Irreversible Degradation of Perovskite Solar Cells. *Energy Environ. Sci.* **2018**, *11* (1), 151–165. https://doi.org/10.1039/C7EE02415K.
(234) Wang, K.-L.; Lu, H.; Li, M.; Chen, C.-H.; Bo Zhang, D.-; Chen, J.; Wu, J.-J.; Zhou, Y.-H.; Wang, X.-Q.; Su, Z.-H.; Shi, Y.-R.; Tian, Q.-S.; Ni, Y.-X.; Gao, X.-Y.; Zakeeruddin, S. M.; Grätzel, M.; Wang, Z.-K.; Liao, L.-S. Ion–Dipole Interaction Enabling Highly Efficient CsPbI3 Perovskite Indoor Photovoltaics. *Adv. Mater.* **2023**, *35* (31), 2210106. https://doi.org/10.1002/adma.202210106.
(235) Lau, C. F. J.; Wang, Z.; Sakai, N.; Zheng, J.; Liao, C. H.; Green, M.; Huang, S.; Snaith, H. J.; Ho-Baillie, A. Fabrication of Efficient and Stable CsPbI3 Perovskite Solar Cells through Cation Exchange Process. *Adv. Energy Mater.* **2019**, *9* (36), 1901685. https://doi.org/10.1002/aenm.201901685.
(236) Ho, J. K. W.; Yin, H.; So, S. K. From 33% to 57% – an Elevated Potential of Efficiency Limit for Indoor Photovoltaics. *J. Mater. Chem. A* **2020**, *8* (4), 1717–1723. https://doi.org/10.1039/C9TA11894B.
(237) Frischknecht, R. Methodology Guidelines on Life Cycle Assessment of Photovoltaic 2020.
(238) Iqbal, Z.; Zu, F.; Musiienko, A.; Gutierrez-Partida, E.; Köbler, H.; Gries, T. W.; Sannino, G. V.; Canil, L.; Koch, N.; Stolterfoht, M.; Neher, D.; Pavone, M.; Muñoz-García, A. B.; Abate, A.; Wang, Q. Interface Modification for Energy Level Alignment and Charge Extraction in CsPbI3 Perovskite Solar Cells. *ACS Energy Lett.* **2023**, *8* (10), 4304–4314. https://doi.org/10.1021/acsenergylett.3c01522.
(239) Joint Research (European Commission); Pant, R.; Zampori, L. *Suggestions for Updating the Organisation Environmental Footprint (OEF) Method*; Publications Office of the European Union, 2019.
(240) Gong, J.; Darling, S. B.; You, F. Perovskite Photovoltaics: Life-Cycle Assessment of Energy and Environmental Impacts. *Energy Environ. Sci.* **2015**, *8* (7), 1953–1968. https://doi.org/10.1039/C5EE00615E.
(241) Piccinno, F.; Hischier, R.; Seeger, S.; Som, C. From Laboratory to Industrial Scale: A Scale-up Framework for Chemical Processes in Life Cycle Assessment Studies. *J. Clean. Prod.* **2016**, *135*, 1085–1097. https://doi.org/10.1016/j.jclepro.2016.06.164.
(242) Third Update Location- and Waste-Specific Life Cycle Inventories of Waste Treatment. https://doi.org/Preprint at https://www.doka.ch/publications.htm (2023).
(243) A Method for Synthesis of Organic Iodides. **2023**, 1–19.

(244) Coeck, R.; Vos, D. E. D. One-Pot Reductive Amination of Carboxylic Acids: A Sustainable Method for Primary Amine Synthesis. *Green Chem.* **2020**, *22* (15), 5105–5114. https://doi.org/10.1039/D0GC01441A.
(245) Coeck, R.; Berden, S.; Vos, D. E. D. Sustainable Hydrogenation of Aliphatic Acyclic Primary Amides to Primary Amines with Recyclable Heterogeneous Ruthenium–Tungsten Catalysts. *Green Chem.* **2019**, *21* (19), 5326–5335. https://doi.org/10.1039/C9GC01310E.
(246) Bobba, S.; Deorsola, F. A.; Blengini, G. A.; Fino, D. LCA of Tungsten Disulphide (WS2) Nano-Particles Synthesis: State of Art and *from-Cradle-to-Gate* LCA. *J. Clean. Prod.* **2016**, *139*, 1478–1484. https://doi.org/10.1016/j.jclepro.2016.07.091.
(247) Joint Research Centre (European Commission); Ceriani, L.; Versteeg, D.; Crenna, E.; Saouter, E.; Zampori, L.; Pant, R.; Biganzoli, F.; Sala, S. *Environmental Footprint: Update of Life Cycle Impact Assessment Methods : Ecotoxicity Freshwater, Human Toxicity Cancer, and Non Cancer*; Publications Office of the European Union, 2020.
(248) Rosenbaum, R. K.; Huijbregts, M. A. J.; Henderson, A. D.; Margni, M.; McKone, T. E.; van de Meent, D.; Hauschild, M. Z.; Shaked, S.; Li, D. S.; Gold, L. S.; Jolliet, O. USEtox Human Exposure and Toxicity Factors for Comparative Assessment of Toxic Emissions in Life Cycle Analysis: Sensitivity to Key Chemical Properties. *Int. J. Life Cycle Assess.* **2011**, *16* (8), 710–727. https://doi.org/10.1007/s11367-011-0316-4.

Appendixes

List of Figures

List of Tables

List of Abbreviations

0D	Zero Dimensional
ATR-FTIR	Attenuated Total Reflectance Fourier Transform Infrared Spectroscopy
CB	Conduction Band
$CsPbI_3$	Cesium Lead Triiodide
CTL	Charge Transport Layer
DMAI	Dimethylammonium Iodide
DMF	N,N-Dimethylformamide
DMSO	Dimethyl sulfoxide
Eg	Bandgap
ETL	Electron Transport Layer
F	Forward Scan (Jsc to Voc)
FF	Fill Factor
FTO	Fluorine-doped Tin Oxide
FWHM	Full Width at Half Maximum
GWP	Global Warming Potential
HOMO	Highest Occupied Molecular Orbital
HTL	Hole Transport Layer
Jsc	Short-Circuit Current Density
J-V	Current Density-Voltage
LUMO	Lowest Unoccupied Molecular Orbital
$MAPbBr_3$	Methylammonium Lead Bromide
MPPT	Maximum Power Point Tracking
NC	Nanocrystral
PCE	Power Conversion Efficiency
PL	Photoluminescence
PLQY	Photoluminescence Quantum Yield
PNCs	Perovskite Nanocrystals
ppm	Parts Per Million
PSC	Perovskite Solar Cell

PVs	Photovoltaics
R	Reverse Scan (Voc to Jsc)
RH	Relative Humidity
Rs	Series Resistance
Rsh	Shunt Resistance
SDSs	Safety Data Sheets
SEM	Scanning Electron Microscopy
SOP	Standard Operating Procedure
Spiro-OMeTAD	2,2',7,7'-Tetrakis[N,N-di(4-methoxyphenyl)amino]-9,9'-spirobifluorene (HTM)
TEM	Transmission Electron Microscopy
TCO	Transparent Conductive Oxide
TRPL	Time-Resolved Photoluminescence
UV-Vis	Ultraviolet-Visible Spectroscopy
VB	Valence Band
Voc	Open-Circuit Voltage
XPS	X-ray Photoelectron Spectroscopy
XRD	X-ray Diffraction

Keywords

Crystallization

In situ

LEDs

Materials

Metal halide perovskites

Nanocomposite

Nanocrystal

Optoelectronics

Passivation

Photovoltaics

Humidity

Semiconductors

Solution-processed

Synthesis

List of Publications

Published

(1) Minguez-Avellan, M.; Farinós-Navajas, N.; **Noguera-Gómez, J**.; Sagra Rodríguez, V.; Vallés-Pelarda, M.; Momblona, C.; Ripolles, T. S.; Boix, P. P.; Abargues, R. Perovskite Nanocomposite: A Step Toward Photocatalytic Degradation of Organic Dyes. *Solar RRL* **2024**, *8* (19), 2400449. https://doi.org/10.1002/solr.202400449.

(2) **Noguera-Gómez, J**.; Boix, P. P.; Abargues, R. Protocol for the Synthesis of Perovskite Nanocrystal Thin Films via in Situ Crystallization Method. *STAR Protocols* **2023**, *4* (4), 102507. https://doi.org/10.1016/j.xpro.2023.102507.

(3) **Noguera-Gómez, J**.; Fernández-Guillen, I.; Betancur, P. F.; Chirvony, V. S.; Boix, P. P.; Abargues, R. Low-Demanding in Situ Crystallization Method for Tunable and Stable Perovskite Nanoparticle Thin Films. *Matter* **2022**. https://doi.org/10.1016/J.MATT.2022.07.017.

(4) Sanchez-Alarcon, I.; **Noguera-Gomez, J**.; Chirvony, V. S.; Pashaeiadl, H.; Boix, P. P.; Alarcón-Flores, G.; Martínez-Pastor, J. P.; Abargues, R. Spray-Driven Halide Exchange in Solid-State CsPbX3 Nanocrystal Films. *Nanoscale* **2022**. https://doi.org/10.1039/D2NR03262G.

(5) **Noguera-Gómez, J**.; García-Tecedor, M.; Sánchez-Royo, J. F.; Liñán, L. M. V.; Mata, M. de la; Herrera-Collado, M.; Molina, S. I.; Abargues, R.; Giménez, S. Solution-Processed Ni-Based Nanocomposite Electrocatalysts: An Approach to Highly Efficient Electrochemical Water Splitting. *ACS Applied Energy Materials* **2021**, *4* (5), 5255–5264. https://doi.org/10.1021/ACSAEM.1C00776.

(6) Silva, A. S.-D.; **Noguera-Gomez, J**.; Rodríguez-Canto, P. J.; Sanchez-Royo, J. F.; Cantarero, A.; Gómez, C. M.; Abargues, R. In Situ Synthesis of Conducting Polymers: A Novel Approach toward Polymer Thermoelectrics. *The Journal of Physical Chemistry C* **2020**, *124* (42), 22884–22892. https://doi.org/10.1021/ACS.JPCC.0C05333.

(7) Andres-Penares, D.; Canet-Albiach, R.; **Noguera-Gomez, J**.; Martínez-Pastor, J. P.; Abargues, R.; Sánchez-Royo, J. F. Two-Dimensional Indium Selenide for Sulphur Vapour Sensing Applications. *Nanomaterials 2020, Vol. 10, Page 1396* **2020**, *10* (7), 1396. https://doi.org/10.3390/NANO10071396.

(8) Fragua, D.; **Noguera-Gomez, J**.; Rodríguez Cantó, P. J.; Valencia, L. M.; de la Mata, M.; Herrera, M.; Molina, S.; Abargues, R. Au–NiOx Nanocomposite for Hot Electron-Assisted Plasmonic Photocatalysis. *Journal of Materials Chemistry C* **2020**, *9*, 2394. https://doi.org/10.1039/D0TC01507E.

In Process

Jaume Noguera-Gómez, Víctor Sagra-Rodríguez, Vladimir S. Chirvony,*, Miriam Minguez-Avellán, Mahesh Eledath Changarath, Juan F. Sánchez-Royo, Juan P. Martínez-Pastor, Pablo P. Boix, Rafael Abargues. *Passivation Mechanism in Highly Luminescent Nanocomposite-based $CH_3NH_3PbBr_3$ Perovskite Nanocrystals*.

Jaume Noguera-Gómez, Miriam Minguez-Avellán, Marta Vallés-Pelarda, Victor Sagra Rodríguez, Sandy Sánchez, Rosario Vidal, Alberola-Borràs J.A, Rafael Abargues, Pablo P. Boix. *Rapid Straightforward and Green Synthesis of all-inorganic $CsPbI_3$ Perovskite Solar Cells via Nickel Acetate Incorporation.*